

Jordan Journal of Mechanical and Industrial Engineering (JJMIE)

JJMIE is a high-quality scientific journal devoted to fields of Mechanical and Industrial Engineering. It is published by the Hashemite University in corporation with the Jordanian Scientific Research Support Fund.

EDITORIAL BOARD

Editor-in-Chief

Prof. Mousa S. Mohsen

Editorial board

Prof. Bilal A. Akash
Hashemite University

Prof. Adnan Z. Al-Kilany
University of Jordan

Prof. Ayman A. Al-Maaitah
Mutah University

Prof. Moh'd A. Al-Nimr
Jordan University of Science and Technology

Prof. Ali A. Badran
University of Jordan

Prof. Naseem M. Sawaqed
Mutah University

Assistant Editor

Dr. Ahmad Al-Ghandoor
Hashemite University

THE INTERNATIONAL ADVISORY BOARD

Abu-Qudais, Mohammad
Jordan University of Science & Technology, Jordan

Abu-Mulaweh, Hosni
Purdue University at Fort Wayne, USA

Afaneh Abdul-Hafiz
Robert Bosch Corporation, USA

Afonso, Maria Dina
Institute Superior Tecnico, Portugal

Badiru, Adedji B.
The University of Tennessee, USA

Bejan, Adrian
Duke University, USA

Chalhoub, Nabil G.
Wayne State University, USA

Cho, Kyu-Kab
Pusan National University, South Korea

Dincer, Ibrahim
University of Ontario Institute of Technology, Canada

Douglas, Roy
Queen's University, U. K

El Bassam, Nasir
International Research Center for Renewable Energy,
Germany

Haik, Yousef
United Arab Emirates University, UAE

Jaber, Jamal
Al- Balqa Applied University, Jordan

Jubran, Bassam
Ryerson University, Canada

Kakac, Sadik
University of Miami, USA

Khalil, Essam-Eddin
Cairo University, Egypt

Mutoh, Yoshiharu
Nagaoka University of Technology, Japan

Pant, Durbin
Iowa State University, USA

Riffat, Saffa
The University of Nottingham, U. K

Saghir, Ziad
Ryerson University, Canada

Sarkar, MD. Abdur Rashid
Bangladesh University of
Engineering & Technology, Bangladesh

Siginer, Dennis
Wichita State University, USA

Sopian, Kamaruzzaman
University Kebangsaan Malaysia, Malaysia

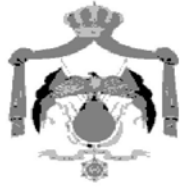
Tzou, Gow-Yi
Yung-Ta Institute of Technology and
Commerce, Taiwan

EDITORIAL BOARD SUPPORT TEAM

Language Editor Publishing Layout
Dr. Abdullah Jaradat MCPD. Osama AlShareet

SUBMISSION ADDRESS:

Prof. Mousa S. Mohsen, Editor-in-Chief
Jordan Journal of Mechanical & Industrial Engineering,
Hashemite University, PO Box 330127, Zarqa, 13133, Jordan
E-mail: jjmie@hu.edu.jo



Hashemite Kingdom of Jordan



Hashemite University

Jordan Journal of
Mechanical and Industrial Engineering

JJMIIE

An International Peer-Reviewed Scientific Journal

<http://jjmie.hu.edu.jo/>

ISSN 1995-6665

Jordan Journal of Mechanical and Industrial Engineering (JJMIE)

JJMIE is a high-quality scientific journal devoted to fields of Mechanical and Industrial Engineering. It is published by the Hashemite University in corporation with the Jordanian Scientific Research Support Fund.

Introduction: The Editorial Board is very committed to build the Journal as one of the leading international journals in mechanical and industrial engineering sciences in the next few years. With the support of the Ministry of Higher Education and Scientific Research and Jordanian Universities, it is expected that a heavy resource to be channeled into the Journal to establish its international reputation. The Journal's reputation will be enhanced from arrangements with several organizers of international conferences in publishing selected best papers of the conference proceedings.

Aims and Scope: Jordan Journal of Mechanical and Industrial Engineering (JJMIE) is a refereed international journal to be of interest and use to all those concerned with research in various fields of, or closely related to, mechanical and industrial engineering disciplines. Jordan Journal of Mechanical and Industrial Engineering aims to provide a highly readable and valuable addition to the literature which will serve as an indispensable reference tool for years to come. The coverage of the journal includes all new theoretical and experimental findings in the fields of mechanical and industrial engineering or any closely related fields. The journal also encourages the submission of critical review articles covering advances in recent research of such fields as well as technical notes.

Guide for Authors

Manuscript Submission

High-quality submissions to this new journal are welcome now and manuscripts may be either submitted online or mail.

Online: For online submission upload one copy of the full paper including graphics and all figures at the online submission site, accessed via E-mail: jjmie@hu.edu.jo. The manuscript must be written in MS Word Format. All correspondence, including notification of the Editor's decision and requests for revision, takes place by e-mail and via the Author's homepage, removing the need for a hard-copy paper trail.

By Mail: Manuscripts (1 original and 3 copies) accompanied by a covering letter may be sent to the Editor-in-Chief. However, a copy of the original manuscript, including original figures, and the electronic files should be sent to the Editor-in-Chief. Authors should also submit electronic files on disk (one disk for text material and a separate disk for graphics), retaining a backup copy for reference and safety.

Note that contributions may be either submitted online or sent by mail. Please do NOT submit via both routes. This will cause confusion and may lead to delay in article publication. Online submission is preferred.

Submission address and contact:

Prof. **Mousa S. Mohsen**, Editor-in-Chief
Jordan Journal of Mechanical & Industrial Engineering,
Hashemite University,
PO Box 330127, Zarqa, 13133 , Jordan
E-mail: jjmie@hu.edu.jo

Types of contributions: Original research papers

Corresponding author: Clearly indicate who is responsible for correspondence at all stages of refereeing and publication, including post-publication. Ensure that telephone and fax numbers (with country and area code) are provided in addition to the e-mail address and the complete postal address. Full postal addresses must be given for all co-authors.

Original material: Submission of an article implies that the work described has not been published previously (except in the form of an abstract or as part of a published lecture or academic thesis), that it is not under consideration for publication elsewhere, that its publication is approved by all authors and that, if accepted, it will not be published elsewhere in the same form, in English or in any other language, without the written consent of the Publisher. Authors found to be deliberately contravening the submission guidelines on originality and exclusivity shall not be considered for future publication in this journal.

Supplying Final Accepted Text on Disk: If online submission is not possible: Once the paper has been accepted by the editor, an electronic version of the text should be submitted together with the final hardcopy of the manuscript. The electronic version must match the hardcopy exactly. We accept MS Word format only. Always keep a backup copy of the electronic file for reference and safety. Label the disk with your name. Electronic files can be stored on CD.

Notification: Authors will be notified of the acceptance of their paper by the editor. The Publisher will also send a notification of receipt of the paper in production.

Copyright: All authors must sign the Transfer of Copyright agreement before the article can be published. This transfer agreement enables Jordan Journal of Mechanical and Industrial Engineering to protect the copyrighted material for the authors, but does not relinquish the authors' proprietary rights. The copyright transfer covers the exclusive rights to reproduce and distribute the article, including reprints, photographic reproductions, microfilm or any other reproductions of similar nature and translations.

PDF Proofs: One set of page proofs in PDF format will be sent by e-mail to the corresponding author, to be checked for typesetting/editing. The corrections should be returned within 48 hours. No changes in, or additions to, the accepted (and subsequently edited) manuscript will be allowed at this stage. Proofreading is solely the author's responsibility. Any queries should be answered in full. Please correct factual errors only, or errors introduced by typesetting. Please note that once your paper has been proofed we publish the identical paper online as in print.

Author Benefits

Page charge: Publication in this journal is free of charge.

Free off-prints: Three journal issues of which the article appears in along with twenty-five off-prints will be supplied free of charge to the corresponding author. Corresponding authors will be given the choice to buy extra off-prints before printing of the article.

Manuscript Preparation:

General: Editors reserve the right to adjust style to certain standards of uniformity. Original manuscripts are discarded after publication unless the Publisher is asked to return original material after use. If online submission is not possible, an electronic copy of the manuscript on disk should accompany the final accepted hardcopy version. Please use MS Word for the text of your manuscript.

Structure: Follow this order when typing manuscripts: Title, Authors, Affiliations, Abstract, Keywords, Introduction, Main text, Conclusions, Acknowledgements, Appendix, References, Figure Captions, Figures and then Tables. For submission in hardcopy, do not import figures into the text - see Illustrations. For online submission, please supply figures imported into the text AND also separately as original graphics files. Collate acknowledgements in a separate section at the end of the article and do not include them on the title page, as a footnote to the title or otherwise.

Text Layout: Use double spacing and wide (3 cm) margins. Ensure that each new paragraph is clearly indicated. Present tables and figure legends on separate pages at the end of the manuscript. If possible, consult a recent issue of the journal to become familiar with layout and conventions. All footnotes (except for table and corresponding author footnotes) should be identified with superscript Arabic numbers. To conserve space, authors are requested to mark the less important parts of the paper (such as records of experimental results) for printing in smaller type. For long papers (more than 4000 words) sections which could be deleted without destroying either the sense or the continuity of the paper should be indicated as a guide for the editor. Nomenclature should conform to that most frequently used in the scientific field concerned. Number all pages consecutively; use 12 or 10 pt font size and standard fonts. If submitting in hardcopy, print the entire manuscript on one side of the paper only.

Corresponding author: Clearly indicate who is responsible for correspondence at all stages of refereeing and publication, including post-publication. The corresponding author should be identified with an asterisk and footnote. Ensure that telephone and fax numbers (with country and area code) are provided in addition to the e-mail address and the complete postal address. Full postal addresses must be given for all co-authors. Please consult a recent journal paper for style if possible.

Abstract: A self-contained abstract outlining in a single paragraph the aims, scope and conclusions of the paper must be supplied.

Keywords: Immediately after the abstract, provide a maximum of six keywords (avoid, for example, 'and', 'of'). Be sparing with abbreviations: only abbreviations firmly established in the field may be eligible.

Symbols: All Greek letters and unusual symbols should be identified by name in the margin, the first time they are used.

Units: Follow internationally accepted rules and conventions: use the international system of units (SI). If other quantities are mentioned, give their equivalent in SI.

Maths: Number consecutively any equations that have to be displayed separately from the text (if referred to explicitly in the text).

References: All publications cited in the text should be presented in a list of references following the text of the manuscript.

Text: Indicate references by number(s) in square brackets in line with the text. The actual authors can be referred to, but the reference number(s) must always be given.

List: Number the references (numbers in square brackets) in the list in the order in which they appear in the text.

Examples:

Reference to a journal publication:

- [1] M.S. Mohsen, B.A. Akash, "Evaluation of domestic solar water heating system in Jordan using analytic hierarchy process". Energy Conversion & Management, Vol. 38, No. 9, 1997, 1815-1822.

Reference to a book:

- [2] Strunk Jr W, White EB. The elements of style. 3rd ed. New York: Macmillan; 1979.

Reference to a conference proceeding:

- [3] B. Akash, S. Odeh, S. Nijmeh, "Modeling of solar-assisted double-tube evaporator heat pump system under local climate conditions". 5th Jordanian International Mechanical Engineering Conference, Amman, Jordan, 2004.

Reference to a chapter in an edited book:

- [4] Mettam GR, Adams LB. How to prepare an electronic version of your article. In: Jones BS, Smith RZ, editors. Introduction to the electronic age, New York: E-Publishing Inc; 1999, p. 281-304

Free Online Color: If, together with your accepted article, you submit usable color and black/white figures then the journal will ensure that these figures will appear in color on the journal website electronic version.

Tables: Tables should be numbered consecutively and given suitable captions and each table should begin on a new page. No vertical rules should be used. Tables should not unnecessarily duplicate results presented elsewhere in the manuscript (for example, in graphs). Footnotes to tables should be typed below the table and should be referred to by superscript lowercase letters.

PAGES	PAPERS
665 – 676	Numerical Modelling of a Turbocharger Splitter-Vaned Centrifugal Impeller at off-Design Conditions Part II: Computation of Forces and Torques <i>A. Fatsis, A. Panoutsopoulou, N.Vlachakis</i>
677 – 684	A Fusion Technique Based on Image - Statistical Analysis for Detection of Throat Cancer Types <i>Adnan Al-Bashir, Bassam Al-Naami</i>
685 – 692	Experiments on Aluminum-Copper Alloys Properties as Solar Absorbers <i>Abdul Hai Alami</i>
693 – 700	Statistical Process Control Tools: A Practical guide for Jordanian Industrial Organizations <i>Rami Hikmat Fouad, Adnan Mukattash</i>
701 - 710	Damage Identification of Welded Structures Using Time Series Models and Exponentially Weighted Moving Average Control Charts <i>P.Srinivasa Rao, Ch.Ratnam</i>
711 – 724	Efficiency of Free Cooling Technique in Air Refrigeration Systems <i>A. Al-Salaymeh, M.R. Abdelkader</i>
725 – 732	Real Time Prediction of Flank Wear by Neuro Fuzzy Technique in Turning <i>D. Dinakaran, Sampathkumar, J. Susai Mary</i>
733 – 738	Analysis of Solar Radiation in Jordan <i>Issa Etier, Anas Al Tarabsheh, and Mohammad Ababneh</i>
739 - 756	Production Inventory Model for Deteriorating Items with On-Hand Inventory and Time Dependent Demand <i>Sri S. V. Uma Maheswara Rao , K. Srinivasa Rao, K. Venkata Subbaiah</i>
757 - 778	Effect of Poisson's Ratio on the Elastic Strain Concentration Factor of Notched Bars under Static Tension and under Pure Bending. <i>H. M. Tilan</i>
779 - 788	Revision of the Recent Heterogeneous Solid Object Modeling Techniques <i>Wisam Abu Jadayil</i>
789 – 796	Hot Water Management of DHW Storage Tank: Supply Features <i>N. Beithou , M. Abu Hilal</i>

Numerical Modelling of a Turbocharger Splitter-Vaned Centrifugal Impeller at off-Design Conditions Part II: Computation of Forces and Torques

A. Fatsis ^a, A. Panoutsopoulou ^b, N.Vlachakis ^a

^(a) Technological University of Chalkis, Department of Mechanical Engineering, 34400 Psachna, Evoias, Greece.

^(b) Hellenic National Defence Systems S.A., 1, Ilioupoleos Avenue, 17236, Greece

Abstract

Forces and torques acting on each individual blade and on the shaft of a centrifugal impeller with splitter vanes working at off-design conditions, are computed by using the pressure integration and the momentum balance method. Two cases are examined simulating the operation of a centrifugal compressor at higher mass flows than the optimum one: the first where the Strouhal number, $S_r = 0.146$, corresponds to subsonic flow inside the impeller and the second one where the Strouhal number, $S_r = 0.225$, corresponds to transonic flow inside the impeller. For the first case, the variation of forces is more distinct in the circumferential location where the volute tongue is located. For the second case a bimodal distribution is observed per impeller rotation. Calculations done for impellers with backward leaned blades and with radial ending blades demonstrate the influence of the impeller exit geometry to the radial force.

© 2010 Jordan Journal of Mechanical and Industrial Engineering. All rights reserved

Keywords: radial force, unsteady forces, centrifugal impeller, splitter blades.

Nomenclature

c	Speed of sound
f	Frequency
t	Time
\vec{F}	Force
L	Length of blade channel
M	Mach number
P	Static pressure
\vec{S}	Surface
S_r	Strouhal number
T	Torque
\vec{V}	Absolute velocity
ρ	Density

Superscripts

bl	Blade
spl	Splitter
$0l$	Total conditions at the impeller inlet

Subscripts

m	Meridian
ps	Blade or splitter pressure side
r	Radial
rel	Relative
ss	Blade or splitter suction side
st	Static
z	Axial
θ	Circumferential
1	Impeller inlet
2	Impeller trailing edge

1. Introduction

When centrifugal compressors work at off-design conditions, the volute type collector creates a circumferentially non-uniform static pressure distribution at the diffuser exit. In case of a vaneless diffuser, the pressure distortion propagates upstream and creates unsteady flow inside the impeller, [1]. This results to a

circumferential variation of the blade loading and fluctuating forces acting on the impeller blades. A first consequence is a non-zero radial force on the impeller shaft and extra load on the bearings. It also means unsteady flow and forces in the rotating blade passages resulting in blade vibrations and additional noise. This increases losses and decreases the operating range of the compressor.

Initially researchers experienced the existence of radial forces exerted on the shaft of centrifugal pumps when they operated at mass flows different from the design one because of failure of the bearings supporting the impeller shaft, [2]. Experimental determination of the magnitude and direction of radial forces acting on the bearings supporting the impeller shaft was done by measuring the bearing reaction [3]. At lower specific speeds there is a relatively large flow rate range over which the minimum force is essentially constant. For higher specific speeds the radial force has a minimum almost at a single point. Deviating on both sides of that point, the rate of increase of the radial force is high. This means that for high specific speeds, a small deviation from the design point is sufficient to create large radial forces, and accordingly a large radial thrust on the bearings of the impeller shaft. The point corresponding to the minimum radial force does not necessarily correspond to 100% design flow rate because the design of the volute may produce circumferentially uniform static pressure at higher or lower mass flow rates, [3].

The effect of the number of blades on the magnitude of the radial force was studied experimentally, [4]. It was found that the magnitude of the radial thrust of the seven-bladed impeller is larger than the one of the three-bladed impeller. On the contrary, the fluctuating range doubles in the case of the three-bladed impeller compared to the seven-bladed impeller.

Empirical investigations were also attempted to correlate the magnitude of the radial force with geometrical data and volume flow rates or the specific speed for pumps [5,6,7]. All these empirical methods, assuming incompressible flows, even though present satisfactory results for the series of pumps that were applied, fail to provide a universal equation for all types of centrifugal pumps or compressors.

A simple numerical model to compute the radial force caused by a volute casing acting on a pump impeller at design and off-design conditions was presented [8]. It was concluded that the magnitude of the predicted force increases linearly on either side of optimum mass flow. Larger discrepancies are observed at higher mass flows and at design point, than at lower mass flows. A simple 1D unsteady model was presented, able to predict the impeller response and radial force due to the circumferential static pressure variation caused by the volute, [9]. The model is applicable for incompressible flows and assumes a circumferentially constant relative outlet flow angle. This is in contrast to experimental observations, where circumferential variations in the relative outlet flow angle were measured.

Calculations of forces acting on blades and on the impeller shaft bearing were also done assuming 2D potential flow inside the impeller. The forces on blades were found by integrating the pressure field on the solid

surfaces of the impeller [10]. There is no analysis of the different contributions to the radial force, because the pressure integration method they used can only give the total force and not its components. The prediction of the magnitude and direction of the forces shows a complete discrepancy with experimental results, [6]. This fact underlines the need of a fully unsteady model to investigate numerically the impeller response.

Two-dimensional unsteady flow numerical models are also found in the literature, aiming to study the centrifugal impeller response due to outlet static pressure distortion, by solving the 2D incompressible Navier Stokes equations and the 2D Euler equations respectively [11,12]. In both studies no information is given on the radial force magnitude and direction, neither on the contributions to this force. One of the limitations of 2D methods is that the three dimensional effects, which are present in the real flow inside a centrifugal impeller, are ignored.

A 3D numerical method was developed in order to study the unsteady flow field inside the impeller due to a circumferential variation of the static pressure at the impeller outlet, for the case of full-bladed impellers, [13]. The present study is an original contribution and the second part and an extension of the article of the same authors entitled "Numerical modelling of a turbocharger splitter-vaned centrifugal impeller at off-design conditions. Part I: Impeller flow field". The present article describes a method to predict forces acting on impeller blades, as well as radial force on the impeller shaft. Computations are performed for centrifugal impeller with splitter vanes, having backward leaned blades for lower and higher mass flows. The contributions to the forces are analysed and commented for impellers for backward leaned blades and for impellers with radial ending blades. Results obtained show that the predicted direction of the radial force is in agreement to experimental observations.

2. Unsteady Flow Computations

2.1. Unsteady flow model

The numerical model applied is well documented in [1,13] and only a summary of it will be given here.

The numerical model used to analyse the unsteady impeller flow field consists of the 3D Euler equations. Adopting the Euler equations means that the viscous terms from the full Navier-Stokes equations are neglected, and the transport of momentum and energy in the fluid is done only by means of convective fluxes. This means that viscous areas of the flow such as boundary layers developed along solid wall boundaries or wakes downstream the blades cannot be evaluated accurately by means of the present method. Since viscous forces are neglected, this implies that the considered model is not valid at relatively low rotational speed. Using the Euler equations compressible rotational flow, steady or unsteady flow fields can be calculated. This simplification results in an affordable computer time and gives useful information on the dynamics of the flow in the case where the impeller is not heavily loaded and flow separation is limited. The model was validated for the case of full-bladed centrifugal impeller, showing fairly good agreement against available

experimental results in the literature and predicting the unsteady flow features that are in agreement with experimental investigations, [1].

The 3D Euler equations in non-dimensional form are written in conservative form in cylindrical coordinates, (r, θ, z) as follows:

$$\frac{\partial \vec{u}}{\partial t} + \frac{1}{r} \cdot \frac{\partial (r f(\vec{u}))}{\partial r} + \frac{1}{r} \cdot \frac{\partial g(\vec{u})}{\partial \theta} + \frac{\partial h(\vec{u})}{\partial z} + \vec{b}(u) = 0 \quad (1)$$

where \vec{u} is the vector of conservative variables, $f(\vec{u})$, $g(\vec{u})$, $h(\vec{u})$ are the vectors of convective fluxes and $\vec{b}(\vec{u})$ is the source term, defined in detail in [1]. The conservative formulation of the equations allows the accurate treatment of flow discontinuities such as shock waves in the flow field.

The space discretization of the equations, centred in space, is done by means of the finite volume technique, offering second order spatial accuracy in smooth grids, [1].

The partial differential equations are written in a semi-discrete form as follows:

$$\frac{d}{dt}(\vec{u}) + \vec{R} = 0 \quad (2)$$

where \vec{R} are the residuals of the equations. The Runge-Kutta four steps scheme, providing second order accuracy for non-linear partial differential equations and extensive stability limits up to a CFL number of $2 \cdot \sqrt{2}$, was used for the time integration, offering a second order accuracy for non-linear problems. Extensive testing of the method in special test cases for which analytical solutions exist, has demonstrated the accuracy of this scheme for unsteady flow predictions, [2]. The time step used for the unsteady flow calculations is a constant one; it relates the rotational speed of the impeller to the number of grid points in the circumferential direction and it satisfies the stability limits of the CFL condition.

Impermeable wall boundary conditions are imposed on the solid walls (i.e. on the blade and splitter suction and pressure side and on the hub and shroud walls) by considering only the static pressure when computing the convective fluxes. At the inflow and outflow boundaries, non-reflecting boundary conditions based on the Fourier decomposition, were used, [13]. Non-reflecting boundary conditions suggest infinitely long pipes upstream and downstream of the impeller and it is shown in [13] that the solution is not affected by the upstream location of the inflow boundary. Since the outflow static pressure is not uniform along the circumference, this means that as the impeller rotates, a virtual point attached at the trailing edge experiences different values of the static pressure throughout a full rotation, which consists the period of the phenomenon. Phase-lagged periodicity conditions were used to simulate this non-uniformity and to compute the fluxes through the upstream and downstream streamlines. Figure 1 shows a meridional (r - z) projection, a blade-to-blade (θ - z) projection and a 3D view of the H-grid used for the calculations. The points in axial, radial and circumferential position were uniformly distributed and the splitter vane was put between two full blades. The consistency and stability analysis of the method are given

in detail in [13] where the numerical scheme was presented in detail.

The model was validated for the cases of full-bladed and splitter-vaned centrifugal impeller, showing fairly good agreement against available experimental results in the literature and predicting the unsteady flow features which are in agreement with experimental investigations [1].

The blade-to-blade projection of the computational domain is shown in Figure 2. Continuous lines indicate the pressure side of a full blade and the suction side of a splitter vane and dashed lines the pressure side of the splitter vane and the suction side of the full blade. Phase-lagged periodicity conditions are used to update the upstream and downstream stagnation pseudo-streamlines AB, CD and EF, GH, respectively, [14]. Implementing phase-lagged periodicity conditions, data obtained from the same rotation, as well as data stored in the computer memory from the previous rotation have to be used. This slows down the convergence to a periodic solution. The points along the pseudo-streamlines upstream and downstream of the splitter vanes (namely KL, MN in Figure 2) are treated as interior points of the numerical domain and simple continuity of the fluxes is imposed. From the same figure it can be observed that the upstream and downstream extension of the computational domain is reduced. This is due to the non-reflecting boundary conditions that used for the inflow and outflow boundaries, [1].

The acoustic Strouhal number can characterize unsteady compressible flows. It is defined as the product of the reduced frequency and the Mach number:

$$S_r = \frac{f \cdot L}{c} \quad (3)$$

where L is the length of a blade passage, whereas f is the number of rotations per second times the number of perturbation waves around the circumference and c is the speed of sound.

It relates the time needed by a pressure wave to travel a distance L , at the speed of sound c to the period of the pressure perturbation $1/f$. Unsteady effects are small for $S_r < 0.1$ and the flow can be evaluated by means of steady calculations. For $S_r > 0.1$ accurate results can be obtained only by means of unsteady flow calculations.

2.2. Convergence of the time accurate calculations

Computations of the unsteady flow field have as initial value the converged solution of the steady state case, where the static pressure at the impeller outflow is circumferentially uniform. Figure 3 shows the converged history of the time-dependent calculations. In such flows convergence is achieved when the circumferential distribution of a flow variable repeats itself after a rotation of the impeller.

From this figure it can be also observed that the imposed static pressure circumferential distribution (which repeats itself over a rotation of the impeller) has a saw tooth profile. This is a typical static pressure distribution for the case of higher mass flows and it is in agreement with experimental results [12]. Such a profile can be also obtained by using a 1D flow model, [9].

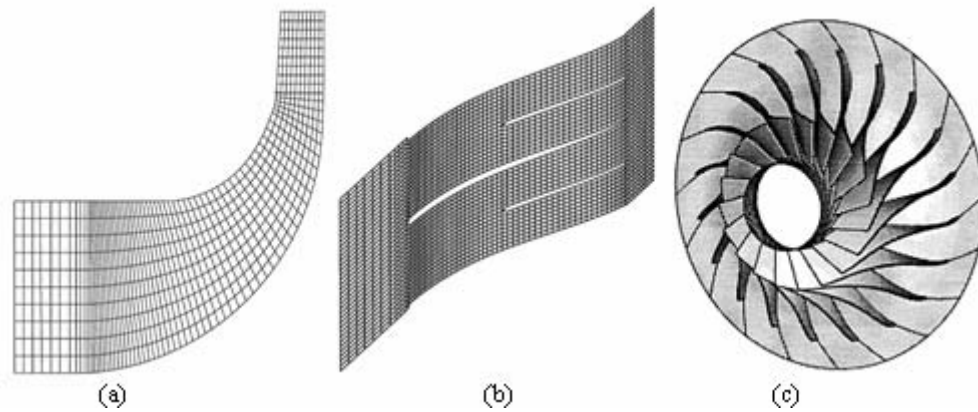


Figure 1: (a)Meridional ($r-z$), (b)Blade-to-blade ($\theta-z$) view of the H-grid used for the calculations, (c)Three-dimensional view of the impeller blades

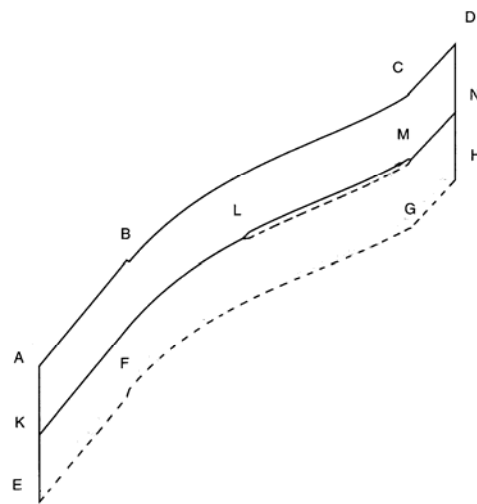


Figure 2: Blade-to blade ($\theta-z$) projection of the computational domain used for the splitter-vaned impeller computations

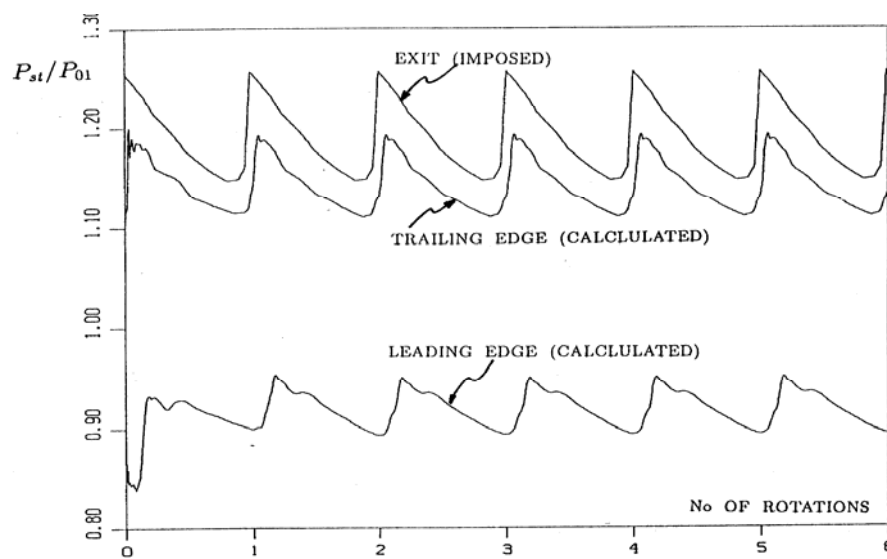


Figure 3: Convergence history of the unsteady flow calculations.

The calculated static pressure distribution at the leading edge shows decreased amplitude with respect to the imposed distribution. This is due to the time needed for a perturbation to propagate from the outlet to the inlet and is a consequence of the way the phase-lagged periodicity conditions are implemented. Information obtained at previous rotation is used when calculating the flow at the current one. Consequently, the results of the first rotation are partly influenced by the steady state solution and it takes several rotations before the unsteady flow is fully established everywhere. The static pressure profiles at trailing and leading edge are distorted by the pressure wave reflections in the impeller.

Figure 4 shows relative Mach number iso-lines in a blade-to blade development of the hub, mean and shroud surfaces of the impeller for transonic flow inside the impeller and $S_r = 0.225$. This figure comes by monitoring the blade channel of Figure 2 during one complete rotation of the impeller. Since the flow field is unsteady, monitoring the blade channel of Figure 2 during one rotation, one will observe different flow patterns and if only one full rotation is completed, he will find back the initial flow conditions. The Mach number variations at the shroud streamsurface are more pronounced than the ones at the hub streamsurface. Waves due to the exit static pressure distortion have to travel a longer path at hub than a shroud. In the later streamsurface the transonic region close to the leading edge suction side of the blade heavily influences them. The upstream-propagated static pressure distortion cannot pass through the transonic flow regime close to shroud suction surface and reflects downstream as a compression wave interacting with incoming pressure waves. The variations in Mach number indicate variations in static pressure and in blade loading during one period of the phenomenon. One can also see that the inflow and outflow boundaries are located close to the impeller.

This was made possible by using non-reflecting boundary conditions at the inlet and outlet boundaries [1].

$$\left(\sum_k \sum_j \rho_{i,j,k} \vec{V}_{i,j,k} \vec{S}_{i,j,k} \vec{V}_R \right)_{out} - \left(\sum_k \sum_j \rho_{i,j,k} \vec{V}_{i,j,k} \vec{S}_{i,j,k} \vec{V}_R \right)_{in} + \left(\sum_k \sum_j \rho_{i,j,k} \vec{V}_{i,j,k} \vec{S}_{i,j,k} \vec{V}_\Theta \right)_{out} - \left(\sum_k \sum_j \rho_{i,j,k} \vec{V}_{i,j,k} \vec{S}_{i,j,k} \vec{V}_\Theta \right)_{in} + \left(\sum_k \sum_j P_{i,j,k} \vec{S}_{i,j,k} \right)_{out} - \left(\sum_k \sum_j P_{i,j,k} \vec{S}_{i,j,k} \right)_{in} = \vec{F} \quad (6)$$

The indices j, k run from suction to pressure side and from hub to shroud, respectively. The flow velocity and static pressure at each circumferential position are the ones obtained from the computation of the unsteady flow field at a given impeller position.

Both methods predict different forces when applied to the same geometry using the results obtained with a coarse grid consisting of $43*11*11$ points. Repeating both calculations on a finer grid having $86*15*15$ points shows almost identical results, which are close to the ones

3. Computation of Forces

3.1. General Formulations

A Cartesian coordinate system is used to define the forces and torques acting on each individual blade and on the impeller shaft. The x -axis is from the shaft centre towards the volute tongue, and the y -axis perpendicular to it. (Figure 5).

Two methods have been used to compute the forces and torques resulting from the outlet circumferential static pressure distortion.

The first one integrates the pressure over the whole impeller surface.

$$\vec{F} = \int \int P_{i,j,k} d\vec{S}_{i,j,k} \quad (4)$$

The total force is computed by adding the contribution of each blade separately. In case of an unshrouded impeller, the pressure on the shroud does not contribute to the forces on the shaft. In case of a shrouded impeller the pressure on the outer side of the shroud should also be integrated.

The second one is the momentum balance method. This method computes the total force acting on the impeller, and not on a single blade because the momentum balance gives the forces acting on the whole channel and not on each surface. The total force \vec{F} is given by:

$$\vec{F}_{\Delta MR} + \vec{F}_{\Delta M\Theta} + \vec{F}_p = \vec{F} \quad (5)$$

where \vec{F}_p is the force due to the static pressure at inlet and outlet section, $\vec{F}_{\Delta MR}$ and $\vec{F}_{\Delta M\Theta}$ are the forces due to the change of radial and tangential momentum. Written in summation form, the previous equation is:

obtained from the pressure integration method on a coarse grid, Figure 6. Similar results, but non shown in this paper, are obtained from the calculation of the Torque around the axis of the impeller, the torque around the y -axis and the axial force acting on the impeller. One can conclude from this that the momentum balance method is more sensitive to the grid density than the pressure integration method.

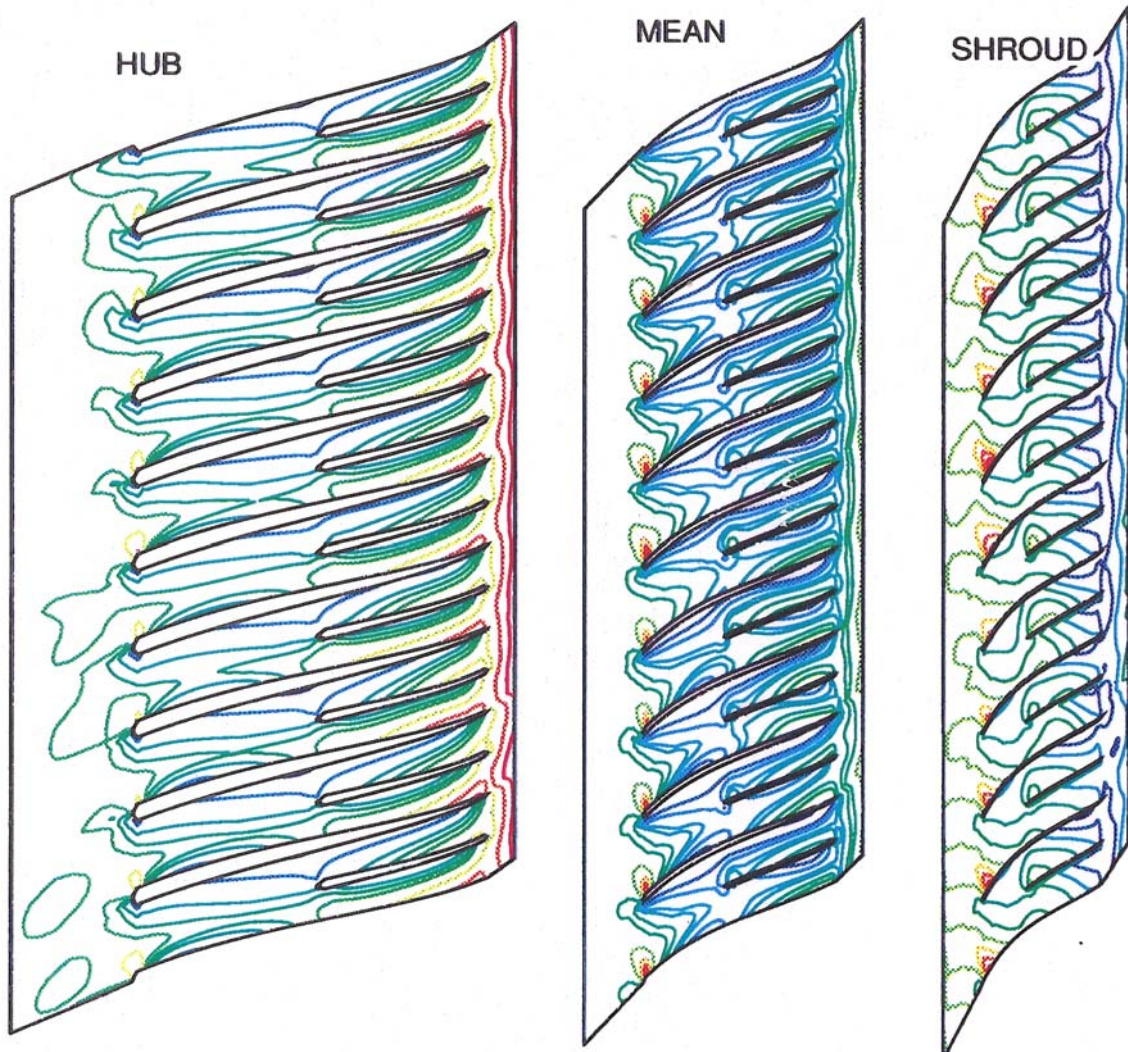


Figure 4: Iso-Mach lines for the hub, mean and shroud streamsurfaces of the impeller.

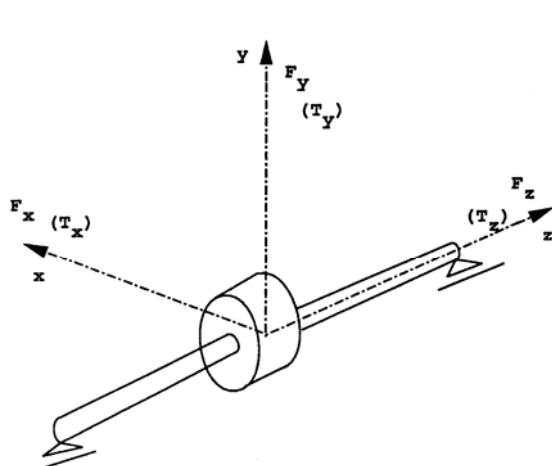


Figure 5: System of coordinates used to calculate forces and torques

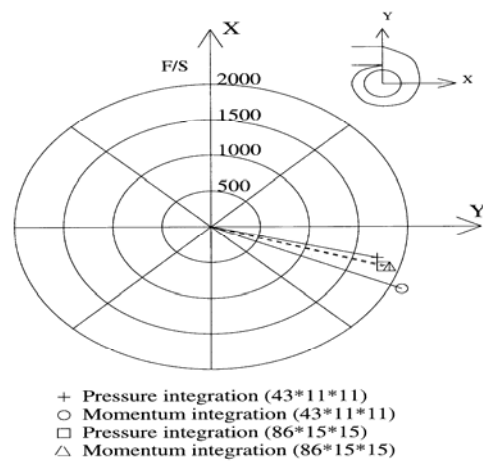


Figure 6: Radial force computation using the pressure integration method and the momentum integration method for two different types of grid density.

Although the momentum balance method does not allow the calculation of forces on individual blades, it allows the evaluation of the individual contributions to the radial force. This is important in the context of an experimental definition of the radial forces in function of the flow quantities at the impeller inlet and outlet. It can answer the question whether it is sufficient to integrate the static pressure distortion over the impeller outlet circumference or if one should also account for the variation in radial and tangential velocity.

3.2. Forces calculations at higher mass flows and different Strouhal numbers

3.2.1. Strouhal number 0.146 corresponding to subsonic flow inside the impeller.

Here, the circumferential variations of the axial, radial force acting on a single blade, and the torque around the z-axis of the impeller will be presented. These distributions are obtained by monitoring one blade during one impeller rotation.

The circumferential variations of the axial force, radial force acting on a single blade and the torque around the z-axis resulting from a single blade are shown in Figure 7. From this figure, one can see that there is a significant variation of the above forces and torques close to the tongue region (which corresponds to 33°) due to the peak in the circumferential variation of static pressure. In regions of smooth variation of the static pressure, these quantities vary smoothly as well.

3.2.2. Strouhal number 0.225 corresponding to transonic flow inside the impeller

The axial force, radial force acting on a single blade and the torque around z-axis resulting from a single blade are shown in Figure 8. From these figures, one can see that there is a bimodal variation of the above forces and torque as a result of the pressure waves reflected at the leading edge, travelling twice upstream and downstream the impeller during one rotation. This was also observed for the case of full-bladed centrifugal impeller operating at higher than optimum mass flows and a similar value of the acoustic Strouhal number, [1]. The two waves per rotation were even more clearly visible because the waves were not perturbed by reflections at the leading edge of the splitter vanes. The amplitude of the variation for the axial force, radial force and torque is larger than for the case of $S_r = 0.146$ discussed previously.

3.3. Calculations at higher and lower mass flows

In Figure 9 one can see the direction and magnitude of the individual components of the radial force in the case of higher (continuous lines) and lower (dashed lines) than design mass flow. The radial force vectors are for both cases in agreement with the experimental results, [16]. For both mass flows, the largest contribution to the radial force is the one resulting from the outlet static pressure. The force component due to non-uniform outlet radial momentum is much smaller and in the opposite direction, as it was concluded from the experimental data in [17].

It results in a decrease of the radial force. The inlet flow distortion also results in a non negligible contribution to the radial force.

3.4. Influence of the impeller geometry

The influence of the impeller geometry on the radial force is illustrated by comparing previous results with those on an impeller with radial ending blades, [1].

The difference in contribution to the radial force can be explained by means of Figure 10. The increase or decrease of the relative velocity is due to the disequilibrium between the pressure rise by the impeller and the imposed outlet pressure. In case of a backward leaned impeller any increase in relative velocity, because of a decrease in outlet pressure, provokes a decrease of tangential velocity and as a consequence a decrease in pressure. As a result, the disequilibrium between the imposed and impeller outlet static pressure gets smaller. This corrective action results in a smaller change in radial velocity and the circumferential variation of the radial momentum, which is proportional to V_{R2}^2 , and its contribution to the radial force is smaller.

The pressure rise in radial ending impellers is less dependent of the radial velocity because it does not involve a variation in $V_{\Theta 2}$, so that the change in radial velocity and radial momentum, for a given pressure change, is much larger.

The different contributions of the tangential momentum at the impeller outlet can also be explained. The increase in radial velocity, due to a local decrease in static pressure, results in a decrease of the tangential velocity for backward leaned blades as indicated on Figure 10a. As a consequence, the product $\rho \cdot V_{m2} \cdot S \cdot V_{\Theta 2}$ is almost constant along the periphery. The contribution of the tangential momentum to the radial force is thus negligible for backward leaned impellers.

In case of radial ending blades, an increase in mass flow does not alter the tangential component of the absolute velocity $V_{\Theta 2}$ (dotted line velocity triangle in Figure 10b). The product $\rho \cdot V_{m2} \cdot S \cdot V_{\Theta 2}$ is not constant along the periphery because only V_{m2} changes. The outlet tangential momentum is therefore not uniform circumferentially, resulting in a significant contribution to the force. Its direction is almost perpendicular to the radial momentum force.

4. Conclusions

In the present study the numerical prediction of forces and torques on individual centrifugal splitter-vaned impeller blades was presented. The total force acting on the impeller is obtained by adding the forces on all blades and the hub surface.

In the case of a shrouded impeller the pressure on the inner and outer side of the shroud should also be integrated. The latter is not predicted by the Euler solver but can be obtained by a suitable model, e.g. [15].

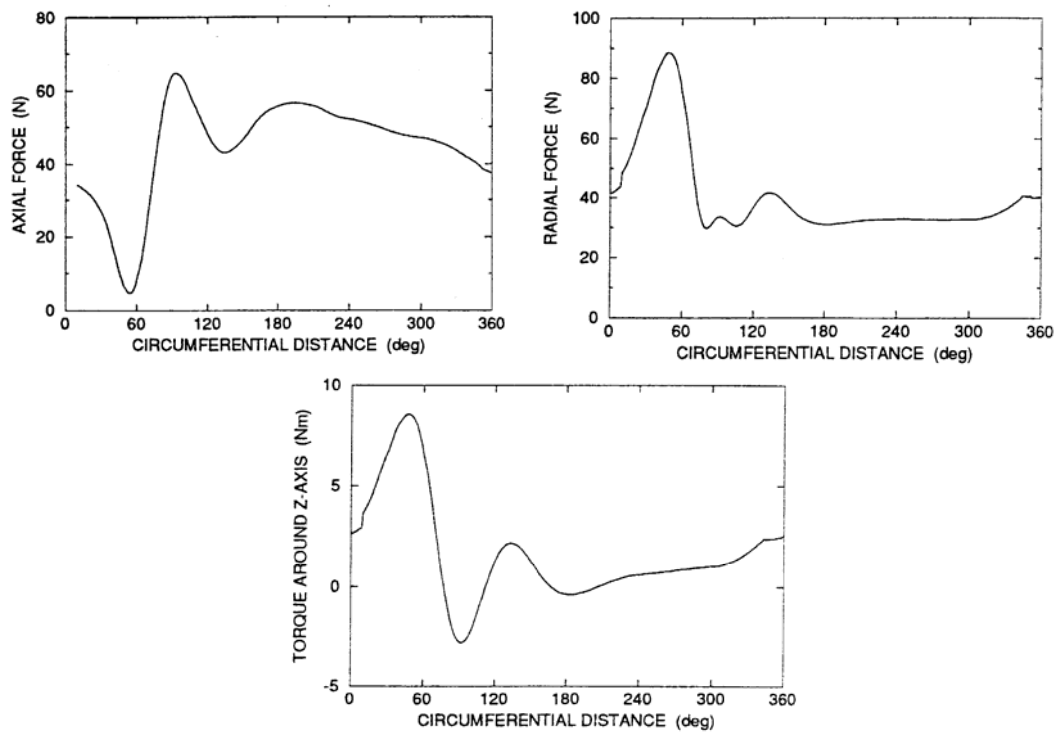


Figure 7: Circumferential variation of Axial Force, Radial Force and Torque around the impeller axis, for $S_r = 0.146$ corresponding to subsonic flow inside the impeller.

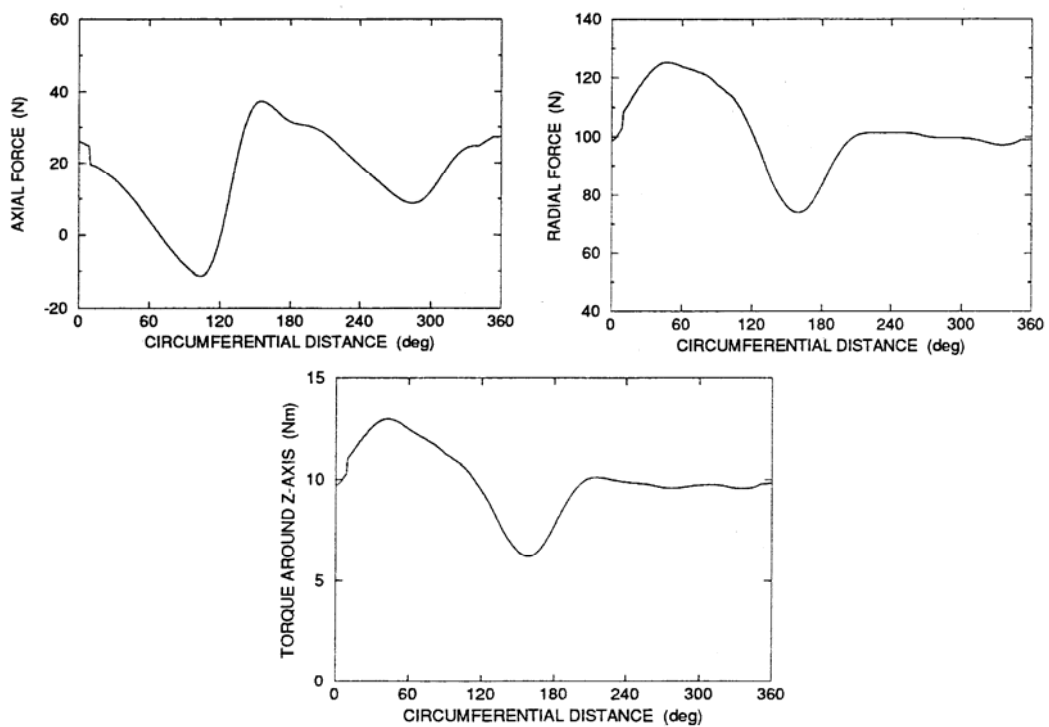


Figure 8: Circumferential variation of Axial Force, Radial Force and Torque around the impeller axis, for $S_r = 0.225$ corresponding to transonic flow inside the impeller.

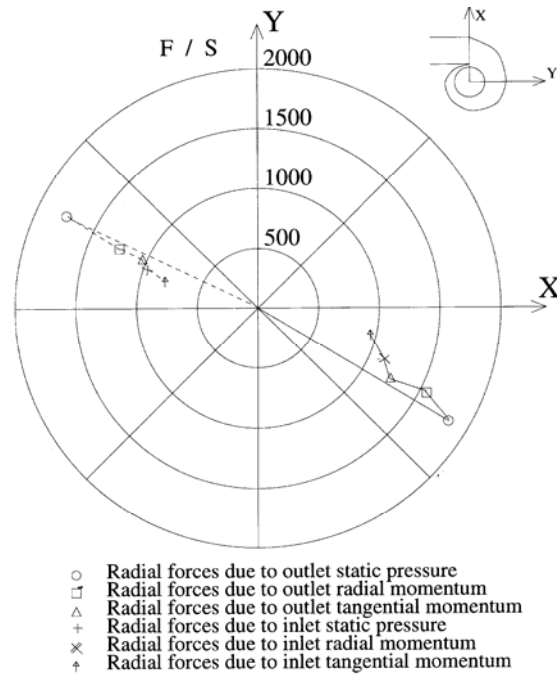


Figure 9: Components of radial force in the splitter-vaned impeller with backward leaned blades. Continuous lines correspond to higher mass flows, and dashed lines correspond to lower mass flows.

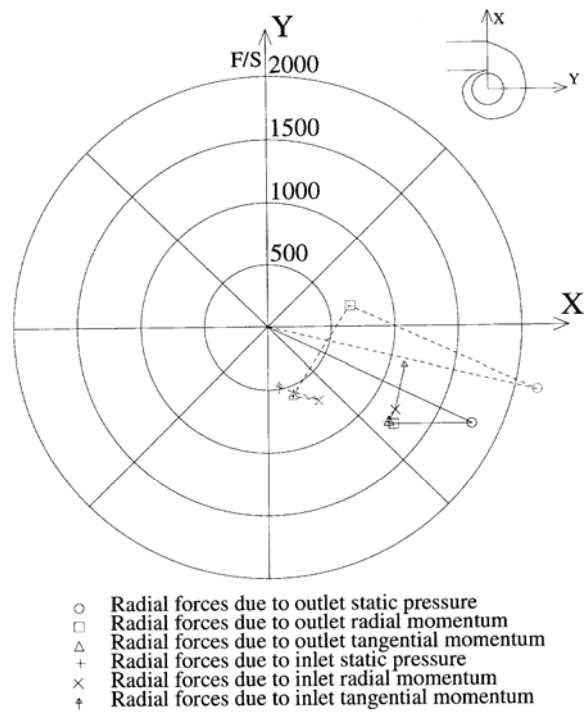


Figure 10: Components of Radial Force in an impeller with backward leaned (continuous lines), and radial ending blades (dashed lines)

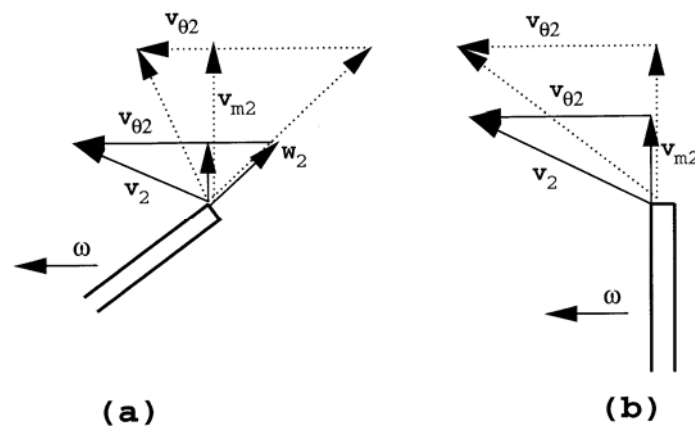


Figure 11: Difference in tangential momentum distribution between impeller with (a) backward leaned blades, and (b) radial ending blades

Experimental data mainly obtained in centrifugal pumps, confirm the existence of rotordynamic forces due to the static pressure fluctuations [18]. These forces are due to the response of the centrifugal impeller to the asymmetric static pressure imposed to the impeller outlet due to the volute [19]. Numerical results by means of commercial computer packages, confirm the prediction of the direction of the radial force acting on the bearings of the impeller shaft [20]. The unsteady forces on the impeller blades produce vibration and increase the noise of the compressor [21, 22].

Calculations were done for higher than optimum mass flows and for $S_r = 0.146$ corresponding to subsonic flow inside the impeller and for $S_r = 0.225$ corresponding to transonic flow conditions. For these cases it was found that the circumferential variations of the axial force, radial force and torque around the axis of the impeller are larger as the Strouhal number increases, which could lead to resonance conditions, as in the case of full-bladed centrifugal impeller, [1]. For the case of $S_r = 0.146$, a large variation of forces and torque is occurring at the circumferential position corresponding to the volute tongue. For the case of $S_r = 0.225$, a bimodal variation is observed for the forces and torque.

Calculations were also done for the case of higher and lower than the optimum mass flow. In the case of higher mass flows the unsteady flow phenomena are more pronounced than in the case of lower mass flow. The radial force direction for both cases is typical and is confirmed by many experimental observations, [16].

Two different methods were applied to compute the radial force caused by the static pressure distortion; namely the pressure integration and the momentum balance. From the calculations done it is shown that the momentum balance method is more sensitive to the grid density than the pressure integration method.

The different contributions to the radial forces are evaluated by means of the momentum balance method. The largest contribution is due to the variation of the outlet static pressure. The resulting radial force is larger at higher

mass flows than at lower mass flows. This is also confirmed by experimental and numerical results in [23].

Integration of the static pressure at the impeller outlet section gives an approximation of the total radial force on the impeller with backward leaned blades. It is completely wrong for radial ending blades where the variation in radial momentum almost completely compensates the pressure forces. The difference in force direction is due to the large contribution of the tangential momentum force, perpendicular to the radial one.

The information provided by this study on the distribution of unsteady forces and torques acting on each individual blade can be used as input to calculate the mechanical structure of the impeller. It also helps to find the rotordynamic behaviour of the impeller shaft to the unsteady fatigue loading, [22].

References

- [1] A. Fatsis, Computation of the 3-Dimensional Unsteady Flow in a Centrifugal Impeller due to a downstream Static Pressure Circumferential Distortion, 1995, Ph.D. Thesis, RUG-Von Karman Institute.
- [2] R.J. Knapp, R.C. Binder, "Experimental Determinations of the Flow Characteristics in Volute of Centrifugal Pumps". Transactions of ASME, Vol. 58 1936, 649-663.
- [3] H. Iversen, R. Rolling, J. Carlson, "Volute pressure distribution, Radial Force on the Impeller, and Volute Mixing Losses of a Radial Flow Centrifugal Pump", ASME Journal Engineering for Power, Vol. 82, 1960, 136-144.
- [4] Y. Hasegawa, K. Kikuyama, T. Maeda, Effects of blade number on Hydraulic Force perturbation on impeller of volute-type Centrifugal Pump. JSME International Journal, Series II. Vol. 33, 1990, 736-742.
- [5] A.J. Stepanoff. Centrifugal and Axial Flow Pumps, second ed. New York: John Wiley and Sons, Inc., 1957.
- [6] A. Agostinelli, D. Nobles, C.R. Mockridge, "An experimental investigation of radial thrust in centrifugal pumps". ASME Journal of Engineering for Power. Vol. 82, 1960, 120-126.

- [7] H.J. Biheller, "Radial force on the impeller of centrifugal pumps with volute, semivolute and fully concentric casings". ASME Journal Engineering for Power. Vol. 87, 1965, 319-323.
- [8] G.T. Csanady, "Radial forces in a pump impeller caused by a volute casing". ASME Journal Engineering for Power, Vol. 84, 1962, 337-340.
- [9] J.A. Lorett, S. Gopalakrishnan, S. "Interaction in between Impeller and Volute of Pumps at off-design conditions". ASME Journal Fluids Engineering, Vol.108, 1986.
- [10] S.M. Miner, R.D. Flack, P. Trevisan, "Potential flow analysis of the forces on a laboratory centrifugal pump impeller". ASME Paper 92-GT-285.
- [11] D. Croba. Modélisation de l'écoulement instationnaire dans les pompes centrifuges. Interaction roue-volute. 1992, PhD Thesis, Institut National Polytechnique de Grenoble.
- [12] M. Sideris. Circumferential distortion of the flow in Centrifugal Compressors due to Outlet Volute, 1988, Ph.D. Thesis, RUG-Von Karman Institute.
- [13] A. Fatsis. Three dimensional unsteady flow calculations in radial components. 1993, Von Karman Institute Lecture Series 1993-01 'Spacecraft Propulsion'.
- [14] J.I. Erdos, E. Alzner, "Computation of Unsteady Transonic Flows through rotating and stationary cascades", 1977, NASA CR 2900.
- [15] D.W. Childs, "Pressure oscillation in the leakage annulus between a shrouded impeller and its housing due to impeller-discharge-pressure disturbances". ASME Journal of Fluids Engineering. Vol. 114, 1992, 61-67.
- [16] J. Meier-Grotian. Untersuchungen der radiale Kraft auf das Laufrad einer Kreiselpumpe bei verschiedenen Spiralgehäuseformen, 1972, Ph.D. Thesis, T.U. Braunschweig.
- [17] D. Hagelstein, K. Hillewaert, R. A. Van den Braembussche, A. Engeda, R. Keiper, M. Rautenberg, "Experimental and Numerical Investigation of the Flow in a Centrifugal Compressor Volute". ASME Journal of Turbomachinery, Vol. 122, No. 1, 2000, 22-32.
- [18] M. Sinha, A. Pinarbasi, and J. Katz, "The Flow Structure During Onset and Developed States of Rotating Stall Within a Vaned Diffuser of a Centrifugal Pump". ASME Journal of Fluids Engineering, Vol.123, No. 3, 2001, 490-500.
- [19] A. Hiwata, Y. Tsujimoto, "Theoretical Analysis of Fluid Forces on an Open-Type Centrifugal Impeller in Whirling Motion". ASME Journal of Fluids Engineering, Vol. 124, No. 2, 2002, 342-348.
- [20] J.J. Moore, DL Ransom, F Viana, "Rotordynamic Force Prediction of Centrifugal Compressor Impellers Using Computational Fluid Dynamics". ASME Paper 2007-GT-28181.
- [21] Q. Liu, D. Qi, Y. Mao, "Numerical calculation of centrifugal fan noise". Proceedings of the Institution of Mechanical Engineers, Part C: Journal of Mechanical Engineering Science, Vol. 220, No. 8, 2006, 1167-1177.
- [22] H.-P. Dickmann, T. S. Wimmel, J. Szwedowicz, D. Filsinger, and Ch.H. Roduner "Unsteady Flow in a Turbocharger Centrifugal Compressor: Three-Dimensional Computational Fluid Dynamics Simulation and Numerical and Experimental Analysis of Impeller Blade Vibration", ASME Journal of Turbomachinery, Vol. 128, No. 3, 2006, 455-466
- [23] M.Zhang, H. Tsukamoto, "Unsteady Hydrodynamic Forces due to Rotor-Stator Interaction on a Diffuser Pump With Identical Number of Vanes on the Impeller and Diffuser". ASME Journal of Fluids Engineering, Vol. 127, No. 4, 2005, 743-752.

A Fusion Technique Based on Image - Statistical Analysis for Detection of Throat Cancer Types

Adnan Al-Bashir ^{a,*}, Bassam Al-Naami ^b

Department of Industrial Engineering, Hashemite University, P.O. Box 150459, Zarqa 13115, Jordan

Department of Biomedical Engineering, Hashemite University, P.O. Box 150459, Zarqa 13115, Jordan

Abstract

The aim of this study is to establish a simple approach to classify the throat tumor type by using statistical analysis techniques without a need for a biopsy or further testing. In this study, around 35 patients were investigated to be classified and to provide appropriate diagnostic for the throat cancer type. MRI images and their properties were processed and converted into number of pixels and intensities that located in the region of interest which covered the area of tumor. This extracted information was employed by traditional statistical methods such as Descriptive Analysis, Box Plots and Testing of Hypothesis to enable reasonable accuracy in differentiation between the tumor types. As a result of this study, it is observed that the using of statistical analysis for the data taken from the MRI images is reliable to diagnose and determine the type of the throat cancer with 95% confidence.

© 2010 Jordan Journal of Mechanical and Industrial Engineering. All rights reserved

Keywords: Throat cancer (TCa), filtration, segmentation, box plot, T-test, Inter Quartile Range (IQR).

1. Introduction

Throat cancer is one of the most dangerous cancer's type and forms in tissues of the pharynx (the hollow tube inside the neck that starts behind the nose and ends at the top of the windpipe and esophagus). Throat cancer includes cancer of the nasopharynx (the upper part of the throat behind the nose), the oropharynx (the middle part of the pharynx), and the hypopharynx (the bottom part of the pharynx). Cancer of the larynx (voice box) may also be included as a type of throat cancer. Most throat cancers are squamous cell carcinomas (cancer that begins in thin, flat cells that look like fish scales). Also called pharyngeal cancer (Fig.1) Estimated new cases and deaths from throat cancer (including cancers of the larynx) in the United States in 2009 are 12,290 (laryngeal) and 12,610 (pharyngeal), while the death cases are 3,660 (laryngeal) and 2,230 (pharyngeal) [1].

In 2004, according to the Jordan National Cancer Registry, (JNCR), about 3,591 new cancer cases have been registered among Jordanians with an incidence rate of 67.1 per 100,000 populations (63.9 for males and 70.5 for females). Among the most common cancers affecting Jordanian population, the throat tumor (TCa) was ranked as the eighth common type in children and the 10th in

adults and the prevalence in males 3.5% more than females (2.1%) [2].

Different diagnostic procedures have been followed in attempt to differentiate between the benign and malignant tumor such as: 1) Physical exam. 2) Indirect laryngoscopy; the doctor looks down your throat using a small, long-handled mirror to check for abnormal areas and to see if your vocal cords move as they should. 3) Direct laryngoscopy; the doctor inserts a thin, lighted tube called a laryngoscope through your nose or mouth. As the tube goes down your throat, the doctor can look at areas that cannot be seen with a mirror. 4) Biopsy is removing tissue to look for cancer cells and a pathologist then looks at the tissue under a microscope to check for cancer cells [1]. A biopsy is the only sure way to know if a tumor is cancerous.

However, it is important in many cases to validate a diagnosis and be certain of its accuracy. On the other hand, hoping for a misdiagnosis should not be used as a way to avoid treatment for a serious medical problem as the throat cancer. Nevertheless, it is sensible to attempt to confirm a diagnosis via methods such as seeking second opinions, consulting specialists, getting further medical tests, and researching information about the medical condition. Also, misdiagnosis can and does occur and is reasonably common with error rates ranging from 1.4% in cancer biopsies to a high 20-40% misdiagnosis rate in emergency or ICU care.

[<http://www.cureresearch.com/intro/overview.htm>].

* Corresponding author. abashir@hu.edu.jo

Therefore, in this paper, we focused on building an algorithm – software based on the use of LabView software to analyze the image of Throat Cancer, where part of this technique was tested in our previous work for brain tumor classification [3]. This target was achieved by the developed algorithm consisted of image enhancement, filtering and applying the region of interest threshold techniques to extract the number of pixels and their intensities for both types of throat cancers (benign and Malignant). This procedure is followed by the statistical analysis based on Box Plot and Test of Hypothesis.

Various segmentation techniques and methods have been cited in the literature for improving the segmentation processes to maximize the possibility and reliability of TCa classification. These techniques can be categorized into:

1) threshold-based segmentation, 2) statistical methods for TCa segmentation and 3) region growing methods [4, 5, 6, 7].

In [4] a semiautomatic system for segmentation of a diverse set of lesions in head and neck CT scans has developed. The system takes as input an approximate bounding box, and uses a multistage level set to perform the final segmentation. Then contours from automatic segmentation were compared to both 2D and 3D gold standard contours manually drawn by three experienced radiologists. The average absolute area error was 21.1% compared to 10.8%, and the average 2D distance was 1.38 mm compared to 0.84 mm between the radiologists. The automatic contours approximated many of the lesions very well. Haibo Zhang et al. developed a new three-dimensional adaptive region growing algorithm for the automatic segmentation of three-dimensional images [5]. The principle of this algorithm is to obtain a satisfactory segment result by self-tuning the homogeneity constraint step by step. Results of segmentation based on the use of this algorithm are close to that of manual segmentation. Shiping Zhu et al. proposed a new segmentation algorithm that each pixel in the image has its own threshold [6]. In this algorithm, the threshold of a pixel in an image is estimated by calculating the mean of the grayscale values of its neighbor pixels, and the square variance of the grayscale values of the neighbor pixels are also calculated as an additional judge condition. The results demonstrate that the proposed algorithm could produce precise image edge, while it is reasonable to estimate the threshold of a pixel through the statistical information of its neighbor pixels. In [7] a novel object identification algorithm was developed in Java to locate immune and cancer cells in images of immune histochemically- stained lymph node tissue. This algorithm focuses on the interactive feature extraction from color images, so that the classification is improved with an interactive visualization system. Then, in order to increase the accuracy it coupled with the statistical learning algorithms and intensive feedback from the user.

Statistical methods represent another important category in the segmentation process and most of the approaches proposed in this category were using some statistical classifications combined with different image processing techniques in order to segment the MRI images [3, 8, 9, and 10].

One of the reliable and suited MRI and CT segmentation techniques is the region growing that can be applied to TCa tumor is generally, presented in many studies [3 and 11-16]. Cheng-Long Chuang et al. proposed an image-based object segmentation algorithm for extracting tumor-like objects in CT images based on intensity regions automatically in a CT volume image [15]. Mancas et al. provided segmentation using region growing threshold; this technique used threshold and spatial information to segment the region of interest [11]. Jiang et al. also provided producer for segmentation and quantification of brain tumor, by semi automatically detecting the area of the tumor in the brain that help the radiologist to treatment [16].

This paper is organized as following: a review about the TCa types and the related work was presented. A detailed description of image preprocessing and extraction parameters from the ROI, data collection, and statistical analysis for the collected data is described in second section. The last section describes the experimental results and discussion and concludes the paper along with outline future direction.

2. Methodology

In this study, the processed images of TCa are divided into two different groups:

The first group is representing the sample of 21 (n_1) images which was already diagnosed as a malignant tumor, and the second group is representing the sample of 12 (n_2) diagnosed as benign tumor were collected randomly. All data were provided by the Hussein Medical City hospitals and the Islamic hospital in 2006 and 2007 respectively, Amman, Jordan. The common procedure of determining throat tumor type was by examining the patient's MRI images by an experienced radiologist. According to these comments, that would be our reference later on, the type of tumor will be decided which may not be accurate as mentioned above as misdiagnoses. Our proposed approach is about using the statistical analysis of the data obtained from MRI images and makes inferences to distinguish between the two different types of tumor which may be more accurate than the traditional method and be supporting technique for the physicians.

2.1. Preprocessing of image data

MRI image should be prepared and treated by applying the steps:

- Convert all images to the gray scale
- Enhancement image to improve quality
- Image segmentation to find the region of interest (ROI).
- Histogram of region of interest (ROI)
- Apply statically process on (ROI) to find the final result that we need to make the comparison between malignant and benign tumors based on the use of test of hypothesis.

The tumor of TCa is surrounding by others part of the neck (nasopharynx, oropharynx, pharynx and the hypopharynx) that looks like tumor in the normal form. Hence, the region that covers the tumor should be carefully enhanced and improved so that after applying the

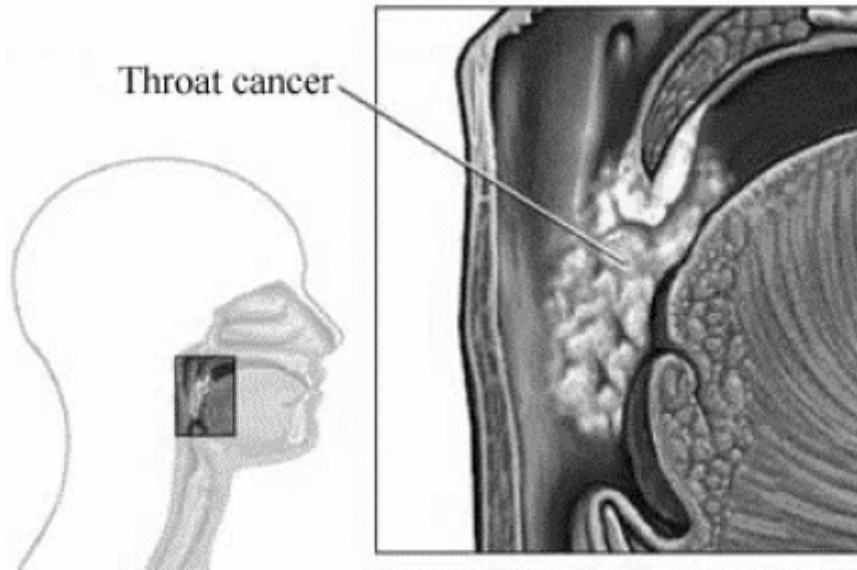


Figure 1: Throat Cancer Tumor

segmentation technique we could extract the needed features accurately.

Some of the images characteristics such a small size, or low contrast can be seen, but this problem was solved by using the special low pass filter. The clarity of the filtered image depends on many factors such as filter mask, original image, boundary option and the standard parameter called alpha. These entire factors were considered in performing the filtration process. The low pass filter is used and implemented using the LabView Software. It allows low frequency data, or data that does not change much from pixel to neighboring pixel, to pass through, For an image that contains a lot of noise, such a filter would smooth out the image and reduce the noise with minimal affect on large features in the image. A low pass filter will affect large features in the image, and will reduce or eliminate the smaller features [17, 3].

The next step is the image segmentation.

In the normal cases, when the throat image of the patient arrives to the radiologist, he studies the up normal regions in the image to discover the type of the tumor. So,

the diagnostic depends on segment these regions. Segmentation process is to divide an image into its constituents regions or objects, then take a specific region; it is called the region of interest (ROI). Histogram is a process followed by segmentation. It counts the total number of pixels in each grayscale value and graphs it.

2.2. Statistical Analysis

For each MRI image the data is collected and tabulated. Analysis of such data will be demonstrated in two ways; the descriptive analysis utilizing the Box Plot presentation, and the testing of hypotheses approach. A hypothesis stated that there is no difference between the malignant and benign will be tested using the difference between two sample t- test.

The test statistics is a single number that calculated from the sample mean, which can be located in the rejection region or in the acceptance region. Depending on the location of test statistics the null hypothesis could be rejected or accepted as illustrated in figure 2.

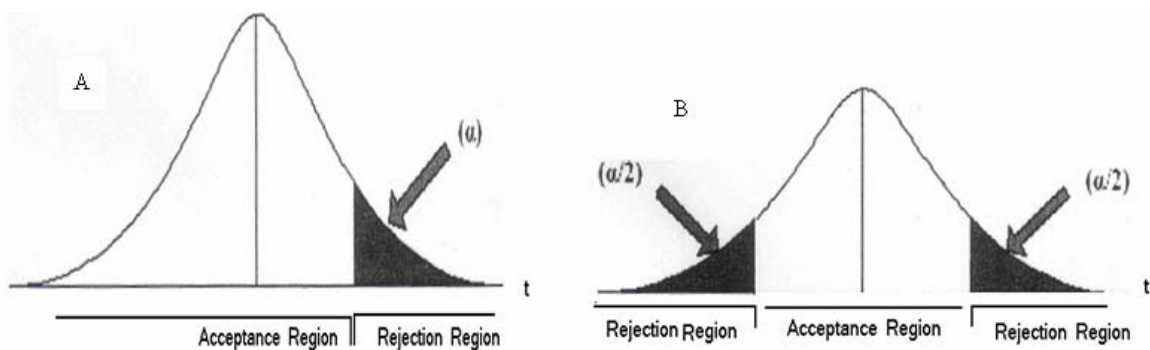


Figure 2: Rejection and acceptance regions for one tail and 2-tail test

Applying the test of hypotheses is done by following these steps [18-20]:

- Null hypotheses $H_0 : (\mu_m - \mu_b) = D_0$, where D_0 is some difference between the mean values .and we will consider $D_0 = 0$.

Test statistics (t_0)

$$t_0 = \frac{(\bar{X}_1 - \bar{X}_2) - D_0}{S_p \sqrt{\left(\frac{1}{n_1} + \frac{1}{n_2}\right)}} \quad (1)$$

$$s_p = \sqrt{\frac{(n_1 - 1)s_1^2 + (n_2 - 1)s_2^2}{n_1 + n_2 - 2}} \quad (2)$$

Where S_p : pooled standard deviation.

d_f : degree of freedom;

$$d_f = n_1 + n_2 - 2 \quad (3)$$

- Find The critical value of t_α OR $t_{\alpha/2}$ depending on α (type I error)
- Compare the two values of the test and decide on H_0

3. Result and Analysis

3.1. Image Preparation

Figures 3 and 4 show the image processing result for malignant and benign tumors respectively contain filtered image and histogram for the selected ROI that contain many statistical variables. It is noted that the output image have higher quality than input image, also there is no difference between applying the enhancement on malignant or benign.

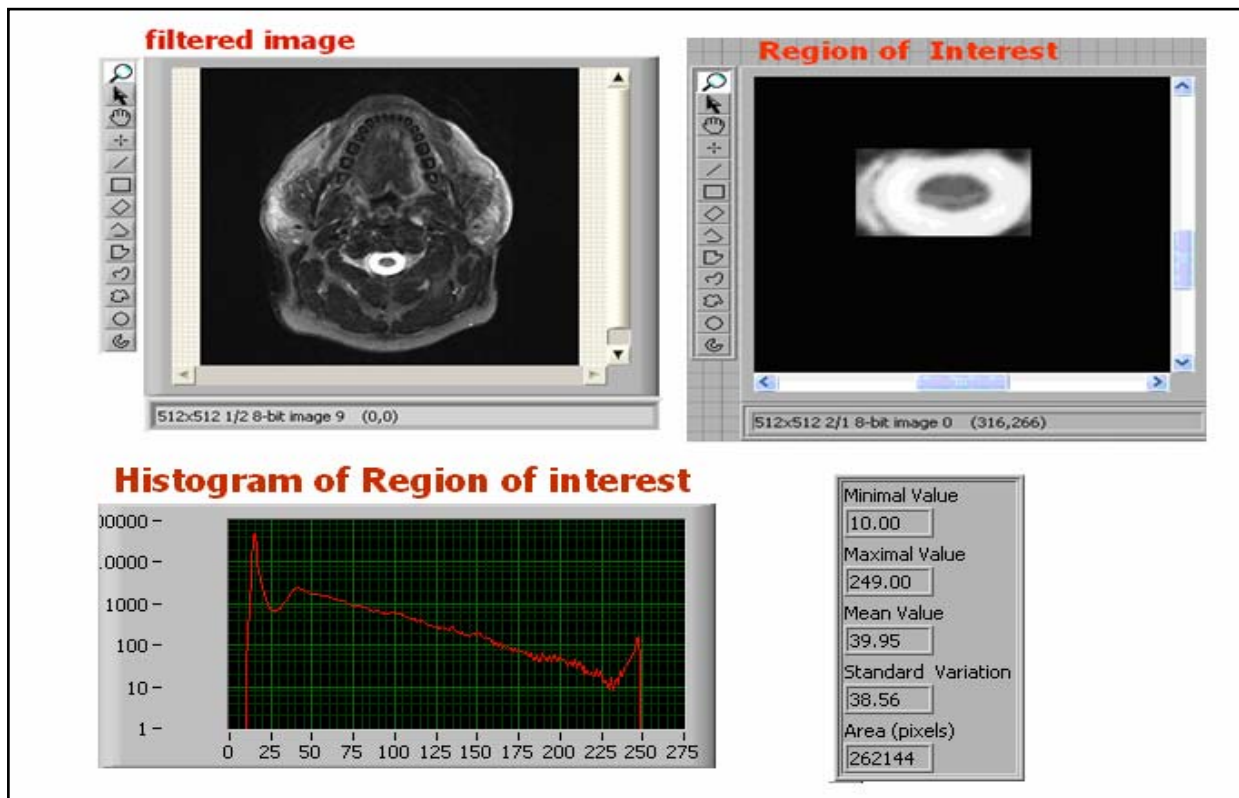


Fig. 3 Image processing result of malignant tumor

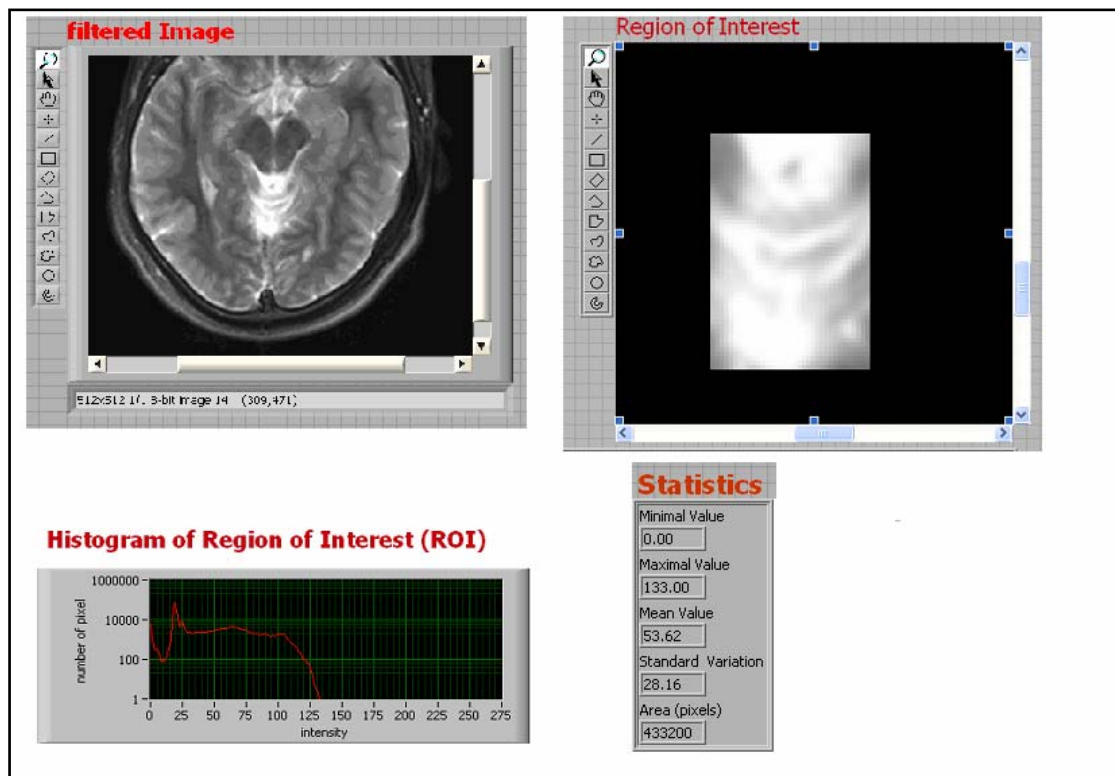


Fig. 4 Image processing result of benign tumor

By comparing figure 3 and figure 4, the two figures, the histogram for ROI in both malignant and benign tumors are different, since the histogram of region of interest in malignant image reaches high level of pixel value than the histogram of region of interest in benign image

4. Statistical Result

Statistical analysis for all images data was performed in two stages; the first stage is the descriptive analysis and construction of the box plot for each type of the tumor, while the second stage is to perform the testing of hypothesis on the mean of the two types.

4.1. Descriptive Result

The average pixel value, the standard deviation and the range for the malignant and for the benign were calculated for the two sample data available. It is noted that there is a difference between the malignant and benign image in many parameters such as, the mean pixel for the malignant image is higher than in the benign images.

Table 1 shows the summary of the descriptive analysis for the maximum and average pixel values in all 21 images and 12 benign images.

The above table shows that there is a difference in the mean value of the averages between the malignant and the benign tumor images. The mean for the malignant images was 95.58 while it was 40.1 for the benign images. It is also noted that the value of the maximum number in benign tumor is small than max value of the malignant

tumor and the average mean of the pixel is below from 100.

The Box Plot in figure 5, clearly indicates the same results that the average value of the malignant tumor which are in the range of (80-115) is higher than the average values of the benign tumor which are in the range of (22-58).

The mean value for the maximum values in malignant images was 227, while the mean value for the maximum values in benign was 163. The standard deviation and median for the malignant is higher than the benign images. Moreover, the maximum and minimum in the malignant is higher than the benign. All the above descriptive give an indication that the malignant images are differ from the benign.

The Box Plot in figure 6, clearly indicates the same results explained in table 1, that is the maximum values of the malignant tumor which are in the range of (208-256) is higher than the maximum values of the benign tumor which are in the range of (135-190).

The difference between the two samples is clearly obvious as is shown in the figures above since the malignant images have a box plot with higher range and higher spread than the benign box plot. Considering the average pixel value to be the criterion to distinguish between the two tumors types, it is clear that the malignant type have greater pixel values than the benign one. Also, the dispersion for the benign tumor is smaller than the malignant one.

Table:1 Statistical parameters for maximum and average pixel values for malignant and benign

Subject	Maximum Pixel Values		Average Pixel Values	
	Malignant Tumor	Benign tumor	Malignant Tumor	Benign tumor
Mean	226.76	163.33	95.58	40.1
Maximum	255	206	120.93	73.29
Minimum	177	123	50.11	14.5
Standard deviation	26.6	29.85	20.02	19.28
Variance	707.79	890.97	400.7	371.85
The lower quartile (Q1)	203.5	134.5	77.93	23.33
the upper quartile (Q3)	251	191.5	114.02	53.09
Range	78	83	70.82	59.04

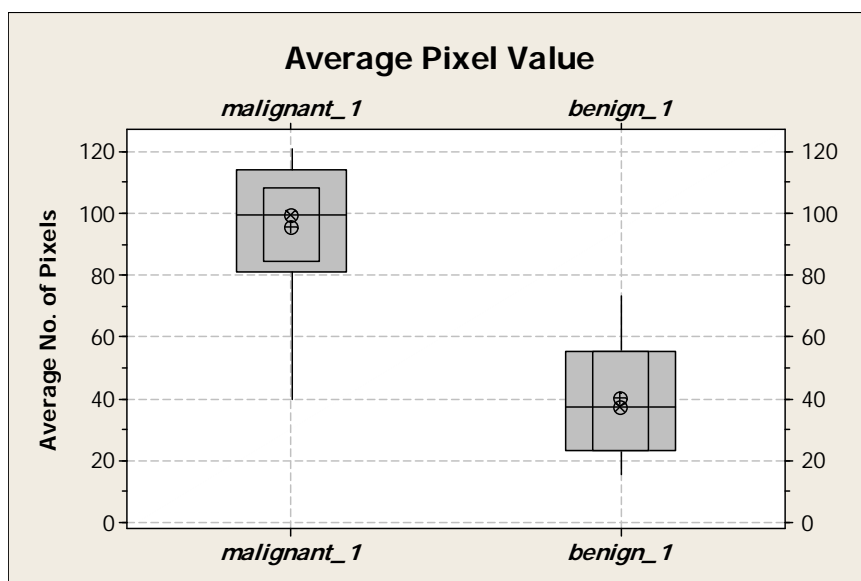


Figure 5: Box plot for the average pixel values

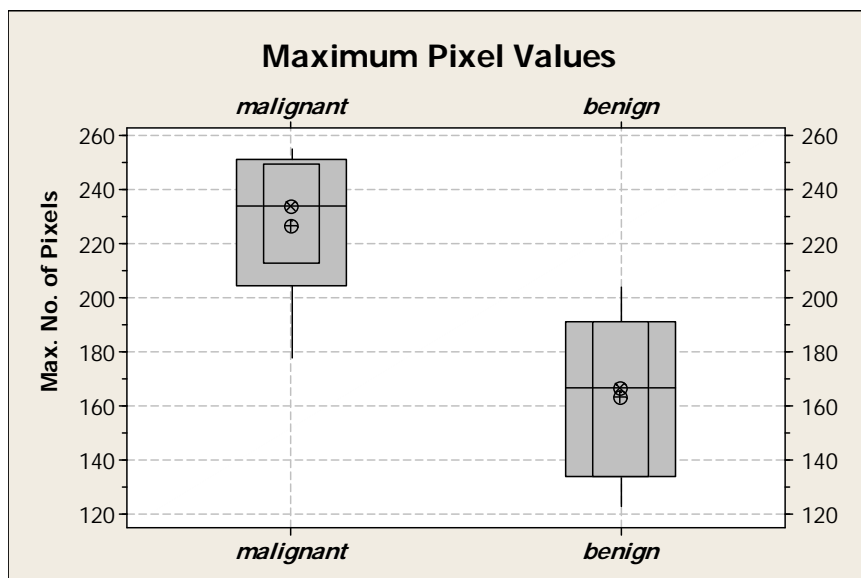


Figure 6: Box plot for the maximum pixel values

4.2. Testing of the Hypothesis

In the pervious section, the information in table 1, is needed to perform the test of hypothesis that say the mean of maximum number of pixel and the mean of average number of pixels in the malignant tumor is higher than from the benign ones .A two sample t – test will be used because the number of the two sample is different and the samples were drawn from a population with unknown variances. .

4.2.1. Test of the hypothesis for mean average number of pixel

In order to make a conclusive decision about the difference between the malignant and the benign images, the null hypothesis is tested against the alternative one as below:

$$H_0 : (\mu_m = \mu_b)$$

$$H_a : (\mu_m \neq \mu_b),$$

Where: H_0 : is the null hypothesis

H_a : is the alternative hypothesis

μ_m is the mean of the average number of pixels in malignant images

μ_b is the mean of the average number of pixels in benign images.

Since the two samples have a probability plot approximately linear, the (t) test for difference between two sample means will be used in testing the null hypothesis. If t- calculated value> t- tabulated value, we reject H_0 and accept H_1 . The results for using the two sample (t) test are shown below; these parameters are used to calculate the (t) statistics.

Table 2: Parameters used in the t test

Parameters	Value
Mean of M	226.8
Mean of B	163.3
Standard deviation S_m	26.6
Standard deviation S_B	29.8
t- calculated value	6.31
Pooled standard deviation S_p	27.7991
Significant level α	0.05
t- tabulated value	1.696
Degree of freedom df	31
Number of sample n_1	21
Number of sample n_2	12

From table 2, the t- calculated value (6.31) > t- tabulated value (1.696), and since the t (calculated) is located in the rejection region, we reject the null hypotheses H_0 and strongly conclude that there is a difference between the mean value of malignant and the mean value of benign images with 95% confidence, this means that type I error is 0.05. Then the average value of the number of pixel of malignant tumor is higher than the average value of the number of pixel of benign.

4.3. Test of the hypothesis for mean maximum number of pixel

Another important testing of hypothesis is that whether the maximum pixel value of the malignant is equal to the maximum pixel value of the benign image.

$$H_0 : (\mu_{mm} = \mu_{mb})$$

$$H_a : (\mu_{mm} > \mu_{mb}),$$

Where: H_0 : is the null hypothesis

H_a : is the alternative hypothesis

μ_{mm} : is the mean of max. Pixel value in malignant images

μ_{mb} : is the mean of max. Pixel value of benign images

. The data and the results for using the two sample (t) test are shown below; these parameters are used to calculate the (t) statistics.

Table 3: Parameters used in the t test

Parameters	Value
Mean of M	95.6
Mean of B	38.5
Standard deviation S_m	20
Standard deviation S_B	19.3
t- calculated value	7.98
Pooled standard deviation S_p	19.7601
Significant level α	0.05
t- tabulated value	1.309
Degree of freedom df	31
Number of sample n_1	21
Number of sample n_2	12

From the table the t- calculated value (7.98)> t- tabulated value (1.309) and since the t(measured) is located in the rejection region, we reject the null hypotheses H_0 and strongly conclude that the maximum pixel value for malignant is greater than the maximum pixel value for benign images with 95% confidence. Then the average of average value of the number of pixel of malignant tumor is higher than the average of average value of the number of pixel of benign.

5. Conclusion

In this study, our goal is to automatically and statistically diagnose the type of tumor in the throat by using MR images. In order to do this, we addressed simple box plot technique to differentiate between the two types. Also, testing of hypothesis was applied for the same purpose. Region of interest, filtration and segmentation techniques were utilized to be the base of the information to get the statistical data for each case. It has been proven that a simple, harmless and accurate statistical technique can efficiently distinguish between the malignant and benign tumor (TCa). The huge advantage of this approach is that there will be no need to make any further tests or examinations on the patient after making the MRI. Some

of these tests or examinations are difficult to be performed or may be dangerous such as throat biopsy.

The diagnosis system achieves accuracy over 95.0% in differentiation between the different tumor types on various qualities of MR images. Although some satisfactory results are obtained, the diagnosis system still needs to be improved. The results of the experiments and application of the proposed method may also be applied to the other areas of medical image analysis. So, another future task is to apply this proposed method to other areas in medical image analysis to improve the achieved accuracy in this study and the previous one in [3].

Some weaknesses of the algorithm are the small area of the overlap between the extreme values of the two different tumor types. To overcome this drawback, it is suggested to increase the number of samples used for the study.

This automatic statistically based diagnosis method is developed to classify the images of large medical databases. Here, this simple and fast diagnosis method may be used to extract information from the large medical databases. An important future work would be measuring the performance of this method in mining medical databases.

References

- [1] National Cancer Institute, USA. <http://www.cancer.gov>.
- [2] King Hussein Cancer Centre, Jordan. <http://www.khcc.jo>.
- [3] B. Al-Naami, A. Bashir, H. Amasha, J. Al-Nabulsi, and A. Almalty, "Statistical Approach for Brain Cancer Classification Using a Region Growing Threshold". *Journal of Medical Systems*, DOI: 10.1007/s10916-009-9382-6.
- [4] S. Ethan, H. Lubomir, S. Berkman, G. Sachin, I. Mohannad, K. Suresh and C. Heang-Ping, "Automated volume analysis of head and neck lesions on CT scans using 3D level set segmentation". *Med Phys.* Vol. 34, No. 11, 2007, 4399–4408.
- [5] Z. Haibo, S. Hong, D. Huichuan, "An Automatic and Robust Algorithm for Segmentation of Three-dimensional Medical Images". *Sixth International Conference on Parallel and Distributed Computing Applications and Technologies (PDCAT'05)*, Dalian, China, 2005.
- [6] Z. Shiping, X. Xi, Z. Qingrong, B. Kamel, "An Image Segmentation Algorithm in Image Processing Based on Threshold Segmentation". *Third International IEEE Conference on Signal-Image Technologies and Internet-Based System*, Shanghai, China, 2007.
- [7] H. Susan, K. Adam and P. Peter, "An Interactive Java Statistical Image Segmentation System". *GemIdent, Journal of Statistical Software*, Vol. 30, No 10, 2009, 1-20.
- [8] M. Justin, K. Iftekharruddin, "Statistical analysis of fractal-based brain tumor detection algorithms". *Magnetic resonance imaging*, Vol. 23, No. 5, 2005, 671-678.
- [9] M. Ashraf, I. Evangelia, S. Dinggang, D. Christos, "Deformable registration of brain tumor images via a statistical model of tumor-induced deformation". *Medical Image Analysis*, Vol. 10, No. 5, 2006, 752-763.
- [10] X. Xiao, L. Qingmin, "Statistical Structure Analysis in MRI Brain Tumor Segmentation. *Image and Graphics*", ICIG. Fourth International Conference, Sichuan, China, 2007.
- [11] M. Mancas, B. Gosselin, B. Macq, "Segmentation Using a Region Growing Thresholding", *Proc. of the Electronic Imaging Conference of the International Society for Optical Imaging SPIE.*, San Jose (California, USA), 2005.
- [12] M. Sezgin, B. Sankur, "Survey over image thresholding techniques and quantitative performance evaluation". *J. Electron. Imaging* Vol. 13, No. 1, 2004, 146-165.
- [13] M. Chowdhury, W. Little, "Image thresholding techniques" *IEEE Pacific Rim Conference on Communications, Computers, and Signal Processing*, Victoria, BC, Canada, 1995.
- [14] Z. Pan, L. Jianfeng, "A Bayes-Based Region-Growing Algorithm for Medical Image Segmentation. *Computing in Science & Engineering*, Vol. 9, No. 4, 2007, 32 – 38.
- [15] C. Cheng-Long, and C. Chun-Ming "A Novel Region-based Approach for Extracting Brain Tumor in CT Images with Precision. *World Congress on Medical Physics and Biomedical Engineering. IFMBE Proceedings*, Vol. 14, No. 4, 2006, 2488-2492.
- [16] J. Chunyan, Z. Xinhua, H. Wanjun, C. Meinel, "Segmentation and quantification of brain tumor, *Virtual Environments*". *IEEE Symposium on Human-Computer Interfaces and Measurement Systems*, Boston, USA, 2004.
- [17] Rafael C. Gonzalez, Richard E. Woods and Steven L. Eddins. *Digital image processing, Second Edition*, Prentice Hall, Upper saddle River, new Jersey, USA, 2004.
- [18] Douglas C. Montgomery and George C. Runger; *Applied Statistics and Probability for Engineers*, Fourth Edition, John Wiley and Sons, New York, USA, 2008.
- [19] Ronald E. Walpole, Roymond H. Myers, Sharon L. Myers and Keying YE; *Probability and statistics for Engineering and Scientists*, Eighth Edition, Prentice Hall, Upper saddle River, new Jersey, USA, 2008.
- [20] Williams W. Hines and D. Montgomery, *Probability and Statistics in Engineering and Management Science*, Forth edition, John Wiley & Sons, Inc., New York, USA 2006.

Experiments on Aluminum-Copper Alloys Properties as Solar Absorbers

Abdul Hai Alami *

Mechanical Engineering Department, The Hashemite University, Zarqa, Jordan

Abstract

In this paper, selecting absorber materials for solar collectors is experimentally investigated. Copper and aluminum alloys were cast at four different percentages of each, then their grain structure was examined and comprehensive solar tests were conducted to measure the heat capacity of each alloy and compare that with the available solar irradiance available at the test site at the Hashemite University in Zarqa, Jordan.

© 2010 Jordan Journal of Mechanical and Industrial Engineering. All rights reserved

Keywords: Aluminum-copper alloys, grain structure, thermal solar absorbance of alloys, effectiveness of alloys.

1. Introduction

For flat-plate solar thermal collectors, copper could be the material of choice to construct the absorber section. But its high cost and weight makes finding an alternative a very viable research area. The importance of using solar collectors have increased many folds in recent years with the constant depletion of fossil fuels and the inevitable need to find alternative methods to rely on renewable sources, such as harnessing the thermal power from the sun. The Hashemite Kingdom of Jordan has more than 300 sunny days a year, making the adaptation of solar energy on a wide scale an economical and environmental advantage.

In literature, there are many different setups for solar collectors, where measuring the efficiency of heat transfer between the solar irradiance and the solar collector as the main concern. One notable effort to combine all literature on selecting the materials used listed in [i], but otherwise, the focus on experimenting with different alloys as absorber materials is limited, or the main focus would be on experimenting with special coating materials [ii,iii]. Hence, the aim of this paper is to research the viability of alloying copper with aluminum, and then select the best percentage to use in the actual absorber.

2. Theoretical background

For the experimental work intended for this research, it is necessary to calculate the heat capacity of the alloys composed of various percentages of aluminum and copper.

The governing equation will include the specific heat for each constituent and multiplied by its mass fraction within the total mass of the alloy. The heat capacity equation is a function of the temperature rise as follows:

$$Q = [m_{Cu}c_{pCu} + m_{Al}c_{pAl}] \Delta T \quad (1)$$

where,

Q is the heat capacity of the total alloy [J]

c_{pCu} is the specific heat of copper, 395 KJ/Kg.k,

c_{pAl} is the specific heat of aluminum, 920 KJ/Kg.k, and

ΔT is the temperature rise in the alloy, in either k or °C

The above equation will be used later to compare the heat gained through each alloy due to its exposure to solar radiation with the available heat irradiation values obtained from the Hashemite University solar station in Zarqa, Jordan. It is worth noting that the values obtained will be divided by the time in seconds required for the temperature rise to obtain the values in Watts and make the units of both the measured values and the readings compatible.

3. Experimental setup

In this section, the preparation of test specimens and the equipment used for their testing will be presented.

3.1. Specimen Preparation

The specimens needed for the experimental tests are alloys cast of four compositions of copper and aluminum formed into two basic geometries; cylindrical specimens for both Scanning Electron Microscope (SEM) tests and the composition test, and also flat plate specimens for the solar tests.

* Corresponding author. alami.hu@gmail.com

3.1.1. Master alloy preparation

To produce the test specimens with the desired composition, four sets of master alloys were cast with copper composition of 20%, 40%, 60% and 80% by weight of the Cu-Al alloy. The master alloys were prepared in specially fabricated graphite crucible (Figure 1).

Graphite was also used as a casting die for cylindrical and flat plate test specimens, as seen in Figure 2, since

graphite can be easily machined into the desired shape and dimensions with no or very minimum contamination of cast specimens and high durability at high temperatures. The molten master alloy is poured from the crucible into the appropriate die to produce the desired geometry, which is either a cylindrical specimen ($\phi=20\text{mm}$, $h=35\text{mm}$), or a flat-plate geometry ($150\times 150\times 10\text{mm}$).



Figure 1 Graphite Crucible



Figure 2 Graphite dies (a) cylindrical specimens and (b) flat plate specimens

3.1.2. Specimen casting

Casting of master alloys was conducted at the casting workshop at the Hashemite University. Pure aluminum in the form of power transmission lines was acquired from the Jordanian Electric Power Company (has a purity percentage of 96%). As for copper, brass nuggets were bought due to budget limitations. The master alloy components were weighed using an electric scale as

fractions of the estimated weight (specimen volume times the density of the components plus 10% error margin). Each composition was then placed in the crucible and placed in the induction oven at the casting workshops and stirred with a special ceramic stirrer to homogenize the metal mix, and then poured in the appropriate dies, as seen in Figure 3.

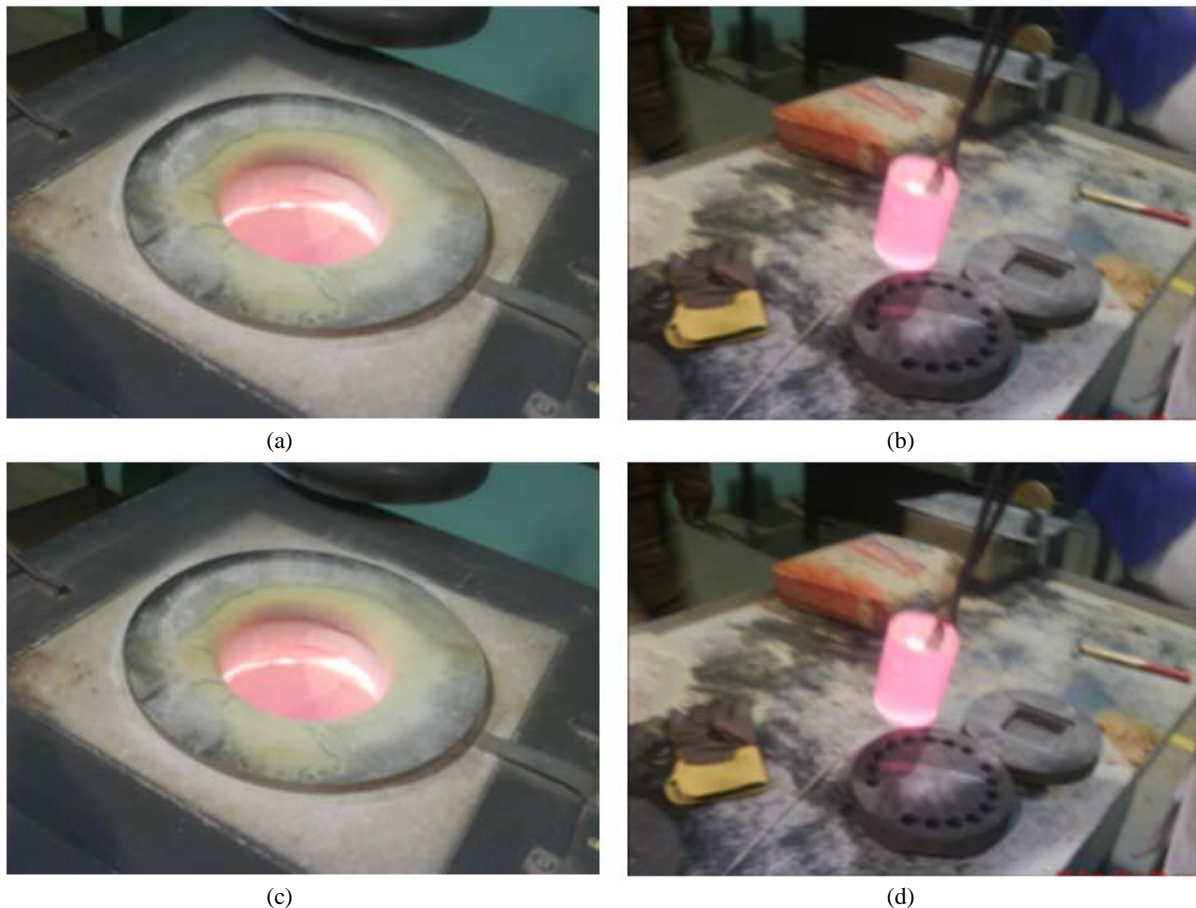


Figure 3 Casting steps: (a) crucible at induction furnace, (b) & (c) pouring, and (d) cast specimens after cooling

The specimens were all allowed to cool at room temperature after casting, and then the cylindrical specimens were cut using the metallurgical saw available at the metallurgy lab at the Hashemite University, with coolant present to remove excess material.

3.2. Composition test

This test was conducted to ensure that the test specimens contain the desired amounts of each component of the alloy. The technique used is X-Ray fluorescence on a computer-controlled Phillips X-Ray spectrometer located at the NDT lab at the Hashemite University. A cylindrical specimen of each composition was used for the test as the machine can accommodate specimens 27-40mm in diameter and up to 40mm height.

3.3. Scanning Electron Microscope (SEM) test

This test was planned to attempt to correlate the grain size, segregation and distribution of the master alloys with their behavior during solar testing. Each of the four compositions were represented by a specimen and all of them were cut at the Metallurgy lab at the Hashemite University, mounted in Backlite, then ground by successively finer sand paper (starting from 600 up to 1200 grit silicon carbide). Then, all specimens were polished using 6-micron diamond paste on an alcohol film on a rotary bed with hand pressure. Care was taken to gently rotate the specimen while grinding it opposite to the rotary bed direction. Finally, the specimen were etched using a solution prepared from 2.5ml Nitric Acid, 1.5ml HCl, 1ml Hf and 95ml water, and the specimens were

examined under the microscope at magnifications of 100x and 200x.

3.4. Solar Test

The purpose of this test is to quantify the effect of altering the Cu-Al composition within the alloy as the chosen material for a solar absorber. The test was scheduled for 21st and 22nd of April 2009 since only one operational thermocouple and data acquisition instrument was available due to budget limitations, and thus the tests were conducted for two specimens, the first was installed one hour before the solar noon (11:45 am, Jordan Standard Time) for those days and a second was installed one hour after, since the solar irradiation of the sun is symmetrical in intensity and incidence angles [i] around the solar noon and for one hour on each side. This means that tests were started before 11:00 am and lasted till around 11:40 am for one specimen, and another specimen is fitted from 11:40 am and left till around 12:30 pm. Tests were conducted at the Hashemite University in Zarqa, Jordan (32N latitude and 36.14 E Longitude). The recorded data will be compared with available solar irradiation readings from the Hashemite University solar station and dedicated to recording solar radiation all year round.

The test assembly shown in **Figure 4** consists of a special high-emissivity glass enclosure that permits the maximum amount of solar radiation due to the low content of iron. The enclosure isolates the test specimens from the convective effects of the wind as the glass box was sealed from the bottom with a commercial sealant.



Figure 4 Solar test setup

The setup was placed in direct sunlight and the azimuth angle (the location of the sun measured away or towards the south) was adjusted manually by rotating the device around its yaw axis 15° per hour as the sun moved across the sky. The device was also inclined at 19° in winter (43.3° in summer) according to the zenith angle for the experimentation location at 32.1° N, 36.1° E, according to [4]. This provision ensures that incident solar rays are perpendicular to the projected area of the surface at all times. A thermocouple was fixed at the bottom of each test specimen and connected to a digital data acquisition device to measure the temperature rise in the specimens. Since the test specimens are cast, each one was accurately weighed and the weight recorded. Actual readings were also taken from the solar station at the Hashemite University that includes a Pyranometer that measures the global radiation on horizontal surfaces. It is mounted on the roof of the

Engineering College, and contains carefully calibrated thermoelectric elements fitted under a glass cover, with data recorded every 5 min and then averaged on hourly, daily, and monthly basis. The sensor is a photodiode detector having a spectral response from 0.4 to 1.1 microns, with a sensitivity of 100 mV per 1000 W/m^2 , and an accuracy of $\pm 5\%$. The effectiveness of each alloy will be calculated as the thermal capacity of each composition according to the following relation:

$$Eff(\%) = \frac{(Cp_{cu} * m_{cu} + Cp_{Al} * m_{Al}) \Delta T}{I_o A_p} \quad (2)$$

where Cp_{cu} , Cp_{Al} are the specific heats of copper and aluminum, respectively as given previously in [KJ/Kg.K], m_{cu} , m_{Al} are the mass fraction of copper and aluminum, respectively, in each alloy in [Kg], ΔT is the temperature rise of each alloy as recorded by the thermocouples [K], and while I_o is the solar radiation intensity (W/m^2) and A_p is the alloy projected area in m^2 .

4. Experimental results

This section presents the results obtained during the experimental stages of this research.

4.1. Composition test

The following tables list the main elements found by running the X-Ray fluorescence test:

1) AL 100%		2) 20% Cu +80%Al		3) 40% Cu +60%Al	
Elem	Percent	Elem	Percent	Elem	Percent
Al	96.0%	Al	69%	Al	56%
Cl	0.4%	Ca	0.1%	Cl	0.81%
Ca	0.25%	Mn	0.84%	Mn	0.61%
Mn	0.27%	Fe	1.99%	Fe	1.1%
Fe	0.91%	Ni	0.16%	Cu	29.5%
Cu	0.15%	Cu	8.3%	Zn	9.37%
Zn	0.16%	Zn	16.5%	Nb	0.2%
Pd	1.8%	Ru	2.4%	Os	0.2%
Re	0.06%	Sb	0.4%	Pb	0.64%

4) 60% Cu +40%Al		5) 80% Cu +20%Al	
Elem	Percent	Elem	Percent
Al	33%	Al	7.4%
Mn	0.73%	Mn	1.00%
Fe	1.6%	Fe	2.64%
Cu	46.4%	Ni	0.21%
Zn	15.1%	Cu	69.1%
Nb	0.3%	Zn	16.9%
Pd	2.0%	Nb	0.4%
Os	0.1%	Ru	1.8%
Pb	0.35%	Pb	0.58%

4.2. SEM test

The following figures are the result of the SEM test for all four percentages:

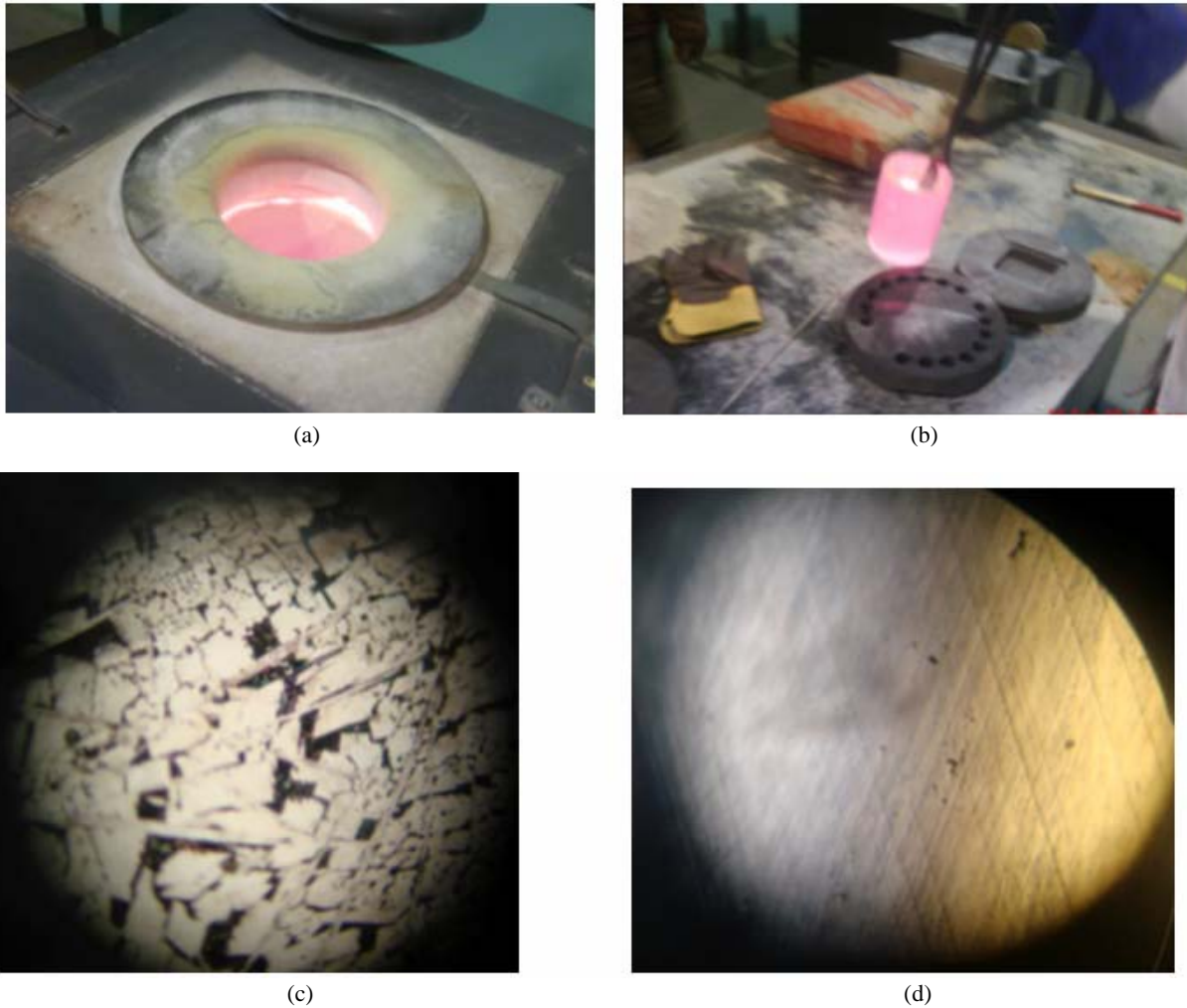


Figure 5 . SEM photos for (a) 20%Cu, (b) 40%Cu, (c) 60%Cu and (d) 80%Cu

4.3. Solar test

This section presents the results of the thermal solar test for the four percentages of copper. The temperature rise for each specimen is a direct indication of its thermal capacity through the duration of the test.

This will be taken as a fraction of the available irradiation values from the Hashemite University solar station (being the maximum amount available) and plotted against time to arrive at instantaneous values for the effectiveness of the heat capacity of the alloy as calculated using equation (2).

4.3.1. Results for 20%Cu-80%Al

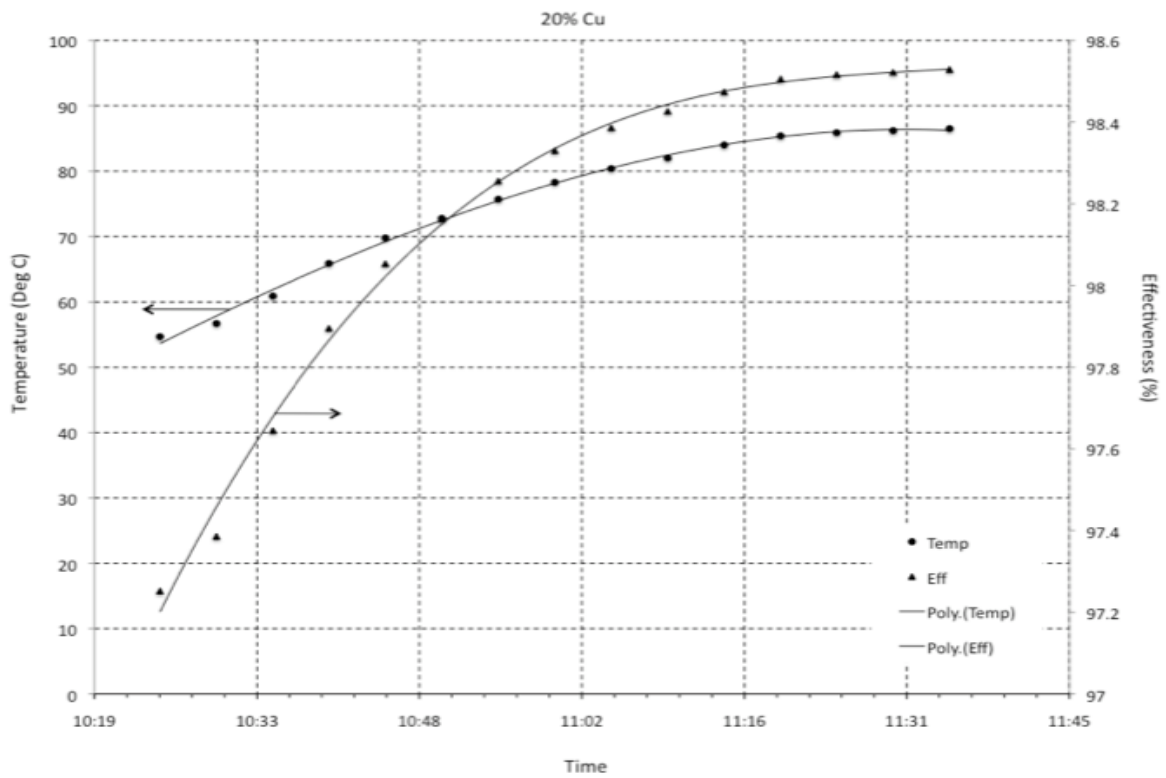


Figure 6 Temperature rise and effectiveness for 20% Cu content

4.3.2. Results for 40%Cu-60%Al

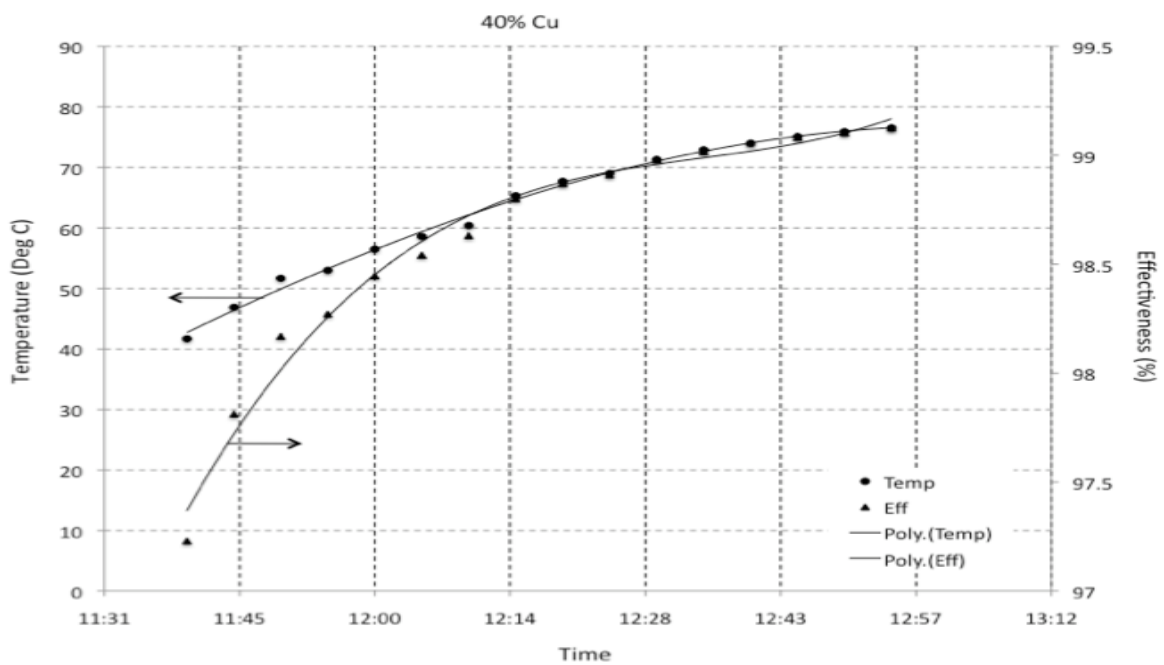


Figure 7 Temperature rise and effectiveness for 40% Cu content

4.3.3. Results for 60%Cu-40%Al

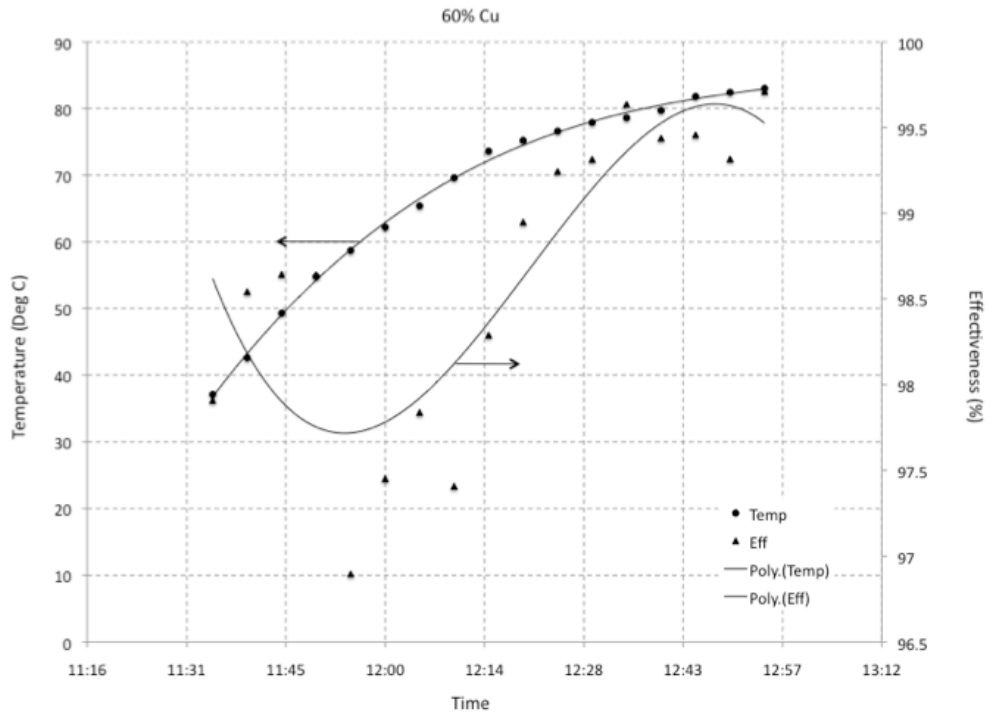


Figure 8 Temperature rise and effectiveness for 60% Cu content

4.3.4. Results for 80%Cu-20%Al

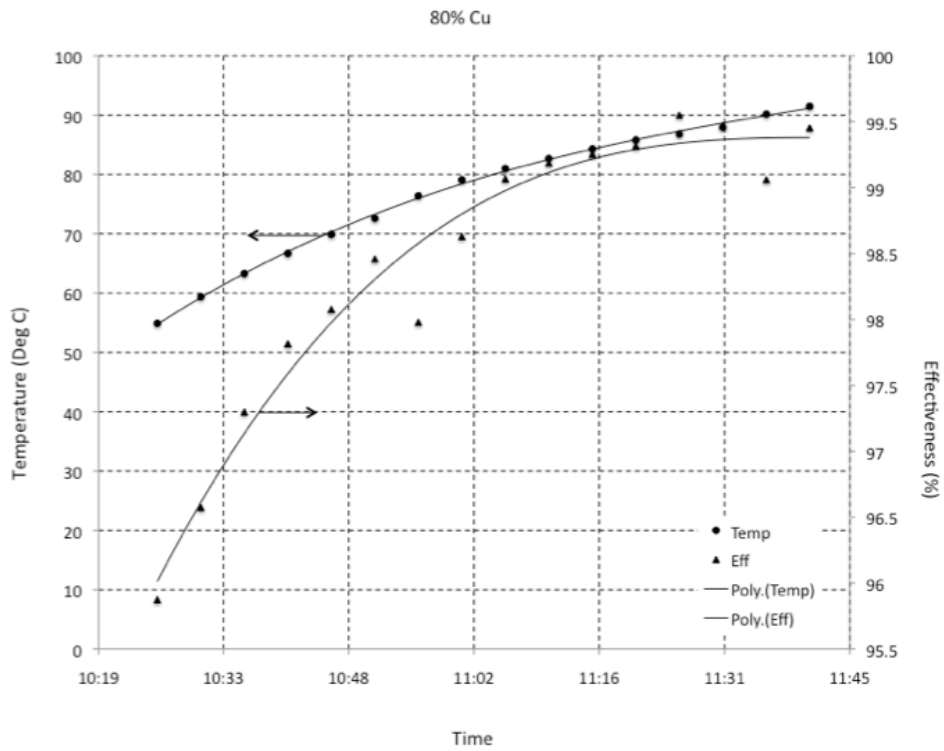


Figure 9 Temperature rise and effectiveness for 60% Cu content

5. Experimental discussion

5.1. Composition test

From the tables presented at section 4.1, it can be clearly detected that there is a high percentage of zinc present in the alloy, and the percentage of copper is lower than the percentage expected (around 13% less copper than expected). This was noted for future experiments, and copper nuggets with higher purity will have to be purchased. But for the purpose of this investigation, the amount of copper in each alloy will be a good indication on the solar capabilities of the material as well as its manufacturability.

5.2. SEM test

All the specimens were allowed to cool down to room temperature without quenching. And since the phase diagram of Al-Cu alloy shows no significant metallurgical changes for alloys with less than 80% Cu composition [i], it is interesting to note the difference in the grain structure for each alloy type depending on the amount of copper and trace materials available in the alloy. For example, with the alloy denoted 20%Cu, the addition of Cu and other elements caused the aluminum grains to exhibit a grain refinement effect [ii], where the aluminum grains are smaller and have almost equal size, as seen in Figure 5 (a). This effect is to be contrasted with the grain structure at the 40%Cu alloy in Figure 5 (b), where aluminum have solidified in the form of dendrites, which would be expected since aluminum is still more dominant than copper (or any other trace materials present), which lead to the formation of Al₂Cu during cooling, which also has a strong grain refinement effect [ii], as can be seen clearly around the dendritic arms in the figure. The more significant result from the SEM graphs was the one for 60%Cu alloy, where the copper grains are seen to be surrounding the aluminum grains in Figure 5 (c), where this diffusion happens around temperatures between 300-400°C when the amount of copper in the master alloy melt allows this diffusion [ii]. This arrangement will be shown to have a significant influence of subsequent solar thermal testing of this alloy as explained in the next section.

5.3. Solar test

By examining the solar test figures (Figure 6 thru Figure 9) a direct relation is seen between the temperature rise within the specimen and its effective increase in heat capacity of each alloy. The figures show small variations in the general trends among each other, except for Figure 8 that displays the variation for the 60% Cu content, where the scatter of the data points is noticeable, but the more interesting observations is that it scored the best effectiveness value (highest values for both minimum and maximum values of effectiveness on the curve).

One possible explanation can be inferred from examining Figure 5(c), that shows the SEM results for the 60%Cu alloy, and shows the grains of copper surrounding the grains of aluminum and being more significant in size

and opacity than in the case of 20%Cu content. This made the 60%Cu alloy more attractive to use as an absorber material than any other alloy, especially when taking another observation into account, that although all the alloys have the same Zn content, the 80%Cu alloy showed high brittleness characteristics which made it extremely difficult to manufacture and handle, and made it more susceptible to damage during installation and operation.

6. Conclusion

This research focused on testing different compositions of copper-aluminum alloys experimentally to determine their effectiveness as solar absorbers. The alloys were prepared by casting, examined under the SEM and solar experiments were conducted on the produced compositions (namely 20%, 40%, 60% and 80% copper content). It was concluded that there is a correlation between the grain structure and the thermal effectiveness of each alloy, especially the 60% Cu one, where the darker copper grains surrounded their aluminum counterparts. This result is primarily attractive when considering alternatives for pure absorber materials, since pure copper has superior heat transfer properties but is heavy and expensive, while with the economic availability of aluminum and its low density, it fails to be an effective replacement to copper alone.

References

- [1] M. Alghoul, et. al., "Review of Materials for Solar Thermal Collectors", Journal of Anti-Corrosion Methods and Materials, Volume: 52 Issue: 4 Page: 199 – 206, 2005.
- [2] Rebecca Powles et. al., "Solar Absorption In Thick And Multilayered Glazings", World Renewable Energy Congress VII, Cologne (DE), 2002.
- [3] F. Kadirgan and M. Sohmen "Development of Black Cobalt Selective Absorber on Copper for Solar Collectors". Turkish Journal of Chemistry, Vol. 23, pp 345-351, 1999
- [4] Basic Heat Transfer, 2nd ed, Frank Kreith, Harper & Row, New York; 1980
- [5] The Science and Engineering of Materials, 4th ed, Donald R. Askeland – Pradeep P. Phulé, New York; 2006
- [6] Adnan I.O. Zaid and AbdulHai M.B. Al-Alami, "The Effect of Vanadium Addition on the Fatigue Life of Aluminum, Grain Refined by Either Titanium or Titanium Plus Boron," 16th International Conference on Production Research (ICPR-16), Prague, Czech Republic, July 2001.
- [7] Osorio Wislei R, et. al. "The Roles of Al₂Cu and of Dendritic Refinement on Surface Corrosion Resistance of Hypoeutectic Al-Cu Alloys Immersed in H₂SO₄", Journal of Alloys and Compounds, vol. 443, no1-2, pp. 87-93, 2007.
- [8] N. A. Dolgoplov, et. al., "Diffusion of Copper Along the Grain Boundaries in Aluminum", Russian Journal of Non-Ferrous Metals, Volume 50, Number 2, 2009.

Statistical Process Control Tools: A Practical guide for Jordanian Industrial Organizations

Rami Hikmat Fouad*, Adnan Mukattash

Department of Industrial Engineering, Hashemite University, Jordan.

Abstract

The general aim of this paper is to identify the key ingredients for successful quality management in any industrial organization. Moreover, to illustrate how is it important to realize the intergradations between Statistical Process Control (SPC) is seven tools (Pareto Diagram, Cause and Effect Diagram, Check Sheets, Process Flow Diagram, Scatter Diagram, Histogram and Control Charts), and how to effectively implement and to earn the full strength of these tools. A case study has been carried out to monitor real life data in a Jordanian manufacturing company that specialized in producing steel. Flow process chart was constructed, Check Sheets were designed, Pareto Diagram, scatter diagrams, Histograms was used. The vital few problems were identified; it was found that the steel tensile strength is the vital few problem and account for 72% of the total results of the problems. The principal aim of the project is to train quality team on how to held an effective Brainstorming session and exploit these data in cause and effect diagram construction. The major causes of nonconformities and root causes of the quality problems were specified, and possible remedies were proposed.

© 2010 Jordan Journal of Mechanical and Industrial Engineering. All rights reserved

Keywords: Statistical Process Control, Check sheets, Process Flow Diagram, Pareto Diagram, Histogram, Scatter Diagram, Control Charts, Brainstorming, and Cause and Effect Diagram.

1. Introduction

Quality is a concept whose definition has changed overtime. In the past, *quality* meant “conformance to valid customer requirements”. That is, as long as an output fell within acceptable limits, called specification limits, around a desired value, called the nominal value (denoted by m), or target value, it was deemed conforming, good, or acceptable. We refer to this as the “goalpost” definition of Quality Gitlow and Levin [5].

The definition of statistics according to Deming, is to study and understand variation in processes and populations, interactions among variables in processes and populations, operational definitions (definitions of processes and populations variables that promote effective communication between people), and ultimately, to take action to reduce variation in a process or population. Hence, statistics can be broadly defined as the study of data to provide a basis for action on a population or process Deming [1].

Total Quality Management tools and techniques divided into the categories of quantitative and non-quantitative. The basic quantitative ones are statistical process control (SPC). SPC often called “The Magnificent Seven” is comprised of seven tools, Pareto Chart, Histogram, Process Flow Diagram, Control Charts, Scatter Diagram, Check Sheets and Cause and Effect Diagram

Besterfield [2]. The main objective of this paper is to apply basic statistical tools of quality control. SPC seeks to maximize profit by the following ways: Improving product quality, improving productivity, reducing waste, reducing defects and improving customer value. A Jordanian manufacturing company was chosen to implement SPC tools and concepts in order to improve the product quality and reduce process variability.

2. Company Background

Jordan Steel (JS) is a Public Limited Shareholding Company (P.L.C.) established in 1993 with a production capacity of 300,000 MT tons per year. It is the largest steel manufacturing company in Jordan. JS produces construction steel (Re bars) (diameters 8 - 32 mm) utilizing a fully automated production line. The manufacturing process at JS controlled, tracked and recorded by computer. Computer’s software at JS enables on line quality test and inspection. JS got ISO 9002 certification in 1998. Quality control procedure at JS works along the value chain starting from the supplier’s evaluation and selection, receiving raw material (Billets) all the way to after sales services. Billets are initially classified according to their chemical composition and stored in predetermined locations. Final products are tested for mechanical properties and results are handed to customers upon request. Production tractability is ensured through a label that shows the date of production and other information such as diameter, length, weight of bundle and grade. In order to develop process definition,

* Corresponding author. rhfouad@hu.edu.jo

understanding, and workflow a process flow chart of JS is shown in Figure 1.

3. SQC TOOLS

QC department at JS is currently implements only one

SPC tool that is the Control Charts. QC department analyze and review quality data once a week. The general purpose of this paper is to promote and implement other statistical tools as follows:

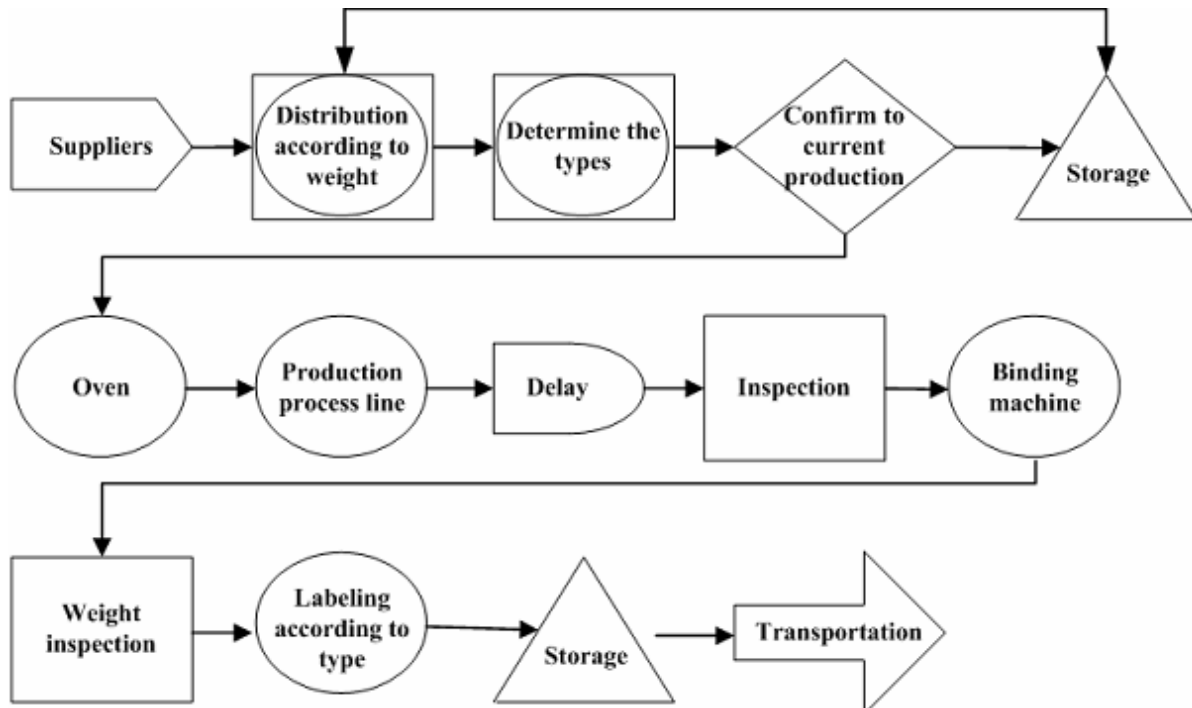


Figure 1: The Process Flow Chart of JS factory.

4. CHECK SHEET

The main purpose of Check Sheets is to insure that the date collected is carefully and accurately by operating personnel. Data should be collected in such manner that it can be quickly and easily used and analyzed. The form of the check sheet is individualized for each situation and is designed by the project team Besterfield [3]. The check sheet shown in Table 1 was created by tallying each type of call defect during a specified time. It shows the types of defects and how many of each type occurred during that period. Keeping track of these data provides management with information on which to base improvement actions.

5. Pareto Chart

The Pareto (pah-ray-toe) chart is a very useful tool whenever one needs to separate the important from trivial Goetsch [3]. A Pareto Chart is simply a frequency distribution (or Histogram) of attribute data arranged by

category Montgomery [7]. It is a special type of bar charts in which the categories of responses are listed on the X-axis, the frequencies of responses (listed from largest to smallest frequency) are shown on the left side Y-axis, and the cumulative percentages of responses are shown on the right side of Y-axis. This diagram named after the Italian economist Alfredo Pareto. Dr. Joseph Juran recognized this concept as a universal that could be applied to many fields. He coined the phrases Vital Few and Useful Many in quality problems Besterfield [1].

Pareto chart was constructed based upon data collected by check sheet for the main tests performed on steel and shown in the following Table 1 and Figure 2. The figure reveals that the tensile strength is the vital few quality problems and represents around 72% of the total cumulative percentage of non-conformities so that the main reason of most rework is the tensile strength. The rest of tests are considered as Useful Many and represents around 28% of the total cumulative percentage

Table 1: Check Sheet for various steel tests with their respective frequency and percentage

Category	Repetition	Frequency	Cumulative Frequency	Percentage	Cumulative percent
Tensile strength		28	28	72%	72%
Yield Strength		5	33	85%	85%
Elongation Percent		3	36	92%	92%
Effective diameter		2	38	97%	97%
Effective Weight		1	39	100%	100%

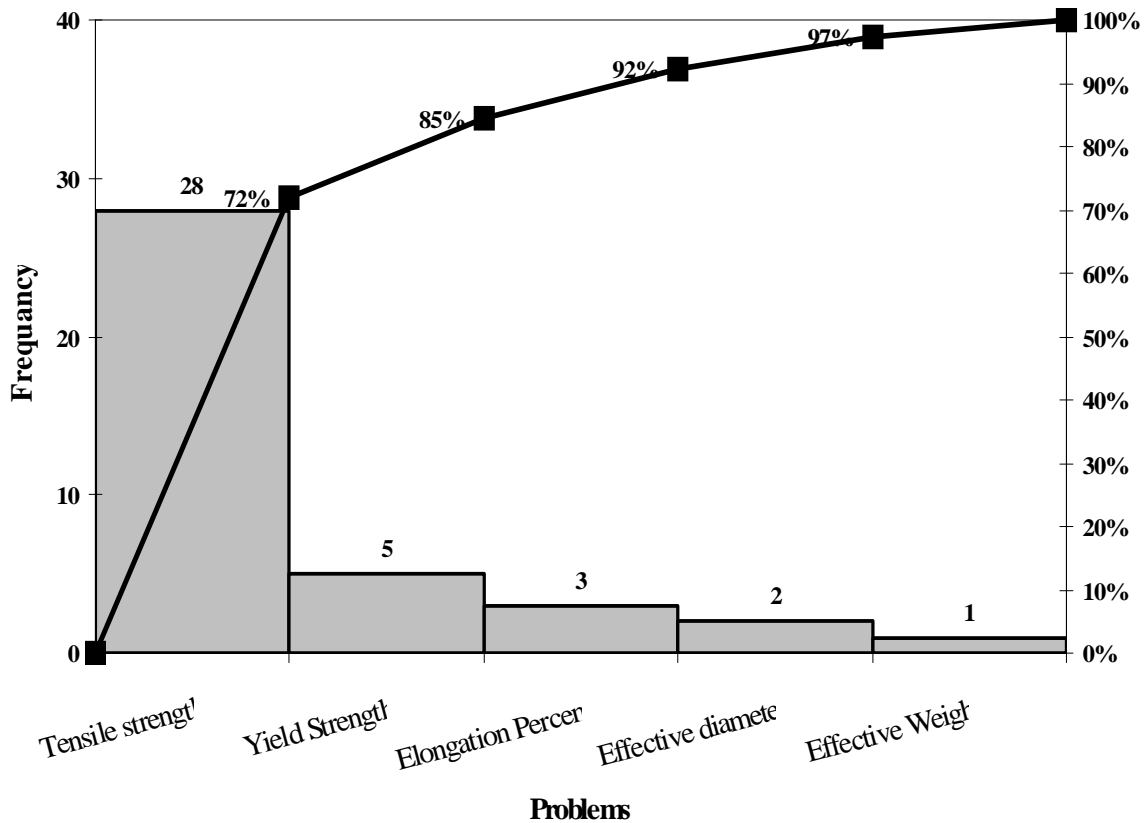


Figure 2: Pareto Chart for tensile strength test

6. Histogram

Histogram is a special bar chart for measurement dat. Histograms is used to chart frequency of occurrences Goetsch [3]. In the histogram, the data is grouped into adjacent numerical categories. Minitab can organize the data into groups, and plot the histogram. The difference

between bar chart and histogram is that the X-axis on a bar chart is a listing of categories; where as the x-axis on a histogram is a measurement scale. In addition, there are no gaps between adjacent bars.

Data concerning the tensile strength test is shown in Table 2 and used to illustrate the histogram in Figure 3.

Table 2: Cell boundaries of tensile strength data

Class	Cell Boundaries		Freq	Class	Cell Boundaries		Freq
1	520.0	538.6	3.0	9	668.8	687.4	14
2	538.6	557.2	3.0	10	687.4	706.0	13
3	557.2	575.8	4.0	11	706.0	724.6	6
4	575.8	594.4	2.0	12	724.6	743.2	11
5	594.4	613.0	10.0	13	743.2	761.8	14
6	613.0	631.6	14.0	14	761.8	780.4	5
7	631.6	650.2	25.0	15	780.4	799.0	6
8	650.2	668.8	10.0				

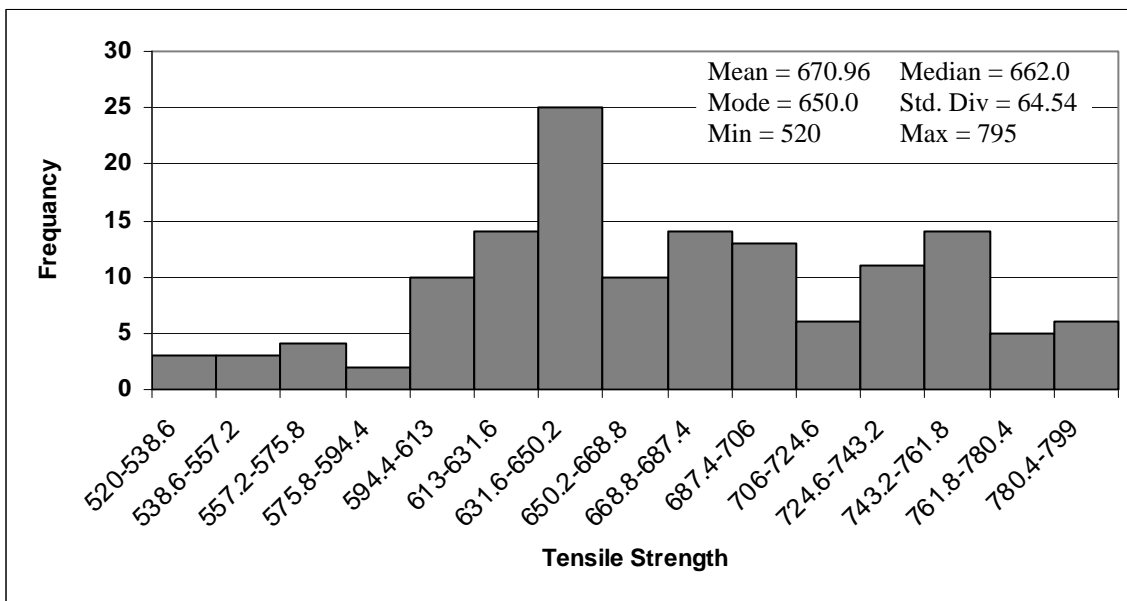


Figure 3: Histogram for tensile strength data.

7. Scatter Diagram

The scatter diagram is the simplest of the seven tools and one of the most useful. The scatter diagram is used to determine the correlation (relationship) between two characteristics (variables) Goetsch [3].

The shape of the scatter diagram often indicates what type of relationship may exist between the two variables. A scatter diagram, shown in **Error! Reference source not found.**, was constructed to find the relationship between water flow used to cool down the steel during various production stages and steel tensile strength using collected data that represent the average for the sample readings per hour for the water flow and tensile strength. The scatter diagrams clarifys that there is no direct relationship exists between tensile strength and water flow.

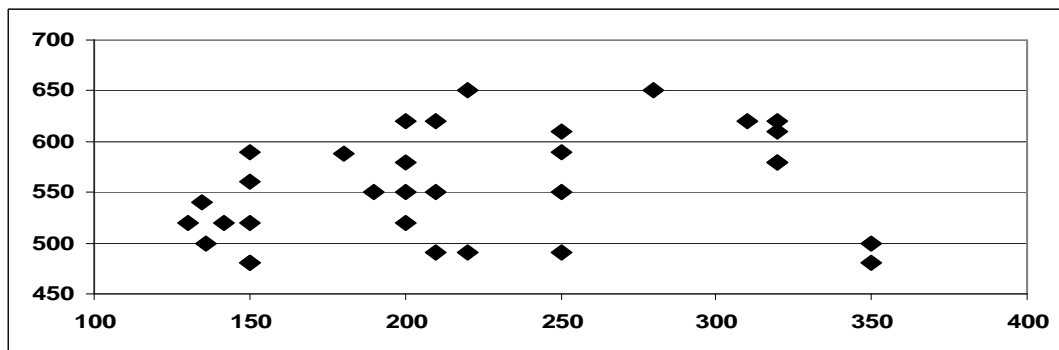


Figure 4: Scatter Diagram between Tensile Strength and Water flow

8. Control Charts

Variable control charts are used to study a process when characteristics is a measurement, for example, cycle time, processing time, waiting time, highest, area, temperature, cost or revenue. Measurement data provides more information than attribute data: consequently, variables charts are more sensitive in detecting special cause variation than are attribute charts. Variable charts are typically used in pairs. One chart studies the variation in a process, and the other studies the process average. The chart that studies variability must be examined before the chart that studies the process average. This is so because the chart that studies the process average assumes that the process variability is stable over time. One of the most commonly employed pair of charts is the Xbar-chart and the R-chart. Through the use of control charts, similar gains can be realized in the manufacturing sector. Users of control charts report savings in scrap, including material

and labor, lower rework costs, reduced inspections, higher product quality, more consistent part characteristics, greater operator confidence, lower trouble shooting, reduced completion time, faster deliveries and others Summers [8].

Figure 5 illustrates the XmR range chart obtained from Minitab for historical data and Figure 5 presenting new real life data.

Comparison between factory historical data and new real life data shows that the historical data is not accurate the reason for that is lack of precision in sampling process, inaccuracy in sampling size and sampling intervals. This contradict with a major objective of SPC is to quickly detect the occurrence of assignable causes of process shifts so that investigations of the process and corrective action may be undertaken before many nonconforming units are manufactured.

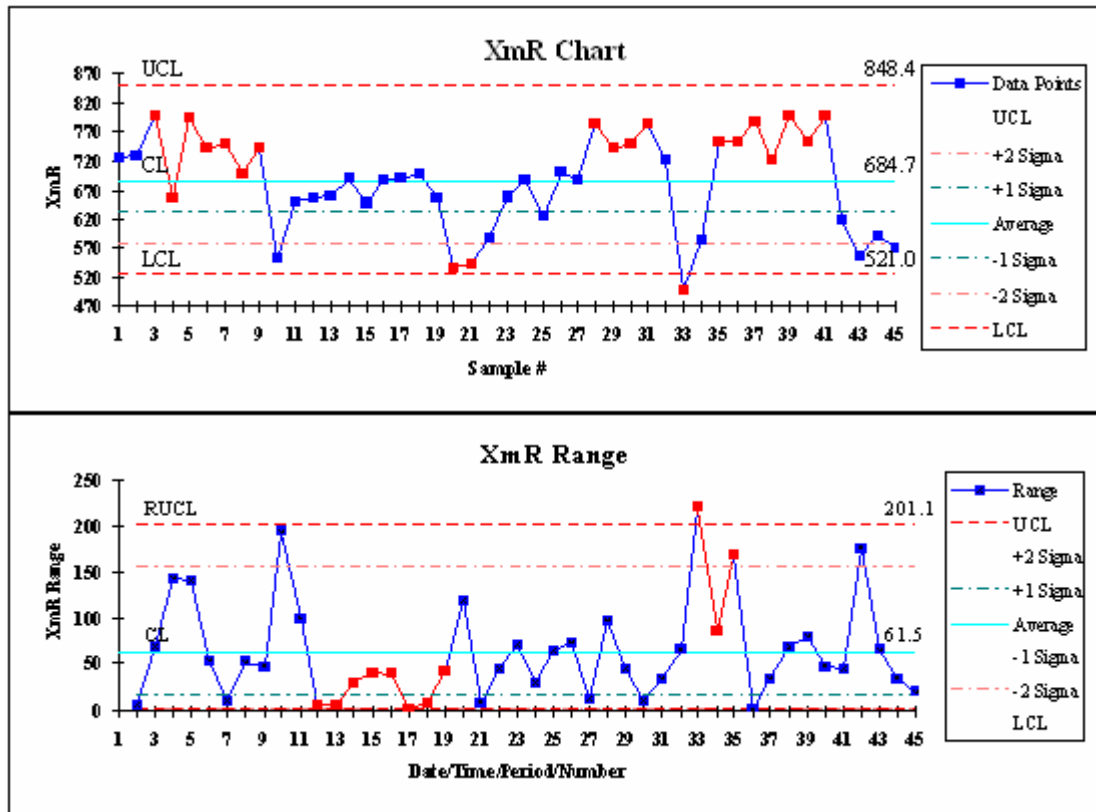


Figure 4: XmR Range and XmR Control Chart for historical data

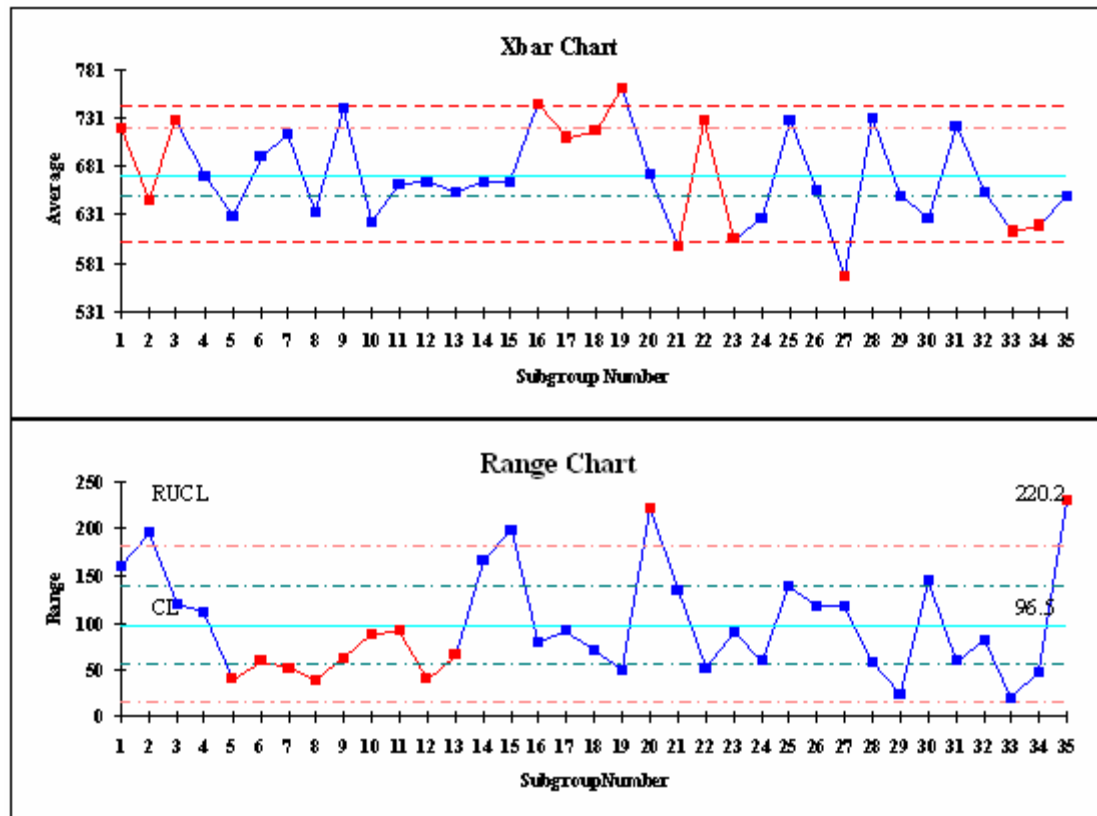


Figure 5: New XmR Range and XmR Control Chart for real life data

9. Brainstorming and Cause and Effect Diagram

Brainstorming is a technique used to elicit a large number of ideas from a team using its collective power. It normally takes place in a structured session involving between 3 to 12 people, with 5 to 6 people being the optimal group size. The team leader keeps the team member focused, prevents distractions, keeps ideas flowing, and records the outputs (or make sure that team members record their own outputs). The brainstorming session should be a closed-door meeting to prevent distractions. Seating should be arranged in a U-shape or circle to promote the flow of ideas among group members Gitlow and Levin [5].

There are specific steps are recommended prior to a brainstorming session as to clarify the subject of brainstorming session. Moreover, many rules should be observed by the participants to ensure that participation is not inhibited. These rules are as follows:

- Do not criticize anyone's ideas, by word or gesture.
- Do not discuss any ideas during the session, except for clarification.
- Do not hesitate to suggest an idea because it sounds "silly". Many times, such as an idea can lead to the problem solution.
- Do not allow any group member to present more than one idea at a time.
- Do not allow any group to be dominated by one or two people.
- Do not let brainstorming because a gripe session.

The above mentioned procedures and rules were taught to the quality team members at JS as to establish the Cause-and-Effect (C&E) diagram.

The Cause-and-Effect (C&E) diagram is a tool used to organize the possible factors that could be negatively impact the stability, centre, spread, and shape of a critical to quality (CTQ) characteristics measure.

A team typically used a Cause-and-Effect (C&E) diagrams to identify and isolate causes of a problem. The late Dr. Kauro Ishikawa, a noted Japanese quality expert, developed the technique, so some times the diagram is called an *Ishikawa diagram*. It is also called a *Fishbone Diagram* because that is what it looks like Goetsch [6]. If it is the Pareto diagram that helps us to prioritize our efforts and focus attention on the most pressing problem or symptom, it is the Cause-and-Effect (C&E) diagram that helps to lead us to the root cause of the problem Devor [4]. The data analyzed by The Cause-and-Effect (C&E) diagram usually comes from a brainstorming session.

The C&E diagrams shown in Figure 6 and Figure 7 were constructed by quality improvement team and through brainstorming sessions involving all employees taking part in the related production and test activities.

10. Conclusions

- Pareto diagram identifies that the tensile strength is the vital view steel characteristic that need attention.
- Scatter diagram proves that there is no direct relationship between tensile strength and flow of water used to cool down steel during different production stages.

- The interpretation of control charts indicates sources of assignable causes were sampling process and specifying the correct sample size and sampling intervals. Sources of chance causes were defined as mistakes such as errors in calculations, poor maintenance plans, having different workers taking samples and using the same chart and poor storage conditions.
- There is a necessity in Jordan Steel to introduce ongoing education and training programs of management and line staff on interrelation between SPC tools and its implementation steps.
- Jordan Steel lacks the ability to properly forming quality teams and hold brainstorming sessions according to standard rules and precedures.

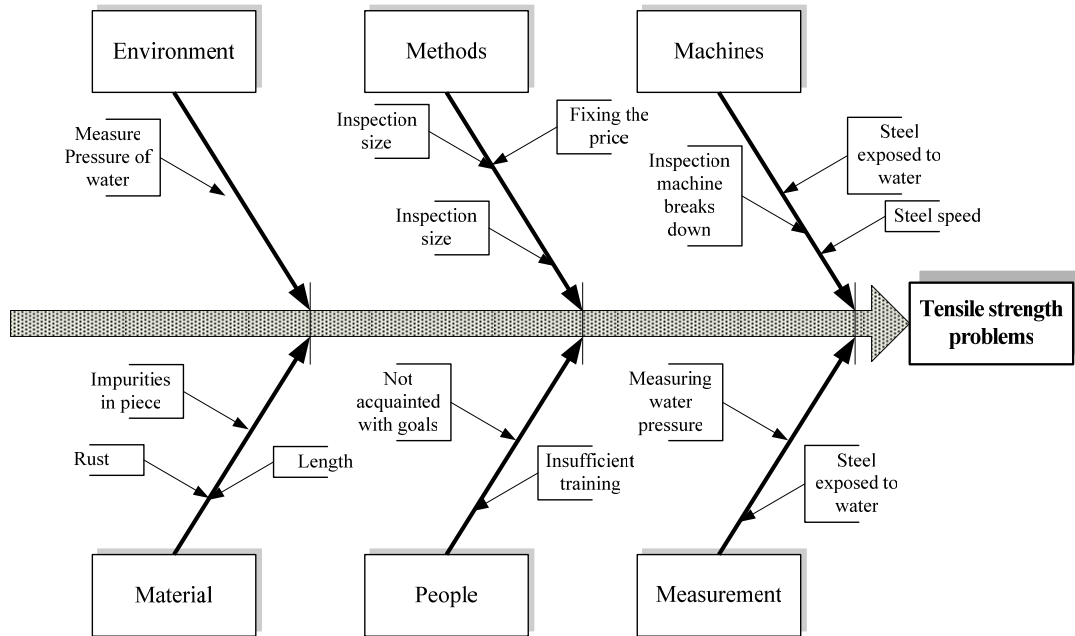


Figure 6: Cause &Effect Diagram for Tensile strength Problems

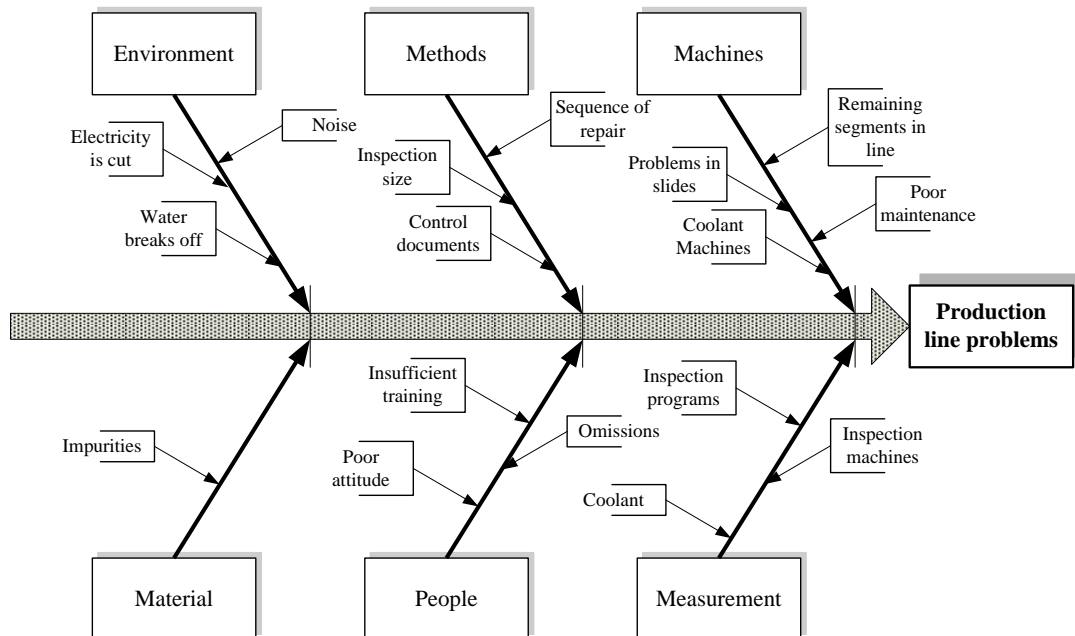


Figure 7: Cause &Effect Diagram for Production Line Problems

References

[1] Deming, W. Edwards, *Some Theory of Sampling*”, 3rd Edition, New York: John Wiley, 1950.
 [2] Besterfield, D. H., *Quality Control*, 8th Edition, Pearson-Prentice Hall, (2009)

[3] Besterfield, D. H., Michna, C. B., Besterfield, G. H., and Sarce, B. M., *Total Quality Management*, 3rd Edition, Prentice Hall, 2003.
 [4] Devor, R. E, Chang, T. and Sutherland, J. W. *Statistical Quality Design and Control: Contemporary Concepts and Methods*, Pearson Prentice Hall, 2nd Edition, 2007.

[5] Gitlow, H. S. and Levine, D. M., "Six Sigma for Green Belts and Champions", FT Press, 7th Edition, 2009.

[6] Goetsch, D. L. and Davis S. B., "Quality Management: Introduction to Total Quality Management for Production, Processes, and Services", Pearson Education, 5th Edition, 2006.

[7] Montgomery, D., Introduction to Statistical Quality Control, 5th Edition, John Wiley, 2005.

[8] Summers, D. C. S., Quality, Pearson Prentice Hall, 4th Edition, 2006.

Damage Identification of Welded Structures Using Time Series Models and Exponentially Weighted Moving Average Control Charts

P.Srinivasa Rao^{a,*}, Ch.Ratnam^a

^a Department of Mechanical Engineering, Andhra University, Visakhapatnam, Andhra Pradesh, India-530003.

Abstract

The main aim of this paper is to demonstrate a new approach for the health monitoring of structures to identify the damage at earliest possible stage using the acceleration-time data obtained from the piezoelectric accelerometers. This paper presents a unique combination of time series models to extract the damage sensitive features and exponentially weighted moving average (EWMA) control charts to monitor the variations of the selected features. First, the damage sensitive features are extracted by fitting a time series prediction model called an auto-regressive (AR) model to the acceleration-time data obtained from the undamaged structure. Then the residual errors are calculated which quantify the difference between the actual acceleration-time data and the prediction from the AR model at each time interval is defined as the damage sensitive feature. The variation of these features is monitored using EWMA control charts. The applicability of the proposed damage identification approach is tested with the welded structure like cantilever plate. The damage is introduced to the test structure by cutting a slot in the weld using electrical discharge machining. Three damage levels are considered and named damage level zero, damage level one and damage level two. As the outliers are statistically significant in number and are increasing as the damage level increases, it is concluded from the EWMA control charts that this approach not only identifies the presence of damage but also sensitive to the severity of the damage.

© 2010 Jordan Journal of Mechanical and Industrial Engineering. All rights reserved

Keywords: Auto regressive model; damage identification; exponentially weighted moving average; acceleration-time data; welded structures.

1. Introduction

Vibration based damage identification is a tool that has received considerable research activity in the field of mechanical, aerospace and civil engineering structures. Most of these structures are welded structures because welding is an economical and efficient method for obtaining a permanent joint. A welded joint offer many advantages like, lighter in weight, less cost, less production time, no stress concentration and provides more strength compared with many other joints [1]. The process of implementing a damage identification strategy for these structures is generally referred to as Structural health monitoring (SHM) [2]. Here damage is defined as changes to the material and/or geometric properties of these systems, including changes to the boundary conditions and system connectivity, which adversely affect the system's performance.

The SHM process involves the observation of a system over time using periodically sampled dynamic response measurements from an array of sensors. Many of these structures continue to be used despite of aging and the associated potential for damage accumulation. Therefore interest in the ability to monitor the structural health and to detect the damage at earliest possible stage is very important for both economical and life safety

point of view. Ideally a robust damage detection method will be able to identify the damage at a very early stage, locate the damage with in sensor resolution being used, and provide some estimate of the severity of the damage. Current damage identification methods are either visual or localized experimental methods such as acoustic or ultrasonic methods, magnetic field methods, radiography, eddy-current methods and thermal field methods [3]. All these experimental techniques require that the vicinity of the damage is known a priori and that the portion of the structure being inspected is readily accessible. Subjected to these limitations the need for the additional global vibration based damage identification methods that can be applied to complex structures has lead to the development of methods that examine changes in vibration characteristics of the structures [4, 5 and 6]. Most of the literature show many different methods for extracting damage sensitive features from vibration response measurements. But few of the cited references take a statistical approach for quantifying the observed changes in those features [2]. The extraction of damage sensitive features from these measurements and the statistical analysis of these features are then used to determine the current state of system health. There are other techniques which use the lamb wave parameters to identify the damage [7].

The basic idea of this global damage identification method is that damage will alter the stiffness, mass or energy dissipation properties of a

system, which in turn alter the measured dynamic response of the system. Therefore all vibration based damage identification methods, namely [8, 9, 10 and 11] depend on experimental data with inherent uncertainties. There are many cases where damage causes a structure to go from a system that can be accurately modeled as a linear system to a system that exhibits a non-linear dynamic response [12]. Common examples of this change in system response are associated with the formation of fatigue cracks that open and close during subsequent dynamic loading and the loss of preload in bolted connections which results in a rattle.

This paper will present the problem of vibration based damage identification method using control chart analysis paradigm, which is one of the most popular method of statistical process control [13, 14]. The applicability of the proposed damage identification approach is tested with the welded structure and the acceleration-time data is collected for the both undamaged and damaged cases. Control charts approach is very efficient and suitable for on line continuous monitoring of the systems [14]. Full automation of the damage identification procedure is necessary for remote i.e., web based monitoring applications.

2. Mathematical Formulation

An AR model is first fitted to the measured acceleration-time histories obtained from the undamaged structure. Residual errors, which quantify the difference between the actual measured time history and the prediction from the AR model at each time interval, are used as the damage-sensitive features. Exponentially weighted moving average (EWMA) control charts are employed to monitor the variation of the selected features. Control limits for the control charts are constructed based on the features obtained from the initial intact structure. The residual errors computed from the new data and the prediction from the AR model are then monitored against the control limits. A statistically significant number of residual errors outside the control limits indicate a system anomaly.

2.1 AR Model

The basic assumption in the use of control charts is the independence of the extracted features. Conventional control charts give false alarms too frequently if the selected features exhibit a high level of correlation over time [15]. Hence it is necessary to remove the correlation in the raw time history before the application of the control charts. As a feature extraction process, an AR model is fitted to the undamaged acceleration time history in order to remove the auto-correlation.

An AR model is essentially an infinite impulse response filter with some additional interpretation placed on it. The notation AR(p) refers to the autoregressive model of order p. The AR(p) model given in [15] is

$$\hat{X}_t = \sum_{i=1}^p a_i (X_{t-i}) + \varepsilon_t \quad (1)$$

where \hat{X}_t is the estimate of the t^{th} time series value, a_1, a_2, \dots, a_p are the parameters or the co-

efficients of the AR model, p is the order of the AR model, X_{t-i} previous measured time series values. ε_t is assumed to be an unobservable random error with zero mean and constant variance (white noise). Here white noise is generated using the Mat lab version 7.0 and is presented in later sections.

If \hat{X}_t represents the estimated acceleration-time measurements from the fitted AR model and X_t represents the measured acceleration-time data from the experiment, then the residuals at time 't' is given by

$$e_t = X_t - \hat{X}_t \quad (2)$$

If the fitted AR model accurately represents the measured signal, the residual should be nearly uncorrelated.

2.1.1 Selection of AR model order 'p'

There are many techniques available for selecting the model order 'p', such as final prediction error (FPE), Akaike's information criteria (AIC) and Bayesian information criteria (BIC). For feature estimation it is not good to select model order p arbitrarily large. Selecting very high order model will result in small estimated white noise variance.

In 1969 Akaike[16] developed FPE criterion to choose the appropriate AR model order to fit to a time series data. By applying FPE criterion select the value of p which will minimize the FPE. In 1973 Akaike[17] developed a more general applicable criterion for selecting the model order is the information criterion of Akaike known as AIC. But in 1989 Hurvich and Tsai[18] suggested a bias-corrected version of the AIC known as AICC. From AIC/BIC criteria the order of the AR model is obtained as 4. Therefore AR(4) model is developed from the acceleration-time data of the undamaged structure.

2.1.2. Calculation of AR parameters

The AR parameters are generally calculated by considering the Yule-walker equations[19]. The AR(p) model given in the equation (1) is based on parameters a_i where $i = 1, \dots, p$. There is a direct correspondence between these parameters and the covariance function of the process, and this correspondence can be inverted to determine the parameters from the autocorrelation function. This is done by using the following Yule-Walker equations,

$$T_p a = \gamma_p \quad (3)$$

$$\sigma^2 = \gamma(0) - a' \gamma_p \quad (4)$$

where T_p is the covariance matrix $[\gamma(i-j)]_{i,j=1}^p$ and $\gamma_p = (\gamma(1), \dots, \gamma(p))'$

The above equations (the Yule-Walker equations) provide one route to estimate the parameters of an AR(p) model, by replacing the theoretical covariances with estimated values. One way of specifying the estimated covariances is equivalent to calculation using least squares regression of values X_i on the 'p' previous values of the same series.

Once the AR model is fitted to the acceleration-time history obtained from the undamaged structure, \hat{x}_t is the predicted time history from the AR model at time 't'. Then the residual errors (e_t) are calculated using equation(2) and is defined as the damage sensitive features used in this work. The control charts provide statistical frame work to detect the changes in the selected damage sensitive features.

2.2 Statistical Process Control

Control charts may be used in variety of ways, but in many applications it is used for on-line process monitoring. General theory of control charts was first proposed by Dr Walter S. Shewhart[15], and control charts developed according to his principles are often called "Shewhart control charts". Basically control chart is a graphical display with limit lines, called control lines.

The purpose of drawing a control chart is to detect any changes in the process that would be evident by any abnormal points listed on the graph from the data collected. If these points are plotted in "real time", the operator will immediately see that the point is exceeding one of the control limits, and can make an immediate action.

When the structure is in good condition, the damage sensitive features derived from the acceleration-time measurements will have some distribution. These features may change if the structure is damaged. Therefore statistical process control provides a framework for monitoring the features and for identifying new data that are inconsistent with past data. EWMA control charts hitherto not used for the present purpose are proposed to monitor the damage sensitive features derived from the acceleration-time measurements. These control charts are very effective against small process shifts.

2.2.1 EWMA control charts

EWMA control charts are generally considered somewhat more advanced techniques than the Shewhart control charts. EWMA quality control chart offers considerable performance improvement relative to Shewhart quality control charts when the magnitude of the shift in process mean is small. The EWMA control chart was introduced by Robert in 1959[20]. For individual observations ($n=1$) the EWMA chart is defined as

$$z_i = \lambda x_i + (1 - \lambda) z_{i-1} \quad (5)$$

Where λ is a constant lies between 0 and 1 and the starting value $z_0 = CL$ is the target mean. Recursively

substituting $\lambda x_{i-j} + (1 - \lambda) z_{i-j-1}$ for z_{i-j} , $j=1,2,\dots,i-1$ in equation (5), it can be shown that z_i is a weighted average of all past and current observations. Then

$$z_i = \lambda \sum_{j=0}^{i-1} (1 - \lambda)^j x_{i-j} + (1 - \lambda)^i z_0 \quad (6)$$

If the observations x_i are independent random variables with variance σ^2 , the variance of z_i is given by the equation,

$$\sigma_{z_i}^2 = \sigma^2 \left(\frac{\lambda}{2 - \lambda} \right) [1 - (1 - \lambda)^{2i}] \quad (7)$$

Therefore, the EWMA control chart would be constructed by plotting z_i versus the sample number i (or time). The upper control limit (UCL), center line (CL) and lower control limit (LCL) for the EWMA control chart is defined as follows

$$\begin{aligned} UCL &= \bar{x} + L\sigma \sqrt{\frac{\lambda}{(2 - \lambda)} [1 - (1 - \lambda)^{2i}]} \\ CL &= \bar{x} \\ LCL &= \bar{x} - L\sigma \sqrt{\frac{\lambda}{(2 - \lambda)} [1 - (1 - \lambda)^{2i}]} \end{aligned} \quad (8)$$

Where, L and λ are the design parameters of EWMA control chart. Since the EWMA control chart can be viewed as a weighted average of all the past and present observations, the distribution of z_i can be reasonably approximated by a normal distribution as a result of the central limit theorem. Therefore, the EWMA chart is insensitive to the normality assumption of individual observations x_i .

3. Experimental setup

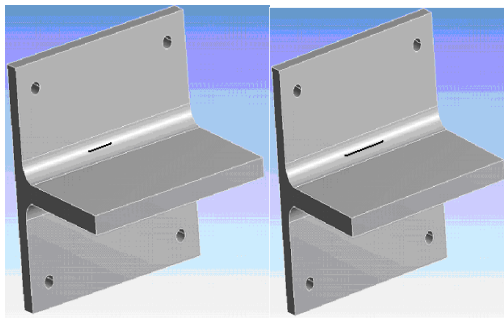
The applicability of the proposed damage identification approach is tested with the test structure (Figure 1) by fixing it to the multi axes electro dynamic vibration shaker. Test structure is made of carbon-steel and the two plates are welded to form a cantilever.



Figure 1. Test structure

The dimensions of the plate which is drilled with four 8 mm through holes at each corner are 150 mm x 150 mm. The centre of the drilled holes is at 18 mm from each corner side of the plate. The dimensions of the other plate which is welded to the above plate, so as to form a cantilever plate is 150 mm x 100 mm. The elastic constants of the material considered are Young's modulus (E), $200 \times 10^9 \text{ N/m}^2$ (200 Gpa), Poisson's ratio (ν), 0.3 and the mass density (ρ), 7850 kg/m^3 .

Damage is introduced into the structure by cutting a slot in the weld. This is done by electrical discharge machining (EDM). Two damage levels are investigated by introducing two such slots in different test structures in which 10 mm slot length is considered as damage level one, whereas 20 mm slot length is considered as damage level two (Diagrammatically represented in Figure 2). However damage level zero refers to the undamaged condition of the structure. The thickness of the slot is 0.6 mm for all the cases.



a) Damage level one b) Damage level two

Figure 2. Diagrammatic representation of damaged structure

The test structure is fitted to the multi axes electro dynamic vibration shaker with the help of four bolts and nuts as shown in Figure 3. Electro-dynamic vibration shaker used for experimentation consists of drive coil connected rigidly to the moving platform and positioned in the magnetic field when an alternate current flow in this drive coil gives rise to a force by converting an electric current into mechanical force which moves the platform. The vibrator can operate from either sine or random input wave form in the required frequency range.



Figure 3. Experimental setup

Table 1. Specifications of multi axes electro dynamic vibration shaker

Peak sine force	$\pm 400 \text{ Kg force}$
Max. displacement	25 mm(pk-pk)
Max. Velocity	1.2meter/second(nominal)
Frequency range	1 Hz to 3000 Hz
Size of moving top platform	160 mm diameter
Max. acceleration on vibrator platform	80 g (at no load)
Max. payload capacity	70 Kg's
Moving armature suspension	Rolling strut type
Moving mass of armature	5 kg
Drive power power amplifier	Through a solid state
Cooling method	Air extraction
Test direction	All three mutually perpendicular directions

Table 1 shows the specifications of the multi axes electro dynamic vibration shaker. Vibration characteristics of a structure can be examined in either actively or passively. In this work active investigation is selected for monitoring the vibration characteristics of a structure. The test structure is instrumented with three piezoelectric single axis accelerometers. Out of three accelerometers one is used for actuator (input) and the other two is for response. The response data from the two accelerometers are recorded and was sampled at 150 Hz. Piezoelectric sensors are electromechanical systems that react on compression the sensing elements show almost zero deflection. Due to this reason the piezoelectric sensors are robust, have an extremely high natural frequency and an excellent linearity over a wide amplitude range. Vibration response data from the structure is recorded using data recorder shown in Figure 4.



Figure 4. Response data recorder

Four channel data acquisition system shown in Figure 5 is used to convert the analog data into digital form. Total of 1024 acceleration-time measurements are acquired for damage level zero, damage level one and damage level two and are stored in MS-excel file. The plots of this data for different damage levels are shown in Figure 6. Figure 7 shows the white noise generated using Mat Lab 7.0 version.



Figure 5 Four channel data-acquisition system

In general selection of the model either physics-based or data based will depend upon the amount of relevant data available and the level of confidence. When nothing is known a priori, about the structure then approach becomes entirely data based [21]. The data based models [22, 23, and 24] are relatively simple to fit to the measured response data and the application of one such model is considered in this work for extracting the damage sensitive features. An AR (4) model is fitted to the acceleration-time history obtained from the undamaged structure. Then the residual errors are calculated, which is the difference between the actual subsequent data and the prediction from the AR (4) model. To compare the residual errors obtained from data measured on the undamaged structure with similar quantities obtained from the damaged structure, EWMA control chart is developed using the acceleration-time data obtained from undamaged structure.

The control limits for EWMA control charts are calculated from the residual errors (features) obtained from the undamaged structure. Then the new data (damaged) are monitored against the control limits. A statistically significant number of residual error terms outside the control limit indicating the structure transit from undamaged to damaged state.

4. Results and discussions

In this study the proposed damage identification approach based on time series models and EWMA control charts were tested on a cantilever plate like welded structure. As explained earlier two damage levels are investigated in this work i.e., damage level one and damage level two. Damage level zero configuration was considered "undamaged" and the structure was assumed to be well described by a linear model when subjected to input excitation.

The original data is checked for autocorrelation and shown in Figure 8. It can be noted from the Figure 8, that the acceleration-time data obtained from the experiment are auto-correlated. Therefore it is necessary to remove the auto-correlation before the application of control charts. To remove the auto-correlation, a linear time prediction model called an AR model is developed from the acceleration-time data obtained from the damage level zero structure. The order of the AR model is calculated as four from the AICBIC criterion for this work. After obtaining the order of AR model, AR parameters are calculated using Yule-walker equations (equations 3 and 4) and the values are tabulated in table 2.

Table 2. AR Parameters

AR parameter	Calculated value from Yule-walker equations
a_1	-1.3644
a_2	0.6061
a_3	-0.6456
a_4	0.4241

Figure 9 presents the acceleration-time data prediction from the AR (4) model for the different damage levels. Then the residual errors are calculated, which is the difference between actual subsequent acceleration-time data and the prediction from AR (4) model. Since it is not possible to estimate the residual error values less than the model order, a total of 1020 residual errors are calculated from 5 to 1024 in each case of damage level and it is presented in Figure 10. Then EWMA quality control charts are plotted using residual errors as data. EWMA control charts are plotted for individual observation ($n=1$) using 1020 residual errors (features) as data. The design parameters of the EWMA control chart L and λ are selected as 2.7 and 0.2 respectively for present case as per [15].

Figure 11 shows the EWMA control charts for damage level zero, damage level one and damage level two. This shows that there are statistically significant number of data points are outside the control limits for the two damage levels considered. This is a clear indication of presence of damage in the structure. However it is seen that the number of outliers are more for damage level two than that of the damage level one, which is clear indication that this approach is sensitive to the severity of damage. It has been observed from Figure 11 (b) for damage level one 66 residual error points are falling outside the control limits, and for damage level two from Figure 11(c), 105 residual error points are falling outside the control limits. Therefore this damage identification approach not only identifies the damage but also sensitive to the severity of the damage.

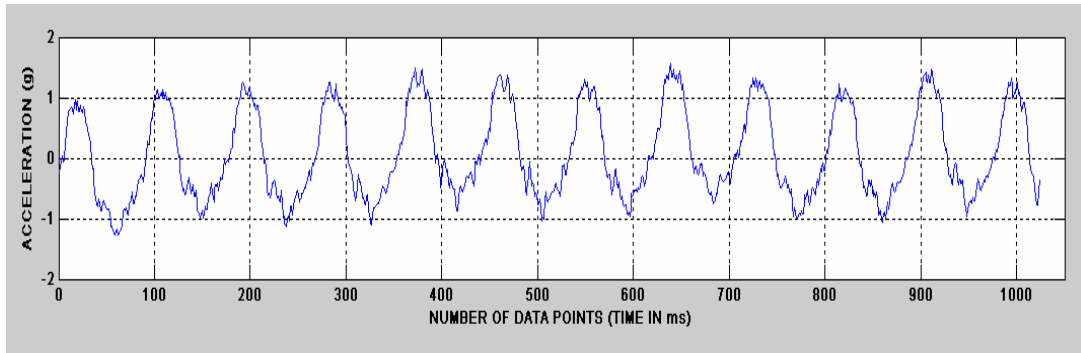
5. Conclusions

In this paper a statistical damage classification technique for vibration based damage identification problem in an unsupervised learning mode is studied. A unique combination of linear prediction model called an AR model to extract the damage sensitive features and EWMA control charts to monitor the variation of the selected features is presented. An experiment on welded structure was conducted using multi axes electro dynamic vibration shaker to study the applicability of statistical damage classification technique.

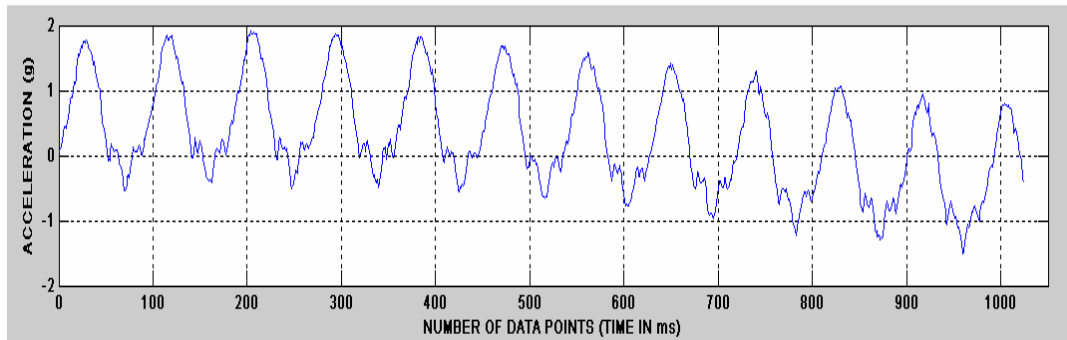
The experimental data obtained from the piezoelectric sensors are auto correlated. To remove the auto correlation an AR (4) model is developed from the acceleration-time data obtained from the damage level zero. Then the residual errors are calculated which quantify the difference between the actual measured time history and the prediction from the AR (4) model at each time interval, are used as the damage-sensitive features. Here two damage levels are considered i.e., damage level one and damage level two. The residual errors are nearly uncorrelated therefore the residual errors are taken as data for plotting the EWMA control charts. It is observed from the EWMA control charts that there are statistically significant number outliers. This suggests the presence of damage in the structure. These outliers are increasing as the damage level increases. This shows that this approach is sensitive to the severity of the damage. Therefore the approach presented in this paper is effective in identifying damage and also identifying its severity in the considered welded structure. Once the presence of damage is conformed in any machine structure it can be inspected thoroughly and can be put back into further service.

References

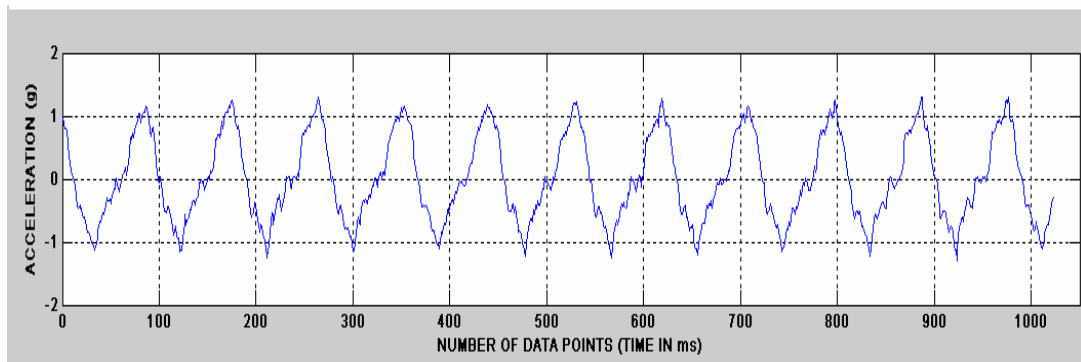
- [1] V B Bhandari. Design of machine elements. New Delhi, India: Tata McGraw-Hill Publishing Company Limited; 2007.
- [2] Hoon Sohn, Charles R. Farrar, Francois M. Hemez, Devin D. Shunk, Daniel W. Stinemates, Brett R. Nadler, Jerry J. Czarnecki "A Review of Structural Health Monitoring Literature: 1996–2001". Los Alamos National Laboratory, USA, February 2004
- [3] Doherty, J. E., "Nondestructive Evaluation," Chapter 12 in Handbook on Experimental Mechanics, A. S. Kobayashi Ed., Society for Experimental Mechanics, Inc.; 1987.
- [4] O.Salawu, "Detection of structural damage through changes in frequency: a review". Engineering structures, Vol.19, No.9, 1997, 718-723.
- [5] Doebling S. W., C. R. Farrar, M. B. Prime, D. W. Shevitz, "A Review of Damage Identification Methods that Examine Changes in Dynamic Properties," Shock and Vibration Digest, Vol.30, No.2, 1998.
- [6] Housner, G.W., et al, "structural control: past, present and future". Journal of Engineering mechanics, ASCE Vol.123, No.9, 1997, 897-971.
- [7] Ch Ratnam, BS Ben, BA Ben "structural damage detection using combined finite-element and model lamb wave propagation parameters". Proceedings of the Institute of Mechanical Engineering Part C -Journal of Mechanical engineering science , Vol. 223, 2009, 769-777.
- [8] Wowk, V. Machinery Vibration Measurement and Analysis. New York: McGraw-Hill Inc.; 1991.
- [9] I. Trendafilova, "Vibration-based damage detection in structures using time series analysis". Proceedings of the Institute of Mechanical Engineering Part C- Journal of mechanical engineering science, Vol. 220, No.3, 2006, 261-272.
- [10] Ch.Ratnam, J.Srinivas, B.S.N Murthy, "Damage detection in mechanical system using Fourier co-efficients". Journal of sound and vibration, Vol. 303, 2007, 909-917.
- [11] A. Deraemaeker, E. Reynders, G. De Roeck, J. Kullaa "Vibration-based structural monitoring using output-only measurements under changing environment". Mechanical systems and signal processing, Vol. 22, 2008, 34-56.
- [12] John F. Schultze, Francois M. Hemez " Statistical based Non-linear model updating using feture extration". Proceeding of IMAC- XIX , the 19th IMAC, 2001.
- [13] E. L. Grant. Statistical quality control. 3rd ed. New York: McGraw-Hill Inc.; 1952.
- [14] M. Basseville, L Mevel, M.Goursat "statistical model based damage detection and localization: subspace-based residuals and damage-to-noise sensitivity ratios". Journal of sound and vibration, Vol. 275, 2004, 769-794.
- [15] Douglas C. Montgomery. Introduction to Statistical Quality Control. 4th ed. Singapore: John Wiley and Sons (ASIA) Pte Ltd; 2004.
- [16] Akaike,H "Fitting autoregressive models for prediction". Annals of the Institute of statistical mathematics, Vol. 21, 1969, 243-247.
- [17] Akaike,H "Information theory and an extension of the maximum likelihood principle". 2nd International symposium on information theory, Akademiai kiado, Budapest , 1973, 267-281.
- [18] Hurvich, C.M, Tasi, C L "Regression and time series model selection in small samples". Biometrika Vol. 76, 1989, 297-307.
- [19] Monson H. Hayes. Statistical digital signal processing and modeling. U.K: John Wiley & sons Inc.; 2008.
- [20] Robert, S. W. "control chart tests based on Geometric moving average". Techno metrics, Vol. 1, 1959.
- [21] J.M.Nichols, S.T.Trickey, M.Seaver, S.R.Motley and E.D.Eisner "using ambient vibrations to detect loosening of a composite-to-metal bolted joint in the presence of strong temperature fluctuations". ASME journal of vibration and acoustics, Vol. 129, pp 710-717,2007
- [22] Box G. E, Jenkins G. M, Reinsel G. C. Time Series Analysis: Forecasting and Control. Prentice-Hall Inc.; 1994.
- [23] Peter J. Brockwell, Richard A .Davis. Introduction to time series and forecasting. New York: Spinger -Verlag Inc.; 2002.
- [24] Diego J. Pedregal, M.Carmen Carnero "Vibration analysis diagnostics by continuous-time models: A case study". Reliability engineering & system safety, Vol. 94, No.2, 2009, 244-253.



6(a) Damage level zero



6(b) Damage level one



6(c) Damage level two

Figure 6. Acceleration-time data from the experiment for different damage levels

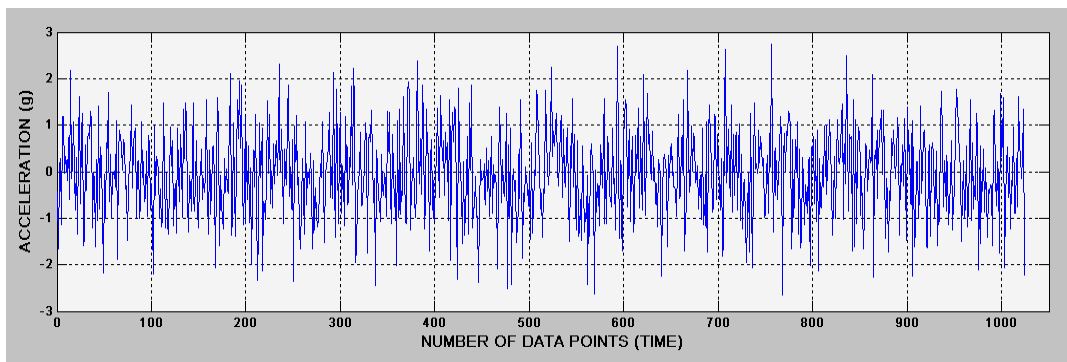
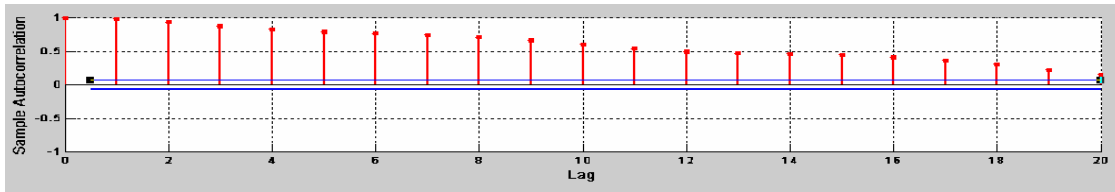
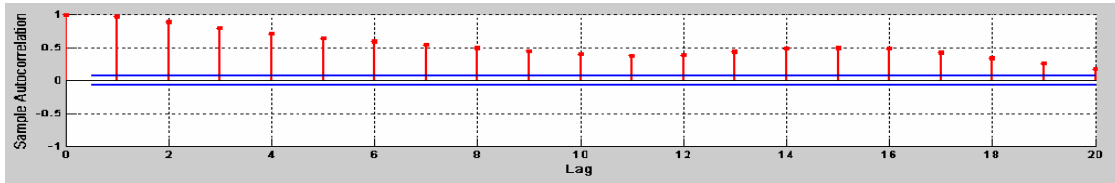


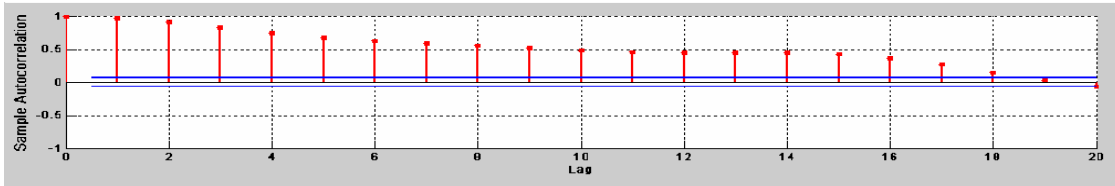
Figure 7. White noise generation with zero mean and constant variance



8(a) Damage level zero

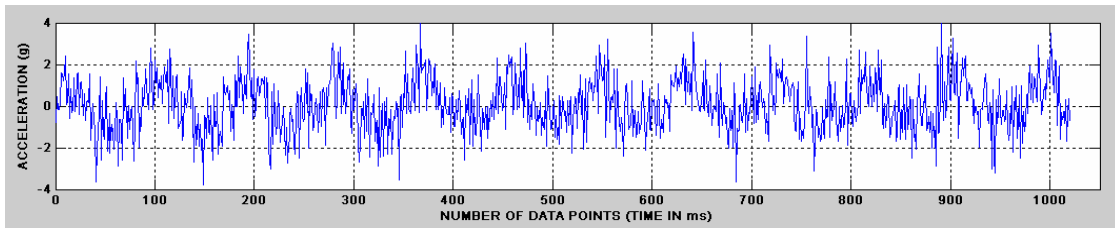


8(b) Damage level one

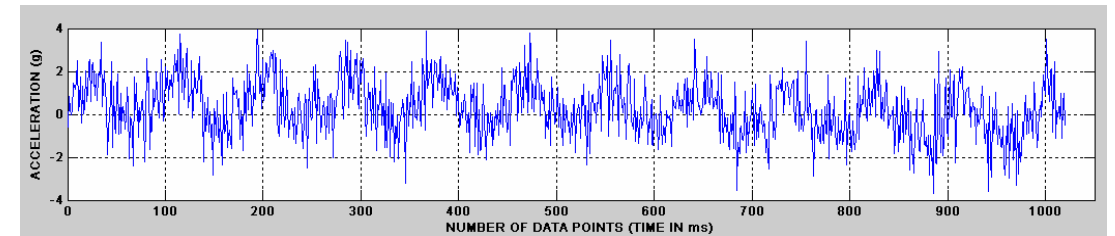


8(c) Damage level two

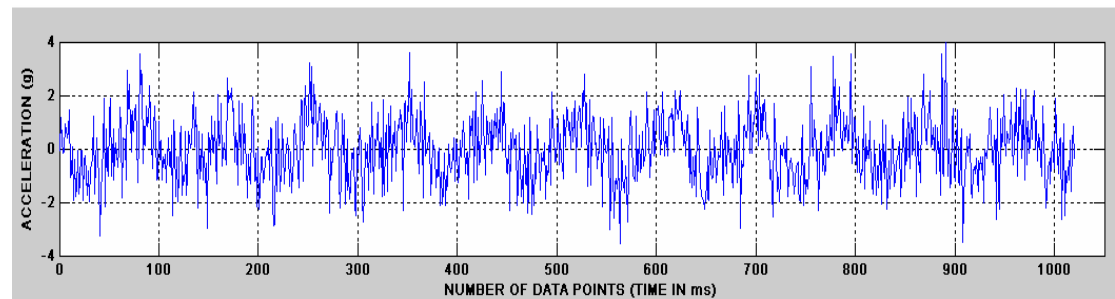
Figure 8. Auto-correlation for the experimental data obtained from different damage levels.



9(a) Damage level zero

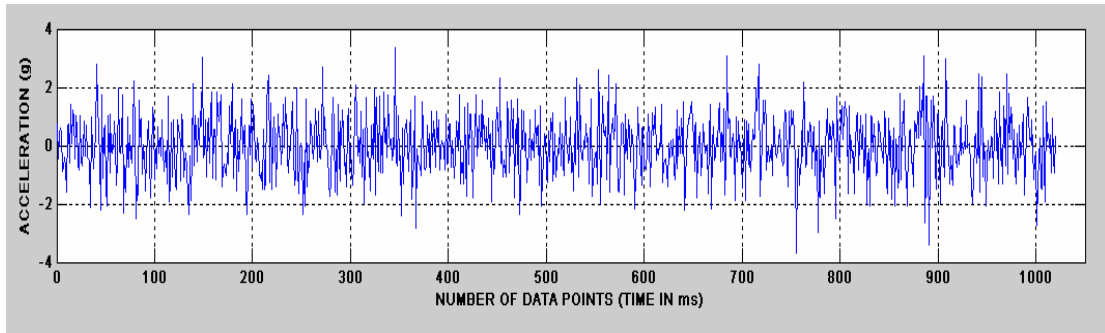


9(b) Damage level one

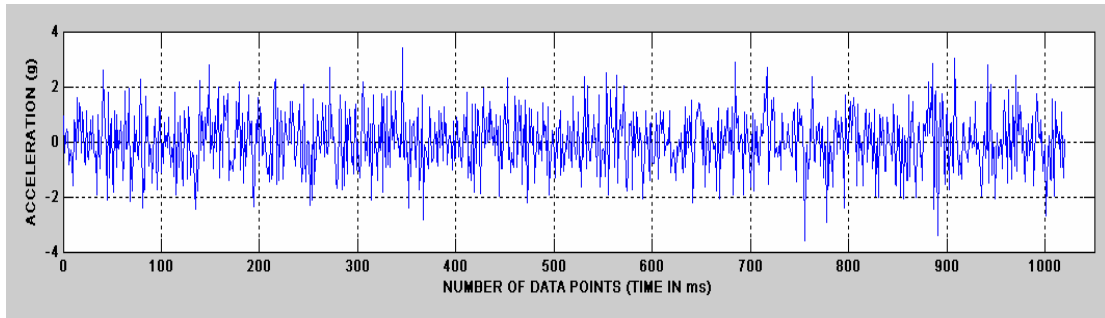


9(c) Damage level two

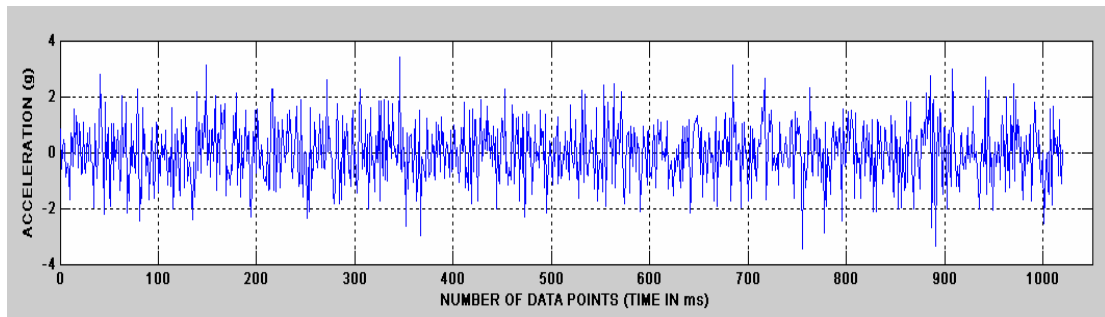
Figure 9. Acceleration-time data prediction from AR (4) model for different damage levels



10(a) Damage level zero

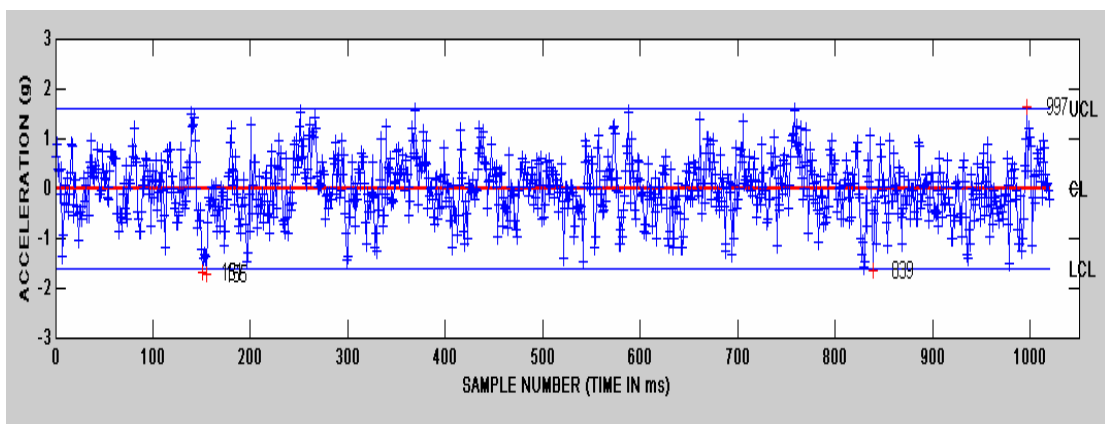


10(b) Damage level one

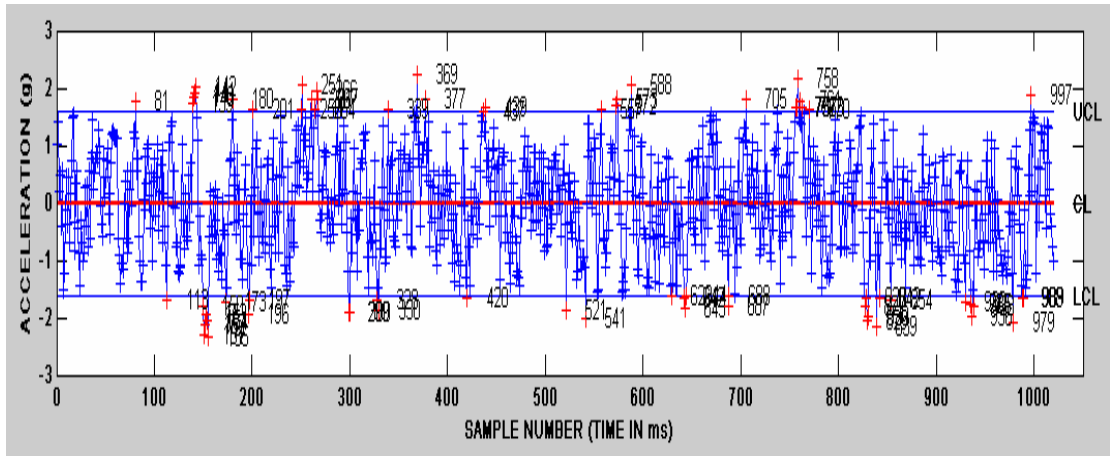


10(c) Damage level two

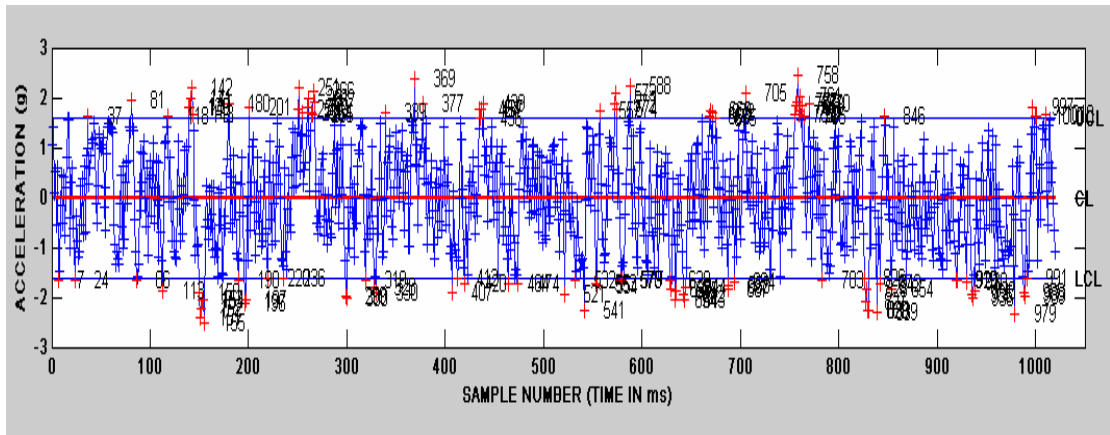
Figure 10. Residual errors (damage sensitive features) for different damage levels



11(a) Damage level zero



11(b) Damage level one



11(c) Damage level two

Figure 11. EWMA control charts (n=1) for residual errors obtained from different damage levels

Efficiency of Free Cooling Technique in Air Refrigeration Systems

A. Al-Salaymeh^{a,*}, M.R. Abdelkader^b

^a Mechanical Engineering Department, Faculty of Engineering and Technology, University of Jordan, Amman 11942, Jordan.

^b Mechanical Engineering Department, Faculty of Engineering and Technology, University of Jordan, Amman 11942, Jordan.

Abstract

Free cooling techniques can be used to substantially reduce energy costs. During cold weather, the outside ambient temperature can help in saving energy in refrigeration systems. The low temperature of the cooling ambient air supply enables free cooling technique to store fresh fruits and vegetables. This energy-efficiency measure can save enough compressor electric power to pay for modulating damper installation costs in approximately one year. Free cooling has a motorized damper that conducts the two flows of internal and external air. When the damper is open it takes the air necessary for cooling directly from the exterior, excluding compressor operation. It starts the evaporator fan that takes external air if $T_{\text{external}} < T_{\text{internal}}$. A case study has been carried out for 17 Ton cooling load in a storage room and the COP can be reached to 24 where the only energy consumption is from the use of evaporative fans.

© 2010 Jordan Journal of Mechanical and Industrial Engineering. All rights reserved

Keywords: Refrigeration, Cooling, Efficiency, Energy Saving.

1. Introduction

Free cooling techniques are used to substantially reduce energy costs. This system effectively provides nearly free cooling using the cooling air during cold weather without the requirement to run a compressor. The compressor is essentially shut off during this period, there by saving energy and also allowing scheduled preventative maintenance to take place. The low temperature of the cooling ambient air supply enables free cooling of cold stores for fruits and vegetables, e.g. Al-Salaymeh et al. [1]. The cooling and air refrigeration systems are designed to cool cold stores to keep the fruits and vegetables for long time without damage. They are designed for internal or external installation. Their use allows eliminating problems caused by high temperatures, dirt and humidity which are present in the environment. The unit, which is basically made up of a sealed cooling circuit where the coolant circulates, is divided into two suctions, hermetically separated from each other, where the air in the environment and the air in the cabinet are treated without coming into the contact with each other. The air refrigeration system that uses free cooling techniques has a motorized damper that conducts the two flows of internal and external air. When the damper is open it takes the air necessary for cooling directly from the exterior, excluding compressor operation, e.g. Al-Salaymeh et al. [1]. If the external temperature is less than the internal temperature,

the damper will be opened and the evaporator fan will start to take external air. If the external temperature is higher than the internal temperature, the damper remains closed and air is recycled.

Refrigeration in the simplest terms is cooling by removing heat. It could also be said that refrigeration is the transfer of heat from one place where it is not wanted to another less objectionable place. The normal strategy in mechanical refrigeration is to get the heat to the refrigerant. Then transfer the refrigerant to a place where the heat can be removed from it. The refrigerant makes the heat transfer possible. Most of the heat transfer occurs because the refrigerant changes state. The liquid refrigerant in the evaporator absorbs its latent heat of vaporization, and in the process changes from a liquid to a vapor. The gas refrigerant within the condenser rejects its latent heat of vaporization, thus changing from a gas to a liquid. It is this cycle change that moves the removed heat from one place to another.

Al-Salaymeh et al. [1] mentioned that free cooling takes place when the external ambient air enthalpy is less than the indoor air enthalpy. They showed that free cooling may be used with mixed outside air and recirculation systems by the use of modulating dampers. Dampers are provided on the outside air intake ductwork, exhaust air ductwork and the recirculation ductwork. In the event of cool outside air the quantity of outside air is increased and the quantity of recalculated air is reduced to provide the required supply air temperature. In this way cooling by means of refrigeration equipment is avoided altogether at certain times of year and often at night times. This system of free cooling uses thermostats to determine when the

* Corresponding author. salaymeh@ju.edu.jo.

outside temperature is lower than the room temperature and the proportion of opening the outside air damper. More accurately the proportion of outside air should be increased when the outside air temperature is lower than the room temperature. When the outside air temperature is higher than the cold store temperature, the dampers will modulate to the minimum outside air position to keep the load on the refrigeration equipment to a minimum.

The coefficient of performance, COP, is simply a ratio of the effect we want (a heat transfer) to the quantity that we must buy (work) in order to cause the desired effect. In the refrigeration system, the COP is the ratio between the heat removed from the low-temperature reservoir in the case of refrigeration to the compressor and fan work. However, if the free cooling is used, the compressor is switched off and the input work is equal to the fan work. Song et al. [2] studied the energy performance of a cooling plant system using the inverter chiller for industrial building. They clarified the energy performance of the cooling plant system in the industrial building using actual measured operating data and numerical simulation analysis. One aspect of industrial buildings is that they have large energy consumption for manufacturing and air conditioning compared with office and commercial buildings. The maximum COP of the inverter chiller reaches about 18 under certain conditions and integrated cooling towers make lower temperature cooling water as the whole capacity is large. The actual operating data in their study indicates satisfied values for chiller and system COP during the running period and the simulation results show that the cooling plant system can cut down annual electric power consumption by about 48% compared with conventional cooling system. Mina et al. [3] investigated a generalized coefficient of performance for conditioning moist air. In air-conditioning systems, the general goal is to effect a change of state of air from one condition to another one that is more desirable. They examined expressions for determining the limiting coefficient of performance for conditioning air in a manner that combines the effects of sensible and latent processes. They developed an expression that accounts for the change in energy and exergy due to change in air temperature and water vapor content of the air, i.e. humidity ratio.

Medved and Arkar [4] made a correlation between the local climate and the free-cooling potential of latent heat storage. They presented studies of the free-cooling potential for different climatic locations. They selected six cities from around Europe with a wide range of climatic conditions for their study. In the majority of the presented free-cooling systems the emphasis is placed mainly on modeling the latent heat thermal energy storage's (LHTES) and less emphasis was placed on the free-cooling efficiency, where various approaches have been tried. Zalba et al. [5] determined the thermal response of a plate latent heat thermal energy storage's for a step change of the inlet temperature. When designing a real free-cooling system a constant ambient air temperature during the night-time and a constant indoor air temperature in the building during the daytime were assumed. Arkar et al. [6] used a project day with an assumed sinusoidal temperature variation for optimizing the geometrical and performance parameters of the LHTES. Arkar et al. [6] studied the efficiency of free cooling using latent heat storage

integrated into the ventilation system of a low energy building. They presented the results of an investigation into the free cooling efficiency in a heavyweight and lightweight low energy building using a mechanical ventilation system with two LHTESs, one for cooling the fresh supply air and the other for cooling the re-circulated indoor air. They found that the free cooling technique enables a reduction in the size of the mechanical ventilation system, provides more favourable temperatures and therefore enables better thermal comfort conditions and also fresh air for the occupants.

Arkar and Medved [7] presented a study of the free cooling of a low-energy building using a LHTES device integrated into a mechanical ventilation system. They developed a numerical model of the LHTES to identify the parameters that have an influence on the LHTES's thermal response, to determine the optimum phase-change temperature and to form the LHTES's temperature-response function. Their analyses of the temperatures in a low-energy building showed that free cooling with an LHTES is an effective cooling technique. Moeske et al. [8] focused in their paper on the impact of management strategies for external mobile shadings and cooling by natural ventilation. For natural ventilation, strategies limiting the flow rate when external temperature drops are found to be efficient to save energy.

Zalba et al. [5] and Zhang et al. [9] defined the free-cooling as a means to store outdoors coolness during the night, to supply indoors cooling during the day. Zhang et al. [9] showed that free-cooling can make the indoor air temperature in the comfortable region all the year if the thermophysical properties of building envelope material are in the desired range. Those properties are obviously related to the outdoor climate condition, internal heat source intensity, building configuration, ventilation mode etc. For a given region and a given building, the critical values of those ideal thermal physical properties can be determined through modeling and simulation. Zalba et al. [5] studied the application of phase change materials (PCM) in free-cooling systems. The use of PCMs is suitable because of the small temperature difference between day indoors and night outdoors. They designed and constructed an installation that allows testing the performance of PCMs in such systems. They performed experiments following the design of experiments strategy and they developed an empirical model in which a real free-cooling system was designed and economically evaluated.

Ghiaus and Allard [10] pointed out that natural ventilation is one of the most effective techniques for cooling. They showed that its potential for cooling may be assessed by using a method based on the indoor-outdoor temperature difference of the free-running building, the adaptive comfort criteria and the outdoor temperature. They demonstrated that the free-running temperature may be used instead of the balance temperature in energy estimation methods. The indoor-outdoor temperature difference of the free-running building becomes a characteristic of the thermal behavior of the building which is decoupled from comfort range and outdoor temperature. They found that a measure related to the energy saved and the applicability of free-cooling is given

by the probabilistic distribution of the degree-hours as a function of the outdoor temperature and time.

In this work, self-developed computer software for calculating the total cooling load for the cold stores that contain fruits or vegetables room storage at each hours of the year has been carried out. The cooling load for refrigeration unit (compressor and fan) or evaporator fans only before and after using free cooling techniques has been made. Then, a monthly electricity cost comparison before and after using free cooling is done and the percentage of the energy saving for each types of product is calculated. Finally, the payback period is calculated to check if the reduction in the electricity cost can cover the cost of the components of the new system in a short time and therefore to know if the free cooling system has a good application in cold stores for fruits and vegetables in Jordan.

2. Economizer Damper

There are two dampers on a typical economizer that modulate when the outdoor conditions are right. An outside damper opens to draw air into the room and a return air damper closes, cutting off the return air flow from the room. When this outdoor damper opens, the extra added air will pressurize inside the room, just like blowing up a balloon. This can cause outside doors to blow open or doors that open to the inside to stick closed. A small amount of pressure can have a big effect. A pressure relief damper is used upstream of the return air damper to relieve this pressure in the room. This maybe a very simple metal square the will swing open under a small amount of pressure or a large mechanical systems will use a mechanical damper that opens in conjunction with the intake damper and a fan to expel the extra air. The free cooling version has a motorized damper that conducts the two flows of internal and external air. When the damper is open it takes the air necessary for cooling directly from the exterior, excluding compressor operation as shown in Figure (1).

The dampers are driven by an electric or pneumatic actuator, which is controlled from an outdoor temperature or enthalpy control. The control switches the system from mechanical cooling to economizer cooling when the outdoor conditions are right. Preferably an enthalpy controls is used to sense both humidity and temperature. Some units have 'temperature only' controls that do not take in to consideration the effects of humidity, which can be considerable. If the enthalpy of the outdoor air is less than the enthalpy of the indoor air by volume, then the outdoor air can be used for cooling the building.

Some economizers use just a temperature control mounted on the intake hood with the minimum damper position controlled by a potentiometer on the actuator. Whenever the fan is running, the damper should drive to the minimum fresh air position. This may only amount to a slight crack in the damper opening but is enough to provide a standard 10% of the total fan volume of fresh air. When ever the fan is off this damper should drive completely closed by a return spring. Turn power off at the roof top unit while the fan is running and you should see the damper move closed.

When the outdoor conditions are below the control set point and the room thermostat is calling for cooling, the supply air fan will start and the economizer damper will modulate without starting the compressor. If the thermostat fan switch is set to "On" position the fan runs continuously and the damper will already be at the minimum fresh air position. A second controls modulates the dampers positions to maintain a constant supply air temperature.

The sensor should be located downstream of the evaporator, this will prevent the air from over cooling if the compressor is running. If the economizer is integrated with the compressor control, it is very important for the sensing bulb to be downstream of the evaporator coil. This will close off the damper when the compressor comes on and stops it from drawing in air that is too cold for the evaporator and prevents the evaporator coil from freezing up. If the outdoor conditions rise above the set point, the dampers will modulate closed to the Minimum fresh air position and the mechanical cooling will start. If the enthalpy control is set too low, the economizer will not open and take advantage of the cool outdoor temperature. If it is set too high, then the building may get too warm, because the economizer cannot provide enough cooling. It may take a few adjustments to determine what set point work best for your system. Systems with integrated controls allow you to set the enthalpy control higher without comprising comfort. An integrated control allows the compressor and the economizer to run at the same time by using a two-stage thermostat. When the first stage calls for cooling, the economizer opens. If the conditions do not improve in the space and the temperature in the cold stores continues to climb, the thermostat will then call for second stage cooling. This brings on the compressor to provide additional cooling required. If the outdoor temperature is too cold to run the compressor another control called a "Low Ambient Lock Out" will prevent the compressor from starting. By keeping the mechanical compressor off a little longer we can maximize the savings with economizer.

3. Case Study

The main objective of air refrigeration system is to maintain the environment in the enclosed spaces at conditions that reached the storage temperature of the product in the spaces. The case study in the present work includes a design for cold stores to storage any types for fruits and vegetables. The calculations of cooling load for the products have been carried out per hour and therefore a self developed software program for calculations has been built. There are many factors that affect the free cooling calculations. When we design the storage room, the heat of respiration must be considered. Also, the period of storage is very important factor and should be taken into account. Sensible cooling load depends on differences of temperatures between inside and outside room storage, and value of chilling factor and chilling time which it varies with the type of product, that chilling time and factor and number of entering products each month. Also, we mustn't neglect the cooling load for boxes which have the same chilling factor and time and depends on the types of it. In addition to the previous calculation of cooling load for the

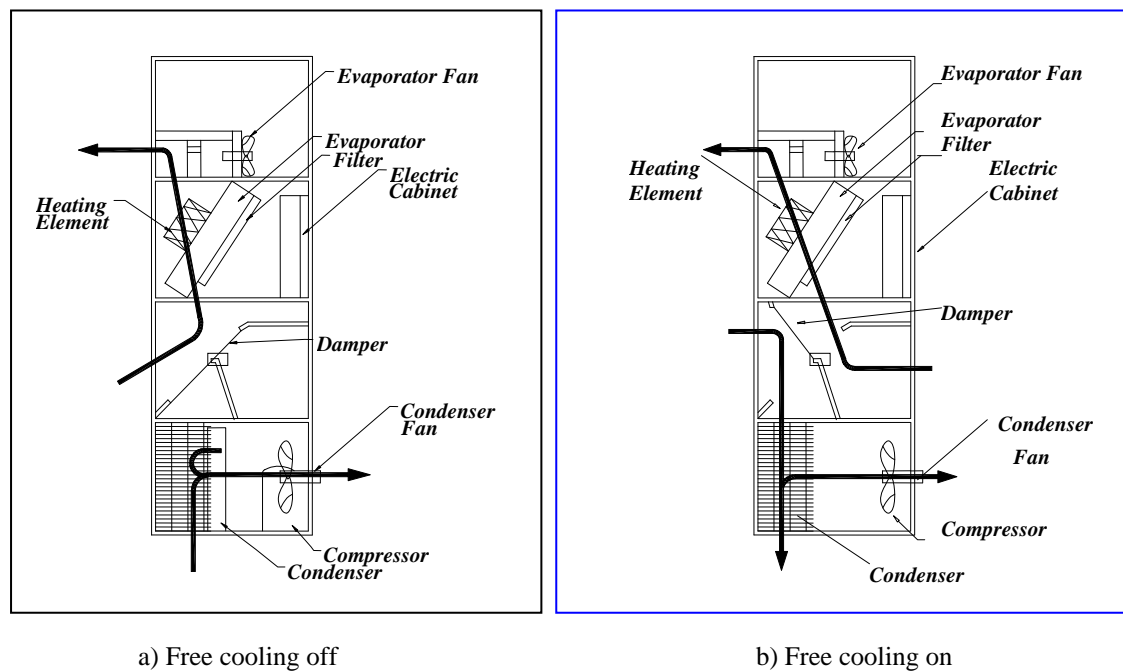


Figure 1: The motorized damper for free cooling purposes in air refrigeration unit which conducts the two flows of internal and external air.

products, another component that have relation to the total cooling load for the room such as walls, ceiling, ground, door, lights, and natural ventilation should be calculated.

After calculating the total cooling load for all hours in the year (8760 hours) for each type of stored products (Potato, Lemon and Tomato), then the maximum cooling load is selected for design purposes. The components of refrigeration cycle such as condensing unit and evaporator unit should be selected based on the maximum cooling load. Also, the total electricity bill which resulted from operating the compressor and fans in the air refrigeration system has been calculated for each hour of the year. Then an economical study has been conducted based on the payback period for the cost of the new components of the free cooling technique such as motorized damper, controller system and sensors which results from the reduction in electricity cost.

In calculating the cooling load for cold stores, the self developed software has been carried out to calculate the cooling load for each hour in the year taken into account all structure components (walls, ceiling door, ground and door), the type of the products, and the type of boxes. Then the total cooling load for the stored products including the natural ventilation, person, and lights are calculated. The selection of the refrigeration cycle components and the new added components for free cooling techniques are based on the calculated cooling load. Then, the cooling load which needs fan work only after using free cooling techniques has been calculated and the reduction in cost by using this technique has been estimated. Finally, the payback period at which the new system covers the cost of the new components is found.

The dimensions of the storage room are 6 m*8 m*6 m and it has a door in the west direction and its dimension is 2.4 m x 2.0 m. Table (1) shows the overall heat transfer coefficients for the room of the cold store. The storage room has 3 lamp lights and the power of each lamp is equal to 250 W. It is assumed that the number of persons who enters the storage room is equal to 3. The period of opening the door of the storage room is assumed to be 3 hours for each time of inserting the products in the room or taking the products from it. The number of air change per hour in the room storage is taken to be equal to 4.84. Three types of products which are potato, lemon and tomato have been stored in the storage room. The type of boxes is taken as wood which has a specific heat of $C_{p,boxes} = 1.38$ kJ/kg.°C.

The total cooling load for the storage room before and after using free cooling has been calculated. Also, the economical study has been carried out and the payback period for the damper system is computed. The values of the outside temperatures for each hour of the year are taken from meteorological department and royal scientific society at Jordan. The heat gain from walls, ceiling, ground and door is calculated and the cooling load temperatures differences (CLTD) correction method is used. The total cooling load for products is divided into sensible cooling load and the heat of respiration. Also, the heat from natural ventilation which depends on the number of change of air in the room for fruits and vegetables is taken into account. After summation all components of the cooling load, the total cooling load for the storage room at each hour around the year is found. The second step was the selection of the components of refrigeration cycles and then determines compressor and fan work and the mass flow rate of air through the fans.

Table (1): Overall heat transfer coefficients for the room of the cold store.

Type of walls	Construction	Thickness (mm)	U value (W/m ² .K)
Wall	L.W Concrete + Insulation	304.8	U _{walls} = 0.642
Ceiling	L.W Concrete + Insulation	203.4	U _c = 0.715
Ground	100 mm Fallen Board + 125 mm Tiles + 75 mm Reinforced Concrete		U _g = 0.375
Door	Type of door is Metal – Steel		U _d = 5.8

For free cooling techniques, all hours around the year at which the outside temperature is less than the inside design temperature are determined. Then, the mass flow required at each hour is calculated. The cost of the electricity for compressor and fan is calculated in the presence of free cooling and in the absence of the free cooling and finally a comparison between the two costs is made. The cooling load which is required from compressor and/or fans before and after using free cooling is calculated. The energy saving for each type of product is estimated.

As it was mentioned above, the selection of the components of refrigeration cycle should be based on the maximum cooling load. In the present work, the selected air cooled condensing unit with semi-Hermetic Reciprocating compressor has a cooling capacity of 67.1 kW and a compressor work of 21.2 kW and it has been selected from Bitzer company. The required evaporator which is selected from Guntner Company has a mass flow rate of 12.48 kg/s and two fans; the work for each fan is 1.4 kW. The motorized damper has a size of 4 x 1.25 m².

4. Theory

The cooling load due to heat transfer from outside to the room of the cold stores through walls and ceiling in the storage room is:

$$Q_{w,c} = U_{w,c} A_{w,c} \Delta T \tag{Eqn. nr. }$$

where U_w is the overall heat transfer coefficient for all construction for the walls, U_c is the overall heat transfer coefficient for all construction for the ceiling, A_w is the area for each wall, A_c is the area for the ceiling and ΔT is the cooling load temperatures differences CLTD and it is taken after correction.

$$(CLTD)_{corr.} = (CLTD_{LM}) k + (25.5 T_i) (T_{o,m} - 29.4) f \tag{2}$$

where CLTD is the cooling load temperatures differences before correction and it depends on the type of material for the walls and ceiling, LM is the latitude correction factor, T_i is the inside design temperature which equals the final storage temperature, $T_{o,m}$ is the outdoor mean temperature, k is the color adjustment factor, and f is the attic or room fan factor. The outdoor mean temperature is equal to:

$$T_{o,m} = \frac{T_{max} + T_{min}}{2} \tag{3}$$

where T_{max} is the average maximum daily temperature, and T_{min} is the average minimum daily temperature. The cooling load due to ground is

$$Q_g = U_g A_g (T_g - T_o) \tag{4}$$

where U_g is the overall heat transfer coefficient for all construction of the ground, A_g is the area for the ground and T_g is the temperature of the ground. The cooling load due to the door is

$$Q_d = U_d A_d (T_o - T_i) \tag{5}$$

where U_d is the overall heat transfer coefficient for the door, A_d is the area of the door, T_o is the outside temperature and T_i is the inside temperature. The cooling load due to light, persons and ventilation is calculated only when the door of the storage room is opened. The cooling load for light, e.g. Dossat and Horan [11], is:

$$Q_{Lt} = \frac{n * P * 3.6}{3600} \tag{6}$$

where P is the power for each lamp light, and n is the number of light lamps. The cooling load for heat gain due to persons, e.g. Dossat and Horan [11], is

$$Q_{person} = \frac{m * 753.62}{3600} \tag{7}$$

where m is the number of persons. The cooling load for natural ventilation is

$$Q_{vent} = \frac{V.c}{\rho} * C_p * (T_o - T_i) \tag{8}$$

where V is the volume of storage room, c is the number of change air per hour, and C_p is the specific heat for air. The cooling load for product consists of two components. The first component is the sensible cooling load from output design temperature to the inside design temperature:

$$Q_{product} = \frac{m_p C_{p,before} (T_o - T_i)}{t * F} \tag{9}$$

where m_p is the mass of the product, $C_{p,before}$ is the specific heat before freezing, t is the chilling time and F is the chilling factor. The second component for the cooling load of the product is the heat of respiration which is equal to:

$$Q_{breathing} = m_p R \tag{10}$$

where R is the reaction factor. The cooling load for boxes is

$$Q_{boxes} = \frac{m_b C_{p,Boxes} (T_o - T_i)}{t * F} \quad (11)$$

where m_b is the mass of boxes, and $C_{p, boxes}$ is the specific heat before freezing. The mass flow rate of the cooling air that is needed to cover the final total cooling load for the room when applying the free cooling techniques is:

$$\dot{m}_{fan} = \frac{Q_{tot}}{C_p (T_o - T_i)} \quad (12)$$

The properties of the three stored products (Potato, Lemon and Tomato) which were used in the present investigation are summarized in Table (2), e.g. Dossat and Horan [11]. As it can be shown in Table (2), the three types of the products have approximately similar properties, but the maximum period for storage is high for potato and low for tomato.

The electricity cost per hour for fan and compressor work can be calculated from the following:

- If the total cooling load is less than or equal zero, then there is no need to use compressor and fans and therefore the electricity cost is zero.
- If the compressor is switched off and the cooling load is resulted from the free cooling, then the fan is operated and the electricity cost equals:

$$\text{Electricity cost}_{fan} = W_{fan} * PF * \text{Electricity cost per kWh} \quad (13)$$

where W_{fan} is the fans work and PF is the product factor.

- If the air refrigeration system is working, then the cooling load is resulted from the fan and compressor work and the electricity cost equals:

$$\text{Electricity cost}_{compressor+fan} = (W_{compressor} + W_{fan}) * PF * \text{Electricity cost per kWh} \quad (14)$$

where $W_{compressor}$ is the compressor work and PF is the product factor.

The coefficient of performance (COP) can be reached a very high value in the case of free cooling. As it is known, the COP is defined as the ratio between the output cooling load and input electrical power. The output cooling load is the same in the two cases which are the presence of free cooling air refrigeration unit and in the absence of free

$$\text{Payback Period} = \frac{\text{Capital Cost for Free Cooling Components}}{\text{Money Saved After Using Free Cooling Technique}} \quad (16)$$

In the case study of the present investigation, it has been found that the payback period for each type of stored product is approximately one year.

cooling. But, the electrical input power is reduced in the case of free cooling and the input power is only the power needed for evaporator fans. The value of the coefficient of performance (COP) is:

$$COP = \frac{Q_{Evaporator}}{W_{Total}} \quad (15)$$

As it can be seen from equation (15), the cooling load from evaporator which is required to keep the storage product at a certain temperature remains the same before and after using the free cooling technique. However, the COP depends on the total work. For the case study in the present work, the fan power in the air refrigeration system is 2.8 kW and the compressor power is 21.2 kW. The required cooling load has been calculated after applying the above equations and it is found to be equal to 67.1 kW. Therefore, the COP before using free cooling techniques is:

$$COP = \frac{Q_{Evaporator}}{W_{Total}} = \frac{Q_{Evaporator}}{W_{Compressor} + W_{Fan}} = \frac{67.1}{21.2 + 2.8} = 2.80$$

On the other hand, the COP after using free cooling

techniques becomes:

$$COP = \frac{Q_{Evaporator}}{W_{Total}} = \frac{Q_{Evaporator}}{W_{Fan}} = \frac{67.1}{2.8} = 23.96$$

These results show that the COP increases to a very high value after using the free cooling techniques. The ratio between the COP before and after using free cooling technique can be calculated as:

$$\frac{COP_{with free cooling}}{COP_{without free cooling}} = \frac{23.96}{2.8} = 8.56$$

Finally, the payback period for the total cost of the new component such as control system and damper for free-cooling technique can be calculated as a ratio between the capital cost of the new component and the total saved money which is resulted from energy saving after the free cooling technique is applied.

5. RESULTS

Self-developed computer software was designed and built to calculate the total cooling load per each hour in the year by using different types of storage products with and

Table (2): Stored Products Properties

	Potato	Limon	Tomato
Storage Temperature (°C)	15	15	15
Max. Period For Storage	(4-6) Months	(1-4) Months	(3-5) Weeks
Chilling Factor	1	1	1
Chilling Time	20	20	34
C _p (before freezing) (kJ/kg°C)	3.60	3.76	3.85
Freezing Point (°C)	-1.80	-2.20	-0.80
Heat of Reaction (kJ/kg. hr)	0.162	0.144	0.302

without free cooling. Utilization of free cooling techniques depends on the if-clause sentences in using mass flow rate of evaporator and with the total cooling load needed. The results of the cooling load which needs compressor work before and after using free cooling are plotted. Then, a comparison between the monthly electricity cost before and after using free cooling for each types of product is carried out as well as the percentage of the electricity cost for fan and compressor to the total cost in each month. The results are drawn for potato to show the performance of free cooling technique.

The free cooling technique is used when the outside temperature is below the inside storage temperature and in this case the evaporator fan is operated without compressor to reduced the electricity cost. Figure (2) shows the hourly ambient temperature for January and July months as a function of month days for Amman city where the cold stores in the present study are found. As we see from this figure, there are many days in the year where the ambient temperature is below the inside desired temperature and therefore free cooling technique can be used beside the air refrigeration device to keep the cold stores at a constant temperature. As we know, the cold stores contain some vegetables or fruit products which have respiration heat and so it needs to be cooled all time around the year. By using free cooling technique, the number of operating hours for the compressor of air refrigeration system can be reduced and therefore the electricity cost can be minimized.

The cooling load at different months which needs compressor work before and after using free cooling technique for potato are presented in Figures (3)-(7) which show that the best month for using free cooling technique is January because the outside temperature is very low. Figure (3) shows that there is no need to switch on the compressor during January month and therefore the compressor work is equal zero. Also, in January month, the fan is switched off in many hours because the heat loss from walls, ceiling and doors is more than the cooling load which needed from the product. Also, it has been found that the total cost of electricity is decreased 83% for potato in this month with respect to the value before using free cooling.

In March month, there is no need to switch on the compressor in some days to keep the potato product in the cold store as shown in Figure (4). Also, the evaporator fan is switched off for short time and this is due to the heat loss from walls, ceiling and doors is higher than the cooling load which is needed from the product. If a new

product is inserted in the cold stores, then the air refrigeration unit should be operated for short time to decrease the temperature of the product to the required value. In this month, it has been found that the percentage of reduction in the total cost of electricity is about 66.5 % with respect to the value before using free cooling. In April month, the effectiveness of the free cooling technique is less than cold months and the percentage of energy saving after using free cooling technique in this month can reach 41%. Figure (5) shows the cooling load in April month that needs compressor work before and after using free cooling technique for potato product. At the end of the month, using of free cooling is very low compared with compressor work and this is due to the fact that a new product was inserted in the cold stores and its cooling load is high.

The summer months such as July and August can be considered as the worst months for using free cooling techniques. The percentage of energy saving in these months is very small and negligible. For example, in August month the percentage of energy saving can not reach more than 5% for all periods of the month as shown in Figure (6). In November month, the ambient temperature is dropped again and therefore the effect of free cooling starts to increase again. Figure (7) presents the cooling load in November month before and after using free cooling technique. It is clear from Figure (7) that the percentage of energy saving is high and the compressor is switched off in the most days of November month.

A comparison of the saved money before and after utilizing of free cooling technique has been carried out and the total money saved for the three studied stored product in each month is presented Table (3). The total cost of operating air refrigeration unit in each month that operates 24 hours per day is the summation of the electricity cost for compressor and evaporator fans and it is the electricity cost for evaporator fans in the presence of free cooling technique. When the compressor switched off, the evaporator fan of the air refrigeration unit is continuously operated and the cost of operating the evaporator fan has been calculated. Usually, a payback period can be taken as guide for justifying the economical aspect of utilizing the free cooling technique in air refrigeration systems. Assuming that the cost of 1.0 kWh electricity in Jordan is about 0.063 JD/kWh, then we can calculate the cost of operating the air refrigeration unit which has 21.2 kW of an electrical input power for the compressor and 2.8 kW of an electrical input power for the two evaporator fans. The cost of electrical energy consumption is calculated by

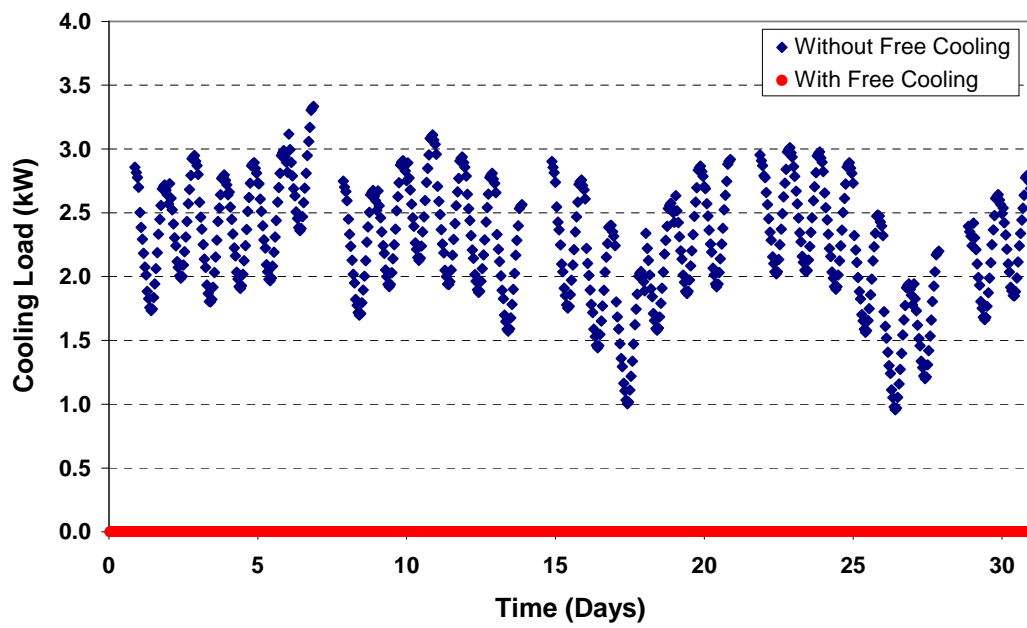


Figure 3: Cooling load in January month which needs compressor work before and after using free cooling technique for potato

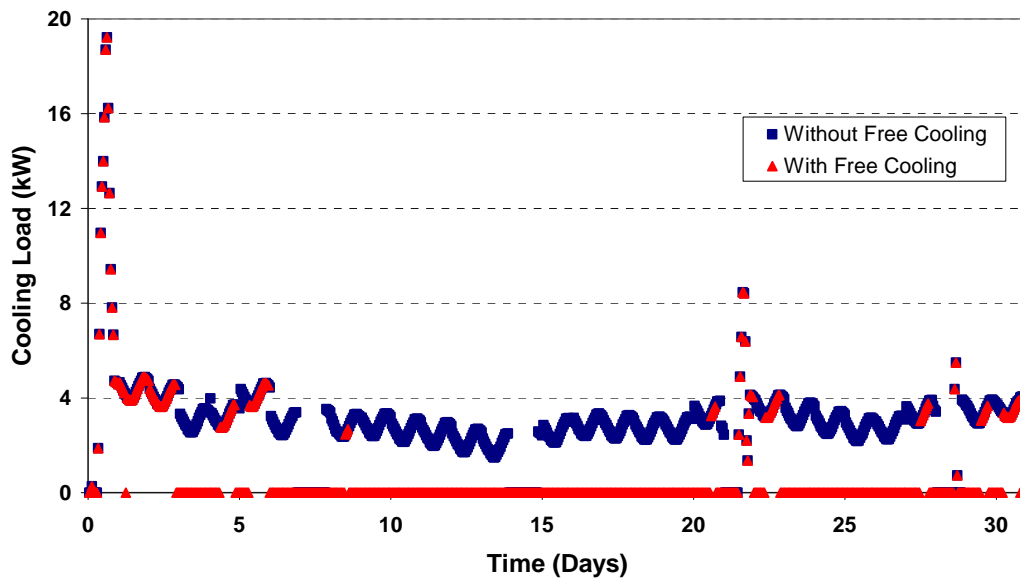


Figure 4: Cooling load in March month which needs compressor work before and after using free cooling technique for potato

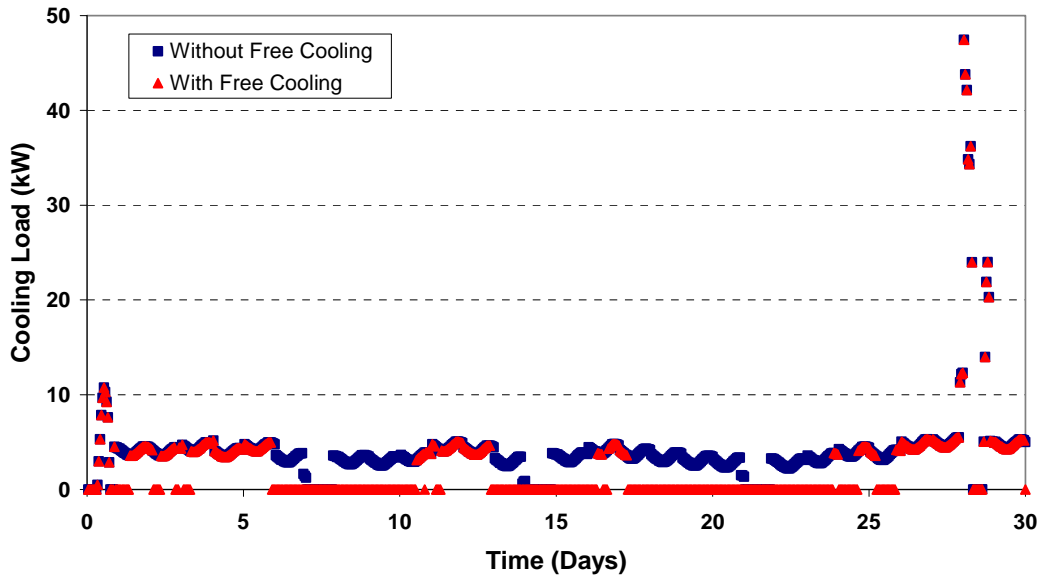


Figure 5: Cooling load in April month which needs compressor work before and after using free cooling technique for potato

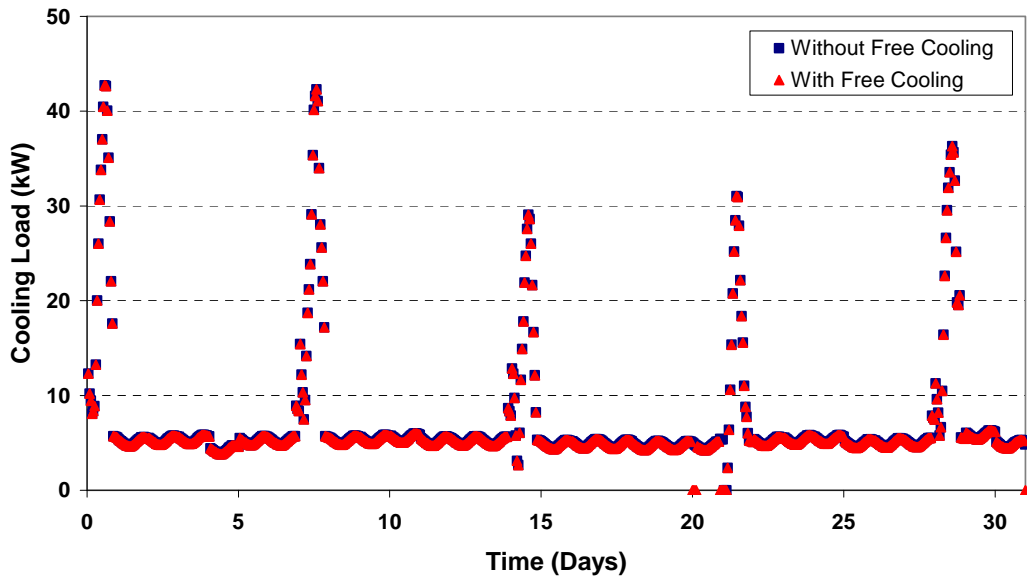


Figure 6: Cooling load in August month which needs compressor work before and after using free cooling technique for potato

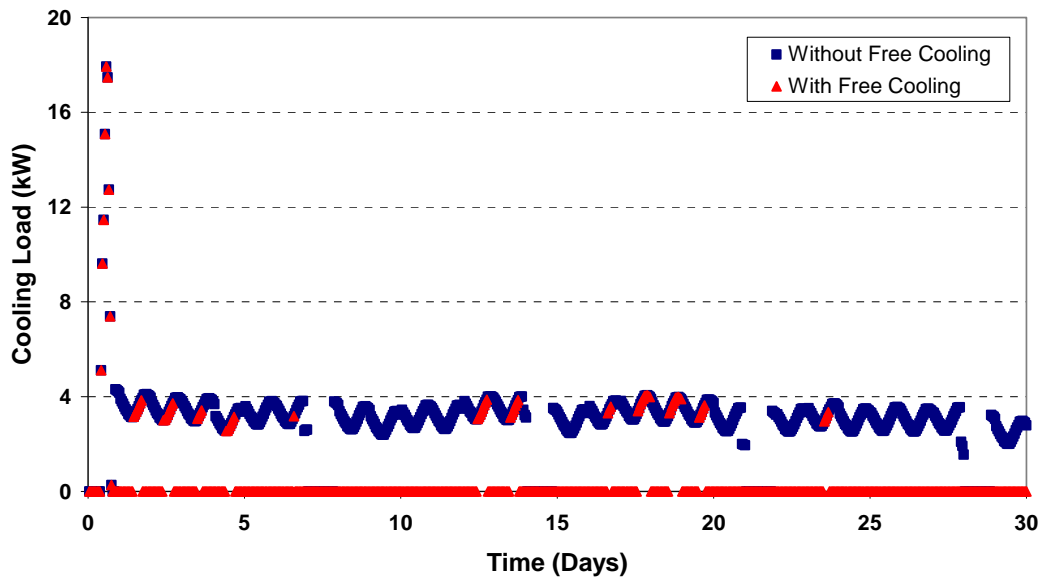


Figure 7: Cooling load in November month which needs compressor work before and after using free cooling technique for potato

Table (3): Money saved in (JD) from using free cooling technique in each month and for three different types of product.

Months	Money Saved (JD)		
	Potato	Lemon	Tomato
January	482.5	482.5	490.0
February	443.4	440.2	446.6
March	406.7	405.6	416.3
April	243.0	243.0	250.4
May	158.1	158.1	154.9
June	103.6	103.6	102.6
July	32.5	33.4	32.5
August	76.9	76.9	69.4
September	75.9	75.9	69.4
October	158.1	209.4	219.0
November	456.7	440.2	452.4
December	479.3	479.3	490.0
Total	3116.7	3148.2	3193.6

multiplying the compressor and fans power with the number of operating hours for air refrigeration unit. The total cost for the components of free cooling technique (control system and motorized damper) for the refrigeration unit in the present investigation is approximately equal to 3000 JD. The data presented in Table (3) shows that the payback period for each type of product is approximately one year. The payback period of free cooling components is reasonable and therefore it is recommended to use free cooling technique in all air-conditioning and air refrigeration units.

A comparison between the monthly saved money for air refrigeration system before and after utilizing of free cooling technique has been carried out and the results are presented in Figure (8). Figure (8) illustrates that there is a saving in electricity and therefore saving money if free

cooling technique is used in the air refrigeration unit and as it is expected, more energy or money can be saved if the free cooling technique is implemented in winter months. Figure (8) presents also the electricity cost for compressor with and without free cooling in addition to the fan at different months that is needed to keep the temperature inside the storage room where the study has been carried out at a constant temperature around 15°C. This figure shows also the electricity cost which resulted from number of daily operating hours for evaporator fan at different months for desired location in Amman city in the case of utilization of free cooling. It is clear from this figure that the electricity cost and therefore number of operating hours for free cooling technique which is represented by evaporator fan decreases in summer where the operating hours for compressor increases. The number of operating

hours for evaporator fan is higher than the number of operating hours for compressor at the most time in year except the summer season. The air refrigeration unit in the storage room is permanently operated and as long as there is vegetables or fruits inside the room and therefore the evaporator fan will be worked in the case at which the compressor is switched off. It is clear from this figure that the number of operating hours for evaporator fan decreases as the number of operating hours for compressor in summer increases. Since our selected air refrigeration unit has a total input electrical power of 24 kW (21.2 kW for compressor and 2.8 kW for fan), therefore the total cost of operating such a unit during each month at the desired location has been calculated. As it is expected, the maximum electricity cost occurs during summer time especially at July and August months.

Figure (8) summarizes the results for the total electricity cost of the selected air refrigeration unit in addition to the cost of the compressor and evaporator fan during all months in the year. There are some of months in the year such as January month where the compressor is

not needed to be operated. The electricity cost for operating air refrigeration unit in the presence of free cooling is lower than the electricity cost in the absence of free cooling. Figure (8) shows that the maximum electricity cost for evaporator fans occurs during winter season. The ratio of the total electricity cost that is resulted from operating the compressor and/or the evaporator fans in the air refrigeration unit with and without free cooling is shown in Figure (9). The results presented in Figure (9) show that 83% from the total cost of electricity can be saved in January month and this value is decreased to be less than 5% in summer months such as July. The capital cost of the free cooling components such as the control system and the motorized dampers can be recovered after one year from operation. A comparison between the total electricity cost for operating the air refrigeration unit in the case of presence or absence of free cooling is shown in Figure (9). The amount of money saving per each month in the case of utilizing free cooling technique is clearly presented in this figure.

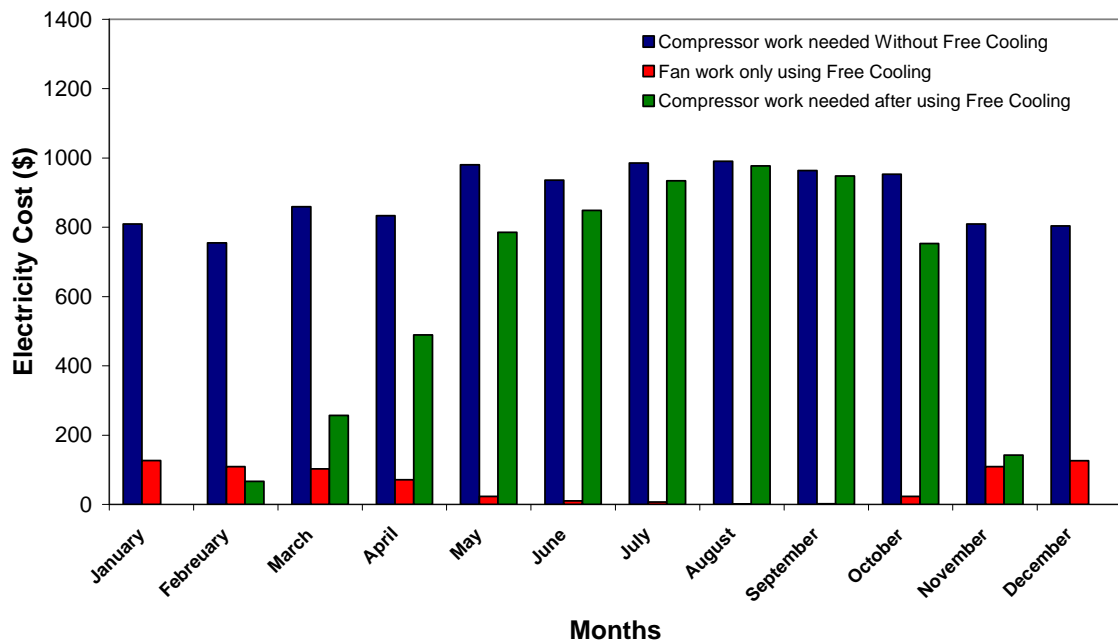


Figure 8: A comparison between the total monthly electricity cost in JD for compressor work with and without using free cooling technique in addition to the evaporator fan in the presence of free cooling for Potato

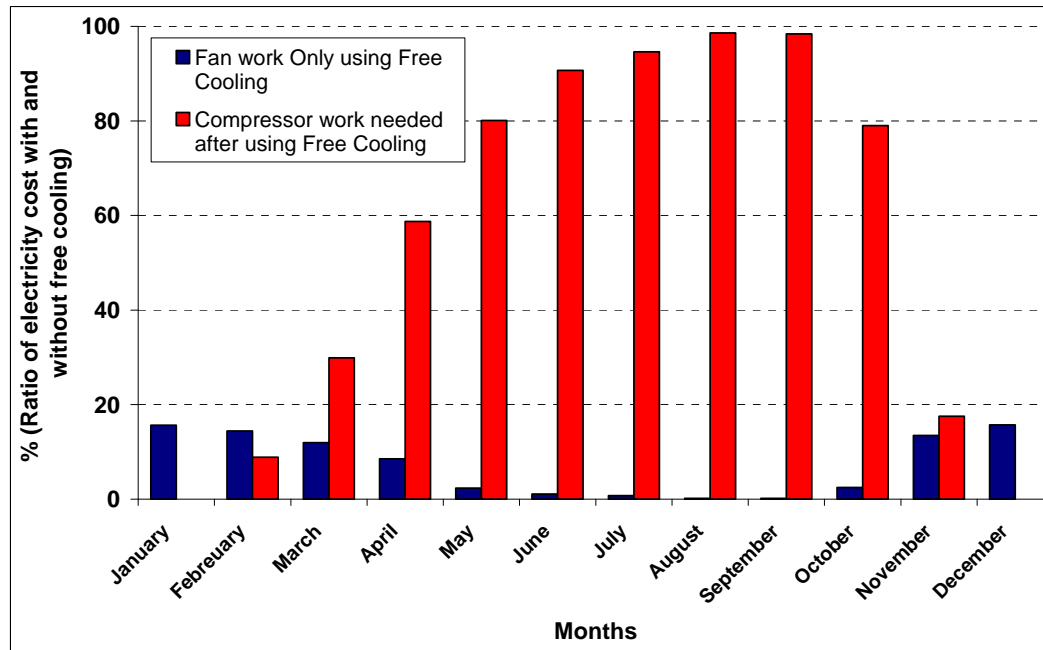


Figure 9: Percentage of the electricity cost for fan and compressor to the final cost in each month for Potato

6. Conclusions

If the outside ambient wet-bulb temperature drops below the required cooling air set-point, then free cooling can be used to save energy whenever. Free cooling technique is environmental friendly and its usage will have a positive impact on reduction the CO₂ emission and on the global warming phenomena. The main purpose of this study is to focus some sheds on the utilizing of free cooling in the air refrigeration system especially for cold stores which contain some vegetable or fruits that required to be cooled all days during the storage period. If the outside temperature is less than the set point of the cold stores, then a cooling load is required due to the heat of respiration of the products. The air refrigeration system in small cold stores uses free cooling techniques to substantially reduce energy costs. The typical value for the coefficient of performance is located between 3 and 5. However there are periods of the year where cooling ambient temperature can be utilized to provide nearly free cooling and the COP can reach to 24 where the only energy consumption is from the use of evaporative fans. Therefore, the coefficient of performance after using free cooling techniques reaches approximately 8 times its value before using this technique.

During free cooling the compressor of the air refrigeration unit is essentially shut off, thereby saving energy and also allowing scheduled preventative maintenance to take place. It has been found that this energy-efficiency measure is economically attractive and can save enough compressor electric work to pay for the installation cost of the damper for free cooling purposes in less than one year in Jordan.

Free cooling system is a good technique to store fresh products such as potato, lemon and tomato in Jordan because the outside temperature is less than the storage temperature of some products in cold months. The

utilization of free cooling techniques in cold stores depends on the location of the stores and a high energy saving can be received if the ambient temperature in the location of the cold stores is low. Free cooling technique is very efficient to be implemented in the air conditioning units and air refrigeration systems during cold or winter months such as January, February, November and December and the percentage in energy reduction can reach more than 80%, because the compressor is switched off most of time in these months. However, in other months such as March and April, the energy saving in these months is good and it can reach 50% after free cooling technique is used. On the other hand, in summer semester the percentage of energy saving that resulted from free cooling technique is less than 10% because the ambient temperature is high.

References

- [1] A. Al-Salaymeh, M. Al-Salaymeh, M. Rabah, M. abdelkader, "Enhancement of the coefficient of performance in Air Conditioning systems by Utilizing Free Cooling", Proceedings of the 2nd International Conference on Thermal Engineering: Theory and Application, Al-Ain, UAE, Jan. 3-6, 2006.
- [2] Y. Song, Y. Akashi, J. Yee, "Energy performance of a cooling plant system using the inverter chiller for industrial building", *Energy and Buildings*, Vol. 39, 2007, p. 289-297.
- [3] E.M. Mina, T.A. Newell, A.M. Jacobi, "A generalized coefficient of performance for conditioning moist air", *International Journal of Refrigeration*, Vol. 28, 2005, p. 784-790.
- [4] S. Medved, C. Arkar, "Correlation between the local climate and the free-cooling potential of latent heat storage", *Energy and Buildings*, Vol. 40, 2008, p. 429-437.
- [5] B. Zalba, J.M. Marin, L.F. Cabeza, H. Mehling, "Free-cooling of buildings with phase change materials", *International Journal of Refrigeration*, Vol. 27, No. 8, 2004, p. 839-849.

- [6] C. Arkar, B. Vidrih, S. Medved, "Efficiency of free cooling using latent heat storage integrated into the ventilation system of a low energy building", *International Journal of Refrigeration*, Vol. 30, No. 1, 2007, p. 134-143.
- [7] C. Arkar, S. Medved, "Free cooling of a building using PCM heat storage integrated into the ventilation system", *Solar Energy*, Vol. 81, 2007, p. 1078-1087.
- [8] G. Moeseke, I. Bruyere, A. Herde, "Impact of control rules on the efficiency of shading devices and free cooling for office buildings", *Building and Environment*, Vol. 42, 2007, p. 784-793.
- [9] Y. Zhang, K. Lin, Q. Zhang, H. Di, "Ideal thermophysical properties for free-cooling (or heating) buildings with constant thermal physical property material", *Energy and Buildings*, Vol. 38, 2006, p. 1164-1170.
- [10] C. Ghiaus, F. Allard, "Potential for free-cooling by ventilation", *Solar Energy*, Vol. 80, 2006, p. 402-413.
- [11] R.J. Dossat, T.J. Horan, "Principles of Refrigeration", 5th Ed. Prentice Hall; 2002.

Real Time Prediction of Flank Wear by Neuro Fuzzy Technique in Turning

D. Dinakaran ^{a,*}, S. Sampathkumar ^b, J. Susai Mary ^c

^a Department of Mechanical Engineering, Hindustan University, Padur, Kancheepuram Dt., Tamil Nadu, India - 603103

^b Department of Mechanical Engineering, College of Engineering, Anna University, Chennai, Tamil Nadu, India – 600025

^c Department of Instrumentation and Control Engineering, B S A Crescent Engineering College, India - 600048

Abstract

Machine tool automation requires reliable online tool wear monitoring techniques for automated manufacturing. Automatic detection of the state of tool wear in metal cutting operations is an important industrial problem. In this paper, an ultrasonic system is presented to monitor the tool wear in turning. The ultrasonic waves reflected from the wear region were analysed and correlated with flank wear. The reflected ultrasonic signal is analysed in both time and frequency domain. Artificial intelligence techniques such as artificial neural networks, fuzzy logic and the neuro-fuzzy technique have proved their potential in monitoring the manufacturing processes. Here, Adaptive Neuro Fuzzy Inference System (ANFIS) is used to identify the tool wear. The experimental validation runs show the system can predict the tool wear with average error of 2.5%. The decision making algorithm (DMA) is presented to determine the status of wear.

© 2010 Jordan Journal of Mechanical and Industrial Engineering. All rights reserved

Keywords: Turning, Condition Monitoring, HSS tool, Neuro Fuzzy system, Machining, Tool wear .

1. Introduction

In machining process, a tool has a fixed life time in accordance with tool manufacturer recommendations or past experiences. This tool change policy has two drawbacks, at one end; a worn tool without being exchanged in time will produce out of specification parts or even cause catastrophic tool breakage, and at the other tools being thrown away prematurely over time will incur a huge waste of manufacturing resource.

Several monitoring methods have been developed during the last few decades by many researchers. These methods may be classified in two groups, direct and indirect methods [1]. Direct methods are based upon direct measurements of the worn area of the tool using optical sensors [2], vision systems [3, 4] etc. These methods have the advantage of high measurement accuracy, but cannot be easily adopted for on-line applications.

Various indirect methods have also been developed in which the state of the wear is estimated from measurable parameters such as cutting forces [5], vibration [6], acoustic emission [7, 8], cutting temperature and surface roughness. However few reliable indirect methods are established for industrial use. This is mainly due to

complexity of machining process and the uncertainty in the correlation between the process parameters and tool wear.

The vision based methods have the advantage of high measuring accuracy, but cannot be easily adopted for online applications because of the interruption of coolant and chips. The identification of tool wear by multi-sensory approach was proposed by many researchers. U.Natarajan et al [9] presented a remarkable work in tool wear monitoring, which uses force, temperature, power signals to quantify the status of the tool wear. Though the multi-sensory approach produces good results, the cost associated with this method have somewhat discouraged its use among researchers.

An ultrasound on-line measurement of gradual wear of the flank during the turning operation was developed by Taysir H Nayfeh [10]. The method relies on inducing ultrasound waves in the tool, which propagates the length of the tool and are reflected by nose and flank surfaces. The amount of reflected energy is correlated with tool wear. The analytical model for tool wear through ultrasonic technique was presented by Nidal H et al [11, 12]. In this work, the change in tool geometry due to gradual wear has been related in a mathematical form, to the change in the acoustic behaviour of the ultrasonic waves inside the body of the cutting tool. Physical laws governing the propagation and reflection of ultrasonic waves along with geometrical analysis of wear area were used in deriving the mathematical model. Wavelet analysis for tool chatter monitoring was presented by the same

* Corresponding author. anbu_dina@yahoo.com

authors, provides different approach in tool wear monitoring [13].

The ultrasonic technique is neither a direct nor an indirect methodology, which combines advantages of both the methods. The ultrasound waves reach both the nose and the flank region of the tool directly and provide information of the nature of the wear through the reflected echoes. Since it is not a secondary signal from the machining, it is affected by the machining parameters to a smaller extent.

In the presented work, the various ultrasonic signal parameters; amplitude, root mean square (RMS) of the signal, pulse width, peak frequency shift and dB loss are used to define the height of the tool wear. The spectral analysis of the ultrasonic signal provides a different approach for tool wear monitoring. The analysis is carried out by a High Speed Steel (H.S.S) tool where the advantage of H.S.S compared with carbide tool and other cutting tools is higher toughness and lower price. This allows the economical and ecological application in the field of lower speed and feed combined with instable cutting conditions.

System modelling based on conventional mathematical tools is not well suited for dealing with ill-defined and uncertain systems [14]. By contrast; a fuzzy inference system employing fuzzy if-then rules can model the qualitative aspects of human knowledge and reasoning processes without employing precise quantitative analysis. Since the tool wear formation is a nonhomogenous continuous process, the analytical and statistical models may not be suitable for online measurement and control [15]. Here ANFIS is used as a modelling algorithm which relates the ultrasonic parameters with tool wear and presented for online prediction.

2. Experimental Details

The flank wear is measured conventionally by a tool maker's microscope of 10 microns accuracy. The flank wear is generally measured from the original cutting edge. The flank height is measured in each stage and the maximum height of flank is considered for experiments. In these stages, the corresponding ultrasonic measurements are also taken. The probe is placed in the backside of the tool to approach the flank wear as shown in Figure 1. The transducer used is a panametrics (V-112-rm) round shaped, operating at a frequency of 10 MHz. Heavy duty soluble oil is pumped through the tool holder to serve as the coupling medium of the transducer to the tool. In addition, slow circulation of the fluid cools the transducer during cutting. The limitation of ultrasound technique is the coupling medium required to induce the ultrasonic waves in the workpiece for flaw measurements. But online measurement uses the coupling medium as coolant.

The HSS tool of 15 mm thick, 100 mm long, side clearance angle of 2 degrees, side cutting edge angle of 3 degrees and with rake angle of zero degree is chosen for accelerated wear testing. In this case, initially for a fresh tool, the received signals are the resulting signal of multiple reflections of ultrasonic waves inside the complex tool geometry.

In the ideal case, the increase in the reflected energy obeys the square law. But in turning, the principles does

not strictly hold since the reflecting surfaces are marred and are at off angles from the normal to the transducer, thus resulting in complex wave interactions. Gradual tool wear manifests in two locations, which are the primary and secondary flanks. The present tool-transducer configuration can detect the first waveform. The second form, crater, can only be detected when it is very severe.

No effort was made to isolate the nose from flank wear, since they are directly related to each other. In addition, isolating the individual wear contributions to the individual ultrasonic echoes is not possible. Gradual wear of the nose and flanks is a comparatively slow process, of the order of minute or perhaps hours in some cases. Several tool wear tests were conducted to evaluate gradual wear measurements of the nose and the flanks. The work material used is EN 29 hardened steel with 60mm diameter and cutting parameters are speed range of 600 rpm, feed of 60 mm/min with 0.5mm depth of cut.

3. Results and discussion

The wave strikes on the flank face, is internally reflected to the top surface or rake face, which is then reflected back, along a different path to the transducer. In the course of cutting, due to wear, flat spots begin to develop at the tool nose and the flank, this change in the geometry of the tool serves to change the total amount of reflected ultrasonic energy.

It is noted that the amplitude of the flank signal increases with the wear land height, since ultrasonic is more sensitive when it hits the flat spots (Figure 2). Due to the same reason the pulse width also increases with wear land height (Figure 3). It is observed that the increase in wear land height increases cumulative pulse width of received signals. This is because an increase in wear land height provides the plane which has lesser inclination compared with end relief angle.

The RMS values for the reflected ultrasonic signals are calculated. From the Figure 4, it is seen that flank wear has a definite trend with RMS values of the ultrasonic signals. In all cases the wear varied randomly at different measurements points, from uniform to somewhat irregular. Tool is tested beyond the standard tool life to verify the behaviour of the correlation.

From the power spectrum, the average power received by the transducer increases with wear. Therefore the dB loss decreases with increase in flank wear height (Table 1). It is also found that the frequency components shift towards the higher frequency as the wear increases. Initially the ultrasonic waves for reference tool have the low frequency components because of multiple internal reflections. It attenuates the high frequency components the wear on the flank promotes the direct reflection of signal and it is received by the ultrasonic probe.

3.1. Tool wear prediction with ANFIS

ANFIS on-line identification of tool wear starts by obtaining the data set (input-output data pairs) and dividing it into training and validating data sets. The training data set is used to find the initial premise parameters for the fuzzy membership functions by equally spacing each membership function. The values of the premise parameters are fixed, so the overall on-line

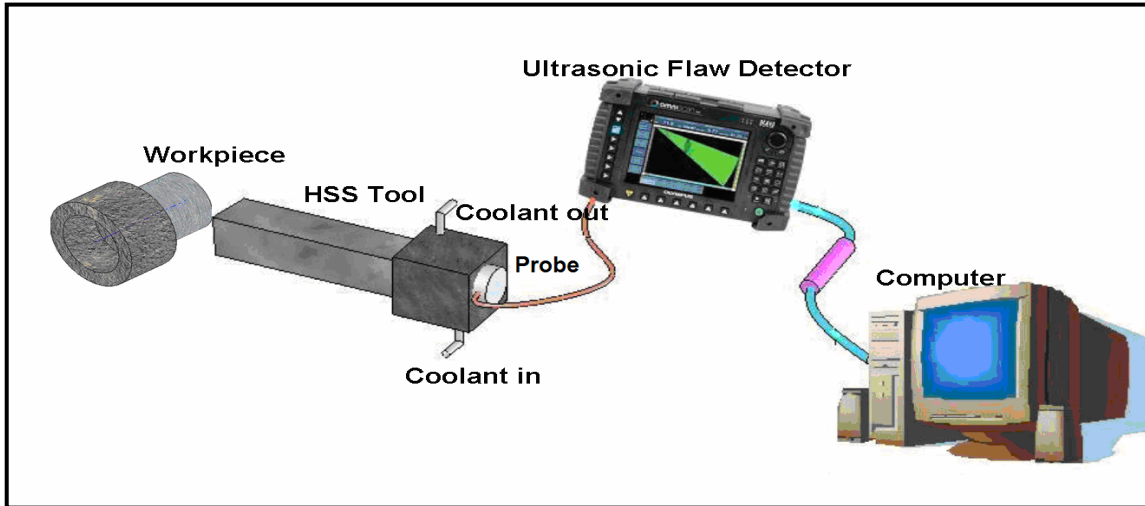


Figure 1 Online setup for flank wear monitoring

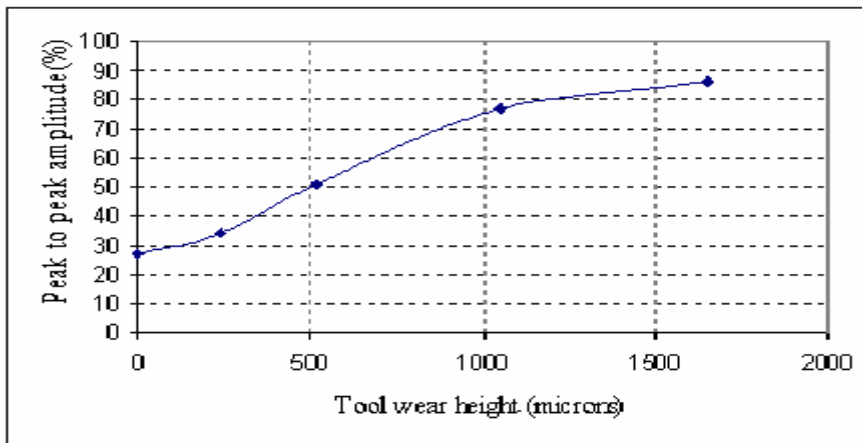


Figure 2 Wear land height Vs Peak to peak amplitude

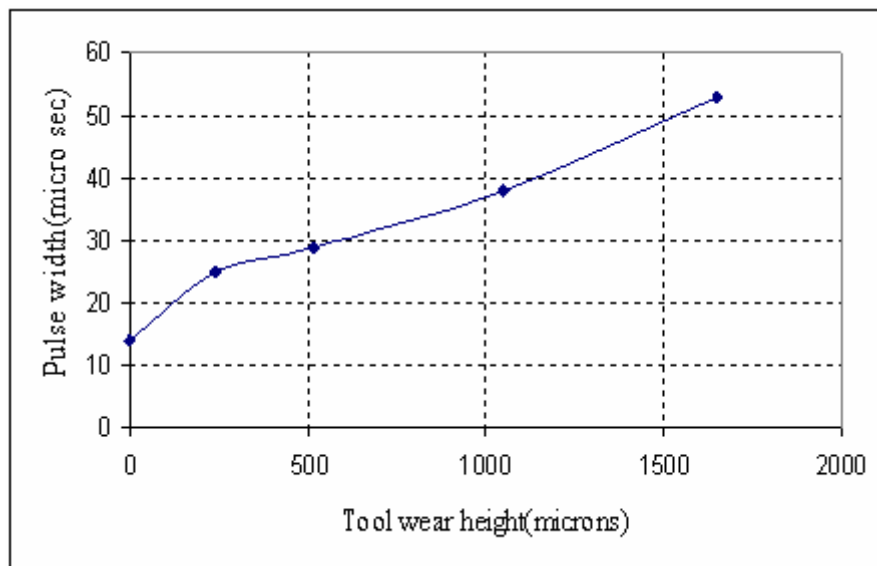


Figure 3 wear land height Vs Pulse width

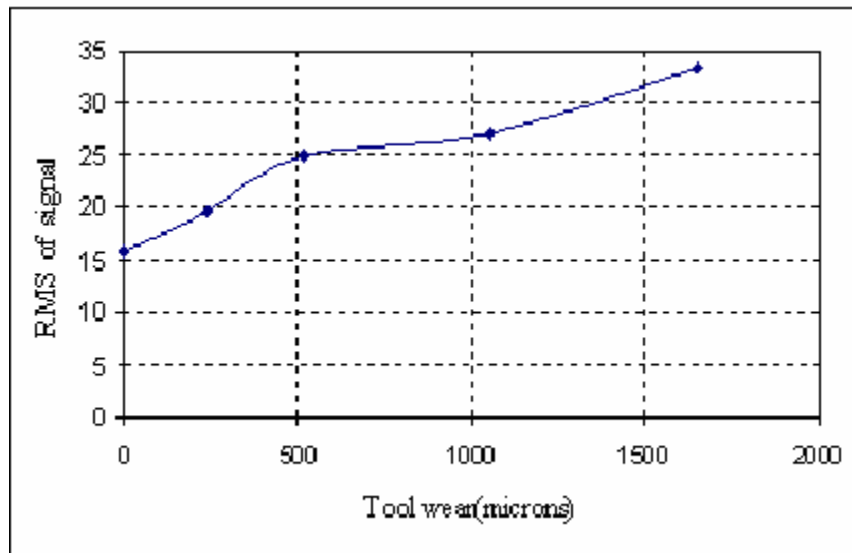


Figure 4 Wear land height Vs RMS value of signal

Table 1 Tool wear Vs Spectral parameters

Tool Wear(microns)	dB loss	Peak Frequency Shift(MHz)
0.00000	0	1.70
242.00000	-4.06	2.60
517.00000	-10.47	3.10
1052.00000	-17.53	4.30
1652.00000	-19.181	4.70

predicted tool wear, can be expressed as a linear combination of consequent parameters.

3.1.1. ANFIS Parameters

Inputs for ANFIS: ANFIS takes the experimental data of the ultrasonic parameters in time domain and frequency domain as input training data of the system. In time domain the peak amplitude, RMS of received signal and pulse width are taken as inputs for ANFIS system. In frequency domain the peak frequency shift, average power of the signal is taken as input.

Architecture of ANFIS: A total of 41 network nodes and 5 fuzzy rules are used to build the ANFIS Architecture as shown in Figure 5.

Membership Function: Bell-shaped membership functions were used to train ANFIS because it achieved the lowest training error of 0.139 at 100 epochs, as shown in the training curve of Figure 6 and error training curve of Figure 7.

The fuzzy logic toolbox of MATLAB 7.1 was used to train the ANFIS. Different ANFIS parameters were tested as training parameters in order to achieve the perfect training and the maximum prediction accuracy.

4. Validation of model

The on-line tool wear prediction system was validated by randomly selecting five independent experimental validating data points which are different from other five points used for ANFIS training, shown in Figure 8. For validation, the amplitude, RMS, Pulse width and spectrum parameters are considered as in training. The set of data points comprise the time and frequency domain parameters are given as an input for FIS validation. The validation results show that the ultrasonic system is capable of monitoring the tool wear with minimal average error of 2.5%

5. Decision making algorithm for tool wear monitoring

The overall purpose of the method is to track progressive tool wear so that catastrophic tool failure can be avoided by taking necessary corrective actions, such as stopping the feed and spindle rotation, in sufficient time. In order to determine the wear status of the cutting tool (sharp, worn but still workable and dull) during any turning operation correctly, a decision making algorithm (DMA) is proposed in this work (Figure 9).

Generally, an average flank wear height of 900 microns is considered as worn tool. But the tool changing is mainly based on the finish required. The ultrasonic parameters are

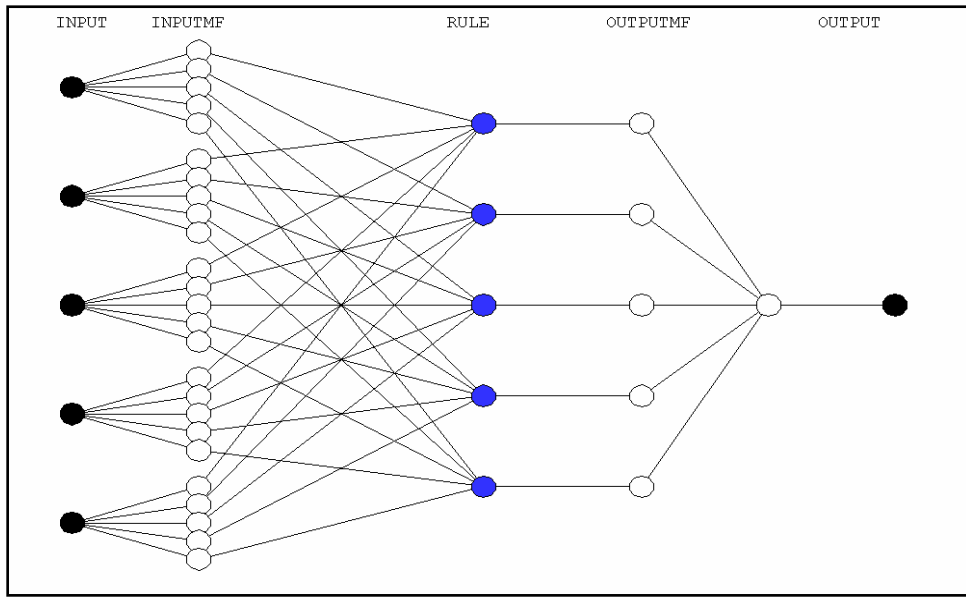


Figure 5 ANFIS Architecture

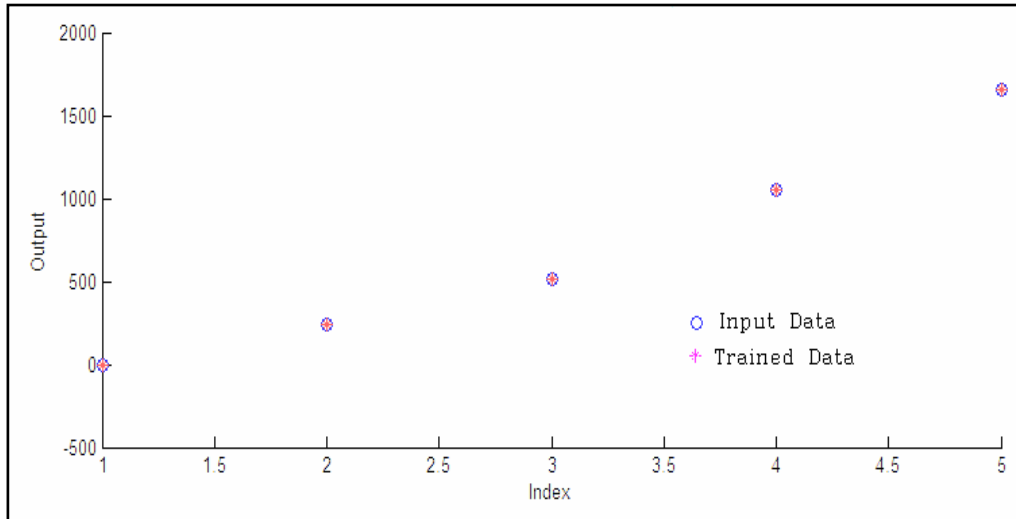


Figure 6 ANFIS training

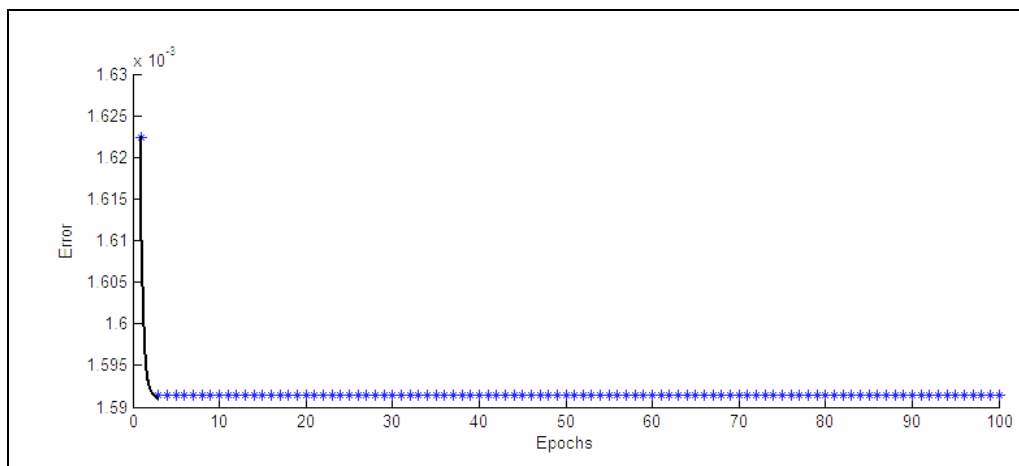


Fig 7 ANFIS training error curve

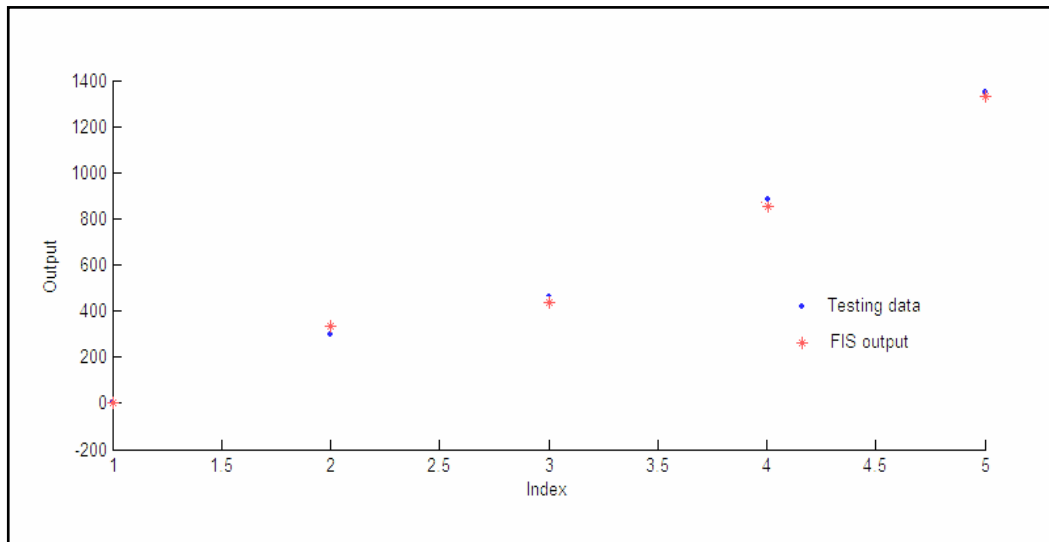


Figure 8 ANFIS Validation diagram

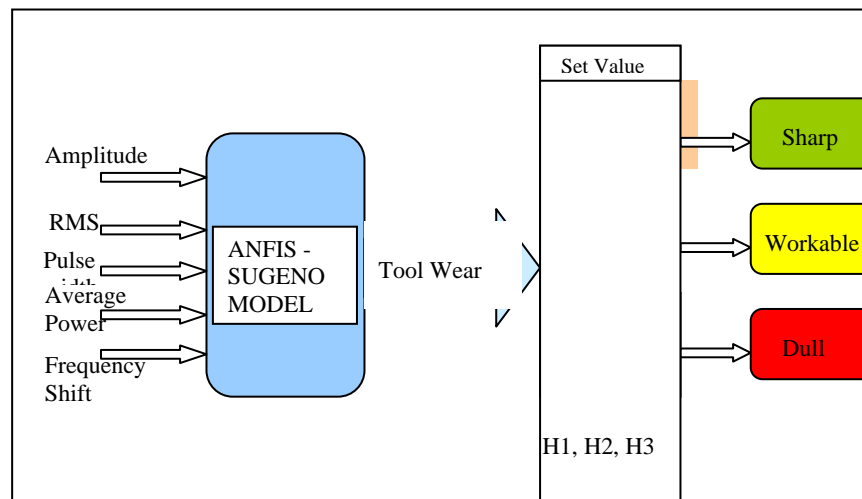


Figure 9 Decision making algorithm for tool wear.

given as input for FIS which gives the flank height. The value of predicted wear will be the input for the decision making algorithm written in C language and interfaced with monitoring system, where the decisions are represented by H1, H2, H3 respectively and have the values as sharp (up to 375 microns), workable (between 375 to 870 microns) and dull stage (above 870 microns).

6. Conclusion

In this work a new approach for tool wear monitoring was introduced by using ANFIS. The basic inferences shows that the amplitude level of ultrasonic signal, RMS of received ultrasonic signal, pulse width duration in TOF mode during cutting process is affected by the tool wear. The frequency domain of signal shows the distribution of frequency components and frequency shift in the received signal which can be related to flank wear.

Correlation between the ultrasonic parameters and flank wear shows that every parameter is contributing in definition of flank wear growth. ANFIS was developed, which considers the ultrasonic parameters in time and

frequency domain. The statistical methods may not be suitable for non linear systems, and for online application. The ANFIS solves the stated problems. The error is minimized upto 2.5%. Thus the system can be used in online monitoring of flank wear in a single point cutting tool. The decision making algorithm presented in this work determines the tool wear status in real time.

References

- [1] J. Tlusty and G. Andrews, "A critical review of sensors for unmanned machining", *Annals of CIRP*, Vol.32, No.2, 1983, 563-572
- [2] Ty G. Dawson and Thomas R. Kurfess, "Quantification of tool wear using white light interferometry and three-dimensional computational metrology", *International Journal of Machine Tools and Manufacture*, Vol.45, No.4-5, 2005, 591-596
- [3] Othman O. Khalifa, Amirasyid Densibali and Waleed Faris, "Image processing for chatter identification in machining process", *International Journal of Advanced Manufacturing Technology*, Vol.31, No.5-6, 2006, 443-449
- [4] J. Jurkovic, M. Korosec and J. Kopac, "New approach in tool wear measuring technique using CCD vision system",

International Journal of Machine Tools and Manufacture, Vol.45, No.9, 2005, 1023-1030.

[5] S. K. Choudhury and K. K. Kishore, "Tool wear measurement in turning using force ratio", International Journal of Machine Tools and Manufacture, Vol. 40, No.6, 2000, 899-909

[6] P. K. Ramakrishna Rao, P. Prasad, M. Vasanth Kumar and V. Shantha, "On-Line Wear Monitoring Of Single Point Cutting Tool Using Vibration Techniques, Trends in NDE Science & Technology", Proceedings of the 14th World Conference on Non-Destructive Testing, New Delhi, 1996, 1151 – 1156

[7] M.T. Telsang and U.S.Katu, "Condition monitoring of single-point cutting tool using Acoustic emission technique", Institution of Engineers (Production Engineering), Vol.84, No.2, 2004, 77-81.

[8] Xiaoli Li, "A Brief Review: Acoustic Emission Method For Tool Wear Monitoring During Turning", International Journal of Machine Tools & Manufacture, Vol.42, No.2, 2002, 157-165.

[9] U.Natarajan, P.Arun and V.M.Periasamy, "Online tool wear monitoring in turning by hidden markov model", Institution of Engineers, Vol. 87, 2007, 31-35.

[10] Taysir H Nayfeh, Osama K Eyada and John C Duke Jr, "An Integrated Ultrasonic Sensor for Monitoring Gradual Wear On-

line During Turning Operations", Journal of Machine Tools Manufacture, Vol.35, No.10,1995, 1385-1395.

[11] Nidal H, Abu-Zahra and Taysir H Nayfeh, "Calibrated Method for Ultrasonic On-line Monitoring of Gradual Wear During Turning Operations", Journal of Machine Tools Manufacture, Vol. 37, No.10, 1997, 1475-1484.

[12] Nidal H, Abu-Zahra, Gang Yu, "Analytical Model for Tool Wear Monitoring in Turning Operations Using Ultrasound Waves", Journal of Machine Tool & Manufacture, Vol.40, No.11, 2000, 1619-1635

[13] N.H.Abu-Zahra and J H Lange, Tool chatter monitoring in turning operations using wavelet analysis of ultrasound waves, International Journal of Advanced Manufacturing Technology,20 (2002), 248-254

[14] Jang, J.S.R., "ANFIS: Adaptive-Network-Based Fuzzy Inference System", IEEE Transactions on Systems, Man and Cybernetics, Vol. 23, No.3, 1993, 665-685.

[15] Murad S. Samhoury and Brian W. Surgenor, "Surface Roughness in Grinding: On-Line Prediction with Adaptive Neuro-Fuzzy Inference System", Transactions of NAMRI/SME, Vol.33, 2005, 57-64

Analysis of Solar Radiation in Jordan

Issa Etier ^a, Anas Al Tarabsheh ^a, and Mohammad Ababneh ^b

^a Department of Electrical Engineering, The Hashemite University, Zarqa, Jordan

^b Department of Mechatronics Engineering, The Hashemite University, Zarqa, Jordan

Abstract

This paper analyzes global radiation, diffused radiation, and other meteorological data needed to give a comprehensive study on the solar radiation in The Hashemite University in Jordan (32.05_N, 36.06_E). Measured and simulated daily, monthly, and annually global radiation averages are presented and analyzed. The measured data is collected by the Dhleel Metrological Center while the simulated data is generated by the METEONORM software (a comprehensive meteorological software). The inclination angle θ is also optimized in this work for every month of the year and for the whole year in order to maximize solar energy production.

© 2010 Jordan Journal of Mechanical and Industrial Engineering. All rights reserved

Keywords: Water Management Global radiation, Diffused radiation, Surface temperature, Solar Energy, Jordan.

1. Introduction

The sun is the largest regenerative source of energy in the world. It is estimated that the annual sun exposure amounts to $3.9 \times 10^{24} J = 1.08 \times 10^{18} kWh$. This corresponds to more than 10,000 times of the present world energy needs [1]. Furthermore, the constant fluctuation in oil prices, as shown in figure 1 [2], has pushed people and institutions to think more seriously about renewable energy resources and somehow reduce their dependence on oil.

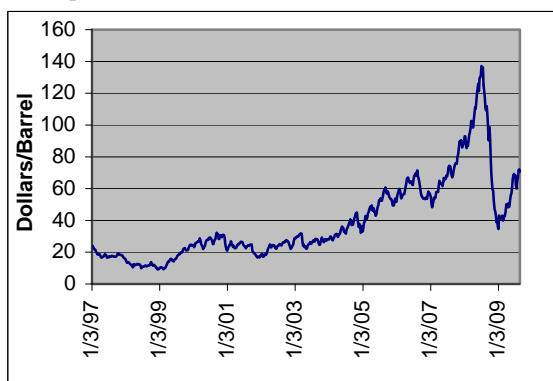


Figure 1: Weekly oil prices from 1997 to 2009

Another urgent reason to seriously consider renewable energy resources is that studies show that the oil depletion point has been reached in 2006 [3]. This is a direct result of consuming oil much faster than it is naturally produced. Since formation of new petroleum is a complicated geological process takes millions of years. In addition, energy demands are increasing at alarming rate as shown

for example for the electrical energy in Jordan in figure 2 [4-11].

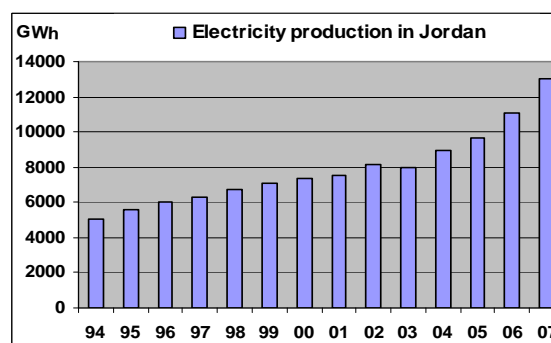


Figure 2: Electricity production in Jordan

We believe that the time is coming soon where world governments are required to offer alternative energy sources to keep their economies running or practice programmed blackouts. One of the solution measures surfacing is the wide spread of national energy centers worldwide to tackle this urgent energy problem. Jordan is no exception, The National Energy Research Center has been established in Amman – Jordan [12] for the purposes of research, development and training in the fields of new and renewable energy; In addition, to raise the efficiency of using energy in the different economic sectors.

In the literature, solar radiation was measured and analyzed in Abu Dhabi area, where hourly, daily and monthly global horizontal radiation were collected and processed [13], the paper showed that PV application in Abu Dhabi is a promising solution to energy expansion in the country. Furthermore, diffused radiation were collected in different locations in China for few years, the data is handled to fit suitable models for radiation

* Corresponding author. etier@hu.edu.jo

estimation in the country [14]. Moreover, a new method, called elevation angle constant (EAC) method, is developed to determine the solar radiation for any location in the world [15]. The EAC method showed great accuracy compared with other methods. However, this paper analyzes the global and diffused radiation and meteorological data to explore the potential of solar energy generation in Jordan (32.05_N, 36.06_E). It also investigates the solar tracking and the optimal inclination angle.

The rest of this paper is divided as follows: Section 2 discusses the global radiation and yearly air temperatures; also it compares measured and simulated meteorological data. Section 3 investigates the tracking and optimal inclination angle and studies average global radiation versus monthly inclination angles. Section 4 discusses the main outcomes of this work. Finally, section 5 presents conclusions and future work.

2. Global Radiations and Temperatures

Global radiation is the most important solar characteristics to be investigated to explore the potential of solar-energy generation in a particular location. In order to study this potential in the area of The Hashemite University, we have obtained measured monthly global radiation data from Dhleel Metrological Center for ten years [16-25]. The center is located 10 Km to the north of The Hashemite University. In addition, the METEONORM 5.0 software is applied to simulate the radiation data. This software is a comprehensive meteorological reference, incorporating a catalogue of meteorological data and calculation procedures for solar applications and system design at any desired location in the world [26]. Measured and simulated monthly radiation data are depicted in figure 3 for comparison purposes.

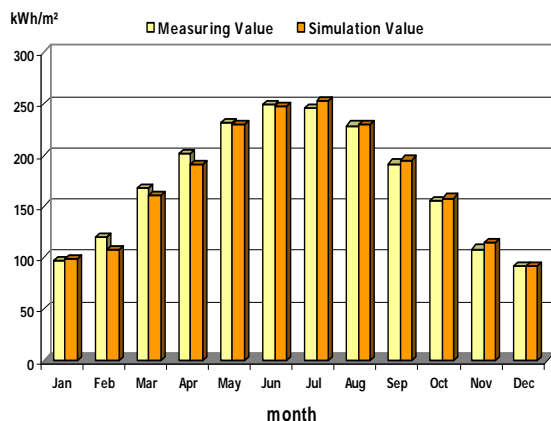


Figure 3: Measured and simulated monthly radiation data.

Furthermore, the simulated and measured data are shown in figure 4 in the x-y coordinates to determine how close the two sets of data to each other, and to decide if this software is reliable to be used for further analyses.

Fortunately, the plotted points are very close to the unity-sloped line and the standard deviation is very small and equal to 2.48%. That means, the simulated data are very close to the measured ones and therefore, the software can be used with a high confidence from now on though out the paper.

Global radiation in a specific location is defined as the sum of direct and diffused radiation reaching that location throughout the day from sunrise to sunset as well as it depends on the day of the year. In addition, diffused radiation in a location depends on the amount of scattered incoming radiation.

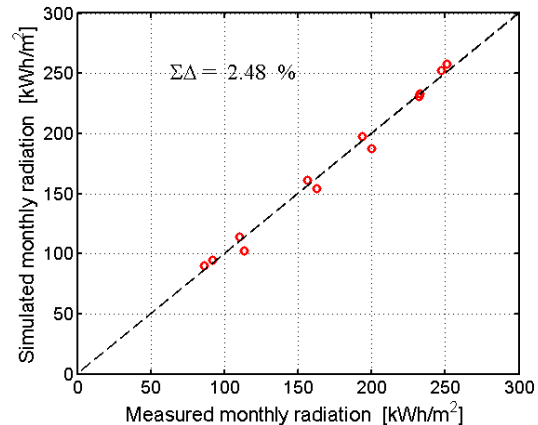


Figure 4: Simulated monthly radiation versus measured monthly radiation.

Daily global, direct and diffused radiations are depicted in figure 5 for the 365 days of the year. The average daily global radiation is 5.7 kWh/m² [27], while the average daily diffused radiation is 1.58 kWh/m²; in addition, the maximum daily global radiation is 8.72 kWh/m² and occurred in 26th June with daily diffused radiation is 1.3 kWh/m² for that day.

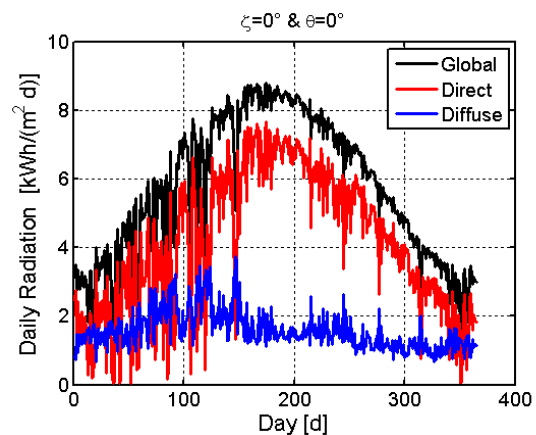


Figure 5: Daily Global, direct and diffused radiation

Furthermore, It is considered that the yearly global radiation is analyzed as a function of inclination and azimuth angles as illustrated in figure 6. High radiation occurs for inclination angles between 10 degrees and 35 degrees and azimuth angle around 0 degree. The radiation range is between 100 W/m² and 280 W/m². Note that the surface is color coded where the dark red indicates high radiation and blue color indicates low radiation, also the global radiation is projected on the lower plane in colored curves to better illustrate the changes in the global radiation.

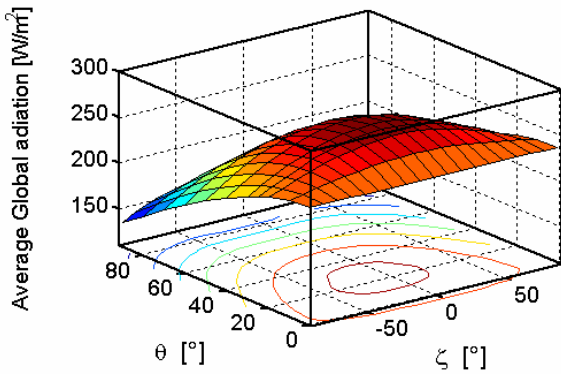


Figure 6: Average global radiation

In addition, this paper studies the yearly-diffused radiation as a function of inclination and azimuth angles as shown in figure 7. The diffused radiation changes between 65 W/m^2 and 75 W/m^2 , and this represents almost one third of the global radiation. Note the high diffused radiation occurs for inclination angles between 40 degrees and 60 degrees and azimuth angle around 0 degree.

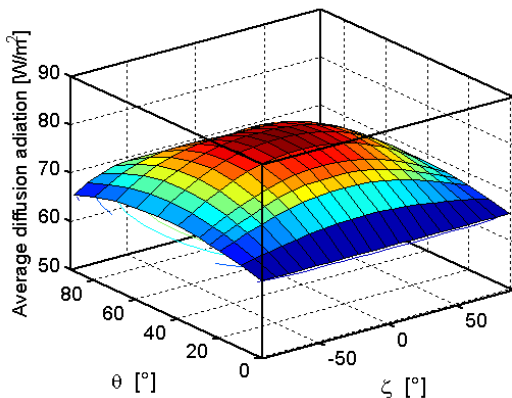


Figure 7: Yearly diffused radiation

It is important to examine the air temperature changes in the location since extreme temperatures might negatively affect the performance of photovoltaic systems. Fortunately, the air temperature in Jordan is appropriate as shown in figure 8. The hourly temperature is depicted in the figure and it varies in a small range of 39°C and -2°C throughout the year. In addition, the daily changes are around few degrees only.

Table 1 lists the global radiation in different locations of the world to better understand the situation here in Jordan [26].

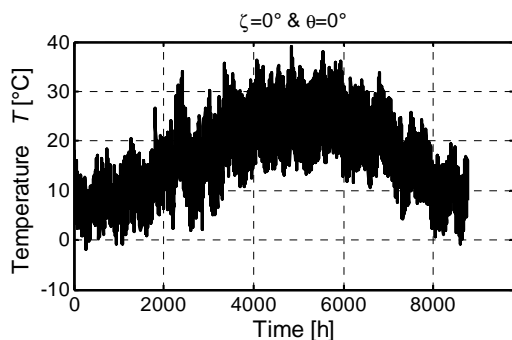


Figure 8: Yearly hourly Temperature

Table 1: Yearly Global radiation for different locations in the world

City	Yearly global radiation (kWh/m ²)
Hashemite University, Jordan	2080
Berlin, Germany	1000
Paris, France	1038
London, UK	944
Cairo, Egypt	2074
Dubai	1929
NY, USA	1427
Hong Kong	1371

Table 1 clearly shows that global radiation in Jordan is one of the highest values worldwide, therefore, with this high global radiation and more than 300 sunny days annually, Jordan has an excellent and promising potential of power generation from solar energy, which basically constitute a national resource waiting to be invested to the full extent.

3.3. Solar Tracking

The generated solar energy is given, in general, as a global radiation on a horizontal PV-panel surface. However, fixed panels receive solar radiation at angle that reduces the amount of energy considerably [28, 29]. Therefore, it is important to determine the optimal angle that generates maximum energy if tracking is not available.

In general, relative sun position with respect to the earth depends on rotation of the earth around the sun and rotation of the earth around itself. The first rotation generates the inclination angle and the second rotation generates the azimuth angle. Moreover, the tracking with respect to inclination angle is called one-axis tracking and the tracking with both inclination and azimuth angles is called two-axis tracking.

Figure 9 considers the one-axis tracking and has shown the average global radiation for all months of the year, the radiation is changing for different months and different inclination angles. December and January months show the lowest global radiation, and June and July months showed the highest global radiation.

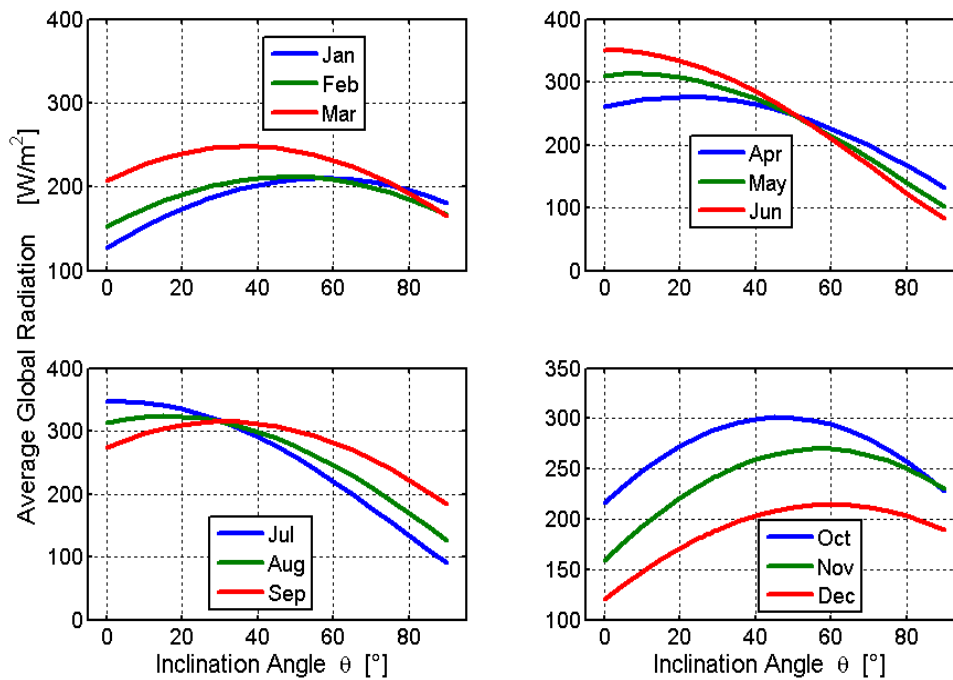


Figure 9: Monthly global radiations

In addition, figure 10 shows the yearly global radiation as a function of inclination angle. The maximum global radiation occurs at 30 degrees, therefore, for fixed panels used in The Hashemite University location and to obtain the maximum solar-energy generation, the PV panels have to be fixed at 30 degrees.

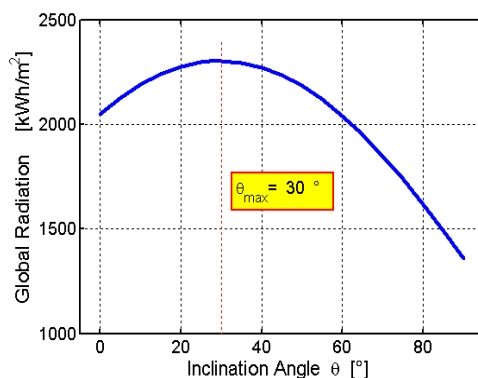


Figure 10: Optimal inclination angle

4. Results and Discussion

The comparison between the simulated and measured monthly radiation with a standard deviation of 2.48% proves the accuracy of applying the METEONORM software throughout this work. Therefore, one can rely on this software in calculating the global radiation for different inclination angles at different times in the year.

Optimizing the inclination angles is accomplished by maximizing the energy yield depending on the sun position. This motivates us to design a solar tracking system relying on the results of this work.

5. Conclusions

Global and diffused radiation and meteorological data were investigated to explore the potential of solar energy generation in the area of The Hashemite University in Jordan (32.05_N, 36.06_E). A comparison was conducted between ten-years-data of measured monthly global radiation from Dhleel Metrological Center and simulated data from METEONORM comprehensive meteorological software. This comparison revealed close match between both sets of data.

Hourly temperature data for the whole year demonstrated changes in a comfortable range for PV systems, the maximum temperature reached was 39°C and minimum temperature reached was -2°C. Furthermore, optimal inclination angle was investigated and monthly inclination angle versus average global radiation was plotted as shown in figure 9, the figure shown different optimal angles for different months; however, figure 10 demonstrated a fixed inclination angle of 30 degree gives the maximum global radiation (2330 kWh/m^2) for the whole year.

Finally, it is important to state that Jordan, with global radiation of 2080 kWh/m^2 and more than 300 sunny days a year, has excellent potential for solar energy generation. Future work is to consider the tracking in two axes versus one axes tracking and investigate its feasibility.

References

- [1] Quaschnig, V.: Understanding Renewable Energy Systems. Earthscan London, 2005.
- [2] IEA: END-USER PETROLEUM PRODUCT PRICES, International Energy Agency
- [3] Boyle G.: Renewable Energy. Oxford, 2004.
- [4] National Electric Power Company: Annual Report, Ad-dustour Commercial Press, Amman, Jordan, 2007.

- [5] National Electric Power Company: Annual Report, Ad-dustour Commercial Press, Amman, Jordan, 2006.
- [6] National Electric Power Company: Annual Report, Ad-dustour Commercial Press, Amman, Jordan, 2005.
- [7] National Electric Power Company: Annual Report, Ad-dustour Commercial Press, Amman, Jordan, 2004.
- [8] National Electric Power Company: Annual Report, Ad-dustour Commercial Press, Amman, Jordan, 2003.
- [9] National Electric Power Company: Annual Report, Ad-dustour Commercial Press, Amman, Jordan, 2002.
- [10] National Electric Power Company: Annual Report, Ad-dustour Commercial Press, Amman, Jordan, 2001.
- [11] National Electric Power Company: Annual Report, Ad-dustour Commercial Press, Amman, Jordan, 2000.
- [12] Web site of The National Energy Research Center <http://www.nerc.gov.jo>.
- [13] El Chaar, L. and Lamont, L., "Global solar radiation: Multiple on-site assessments in Abu Dhabi", *Renewable Energy* 35 (2010) 1596–1601.
- [14] Rensheng, C., Ersi, K., Jianping, Y., Shihua, L., Wenzhi, Z., and Yongjian, D., "Estimation of horizontal diffuse solar radiation with measured daily data in China", *Renewable Energy* 29 (2004) 717–726.
- [15] El Chaar, L. and Lamont, L., "Global solar radiation: Multiple on-site assessments in Abu Dhabi", *Renewable Energy* 35 (2010) 1596–1601.
- [16] Jordan Meteorological Department: Jordan Annual Climate Bulletin, JMD, Amman, Jordan, 2007.
- [17] Jordan Meteorological Department: Jordan Annual Climate Bulletin, JMD, Amman, Jordan, 2006.
- [18] Jordan Meteorological Department: Jordan Annual Climate Bulletin, JMD, Amman, Jordan, 2005.
- [19] Jordan Meteorological Department: Jordan Annual Climate Bulletin, JMD, Amman, Jordan, 2004.
- [20] Jordan Meteorological Department: Jordan Annual Climate Bulletin, JMD, Amman, Jordan, 2003.
- [21] Jordan Meteorological Department: Jordan Annual Climate Bulletin, JMD, Amman, Jordan, 2002.
- [22] Jordan Meteorological Department: Jordan Annual Climate Bulletin, JMD, Amman, Jordan, 2001.
- [23] Jordan Meteorological Department: Jordan Annual Climate Bulletin, JMD, Amman, Jordan, 2000.
- [24] Jordan Meteorological Department: Jordan Annual Climate Bulletin, JMD, Amman, Jordan, 1999.
- [25] Jordan Meteorological Department: Jordan Annual Climate Bulletin, JMD, Amman, Jordan, 1998.
- [26] Switzerland, Meteotest: METEONORM Global Meteorological Database for Engineers, Planners and Education, Version 5.0, Edition 2003.
- [27] A. Al-Salaymeh, "Modelling of Global Daily Solar Radiation on Horizontal Surfaces for Amman City"; *Emirates Journal for Engineering Research*, 11 (1), 49-56 (2006).
- [28] Luque, A., Hegedus, S.: *Handbook of Photovoltaic Science and Engineering*. John Wiley & Sons Ltd, 2003.
- [29] Hanitsch, R., Etier, I., Ertürk, N., Heumann, K., Munschauer, M., Simulation and comparison of a tracked PV system with a model based on the measurement of the sky irradiance distribution, EuroSun98, 2nd ISES-Europe, Portoroz, Slovenia. 1998.

Production Inventory Model for Deteriorating Items with On-Hand Inventory and Time Dependent Demand

Sri S. V. Uma Maheswara Rao ^{a,*}, K. Srinivasa Rao ^b, K. Venkata Subbaiah ^c

^a Department of Marine Engineering, Andhra University, Visakhapatnam, India.

^b Department of Mechanical Engineering, Andhra University, Visakhapatnam, India.

^c Department of Statistics, Andhra University, Visakhapatnam, India.

Abstract

Production inventory model plays a dominant role in production scheduling and planning. For the determination of optimal downtime, uptime of production and production quantity, it is required to minimize the expected total cost. The total cost of production is dependent on demand, production rate and rate of decay in deteriorating items. In this paper, we develop and analyze the production inventory model for deteriorating items by assuming that the demand is a function of both on-hand inventory and time. It is also assumed that the lifetime of commodity is random and follows a Weibull distribution. The sensitivity of the model is analyzed with respect to the parameters and costs. A case study is carried out to determine production schedules in a pickle manufacturing industry. This model also includes other production-level inventory models as particular cases for specific values of the parameters.

© 2010 Jordan Journal of Mechanical and Industrial Engineering. All rights reserved

Keywords: Production cycle, Weibull decay, On-hand inventory and time, Production scheduling.

1. Introduction

Recently much emphasis is given to study the control and maintenance of production inventories of the deteriorating items. The deterioration of inventory on stocks during the storage period constitutes an important factor. The deterioration in general may be considered because of various effects on the stock, some of which are damage, spoilage, obsolescence, decay, decreasing usefulness and many more. For example, in manufacturing industries like drugs, pharmaceuticals, food products, radioactive substances, the item deteriorates over a period. Nahmias [1], Raafat [2], Goyal and Giri [3] reviewed inventory models for deteriorating items. Cohen [4], Aggarwal [5], Dave and Shah [6], Pal [7], Kalpakham and Sapna [8], Giri and Chaudhari [9] developed the inventory models with exponential lifetime. Tadikamalla [10] developed inventory model with Gamma distribution for deterioration. Covert and Philip [11], Philip [12], Goel and Aggarwal [13], Hwang [14] and Venkatasubbaiah et.al [15] discussed inventory models with Weibull distribution for the lifetime of the commodity. Nirupamadevi et.al [16], [17] studied the inventory models with the assumption that the lifetime of the commodity follows a mixture of Weibull distribution. Lakshminarayana et.al [18] suggested inventory models for deteriorating items with

exponential, Weibull and mixture of Weibull lifetime distributions having seconds' sale.

In all these papers, they assumed that the replenishment is instantaneous but in production processes, the replenishment is finite. Srinivasa Rao et.al [19] developed a production inventory model with generalized Pareto lifetime and time dependent demand. Mahapatra and Maity [20], Halim, Giri and Chaudhuri [21] studied the production inventory models for deteriorating items with fuzzy deterioration rate. In these models, they assumed that the demand is dependent on stock or on-hand inventory. Ouyang et.al [22] studied the inventory models with stock dependent demand. Bhowmick et.al [23] suggested a continuous deterministic inventory system for deteriorating items with inventory-level dependent time varying demand. Jie Min et.al. [24] proposed a perishable inventory model with a stock dependent selling rate. They also considered the demand rate is dependent on the negative inventory level during the stock out period. Lee and Hsu [25] developed a two-warehouse inventory model for deteriorating items with time-dependent demand. Manna and Chiang [26] developed two deterministic economic production quantity models for Weibull-distribution deteriorating items with demand rate as a ramp type function of time. Tripathy and Mishra [27] studied an inventory model for weibull deteriorating items with price dependent demand and time-varying holding cost. In all these papers, they have considered that the demand is a function of either stock dependent or time dependent. However, in many manufacturing processes of deteriorating items, the demand is a function of both on-

* Corresponding author. svumrao@yahoo.co.in

hand inventory and time. For example, in Seafood processing units, the rate of deterioration is variable and time dependent. Hence, in this paper, we develop and analyze an inventory model for deteriorating items with the assumption that the lifetime of commodity is random and follows a Weibull distribution. The Weibull rates of decay include increasing/ decreasing/ constant rates of decay. We also assume that the demand is a linear function of on hand inventory and power pattern demand. This model is a general one as it includes several of the earlier models as particular cases for specific values of parameters. We have developed two models by considering with and without shortages where as with shortages model is discussed in detail.

2. Assumptions and Notations

The production inventory model for deteriorating items is developed under the following assumptions and notations:

2.1. Assumptions

- i) The production inventory system involves only one type of item.
- ii) The life time of commodity is random and follows a three parameter Weibull distribution with probability density function of the form

$$f(t) = \alpha\beta(t - \gamma)^{\beta-1} e^{-\alpha(t-\gamma)^\beta}, \alpha, \beta > 0, t > \gamma;$$

(Johnson et.al,1995) [28]

$$D(t) = \left\{ \tau + \phi_1 I(t) + \phi_2 \frac{rt^{\frac{1}{n}-1}}{nT^{\frac{1}{n}}} \right\}, \quad 0 < t \leq T, \quad 0 \leq \phi_1 < 1, 0 \leq \phi_2 < 1, \tau > 0 \quad (1)$$

where, r is demand rate, n is pattern index; ϕ_1, ϕ_2 (ϕ_i) and τ (τ) are positive constants which can be varied depending on the demand rate. This assumption is considered taking the linear relationship between production and demand. If $\phi_1 = 0, \phi_2 = 0$, the rate of demand becomes constant and $D(t) = \tau$.

If $\phi_1 = 0$ and $\tau = 0$, the demand rate becomes power pattern demand. If $\phi_2 = 0$, the demand rate becomes stock dependent demand.

- vi) In shortages model, shortages are allowed and fully backlogged. During the shortages period, the backlogging rate is the surplus available after fulfilling the on hand demand and there is a penalty (π) (π) for not meeting the demand.

2.2. Notations

The notations employed in this paper are as given below:

- A - Setup cost
- C - Unit cost
- h - Holding cost of a unit per unit time
- π - Shortage cost
- $K(t_1, t_3, T)$ - The total cost of the system per unit time with shortages model
- Q - Total quantity of items produced per unit time
- R - Rate of Production of items per unit time

where, α (alpha) is the shape parameter, β (beta) is the scale parameter and γ (gamma) is the location parameter. The Weibull distribution for deterioration is assumed since in many deteriorating items, the rate of deterioration is a variable depending on time having increasing / decreasing / constant rates of decay. It is reasonable to assume that the deterioration starts only after certain period of life, which is equivalent to γ , hence, the instantaneous rate of deterioration is

$$h(t) = \frac{f(t)}{1 - F(t)} = \alpha\beta(t - \gamma)^{\beta-1}, \quad t > \gamma$$

where, $F(t)$ is the cumulative density function of the Weibull distribution.

This Weibull distribution includes exponential distribution as particular case when $\beta = 1, \gamma = 0$ and truncated exponential distribution when $\beta = 1$.

- iii) There is no repair or replacement of the deteriorated item during the production cycle and the deteriorated item is thrown as a scrap.
- iv) The rate of production is governed by supply and is finite say (R). The production rate is greater than demand rate and system is in steady state during production.
- v) The rate of demand is a function of quantity as equation(1)

$I(t)$ - On hand inventory at time t

γ - The time point at which deterioration starts

t_1 - The time point at which production stopped

t_2 - The time point at which shortages occur

t_3 - The time point at which the production re commences

T - Production cycle time

3. Mathematical Modeling

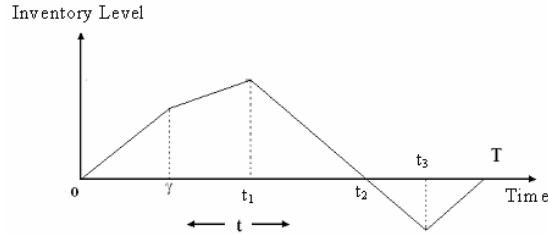
Here, we have considered a production inventory system for deteriorating items, which is assumed to follow the pattern as, described. The production starts when inventory is zero and the produced items meet the demand and deterioration. The production is stopped, when stock reaches to a maximum inventory level and allowed to reach zero gradually due to the demand and deterioration. Shortages are allowed and backlogged until some time interval and at the same time production starts to clear the backlogging and the regular demand until stock becomes zero.

Consider a production-level inventory model, in which shortages are allowed. The production starts at time $t = 0$, when the stock is zero and reaches to a maximum inventory level at time $t = t_1$. The time interval is divided into two non-overlapping intervals $(0, \gamma)$ and (γ, t_1) .

During the interval $(0, \gamma)$, the produced items partly meet the demand and during interval (γ, t_1) , the produced items are partly consumed due to the demand and deterioration and excess items are stored. The production is stopped at time $t = t_1$ and the stock level is allowed to reduce gradually due to the demand and deterioration and at time t

until time $t = t_3$ and production starts at this instant of time. During the time period (t_3, T) , all the backlogged shortages are cleared in addition to fulfilling the on hand demand and the cycle repeats thereafter. The above inventory model is represented in Fig.1.

Fig.1 The inventory system - with shortages.



$t = t_2$, the inventory becomes zero. Shortages are permitted

Let $I(t)$ denote the inventory level of the system at time t ($0 \leq t \leq T$).

The differential equations describing the instantaneous state of $I(t)$ in the interval $(0, T)$ are given by

$$\frac{d}{dt} I(t) = R - \left\{ \tau + \varphi_1 I(t) + \varphi_2 \frac{rt^{\frac{1}{n}-1}}{nT^{\frac{1}{n}}} \right\}, \quad 0 \leq t \leq \gamma \tag{1}$$

$$\frac{d}{dt} I(t) + \alpha\beta(t - \gamma)^{\beta-1} I(t) = R - \left\{ \tau + \varphi_1 I(t) + \varphi_2 \frac{rt^{\frac{1}{n}-1}}{nT^{\frac{1}{n}}} \right\}, \quad \gamma \leq t \leq t_1 \tag{2}$$

$$\frac{d}{dt} I(t) + \alpha\beta(t - \gamma)^{\beta-1} I(t) = - \left\{ \tau + \varphi_1 I(t) + \varphi_2 \frac{rt^{\frac{1}{n}-1}}{nT^{\frac{1}{n}}} \right\}, \quad t_1 \leq t \leq t_2 \tag{3}$$

$$\frac{d}{dt} I(t) = -\tau, \quad t_2 \leq t \leq t_3 \tag{4}$$

$$\frac{d}{dt} I(t) = R - \tau, \quad t_3 \leq t \leq T \tag{5}$$

with the boundary conditions $I(0) = 0$, $I(t_2) = 0$ and $I(T) = 0$

By solving the equations (1), (2), (3), (4), and (5) and using boundary conditions, we obtain the instantaneous state of inventory at any given time t , during the interval $(0, \gamma)$ is

$$I(t) = e^{-\varphi_1 t} \int_0^t \left[R - \left\{ \tau + \varphi_2 \frac{ru^{\frac{1}{n}-1}}{nT^{\frac{1}{n}}} \right\} \right] e^{\varphi_1 u} du, \quad 0 \leq t \leq \gamma \tag{6}$$

The instantaneous state of inventory at any time t , during the interval (γ, t_1) is

$$I(t) = e^{-\{\alpha(t-\gamma)^\beta + \varphi_1 t\}} \left[\int_\gamma^t \left[R - \left\{ \tau + \varphi_2 \frac{ru^{\frac{1}{n}-1}}{nT^{\frac{1}{n}}} \right\} \right] e^{\alpha(u-\gamma)^\beta + \varphi_1 u} du + \int_0^\gamma \left[R - \left\{ \tau + \varphi_2 \frac{ru^{\frac{1}{n}-1}}{nT^{\frac{1}{n}}} \right\} \right] e^{\varphi_1 u} du \right], \quad \gamma \leq t \leq t_1 \tag{7}$$

The instantaneous state of inventory at any time t , during the interval (t_1, t_2) is

$$I(t) = e^{-\{\alpha(t-\gamma)^\beta + \varphi_1 t\}} \left[\int_t^{t_2} \left\{ \tau + \varphi_2 \frac{ru^{\frac{1}{n}-1}}{nT^{\frac{1}{n}}} \right\} e^{\alpha(u-\gamma)^\beta + \varphi_1 u} du \right], \quad t_1 \leq t \leq t_2 \tag{8}$$

The instantaneous state of inventory at any time t , during the interval (t_2, t_3) is

$$I(t) = \tau(t_2 - t), \quad t_2 \leq t \leq t_3 \quad (9)$$

The instantaneous state of inventory at any time t , during the interval (t_2, T) is

$$I(t) = (R - \tau)(t - T), \quad t_3 \leq t \leq T, \quad (10)$$

From the equations (9) and (10), we get

$$t_2 = \frac{Rt_3 - (R - \tau)T}{\tau}, \quad (11)$$

The total production in the cycle time T is

$$Q = R t_1 + R (T - t_3), \quad (12)$$

The Stock loss due to deterioration in the interval $(0, T)$ is given by

$$L(t) = R t_1 - \int_0^T \left\{ \tau + \varphi_1 I(t) + \varphi_2 \frac{rt^{\frac{1}{n}-1}}{nT^{\frac{1}{n}}} \right\} dt, \quad (13)$$

Backlogged demand at time t is

$$B(t) = \int_{t_2}^{t_3} \left\{ \tau + \varphi_1 I(t) + \varphi_2 \frac{rt^{\frac{1}{n}-1}}{nT^{\frac{1}{n}}} \right\} dt, \quad (14)$$

The total cost per unit time $K(t_1, t_3, T)$ is the sum of the set up cost per unit time, purchasing cost per unit time, holding cost per unit time and shortage cost per unit time.

Therefore,

$$K(t_1, t_3, T) = \frac{A}{T} + \frac{C}{T}Q + \frac{h}{T} \left[\int_0^\gamma I(t)dt + \int_\gamma^{t_1} I(t)dt + \int_{t_1}^{t_3} I(t)dt \right] + \frac{\pi}{T} \left[\int_{t_2}^{t_3} -I(t)dt + \int_{t_3}^T -I(t)dt \right], \quad (15)$$

By substituting the values of $I(t)$ and Q from the equations (6) to (10) and (12) in equation (15), we get

$$\begin{aligned} K(t_1, t_3, T) = & \frac{A}{T} + \frac{C}{T} [Rt_1 + R(T - t_3)] + \frac{h}{T} \left[\int_0^\gamma e^{-\varphi_1 t} \int_0^t \left[R - \left\{ \tau + \varphi_2 \frac{ru^{\frac{1}{n}-1}}{nT^{\frac{1}{n}}} \right\} \right] e^{\varphi_1 u} du dt \right. \\ & + \int_\gamma^{t_1} e^{-\{\alpha(t-\gamma)^\beta + \varphi_1 t\}} \left[\int_\gamma^t \left[R - \left\{ \tau + \varphi_2 \frac{ru^{\frac{1}{n}-1}}{nT^{\frac{1}{n}}} \right\} \right] e^{\alpha(u-\gamma)^\beta + \varphi_1 u} du + \int_0^\gamma \left[R - \left\{ \tau + \varphi_2 \frac{ru^{\frac{1}{n}-1}}{nT^{\frac{1}{n}}} \right\} \right] e^{\varphi_1 u} du \right] dt \\ & \left. + \int_{t_1}^{t_2} e^{-\{\alpha(t-\gamma)^\beta + \varphi_1 t\}} \left[\int_t^{t_2} \left\{ \tau + \varphi_2 \frac{ru^{\frac{1}{n}-1}}{nT^{\frac{1}{n}}} \right\} e^{\alpha(u-\gamma)^\beta + \varphi_1 u} du \right] dt \right] + \frac{\pi}{T} \left[\int_{t_2}^{t_3} -\tau(t_2 - t)dt + \int_{t_3}^T -(R - \tau)(t - T)dt \right] \quad (16) \end{aligned}$$

Using the truncated Taylor's series expansion for exponential function and on integrating and simplifying the equation (16), we get

$$\begin{aligned} K(t_1, t_3, T) = & \frac{A}{T} + \frac{C}{T} [Rt_1 + R(T - t_3)] + \frac{h}{T} \left[\frac{R - \tau}{\varphi_1} \left\{ \gamma + \frac{e^{-\varphi_1 \gamma} - 1}{\varphi_1} \right\} - \frac{n\varphi_2 r}{T^{\frac{1}{n}}} \left\{ \frac{\gamma^{\frac{1}{n}+1}}{1+n} - \frac{\varphi_1 \gamma^{\frac{1}{n}+2}}{1+2n} \right. \right. \\ & \left. \left. + \frac{\varphi_1 \gamma^{\frac{1}{n}+2}}{(1+n)(1+2n)} - \frac{\varphi_1 \gamma^{\frac{1}{n}+3}}{(1+n)(1+2n)} \right\} + (R - \tau) \left[\frac{t_1^2}{2} - \frac{\gamma^2}{2} + \frac{\alpha(t_1 - \gamma)^{\beta+2}}{(\beta+1)(\beta+2)} + \frac{\varphi_1}{6} (t_1^3 - \gamma^3) \right. \right. \\ & \left. \left. - \frac{\alpha}{(\beta+1)} \left\{ t_1 (t_1 - \gamma)^{\beta+1} - \frac{(t_1 - \gamma)^{\beta+2}}{\beta+2} \right\} - \frac{\alpha^2 (t_1 - \gamma)^{2(\beta+1)}}{2(\beta+1)^2} - \frac{\alpha \varphi_1}{2} \left\{ t_1^2 \frac{(t_1 - \gamma)^{\beta+1}}{\beta+1} - \frac{2}{(\beta+1)(\beta+2)} \right. \right. \end{aligned}$$

$$\begin{aligned}
& \left\{ t_1 (t_1 - \gamma)^{\beta+2} - \frac{(t_1 - \gamma)^{\beta+3}}{\beta+3} \right\} - \frac{\Phi_1}{3} (t_1^3 - \gamma^3) - \frac{\alpha \Phi_1}{\beta+1} \left\{ \frac{t_1 (t_1 - \gamma)^{\beta+2}}{\beta+2} - \frac{(t_1 - \gamma)^{\beta+3}}{(\beta+2)(\beta+3)} \right\} \\
& - \frac{\Phi_1^2}{8} (t_1^4 - \gamma^4) - \frac{\Phi_2 \Gamma}{n \Gamma^{\frac{1}{n}}} \left[\frac{n^2}{1+n} \left(t_1^{\frac{1}{n+1}} - \gamma^{\frac{1}{n+1}} \right) + \alpha \left\{ \frac{n}{1+\beta n} \left\{ \frac{n}{1+n\beta+n} \left(t_1^{\frac{1}{n+\beta+1}} - \gamma^{\frac{1}{n+\beta+1}} \right) \right. \right. \right. \right. \\
& \left. \left. \left. - \gamma^{\frac{1}{n+\beta}} (t_1 - \gamma) \right\} - \frac{n\beta\gamma}{1-n+\beta n} \left(\frac{n}{1+n\beta} \left(t_1^{\frac{1}{n+\beta}} - \gamma^{\frac{1}{n+\beta}} \right) - \gamma^{\frac{1}{n-1+\beta}} (t_1 - \gamma) \right) \right\} + \frac{\Phi_1 n^2}{(1+n)(1+2n)} \right. \\
& \left. \left(t_1^{\frac{1}{n+2}} - \gamma^{\frac{1}{n+2}} \right) - \alpha n \left\{ \frac{n}{1+n\beta+n} \left(t_1^{\frac{1}{n+\beta+1}} - \gamma^{\frac{1}{n+\beta+1}} \right) - \frac{n\beta\gamma}{1+n\beta} \left(t_1^{\frac{1}{n+\beta}} - \gamma^{\frac{1}{n+\beta}} \right) \right\} \right. \\
& \left. - \alpha^2 \left\{ \frac{n}{1+\beta n} \left\{ \frac{n}{1+2\beta n+n} \left(t_1^{\frac{1}{n+2\beta+1}} - \gamma^{\frac{1}{n+2\beta+1}} \right) - \frac{n\beta\gamma}{1+2\beta n} \left(t_1^{\frac{1}{n+2\beta}} - \gamma^{\frac{1}{n+2\beta}} \right) - \frac{\gamma^{\frac{1}{n+\beta}}}{\beta+1} (t_1 - \gamma)^{\beta+1} \right\} \right. \right. \\
& \left. \left. - \frac{n\beta\gamma}{1-n+\beta n} \left\{ \frac{n}{1+2\beta n} \left(t_1^{\frac{1}{n+2\beta}} - \gamma^{\frac{1}{n+2\beta}} \right) - \frac{n\beta\gamma}{1+2\beta n-n} \left(t_1^{\frac{1}{n+2\beta-1}} - \gamma^{\frac{1}{n+2\beta-1}} \right) - \frac{\gamma^{\frac{1}{n-1+\beta}}}{\beta+1} (t_1 - \gamma)^{\beta+1} \right\} \right\} \right. \\
& \left. - \frac{\alpha \Phi_1 n}{1+n} \left\{ \frac{n}{1+2n+\beta n} \left(t_1^{\frac{1}{n+2+\beta}} - \gamma^{\frac{1}{n+2+\beta}} \right) - \frac{n\beta\gamma}{1+\beta n+n} \left(t_1^{\frac{1}{n+\beta+1}} - \gamma^{\frac{1}{n+\beta+1}} \right) \right\} - \frac{\Phi_1 n^2}{1+2n} \left(t_1^{\frac{1}{n+2}} - \gamma^{\frac{1}{n+2}} \right) \right. \\
& \left. - \alpha \Phi_1 \left\{ \frac{n}{1+\beta n} \left\{ \frac{n}{1+2n+\beta n} \left(t_1^{\frac{1}{n+2+\beta}} - \gamma^{\frac{1}{n+2+\beta}} \right) - \frac{\gamma^{\frac{1}{n+\beta}}}{2} (t_1^2 - \gamma^2) \right\} - \frac{n\beta\gamma}{1-n+\beta n} \left\{ \frac{n}{1+\beta n+n} \right. \right. \right. \\
& \left. \left. \left(t_1^{\frac{1}{n+\beta+1}} - \gamma^{\frac{1}{n+\beta+1}} \right) - \frac{\gamma^{\frac{1}{n-1+\beta}}}{2} (t_1^2 - \gamma^2) \right\} \right\} - \frac{\Phi_1^2 n^2}{(1+n)(1+3n)} \left(t_1^{\frac{1}{n+3}} - \gamma^{\frac{1}{n+3}} \right) \right] + \tau \left\{ t_2 (t_2 - t_1) - \frac{(t_2^2 - t_1^2)}{2} \right\} \\
& + \frac{\alpha}{\beta+1} \left\{ (t_2 - \gamma)^{\beta+1} (t_2 - t_1) - \frac{(t_2 - \gamma)^{\beta+2}}{\beta+2} + \frac{(t_1 - \gamma)^{\beta+2}}{\beta+2} \right\} + \frac{\Phi_1 t_2^2}{2} (t_2 - t_1) - \frac{\Phi_1}{6} (t_2^3 - t_1^3) \left\{ \right. \\
& \left. + \frac{\Phi_2 \Gamma}{n \Gamma^{\frac{1}{n}}} \left\{ n t_2^{\frac{1}{n}} (t_2 - t_1) - \frac{n^2}{1+n} \left(t_2^{\frac{1}{n+1}} - t_1^{\frac{1}{n+1}} \right) + \alpha \left\{ \frac{n}{n\beta+1} \left\{ t_2^{\frac{1}{n+\beta}} (t_2 - t_1) - \frac{n}{1+\beta n+n} \left(t_2^{\frac{1}{n+\beta+1}} - t_1^{\frac{1}{n+\beta+1}} \right) \right\} \right. \right. \right. \\
& \left. \left. - \frac{\beta\gamma n}{1-n+\beta n} \left\{ t_2^{\frac{1}{n-1+\beta}} (t_2 - t_1) - \frac{n}{1+\beta n} \left(t_2^{\frac{1}{n+\beta}} - t_1^{\frac{1}{n+\beta}} \right) \right\} \right\} + \frac{n\Phi_1}{1+n} \left\{ t_2^{\frac{1}{n+1}} (t_2 - t_1) - \frac{n}{1+2n} \left(t_2^{\frac{1}{n+2}} - t_1^{\frac{1}{n+2}} \right) \right\} \right\} \\
& - \alpha \tau \left\{ \frac{t_2}{\beta+1} \left\{ (t_2 - \gamma)^{\beta+1} - (t_1 - \gamma)^{\beta+1} \right\} - \frac{1}{\beta+1} \left\{ t_2 (t_2 - \gamma)^{\beta+1} - t_1 (t_1 - \gamma)^{\beta+1} - \frac{1}{\beta+2} \left\{ (t_2 - \gamma)^{\beta+2} \right. \right. \right. \\
& \left. \left. - (t_1 - \gamma)^{\beta+2} \right\} + \frac{\alpha}{(\beta+1)^2} \left\{ (t_2 - \gamma)^{\beta+1} \left\{ (t_2 - \gamma)^{\beta+1} - (t_1 - \gamma)^{\beta+1} \right\} - \frac{(t_2 - \gamma)^{2(\beta+1)}}{2} + \frac{(t_1 - \gamma)^{2(\beta+1)}}{2} \right\} \right. \\
& \left. + \frac{\Phi_1}{2} \left\{ \frac{-t_2^2}{\beta+1} (t_1 - \gamma)^{\beta+1} \right\} - \left\{ -\frac{t_1^2}{\beta+1} (t_1 - \gamma)^{\beta+1} - \frac{2}{(\beta+1)(\beta+2)} \left\{ t_2 (t_2 - \gamma)^{\beta+1} - t_1 (t_1 - \gamma)^{\beta+2} \right. \right. \right.
\end{aligned}$$

This implies

$$\begin{aligned}
\frac{\partial K(t_1, t_3, T)}{\partial t_1} &= \frac{C}{T} R + \frac{h}{T} \left[(R - \tau) \left\{ t_1 + \frac{\alpha(t_1 - \gamma)^{\beta+1}}{\beta+1} + \frac{\varphi_1 t_1^2}{2} - \frac{\alpha}{\beta+1} \left\{ (t_1 - \gamma)^\beta (2t_1 - \gamma + t_1 \beta) - (t_1 - \gamma)^{\beta+1} \right\} \right. \right. \\
&\quad \left. \left. - \frac{\alpha^2 (t_1 - \gamma)^{2\beta+1}}{\beta+1} - \frac{\alpha \varphi_1}{2} \left\{ \frac{(t_1 - \gamma)^\beta}{\beta+1} (3t_1^2 - 2t_1 \gamma + t_1^2 \beta) - \frac{2}{(\beta+1)(\beta+2)} \left\{ (t_1 - \gamma)^{\beta+1} \right. \right. \right. \right. \\
&\quad \left. \left. \left. (3t_1 - \gamma + t_1 \beta) - (t_1 - \gamma)^{\beta+2} \right\} \right\} - \varphi_1 t_1^2 - \frac{\alpha \varphi_1}{\beta+1} \left\{ \frac{(t_1 - \gamma)^{\beta+1}}{\beta+2} (3t_1 - \gamma + t_1 \beta) - \frac{(t_1 - \gamma)^{\beta+2}}{\beta+2} \right\} - \frac{\varphi_1^2 t_1^3}{2} \right] \\
&\quad - \frac{\varphi_2 r}{n T^{\frac{1}{n}}} \left[n t_1^{\frac{1}{n}} + \alpha \left\{ \frac{n}{1+\beta n} \left\{ t_1^{\frac{1}{n+\beta}} - \gamma^{\frac{1}{n+\beta}} \right\} - \frac{n \beta \gamma}{1-n+\beta n} \left\{ t_1^{\frac{1}{n+\beta-1}} - \gamma^{\frac{1}{n+\beta-1}} \right\} \right\} + \frac{\varphi_1 n}{1+n} t_1^{\frac{1}{n+1}} \right. \\
&\quad \left. - \alpha n \left\{ t_1^{\frac{1}{n+\beta}} - \beta \gamma t_1^{\frac{1}{n+\beta-1}} \right\} - \alpha^2 \left\{ \frac{n}{1+\beta n} \left\{ t_1^{\frac{1}{n+2\beta}} - \beta \gamma t_1^{\frac{1}{n+2\beta-1}} - \gamma^{\frac{1}{n+\beta}} (t_1 - \gamma)^\beta \right\} - \frac{n \beta \gamma}{1-n+\beta n} \left\{ t_1^{\frac{1}{n+2\beta-1}} \right. \right. \right. \\
&\quad \left. \left. \left. - \beta \gamma t_1^{\frac{1}{n+2\beta-2}} - \gamma^{\frac{1}{n+\beta-1}} (t_1 - \gamma)^\beta \right\} \right\} - \frac{\alpha \varphi_1 n}{1+n} \left\{ t_1^{\frac{1}{n+\beta+1}} - \beta \gamma t_1^{\frac{1}{n+\beta}} \right\} - \varphi_1 n t_1^{\frac{1}{n+1}} - \alpha \varphi_1 \left\{ \frac{n}{1+\beta n} \left\{ t_1^{\frac{1}{n+\beta+1}} \right. \right. \right. \\
&\quad \left. \left. \left. - \gamma^{\frac{1}{n+\beta}} t_1 \right\} - \frac{n \beta \gamma}{1-n+\beta n} \left\{ t_1^{\frac{1}{n+\beta}} - \gamma^{\frac{1}{n+\beta-1}} \right\} \right\} - \frac{\varphi_1^2}{1+n} t_1^{\frac{1}{n+2}} \right\} + \tau \left\{ -t_2 + t_1 + \frac{\alpha}{\beta+1} \left\{ (t_1 - \gamma)^{\beta+1} \right. \right. \\
&\quad \left. \left. - (t_2 - \gamma)^{\beta+1} \right\} - \frac{\varphi_1 t_2^2}{2} + \frac{\varphi_1 t_1^2}{2} \right\} + \frac{\varphi_2 r}{n T^{\frac{1}{n}}} \left[n t_1^{\frac{1}{n}} - n t_2^{\frac{1}{n}} + \alpha \left\{ \frac{n}{n \beta + 1} \left\{ t_1^{\frac{1}{n+\beta}} - t_2^{\frac{1}{n+\beta}} \right\} - \frac{\beta \gamma n}{1-n+\beta n} \right. \right. \\
&\quad \left. \left. \left\{ t_1^{\frac{1}{n-1+\beta}} - t_2^{\frac{1}{n-1+\beta}} \right\} \right\} + \frac{n \varphi_1}{1+n} \left\{ t_1^{\frac{1}{n+1}} - t_2^{\frac{1}{n+1}} \right\} \right] - \tau \alpha \left\{ -t_2 (t_1 - \gamma)^\beta - \frac{1}{\beta+1} \left\{ (t_1 - \gamma)^\beta (2t_1 - \gamma + t_1 \beta) \right. \right. \\
&\quad \left. \left. + (t_1 - \gamma)^{\beta+1} \right\} + \frac{\alpha}{(\beta+1)} \left\{ (t_1 - \gamma)^{2\beta+1} - (t_2 - \gamma)^{\beta+1} (t_1 - \gamma)^\beta \right\} + \frac{\varphi_1}{2} \left\{ -t_2^2 (t_1 - \gamma)^\beta - \left\{ -\frac{1}{\beta+1} (t_1 - \gamma)^\beta \right. \right. \right. \\
&\quad \left. \left. \left. (3t_1^2 - 2t_1 \gamma + t_1^2 \beta) - \frac{2}{(\beta+1)(\beta+2)} \left\{ -(t_1 - \gamma)^{\beta+1} (3t_1 - \gamma + t_1 \beta) + (t_1 - \gamma)^{\beta+2} \right\} \right\} \right\} - \frac{\alpha \varphi_2 r}{n T^{\frac{1}{n}}} \left[n \left\{ t_1^{\frac{1}{n+2\beta}} \right. \right. \\
&\quad \left. \left. - t_2^{\frac{1}{n}} (t_1 - \gamma)^\beta - \beta \gamma t_1^{\frac{1}{n+2\beta-1}} \right\} + \alpha \left\{ \frac{n}{n \beta + 1} \left\{ -t_2^{\frac{1}{n+\beta}} (t_1 - \gamma)^\beta + t_1^{\frac{1}{n+2\beta}} + \beta \gamma t_1^{\frac{1}{n+2\beta-1}} \right\} - \frac{\beta \gamma n}{1-n+\beta n} \right. \right. \\
&\quad \left. \left. \left\{ -t_2^{\frac{1}{n+\beta-1}} (t_1 - \gamma)^\beta + t_1^{\frac{1}{n+2\beta-1}} - \beta \gamma + t_1^{\frac{1}{n+2\beta-2}} \right\} \right\} + \frac{n \varphi_1}{1+n} \left\{ -t_2^{\frac{1}{n+1}} (t_1 - \gamma)^\beta + t_1^{\frac{1}{n+\beta+1}} - \beta \gamma t_1^{\frac{1}{n+\beta}} \right\} \right] \\
&\quad - \varphi_1 \tau \left\{ -t_2 t_1 + t_1^2 + \frac{\alpha}{\beta+1} \left\{ -t_1 (t_2 - \gamma)^{\beta+1} - \frac{1}{\beta+2} \left\{ (t_1 - \gamma)^{\beta+1} (3t_1 - \gamma + t_1 \beta) \right\} - \frac{1}{\beta+2} (t_1 - \gamma)^{\beta+2} \right\} \right\} \\
&\quad + \frac{\varphi_1}{2} \left\{ -t_1 t_2^2 + t_1^3 \right\} - \frac{\varphi_1 \varphi_2 r}{n T^{\frac{1}{n}}} \left[n \left\{ -t_1 t_2^{\frac{1}{n}} + t_1^{\frac{1}{n+1}} \right\} + \alpha \left\{ \frac{n}{n \beta + 1} \left\{ -t_1 t_2^{\frac{1}{n+\beta}} + t_1^{\frac{1}{n+\beta+1}} \right\} - \frac{\beta \gamma n}{1-n+\beta n} \left\{ -t_1 t_2^{\frac{1}{n+\beta-1}} \right. \right. \right.
\end{aligned}$$

$$+ t_1^{\frac{1}{n} + \beta} \left. \right\} + \frac{n\phi_1}{1+n} \left\{ -t_1 t_2^{\frac{1}{n} + 1} + t_1^{\frac{1}{n} + 2} \right\} = 0, \quad (18)$$

The total cost per unit time is to be minimized for obtaining the optimal production scheduling policies. For a given t_1 , $K(t_1, t_3, T)$ is a convex function of t_3 , we obtain the necessary condition which minimizes $K(t_1, t_3)$ with respect to t_1 is

$$\frac{\partial K(t_1, t_3, T)}{\partial t_3} = 0.$$

$$\begin{aligned} \frac{\partial K(t_1, t_3, T)}{\partial t_3} = & \frac{C}{T}(-R) + \frac{h}{T} \left[\tau \left\{ 2xy - t_1 y - xy + \frac{\alpha}{\beta+1} \left\{ x(\beta+1)(x-\gamma)^\beta y + (x-\gamma)^{\beta+1} y - (\beta+1)(x-\gamma)^\beta \right. \right. \right. \\ & \left. \left. \left. y t_1 - (x-\gamma)^{\beta+1} y \right\} + \frac{3\phi_1}{2} x^2 y - t_1 \phi_1 xy - \frac{\phi_1}{2} x^2 y \right\} + \frac{\phi_2 r}{nT^{\frac{1}{n}}} \left\{ n(1+n)x^{\frac{1}{n}} y - t_1 x^{\frac{1}{n}-1} y - nx^{\frac{1}{n}} y \right. \right. \\ & + \alpha \left\{ \frac{n}{n\beta+1} \left\{ \left(\frac{1}{n} + \beta + 1 \right) x^{\frac{1}{n} + \beta} y - t_1 y \left(\frac{1}{n} + \beta \right) x^{\frac{1}{n} + \beta - 1} - x^{\frac{1}{n} + \beta} y \right\} - \frac{\beta \gamma n}{1-n+\beta n} \left\{ y \left(\frac{1}{n} + \beta \right) x^{\frac{1}{n} + \beta - 1} \right. \right. \\ & \left. \left. - t_1 y \left(\frac{1}{n} - 1 + \beta \right) x^{\frac{1}{n} + \beta - 2} - y x^{\frac{1}{n} + \beta - 1} \right\} \right\} + \frac{n\phi_1}{1+n} \left\{ y \left(\frac{1}{n} + 2 \right) x^{\frac{1}{n} + 1} - t_1 y \left(\frac{1}{n} + 1 \right) x^{\frac{1}{n}} - x^{\frac{1}{n} + 1} y \right\} \left. \right\} \\ & - \alpha \tau \left\{ \frac{y}{\beta+1} \left\{ (t_1 - \gamma)^{\beta+1} + (x - \gamma)^{\beta+1} \right\} + \frac{\alpha y}{(\beta+1)} \left\{ 2(x - \gamma)^{2\beta+1} - (t_1 - \gamma)^{\beta+1} (x - \gamma)^\beta - (x - \gamma)^{2\beta+1} \right\} \right. \\ & + \frac{\phi_1 xy}{(\beta+1)} \left\{ - (t_1 - \gamma)^{\beta+1} + (x - \gamma)^{\beta+1} \right\} - \frac{\alpha \phi_2 r}{nT^{\frac{1}{n}}} \left\{ n \left\{ \frac{1}{\beta+1} \left\{ x^{\frac{1}{n}} y (\beta+1)(x-\gamma)^{\beta+1} + (x-\gamma)^{\beta+1} \right. \right. \right. \\ & \left. \left. \left. \frac{x^{\frac{1}{n}-1}}{n} y - (t_1 - \gamma)^{\beta+1} y \frac{x^{\frac{1}{n}-1}}{n} \right\} - y x^{\frac{1}{n} + \beta} + y \beta \gamma x^{\frac{1}{n} + \beta - 1} \right\} + \alpha \left\{ \frac{n}{n\beta+1} \left\{ \frac{1}{\beta+1} \left\{ x^{\frac{1}{n} + \beta} (\beta+1)(x-\gamma)^\beta y \right. \right. \right. \right. \\ & \left. \left. \left. + (x-\gamma)^{\beta+1} \left(\frac{1}{n} + \beta \right) x^{\frac{1}{n} + \beta - 1} y - (t_1 - \gamma)^{\beta+1} \left(\frac{1}{n} + \beta \right) x^{\frac{1}{n} + \beta - 1} y \right\} - x^{\frac{1}{n} + 2\beta} y + \beta \gamma x^{\frac{1}{n} + \beta - 1} y \right\} - \frac{\beta \gamma n}{1-n+\beta n} \right. \\ & \left. \left\{ \frac{y x^{\frac{1}{n} + \beta - 1}}{\beta+1} \left\{ (\beta+1)(x-\gamma)^\beta + (x-\gamma)^{\beta+1} \left(\frac{1}{n} + \beta - 1 \right) - (t_1 - \gamma)^{\beta+1} \left(\frac{1}{n} + \beta - 1 \right) \frac{1}{x} \right\} - y x^{\frac{1}{n} + 2\beta - 1} \right. \right. \\ & \left. \left. + \beta \gamma y x^{\frac{1}{n} + 2\beta - 2} \right\} \right\} + \frac{n\phi_1}{1+n} \left\{ \frac{1}{\beta+1} \left\{ y x^{\frac{1}{n} + 1} (\beta+1)(x-\gamma)^\beta + (x-\gamma)^{\beta+1} \left(\frac{1}{n} + 1 \right) y x^{\frac{1}{n}} - (t_1 - \gamma)^{\beta+1} \right. \right. \\ & \left. \left. \left(\frac{1}{n} + 1 \right) y x^{\frac{1}{n}} \right\} - y x^{\frac{1}{n} + \beta + 1} + \beta \gamma y x^{\frac{1}{n} + \beta} \right\} - \phi_1 \tau \left\{ \frac{3}{2} x^2 y - \frac{t_1^2 y}{2} - x^2 y + \frac{\alpha}{\beta+1} \left\{ \frac{1}{2} \left\{ x^2 y (\beta+1)(x-\gamma)^\beta \right. \right. \right. \\ & \left. \left. \left. + 2xy(\beta+1)(x-\gamma)^{\beta+1} - t_1^2 y(\beta+1)(x-\gamma)^\beta \right\} - x(x-\gamma)^{\beta+1} \right\} + \frac{\phi_1}{2} \left\{ 2x^3 y - t_1^2 xy - x^3 y \right\} \right. \\ & \left. - \frac{\phi_1 \phi_2 r}{nT^{\frac{1}{n}}} \left\{ ny \left\{ \frac{1}{2} \left(\frac{1}{n} + 2 \right) x^{\frac{1}{n}} - \frac{t_1^2}{2n} x^{\frac{1}{n}-1} - x^{\frac{1}{n} + 1} \right\} + \alpha \left\{ \frac{n}{n\beta+1} \left\{ \frac{x^{\frac{1}{n} + \beta} y}{2} \left\{ \left(\frac{1}{n} + 2 + \beta \right) x - \frac{t_1^2}{x} \left(\frac{1}{n} + \beta \right) \right. \right. \right. \right. \right. \right. \end{aligned}$$

$$\begin{aligned}
 & -x^{\frac{1}{n}+\beta+1}y \left\{ -\frac{\beta\gamma n x^{\frac{1}{n}+\beta}y}{1-n+\beta n} \left[\frac{1}{2} \left\{ \left(\frac{1}{n} + \beta - 1 \right) - \left(\frac{1}{n} + \beta - 1 \right) \frac{t_1^2}{x^2} \right\} - 1 \right] \right\} + \frac{n\phi_1 x^{\frac{1}{n}}y}{1+n} \left\{ \frac{1}{2} \left[\left(\frac{1}{n} + 3 \right) x^2 \right. \right. \\
 & \left. \left. - t_1^2 \left(\frac{1}{n} + 1 \right) \right] - x^2 \right\} \left. \right\} + \frac{\pi}{T} \left[\tau \left\{ t_3 + \frac{R^2 t_3}{\tau^2} - \frac{R(R-\tau)\Gamma}{\tau^2} - \frac{2Rt_3}{\tau} + \frac{(R-\tau)\Gamma}{\tau} \right\} + (R-\tau)(t_3 - T) \right] \\
 & \text{where } x = \frac{1}{\tau} \{ Rt_3 - (R-\tau)\Gamma \} \text{ and } y = \frac{R}{\tau}, \tag{19}
 \end{aligned}$$

Solving the equations (18) and (19), using numerical methods, we obtain the optimal production down time t_1 as t_1^* and t_3 as t_3^* . Substituting t_3^* in equation (11), t_1^* and t_3^* in equation (12), we obtain t_2^* and optimal production quantity Q as Q^* respectively.

and the records verified to decide the values of various parameters.

Let the inventory system with shortages has the following parameter values:

$R = 30$ units $r = 10$ units $\tau = 12$ units $h = \text{Rs.}10/-$
 $C = \text{Rs.}10/-$ $A = \text{Rs.}75/-$
 $n = 3$ $T = 4$ months $\pi = \text{Rs.}15/-$

4. Case Study

Consider the case of deriving the economic production quantity and other optimal policies for a pickle-manufacturing unit. Here, the product is deteriorating type and has random lifetime and assumed to follow a three-parameter Weibull distribution. Discussions held with the personnel connected with the production and marketing

For the assigned values of deterioration parameters $(\alpha, \beta, \gamma) = (0.1, 1.0, 0.01)$ and demand parameters $(\phi_1, \phi_2) = (0.1, 0.1)$, the optimal values of time (t_1^*), production quantity (Q^*), total system cost (K^*) have been determined. The values of above parameters are varied further to observe the trend in optimal policies and the results obtained are shown in Table 1.

Table 1. Effect of demand and deterioration parameters on optimal policies – Demand is function of on hand inventory and time - with shortages

PARAMETERS													OPTIMAL POLICIES				
α	β	γ	ϕ_1	ϕ_2	τ	r	R	h	C	π	n	A	t_1^*	t_2^*	t_3^*	Q^*	K^*
0.10 0.08 0.09 0.11 0.12	1.0	0.01	0.1	0.1	12	10	30	10	10	15	3	75	0.173	2.383	3.353	24.60	196.487
													0.137	2.373	3.370	23.77	197.668
													0.103	2.363	3.386	22.94	198.706
													0.071	2.356	3.402	22.07	199.627
													0.042	2.345	3.416	21.28	200.402
	1.4												0.205	2.293	3.317	26.64	204.124
	1.8												0.229	2.205	3.282	28.41	210.941
	2.2												0.246	2.125	3.250	29.88	217.104
	2.6												0.259	2.053	3.221	31.14	222.720
		0.00											0.449	2.428	3.371	32.34	175.151
		0.04											0.356	2.413	3.365	29.73	182.911
		0.08											0.264	2.398	3.359	27.15	190.019
		0.12											0.084	2.370	3.348	22.08	202.309
			0.12										0.207	2.455	3.382	24.75	198.721
			0.14										0.239	2.520	3.408	24.93	200.780
			0.16										0.268	2.580	3.432	25.08	202.671
			0.18										0.295	2.637	3.455	25.20	204.398
				0.12									0.175	2.385	3.354	24.63	196.344
				0.14									0.176	2.387	3.355	24.63	196.221
				0.16									0.177	2.390	3.356	24.63	196.143
				0.18									0.178	2.390	3.356	24.66	196.064
					14								0.173	2.383	3.353	24.60	197.737
					16								0.173	2.383	3.353	24.60	198.987
					18								0.173	2.383	3.353	24.60	200.237
					20								0.173	2.383	3.353	24.60	201.487
						12							0.179	2.385	3.354	24.75	196.664
						14							0.185	2.387	3.355	24.90	196.839
						16							0.191	2.390	3.356	25.05	197.041
						18							0.197	2.390	3.356	25.23	197.226
							31						0.137	2.373	3.370	23.77	197.668
							32						0.103	2.363	3.386	22.94	198.706
							33						0.071	2.356	3.402	22.07	199.627
							34						0.042	2.345	3.416	21.28	200.402

								11					0.205	2.293	3.317	26.64	204.124
								12					0.229	2.205	3.282	28.41	210.941
								13					0.246	2.125	3.250	29.88	217.104
								14					0.259	2.053	3.221	31.14	222.720
									7				0.449	2.428	3.371	32.34	175.151
									8				0.356	2.413	3.365	29.73	182.911
									9				0.264	2.398	3.359	27.15	190.019
									11				0.084	2.370	3.348	22.08	202.309
										16			0.207	2.455	3.382	24.75	198.721
										17			0.239	2.520	3.408	24.93	200.780
										18			0.268	2.580	3.432	25.08	202.671
										19			0.295	2.637	3.455	25.20	204.398
											3.5		0.175	2.385	3.354	24.63	196.344
											4.0		0.176	2.387	3.355	24.63	196.221
											4.5		0.177	2.390	3.356	24.63	196.143
											5.0		0.178	2.390	3.356	24.66	196.064
												80	0.173	2.383	3.353	24.60	197.737
												85	0.173	2.383	3.353	24.60	198.987
												90	0.173	2.383	3.353	24.60	200.237
												95	0.173	2.383	3.353	24.60	201.487

The increase in deterioration parameter α has shown decreasing trend in all optimal values of time (t_1^* , t_2^* , t_3^*) and production quantity (Q) viz., (0.137 to 0.042, 2.373 to 2.345, 3.370 to 3.416 months) and (23.77 to 21.28 units) but increase in total cost (K^* , Rs.197.668 to 200.402) respectively. Increase in β results in increase in t_1^* (0.173 to 0.259 months), Q^* (24.60 to 31.14 units) and K^* (Rs.196.487 to 222.720) respectively. Increase in γ results decrease in all optimal policies. Increase in demand parameter (Φ_1) and shortage cost (π) has shown increase in all the optimal policies. The increase in production rate (R, 30 to 34 units) and unit cost (C, Rs.7 to 11) has decreasing effect on all optimal values of time (t_1^* , t_2^* , t_3^*), production quantity (Q^*) i.e. (t_1^* , t_2^* , t_3^* = 0.173 to 0.042, 2.383 to 2.345, 3.353 to 3.416, 0.449 to 0.084, 2.428 to 2.370, 3.371 to 3.348 months respectively) and (Q^* , 24.60 to 21.28, 32.34 to 22.08 units) respectively. However, they have shown increasing trend in total cost (K^* , Rs.196.487 to 200.402, Rs.175.151 to 202.309).

5. SENSITIVITY ANALYSIS

A sensitivity analysis has been carried out to explore the effect on the optimal policies by varying the value of each parameter at a time and all parameters together. The results obtained by changing parameters by -15%, -10%, -5%, +5%, +10% and +15% are tabulated in Table 2.

It is noticed that the increase in deterioration parameters (α, β) has increasing trend in optimal production downtime, t_1^* (0.173 to 0.193, 0.173 to 0.177 months) but mixed response in production uptime, t_3^* (3.353 to 3.360, 3.353 to 3.349 months) respectively. The increase in shortage cost, π (from -15% to +15%) has

increasing effect on optimal times (t_1^* , 0.087 to 0.246 and t_3^* , 3.281 to 3.414 months), quantity Q^* (24.18 to 24.96 units) and total system cost K^* (Rs.190.6 to 201.268).

The graphical representation of the parameters variation effect on optimal policies is shown in Fig.2

6. CONCLUSION

- This model considers the delayed nature of decay by considering the location parameter in the decay distribution.
- This model includes increasing, decreasing and constant rates of decay which is a more general type of distribution for decay.
- In this model, the demand function considered includes a spectra of demand patterns like time dependent demand, stock dependent demand, constant rate of demand, both time and on-hand inventory dependent demand. Hence, this model can be viewed as a generalized EPQ, which serves several types of demands.
- This model is also can be generalized by assuming that product under consideration follows a general distribution like Pearson type distribution which includes Weibull as a particular case. Since, it is capable of providing optimal production schedules it can be commercialized by developing user-friendly software package which serve as robust model for production scheduling and inventory control. '

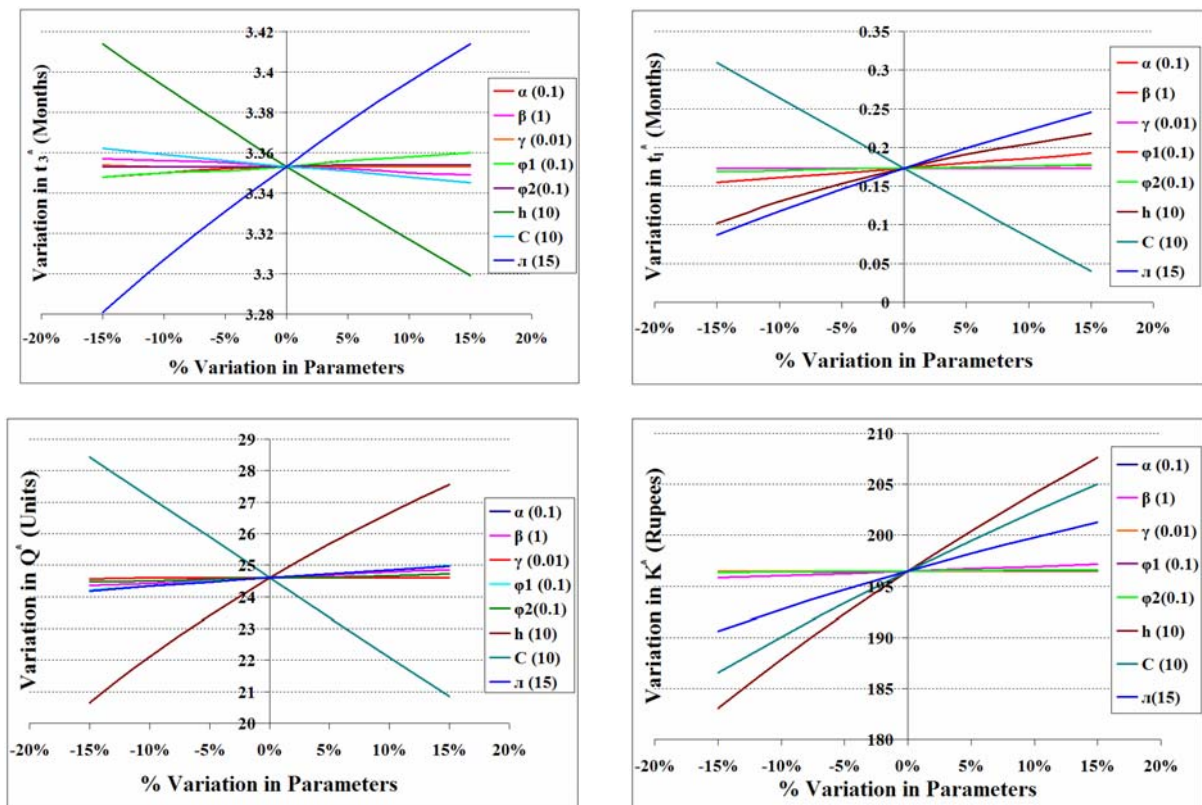
We also reduced the model to without shortages (see Appendix) by formulating the governing equations and obtaining the solutions.

Table-2: Sensitivity analysis of Optimal Policies -Demand is function of on hand inventory and time – with shortages

Parameters	Optimal Policies	- 15 %	- 10 %	- 5 %	0	+ 5 %	+ 10 %	+ 15 %
α (0.1)	t_1^*	0.155	0.161	0.167	0.173	0.180	0.186	0.193
	t_3^*	3.348	3.350	3.352	3.353	3.356	3.358	3.360
	Q^*	24.21	24.33	24.45	24.60	24.72	24.84	24.99
	K^*	196.335	196.389	196.435	196.487	196.502	196.523	201.535
β (1)	t_1^*	0.169	0.170	0.172	0.173	0.175	0.176	0.177
	t_3^*	3.357	3.356	3.355	3.353	3.352	3.350	3.349
	Q^*	24.36	24.42	24.51	24.60	24.69	24.78	24.84
	K^*	195.822	196.029	196.235	196.487	196.695	196.919	197.158
γ (0.01)	t_1^*	0.173	0.173	0.173	0.173	0.173	0.173	0.173
	t_3^*	3.354	3.353	3.353	3.353	3.353	3.353	3.353
	Q^*	24.57	24.60	24.60	24.60	24.60	24.60	24.60
	K^*	196.467	196.484	196.485	196.487	196.489	196.491	196.493
ϕ_1 (0.1)	t_1^*	0.155	0.161	0.167	0.173	0.180	0.186	0.193
	t_3^*	3.348	3.350	3.351	3.353	3.356	3.358	3.360
	Q^*	24.21	24.33	24.48	24.60	24.72	24.84	24.99
	K^*	196.340	196.393	196.422	196.487	196.500	196.519	196.529
ϕ_2 (0.1)	t_1^*	0.169	0.170	0.172	0.173	0.175	0.176	0.178
	t_3^*	3.353	3.353	3.353	3.353	3.354	3.354	3.354
	Q^*	24.48	24.51	24.57	24.60	24.63	24.66	24.72
	K^*	196.342	196.390	196.439	196.487	196.521	196.569	196.617
τ (12)	t_1^*	0.010	0.064	0.119	0.173	0.228	0.283	0.339
	t_3^*	3.435	3.407	3.380	3.353	3.328	3.303	3.279
	Q^*	17.25	19.71	22.17	24.60	27	29.4	31.8
	K^*	174.099	181.903	189.339	196.487	203.264	209.733	215.887
r (10)	t_1^*	0.169	0.17	0.172	0.173	0.175	0.176	0.178
	t_3^*	3.353	3.353	3.353	3.353	3.354	3.354	3.354
	Q^*	24.48	24.51	24.57	24.60	24.63	24.66	24.72
	K^*	196.342	196.390	196.439	196.487	196.521	196.569	196.617
R (30)	t_1^*	0.374	0.299	0.233	0.173	0.12	0.071	0.027
	t_3^*	3.268	3.298	3.327	3.353	3.378	3.402	3.423
	Q^*	28.20	27.02	25.82	24.60	23.373	22.07	20.83
	K^*	189.030	191.972	194.423	196.487	198.184	199.627	200.767
h (10)	t_1^*	0.102	0.130	0.153	0.173	0.191	0.205	0.218
	t_3^*	3.414	3.393	3.373	3.353	3.335	3.317	3.299
	Q^*	20.64	22.11	23.4	24.60	25.68	26.64	27.57
	K^*	183.086	187.832	192.312	196.487	198.184	199.627	200.767
C (10)	t_1^*	0.310	0.264	0.219	0.173	0.129	0.084	0.04
	t_3^*	3.362	3.359	3.356	3.353	3.351	3.348	3.345
	Q^*	28.44	27.15	25.89	24.60	23.34	22.08	20.85
	K^*	186.533	190.019	193.318	196.487	199.453	202.309	205.010
π (15)	t_1^*	0.087	0.118	0.146	0.173	0.199	0.223	0.246
	t_3^*	3.281	3.307	3.331	3.353	3.375	3.395	3.414
	Q^*	24.18	24.33	24.45	24.60	24.72	24.84	24.96
	K^*	190.600	192.704	194.662	196.487	198.193	199.788	201.268
n (3)	t_1^*	0.172	0.172	0.173	0.173	0.174	0.174	0.175
	t_3^*	3.352	3.353	3.353	3.353	3.354	3.354	3.358

	Q^*	24.60	24.57	24.60	24.60	24.60	24.60	24.63
	K^*	196.608	196.576	196.530	196.487	196.432	196.393	196.356
A(75)	t_1^*	0.173	0.173	0.173	0.173	0.173	0.173	0.173
	t_3^*	3.353	3.353	3.353	3.353	3.353	3.353	3.353
	Q^*	24.60	24.60	24.60	24.60	24.60	24.60	24.60
	K^*	193.675	194.612	195.550	196.487	197.425	198.362	199.300
All	t_1^*	0.13	0.144	0.158	0.173	0.19	0.208	.227
	t_3^*	3.347	3.349	3.351	3.353	3.357	3.361	3.367
	Q^*	19.967	21.465	23	24.60	26.239	27.951	29.67
	K^*	143.615	160.179	177.915	196.487	215.954	236.298	257.615

Fig.2. Graphical representation of sensitivity analysis of important parameters –with shortages



Appendix

II (Without Shortages)

In this section, we consider the production level inventory model in which shortages are not allowed. The production starts at time $t = 0$, when the stock is zero and reaches to a maximum inventory level at time $t = t_1$. The time interval is divided into two non-overlapping intervals $(0, \gamma)$ and (γ, t_1) . During the interval $(0, \gamma)$, the produced

items partly meet the demand and during interval (γ, t_1) , the produced items are partly consumed due to the demand and deterioration and excess items are stored. The production is stopped at time $t = t_1$ and the stock level is allowed to reduce gradually due to the demand and deterioration and at time $t = t_2$, the inventory becomes zero. At this time, the production starts again and the cycle repeats thereafter. The inventory model explained above is shown in Fig.3.

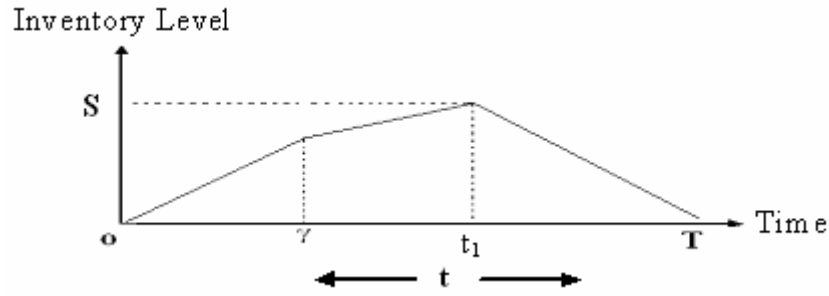


Fig.3 The inventory system – without shortages

Let $I(t)$ denote the inventory level of the system at time t ($0 \leq t \leq T$), then the differential equations governing the instantaneous state of inventory $I(t)$ at any time t are given by

$$\frac{d}{dt} I(t) = R - \left\{ \tau + \phi_1 I(t) + \phi_2 \frac{rt^{\frac{1}{n}-1}}{nT^{\frac{1}{n}}} \right\}, \quad 0 \leq t \leq \gamma \tag{1}$$

$$\frac{d}{dt} I(t) + \alpha\beta(t-\gamma)^{\beta-1} I(t) = R - \left\{ \tau + \phi_1 I(t) + \phi_2 \frac{rt^{\frac{1}{n}-1}}{nT^{\frac{1}{n}}} \right\}, \quad \gamma \leq t \leq t_1 \tag{2}$$

$$\frac{d}{dt} I(t) + \alpha\beta(t-\gamma)^{\beta-1} I(t) = - \left\{ \tau + \phi_1 I(t) + \phi_2 \frac{rt^{\frac{1}{n}-1}}{nT^{\frac{1}{n}}} \right\}, \quad t_1 \leq t \leq T \tag{3}$$

with the boundary conditions $I(0) = 0$ and $I(T) = 0$.

By solving the equations (1), (2) and (3) and using boundary conditions, we obtain the instantaneous state of inventory at any given time t , during the interval $(0, \gamma)$ is

$$I(t) = e^{-\phi_1 t} \int_0^t \left[R - \left\{ \tau + \phi_2 \frac{ru^{\frac{1}{n}-1}}{nT^{\frac{1}{n}}} \right\} \right] e^{\phi_1 u} du, \quad 0 \leq t \leq \gamma \tag{4}$$

The instantaneous state of inventory at any time t , during the interval (γ, t_1) is

$$I(t) = e^{-\{\alpha(t-\gamma)^\beta + \phi_1 t\}} \left[\int_\gamma^t \left[R - \left\{ \tau + \phi_2 \frac{ru^{\frac{1}{n}-1}}{nT^{\frac{1}{n}}} \right\} \right] e^{\alpha(u-\gamma)^\beta + \phi_1 u} du + \int_0^\gamma \left[R - \left\{ \tau + \phi_2 \frac{ru^{\frac{1}{n}-1}}{nT^{\frac{1}{n}}} \right\} \right] e^{\phi_1 u} du \right], \quad \gamma \leq t \leq t_1 \tag{5}$$

Since the production is stopped after reaching maximum inventory level, at any time t during the interval (t_1, T) is

$$I(t) = e^{-\{\alpha(t-\gamma)^\beta + \phi_1 t\}} \left[\int_t^T \left\{ \tau + \phi_2 \frac{ru^{\frac{1}{n}-1}}{nT^{\frac{1}{n}}} \right\} e^{\alpha(u-\gamma)^\beta + \phi_1 u} du \right], \quad t_1 \leq t \leq T \tag{6}$$

The production quantity during the cycle time $(0, T)$ is the production rate (R) multiplied by time period of production (t_1) and is given by

$$Q = R t_1 \tag{7}$$

The total cost per unit time $K(t_1, T)$ is the sum of the set up cost per unit time, purchasing cost per unit time and holding cost per unit time and shortage cost per unit time i.e.,

$$K(t_1, T) = \frac{A}{T} + \frac{C}{T} Q + \frac{h}{T} \left[\int_0^\gamma I(t) dt + \int_\gamma^{t_1} I(t) dt + \int_{t_1}^T I(t) dt \right], \tag{8}$$

By substituting the values for $I(t)$ and Q from the equations (4),(5),(6) and (7) in equation (8), we get

$$\begin{aligned}
 K(t_1, T) = & \frac{A}{T} + \frac{C}{T} R t_1 + \frac{h}{T} \left[\int_0^\gamma e^{-\phi_1 t} \int_0^t \left[R - \left\{ \tau + \phi_2 \frac{r u^{\frac{1}{n}-1}}{n T^{\frac{1}{n}}} \right\} \right] e^{\phi_1 u} du \right. \\
 & + \int_\gamma^{t_1} e^{-\{\alpha(t-\gamma)^\beta + \phi_1 t\}} \left[\int_\gamma^t \left[R - \left\{ \tau + \phi_2 \frac{r u^{\frac{1}{n}-1}}{n T^{\frac{1}{n}}} \right\} \right] e^{\alpha(u-\gamma)^\beta + \phi_1 u} du + \int_0^\gamma \left[R - \left\{ \tau + \phi_2 \frac{r u^{\frac{1}{n}-1}}{n T^{\frac{1}{n}}} \right\} \right] e^{\phi_1 u} du \right. \\
 & \left. \left. + \int_{t_1}^T e^{-\{\alpha(t-\gamma)^\beta + \phi_1 t\}} \left[\int_t^T \left\{ \tau + \phi_2 \frac{r u^{\frac{1}{n}-1}}{n T^{\frac{1}{n}}} \right\} e^{\alpha(u-\gamma)^\beta + \phi_1 u} du \right] \right] \right], \tag{9}
 \end{aligned}$$

The above equation was simplified similar fashion as done for shortages model.

By minimizing the total cost per unit time with respect to t_1 , we can obtain the optimal production start up time t_1 and the optimal economic production quantity Q . Since $K(t_1, T)$ is a convex function of t_1 for a given T , we obtain the necessary condition, which minimizes $K(t_1, T)$ is $\frac{\partial K(t_1, T)}{\partial t_1} = 0$.

Solving the above non- linear equation of for t_1 , by using numerical methods, we can obtain the optimal value

of t_1 as t_1^* . Substituting t_1^* in equation (7) we can obtain the optimal production quantity Q as $Q^* = R t_1^*$.

The results and the pictorial / graphical representations are presented in Table-3, Table-4, Figure- 3 and Figure-4.

7. Acknowledgements

The authors are very much thankful to the editor and anonymous referees for their valuable suggestions and comments, which contributed to the improvement of the paper to the present level.

Table-3: Effect of demand and deterioration parameters on optimal policies - Demand is function of on hand inventory and time – without shortages

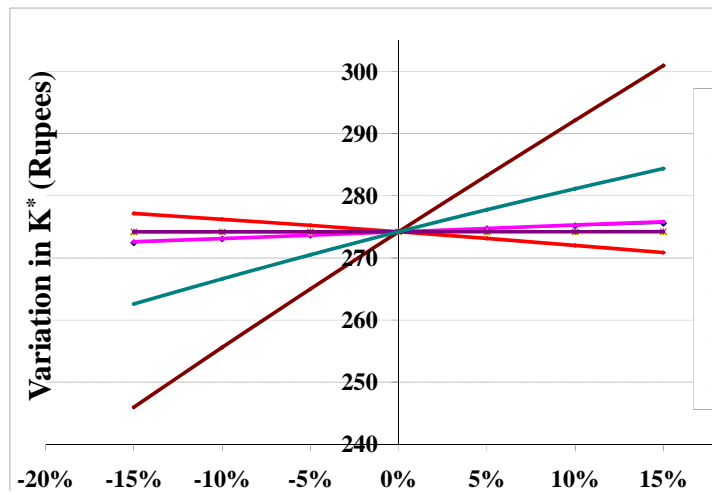
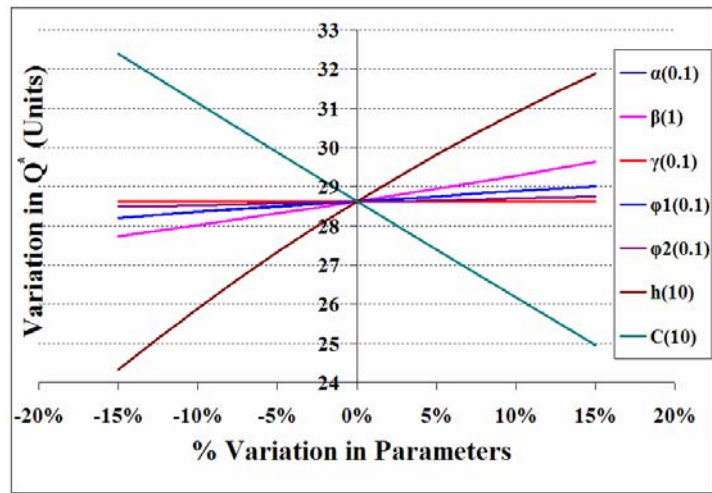
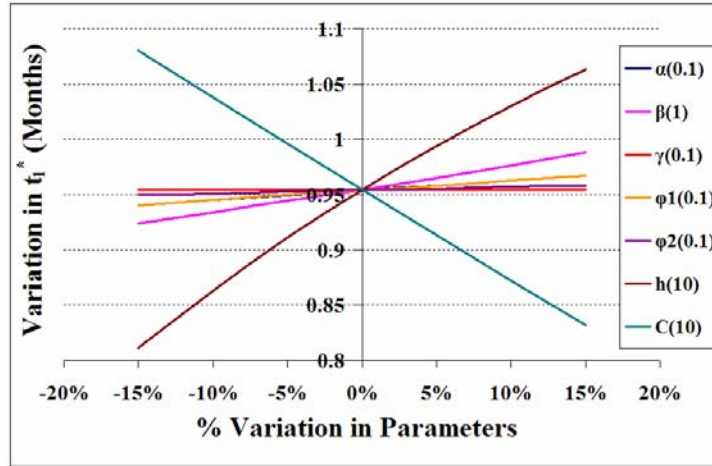
PARAMETERS												OPTIMAL POLICIES		
α	β	γ	ϕ_1	ϕ_2	τ	r	R	h	C	n	A	t_1^*	Q^*	K^*
0.10	1.0	.01	0.10	0.10	12	10	30	10	10	3	75	0.954	28.62	274.210
0.08												0.935	28.05	271.756
0.09												0.945	28.35	273.074
0.11												0.963	28.89	275.166
0.12												0.971	29.13	275.942
	1.4											1.053	31.59	278.026
	1.8											1.186	35.58	276.020
	2.2											1.354	40.62	251.760
	2.6											1.530	45.90	160.750
		0.00										0.953	28.59	274.230
		0.04										0.956	28.68	273.960
		0.08										0.958	28.74	273.650
		0.12										0.960	28.80	273.350
			0.12									0.971	29.13	269.650
			0.14									0.985	29.55	264.380
			0.16									0.996	29.88	258.410
			0.18									1.006	30.18	251.740
				0.12								0.959	28.77	274.240
				0.14								0.965	28.95	274.260
				0.16								0.970	29.10	274.270
				0.18								0.975	29.25	274.290
					14							1.197	35.91	296.350
					16							1.426	42.78	313.100
					18							1.642	49.26	324.940
					20							1.848	55.44	332.250
						12						0.959	28.77	274.240
						14						0.965	28.95	274.260
						16						0.970	29.10	274.270
						18						0.975	29.25	274.290
							31					0.954	28.62	274.210
							32					0.905	28.05	277.600
							33					0.858	27.46	280.760
							34					0.813	26.83	283.710

											0.771	26.21	286.470	
								11			1.030	30.90	292.200	
								12			1.094	32.82	309.690	
								13			1.150	34.50	326.780	
								14			1.198	35.94	343.570	
									7		1.211	36.33	249.447	
									8		1.123	33.69	258.373	
									9		1.038	31.14	266.620	
									11		0.872	26.16	281.159	
										3.5	0.954	28.62	273.951	
										4.0	0.953	28.59	273.744	
										4.5	0.953	28.59	273.575	
										5.0	0.953	28.59	273.434	
											80	0.954	28.62	275.460
											85	0.954	28.62	276.710
											90	0.954	28.62	277.960
											95	0.954	28.62	279.210

Tab-4: Sensitivity analysis of Optimal Policies - Demand is function of on hand inventory and time – without shortages

Parameters	Optimal Policies	-15%	-10%	-5%	0	+5%	+10%	+15%
α (0.1)	t_1^*	0.940	0.945	0.949	0.954	0.958	0.963	0.967
	Q^*	28.2	28.35	28.47	28.62	28.74	28.89	29.01
	K^*	272.438	273.074	273.666	274.210	274.711	275.166	275.576
β (1.0)	t_1^*	0.924	0.934	0.944	0.954	0.965	0.976	0.988
	Q^*	27.72	28.02	28.32	28.62	28.95	29.28	29.64
	K^*	272.600	273.126	273.664	274.210	274.758	275.302	275.835
γ (0.1)	t_1^*	0.954	0.954	0.954	0.954	0.954	0.954	0.954
	Q^*	28.62	28.62	28.62	28.62	28.62	28.62	28.62
	K^*	274.223	274.219	274.215	274.210	274.206	274.202	274.198
ϕ_1 (0.1)	t_1^*	0.940	0.945	0.950	0.954	0.958	0.963	0.967
	Q^*	28.20	28.35	28.50	28.62	28.74	28.89	29.01
	K^*	277.161	276.223	275.239	274.210	273.137	272.018	270.855
ϕ_2 (0.1)	t_1^*	0.950	0.951	0.953	0.954	0.955	0.957	0.958
	Q^*	28.50	28.53	28.59	28.62	28.65	28.71	28.74
	K^*	274.191	274.198	274.204	274.210	274.217	274.222	274.229
τ (12)	t_1^*	0.723	0.802	0.878	0.954	1.028	1.101	1.173
	Q^*	21.69	24.06	26.34	28.62	30.84	33.03	35.19
	K^*	249.224	258.113	266.437	274.210	281.451	288.173	294.391
r (10)	t_1^*	0.95	0.951	0.953	0.954	0.955	0.957	0.958
	Q^*	28.50	28.53	28.59	28.62	28.65	28.71	28.74
	K^*	274.191	274.198	274.204	274.210	274.217	274.222	274.229
R (30)	t_1^*	1.215	1.12	1.034	0.954	0.881	0.813	0.75
	Q^*	30.983	30.24	29.469	28.62	27.752	26.829	25.875
	K^*	255.597	262.484	268.659	274.210	279.207	283.712	287.778
h (10)	t_1^*	0.811	0.863	0.911	0.954	0.994	1.03	1.063
	Q^*	24.33	25.89	27.33	28.62	29.82	30.9	31.89
	K^*	245.954	255.578	264.986	274.210	283.273	292.197	300.997
C (10)	t_1^*	1.08	1.038	0.996	0.954	0.913	0.872	0.832
	Q^*	32.4	31.14	29.88	28.62	27.39	26.16	24.96
	K^*	262.581	266.620	270.496	274.210	277.763	281.159	284.397
n (3)	t_1^*	0.955	0.954	0.954	0.954	0.954	0.954	0.954
	Q^*	28.65	28.62	28.62	28.62	28.62	28.62	28.62
	K^*	274.506	274.400	274.302	274.210	274.126	274.047	273.974
A (75)	t_1^*	0.954	0.954	0.954	0.954	0.954	0.954	0.954
	Q^*	28.62	28.62	28.62	28.62	28.62	28.62	28.62
	K^*	271.398	272.335	273.273	274.210	275.148	276.085	277.023
All	t_1^*	0.893	0.913	0.933	0.954	0.975	0.996	1.017
	Q^*	22.772	24.651	26.591	28.62	30.712	32.868	35.086
	K^*	199.780	223.449	248.292	274.210	301.078	328.731	356.961

Fig. 4: Graphical representation of sensitivity analysis of important parameters- without shortages



References

- [1] S. Nahamias, "Perishable inventory theory: A review". *Opsearch*, Vol. 30, No.4, 1982, 680-708.
- [2] F. Raafat, "Survey of literature on continuously deteriorating inventory models". *Journal of Operation Research Society*, Vol. 42, No.5, 1991, 27-37.
- [3] S.K. Goyal, B. Giri, "Recent trends in modeling of deteriorating inventory". *European Journal of Operational Research*, Vol. 134, No.1, 2001, 1- 16.
- [4] M.A. Cohen, "Analysis of single critical number ordering policies for Perishable inventories". *Opsearch*, Vol. 24, 1976, 726-741.
- [5] S.P. Aggarwal, "A note on an order level inventory model for a system with constant rate of deterioration". *Opsearch*, Vol. 15, No.4, 1978, 184-187.
- [6] U. Dave, Y.K. Shah, "A probabilistic inventory model for deteriorating items with lead time equal to one scheduling period". *European Journal of Operational Research*, Vol.9, No.3, 1982, 281-285.
- [7] M. Pal, "An inventory model for deteriorating items when demand is random", *Calcutta Statistic Association Bulletin*, Vol.39, 1990, 201-207.
- [8] S. Kalpakham, K.P. Sapna, "A lost sales (S-1, s) perishable inventory system with renewal demand". *Naval Research Logistics*, Vol. 43, 1996, 129 – 142.
- [9] B.C. Giri, K.S. Chaudhuri, "Deterministic models of perishable inventory with stock - dependent demand and non-linear holding cost". *European Journal of Operational Research*, Vol.105, 1998, 467-474.
- [10] P.R. Tadikamalla, "An EOQ inventory model for items with gamma distributed deterioration". *AIIE Transactions*, Vol. 10, No.1, 1978, 100-103.
- [11] R.P. Covert, G.C. Philip, "An EOQ model for items with Weibull distribution deterioration". *AIIE Transactions*, Vol.5, 1973, 323 – 326.
- [12] G.C. Philip, "A generalized EOQ model for items with Weibull distribution deterioration, *AIIE Transactions*, Vol. 6, 1974, 159-162.
- [13] S.K. Goyal, B. Giri, "Recent trends in modeling of deteriorating inventory". *European Journal of Operational Research*, Vol. 134, No.1, 2001, 1- 16
- [14] H. Hwang, "An EPQ model for deteriorating items under LIFO Policy". *Journal of Operations Research Society, Japan*, Vol. 25, 1982, 48-57.
- [15] K. Venkata Subbaiah, K. Srinivasa rao, B. Satyanarayana, "Inventory models for perishable items having demand rate dependent on stock level". *Opsearch*, Vol.41, No.4, 2004, 222-235.
- [16] K. Nirupamadevi, K. Srinivasa Rao, J. Lakshminarayana, "Perishable inventory models with mixture of Weibull distributions having demand as a power function of time". *Assam Statistical Review*, Vol.15, No.2, 2001, 70 – 80
- [17] K. Nirupamadevi, K. Srinivasa Rao, J. Lakshminarayana, "Optimal policy and ordering policy for deteriorating inventory having mixed Weibull rate of decay". *Proceedings of AP Akademi of Sciences*, Vol. 8, 2004, 125-132.
- [18] J. Lakshminarayana, K. Srinivasa Rao, N. Madhavi, "Ordering and pricing policies of an inventory model for deteriorating items with seconds sale". *Indian Journal of Mathematics and Mathematical Sciences*, Vol.1, No. 2, 2005, 83 – 92.
- [19] K. Srinivasa Rao, K.J. Begum, M.V. Murthy, "Optimal ordering policies of inventory model for deteriorating items having generalized Pareto life time". *Current Science*, Vol. 93, No.10, 25 Nov 2007
- [20] N.K. Mahapatra, M. Maity, "Decision process for multi-objective, multi-item production inventory system via interactive fuzzy satisfying technique". *International Journal of Computers and Mathematics with Applications*, Vol.49, No. 5-6, 2005, 805-821.
- [21] K.A. Halim, B.C. Giri, K.S. Chaudhuri, "Fuzzy Economic Order Quantity model for perishable items with stochastic demand, partial backlogging and fuzzy deterioration rate". *International Journal of Operational Research*, Vol.3, No.1/2, 2008, 77 – 96.
- [22] Liang-Yuh Ouyang, Tsu-Pang Hsieh, Chung-Yuan Dye, Hung-Chi Chang, "An inventory model for deteriorating items with stock-dependent demand under the conditions of inflation and time-value of money". *The Engineering Economist*, January 1, 2003.
- [23] J. Bhowmick, G.P. Samanta, "A continuous deterministic inventory system for deteriorating items with inventory-level-dependent time varying demand rate- Report". *Tamsui Oxford Journal of Mathematical Sciences*, November 1, 2007, 173-184.
- [24] Yong-Wu Zhou Jie Min, "A perishable inventory model under stock dependent selling rate and shortage-dependent partial backlogging with capacity constraint". *International Journal of Systems Science*, Vol. 40, Issue 1, 2009, 33 – 44.
- [25] Chun Chen Lee, Shu-Lu Hsu, "A two-warehouse production model for deteriorating items with time-dependent demands". *European Journal of Operational Research*, Vol. 194, Issue 3, 2009, 700 – 710.
- [26] S.K. Manna, Chi Chiang, "Economic production quantity models for deteriorating items with ramp type demand". *International Journal of Operational Research*, Vol. 7, No.4, 2010, 429-444.
- [27] C. K. Tripathy, U. Mishra, "An inventory model for Weibull deteriorating items with price dependent demand and time-varying holding cost". *Applied Mathematical Sciences*, Vol. 4, No.44, 2010, 2171-2179.
- [28] N.L. Johnson, S. Kotz, N. Balakrishnan, *Continuous Univariate Distributions*, 2nd ed. New York: John Wiley & Sons; 1995.

Effect of Poisson's Ratio on the Elastic Strain Concentration Factor of Notched Bars under Static Tension and under Pure Bending.

H. M. Tlilan

Department of Mechanical Engineering, The Hashemite University, 13115 Zarqa, Jordan

Abstract

As a contribution to the field of strain concentration studies, the coupled influences of Poisson's ratio and the geometric configuration upon the strain concentration factor, defined under triaxial stress state, of notched bars with U-notch, are investigated using the finite element method. Circumferentially U-notched cylindrical bars under tension and rectangular bars with a single edge U-notch under bending with different notch depths are employed here. The results clearly show that the Poisson's ratio has a significant effect on the strain concentration factor, especially for deep and intermediate notch depths. For shallow notches, the elastic strain concentration factor nearly independent of Poisson's ratio. However, for any notch depth the effect of Poisson's ratio becomes prominent with decreasing notch radius. Finally, by fitting the results of FEM analysis, a set of convenient formulas of the elastic strain concentration factor as a function of Poisson's ratio are introduced. These formulas will be useful for any notch depth and radius under the same type of loading employed in the present study.

© 2010 Jordan Journal of Mechanical and Industrial Engineering. All rights reserved

Keywords: Bending; Notched bars; Strain concentration factor; Tension; Poisson's ratio.

Nomenclature

		t_o	Initial notch depth
		ϵ_z	Axial strain
		$(\epsilon_z)_{av}$	Average axial strain
		$(\epsilon_z)_{max}$	Maximum axial strain at the notch root
		ν	Poisson's ratio
		ρ_o	Initial notch radius
		σ_r	Radial stress
		σ_z	Axial stress
		σ_θ	Tangential stress
		$(\sigma_z)_{av}$	Average axial stress at the net section (= P/A)
		$(\sigma_z)_{max}$	Axial stress at the notch root
		$(\sigma_\theta)_{max}$	Tangential stress at the notch root
		F	Transverse load per unit width
A	Current net-section area	$(\epsilon_x)_n$	Nominal strain for pure bending; (Fig. 3)
a	Current distance from the transverse load F to support; (Fig. 1b)	ϵ_x	Longitudinal strain; (Fig. 3)
ao	Initial distance from the transverse load F to support; (Fig. 1b)	$(\epsilon_x^t)_{max}$	Maximum tensile longitudinal strain at the notch root; (Fig. 3)
Do	Initial gross diameter; (Fig. 1a)	σ_x	Longitudinal stress
E	Young's modulus	σ_y	Transverse stress
hc	Current height under compressive $\square x$ at the net section; (Fig. 3)	σ_z	Stress in the width direction
ht	Current height under tensile $\square x$ at the net section; (Fig. 3)	ψ	Distance from the current center of the net section; (Fig. 3)
ho	Initial thickness at the net section; (Fig. 3)	Y	Distance from the current neutral surface; (Fig. 3)
Ho	Initial thickness at the gross section; (Fig. 3)		
$K \square T$	strain-concentration factor under static tension		
$K \square PB$	strain-concentration factor under pure bending		
M	Bending moment per unit width = Fa		
P	Tensile load		
r	Current distance from the center of the net-section ($0 \leq r \leq r_n$)		
r_n	Current net-section radius (= $d/2$)		
s	= r/r_n ($0 \leq s \leq 1.0$)		

* Corresponding author. siva_appisetty1@yahoo.co.in

1. Introduction

Many machines or structural members contain the stress raisers in the form of notches, holes, and fillets. In reality, this kind of stress raisers often the origin of cracks nucleating, growing and easily initiating fracture. The classical solution obtained by researchers has a direct relation with notch geometrical configuration, i.e. notch radius, the notch depth [1, 2]. All these studies results are published and used for engineering design [3]. Almost from the earliest time most of the previous works were based on the stress concentration factor as a tool to predict fracture of machine elements that contains geometrical irregularities [1, 3 – 6]. The stress and conventional strain concentration factors being studied for different types of loading and geometries. It has been concluded that the strain concentration factor is more effective in predicting fracture than the stress concentration factor [7-10]. It should be noted that the conventional strain concentration factor has been defined under uniaxial stress state, while the new strain concentration factor has been defined under triaxial stress state [7,8]. This new definition expresses the concave distribution of the axial strain on the net section from elastic upto general yielding [7-10]. On the other hand, the conventional strain concentration factor failed to express the real irregularities effect as well as the stress concentration factor, especially in plastic deformation. However, the effects of specimen geometry on strain concentration factor have not been completely validated. Tlilan et al. investigated the effect of notch root radius and notch depth on strain concentration factor for circumferential U-notch and single edge U-notch under static tension and pure bending, respectively [8-10].

For three-dimensional problems, i.e. triaxial stress state, the stress and strain concentration factors may change with different material properties such as Poisson's ratio. However, few studied have been done on the effect of material properties on strain concentration factor, especially the new one, which has been defined under triaxial stress state [8-10]. Moreover, few researchers have been considering the mechanical properties effect on stress and strain concentration factors. Since both factors are non-dimensional factors and as it will be shown later, the mechanical property that affects the stress and strain concentration factor is the Poisson's ratio.

Poisson's ratio is defined as the negative of the lateral strain divided by the longitudinal strain. Practically, all ordinary materials, which undergo a lateral contraction when stretched and a lateral expansion when compressed, exhibit a positive Poisson ratio from 0 to 0.5 [11]. The Poisson ratios for various isotropic homogeneous materials are approximately; 0.14-0.16 for SiC, 0.20 for Concrete, 0.21-0.26 for Cast Iron, 0.27-0.3 for steel, 0.42 for Gold, 0.35 for Magnesium, 0.33 Aluminum Alloy, 0.42 for silicon, 0.45 for lead, and nearly 0.5 for rubbers and soft biological tissues [5, 12-15]. Poisson's ratio ν has to be involved in stress and strain concentrations study especially under a three-dimensional or triaxial stress state. The influence of Poisson's ratio on the stress concentration factor varies with the geometric configuration. This is because the stress distributions depend on the change of the element volume and the change of the element volume; depends on Poisson's ratio. For a hyperbolic

circumferential groove in a round bar under tensile load, the stress concentration factors in the axial and circumferential directions are the functions of Poisson's ratio [14]. However, the effect of Poisson's ratio on strain concentration factor has not studied, especially for the newly defined strain concentration factor. Moreover, most of the published works have studied the effect of Poisson's ratio on the conventional strain concentration factor, which has been defined under uniaxial stress state [15].

To this end, the objective of this work is principally to study the effect of Poisson's ratio on the strain concentration factor, defined under triaxial stress state, of notched bars under static tension and pure bending. The influence of Poisson's ratio on the strain concentration factors of circumferential U-notch under tension and single edge U-notch under pure bending have been systematically investigated by use of finite element method (FEM). A set of useful formulae has been obtained with satisfied accuracy by fitting the numerical results.

2. Specimen Geometries and material properties

Two specimens are employed, as shown in Fig.1 ; Cylindrical bar with circumferential U-notch for static tension and rectangular bar with single edge U-notch for pure bending. For static tension, the length of the cylindrical bar is 50.0 mm and the gross diameter D_o is 8.35 mm. Where as, the rectangular bar has length of 160.0 mm, gross thickness H_o of 16.7 mm, and width b_o of 1.0 mm. The computations were performed for under constant gross diameter. While, the notch depth t_o was changed in order to vary the ratio of notch depth to gross diameter (t_o/D_o) and to gross thickness (t_o/H_o) from 0.05 to 0.80. The notch radii employed are 0.5 and 1.0 mm for all cases. To study the effect of Poisson's ratio of the elastic strain concentration factor, Poisson's ratio has been varied from 0.05 to 0.45. Since the analyses is linear elastic, the modulus of elasticity (Young's modulus E) has been chosen to be 200 GPa. This will affect only the displacement and strains but not the stresses. As a result the value of the Young's modulus will not affect the values of the elastic strain concentration factor, because it is a nondimensional factor, which will be shown later in this article.

3. Finite element modeling

The FE method with the eight-node isoparametric quadrilateral element was used in the context of triaxial stress state isotropic elasticity for all the computations. Because of the symmetry of the bar, one-quarter of the specimen is modeled for static tension, whereas one half of the specimen is modeled for pure bending, as shown in Fig.2. The boundary conditions for every model used in the calculations are indicated in the same Figure. A uniform tensile load was applied to the end of the unnotched part of the bar for static tension. For pure bending, a transverse load F of 1 N/mm was applied at 45 mm from the net section, which is enough to obtain the notch effect.

The accuracy of the finite element analysis models was checked by monitoring the strain distribution on the net section. There are a total of 540 elements and 1667 nodes

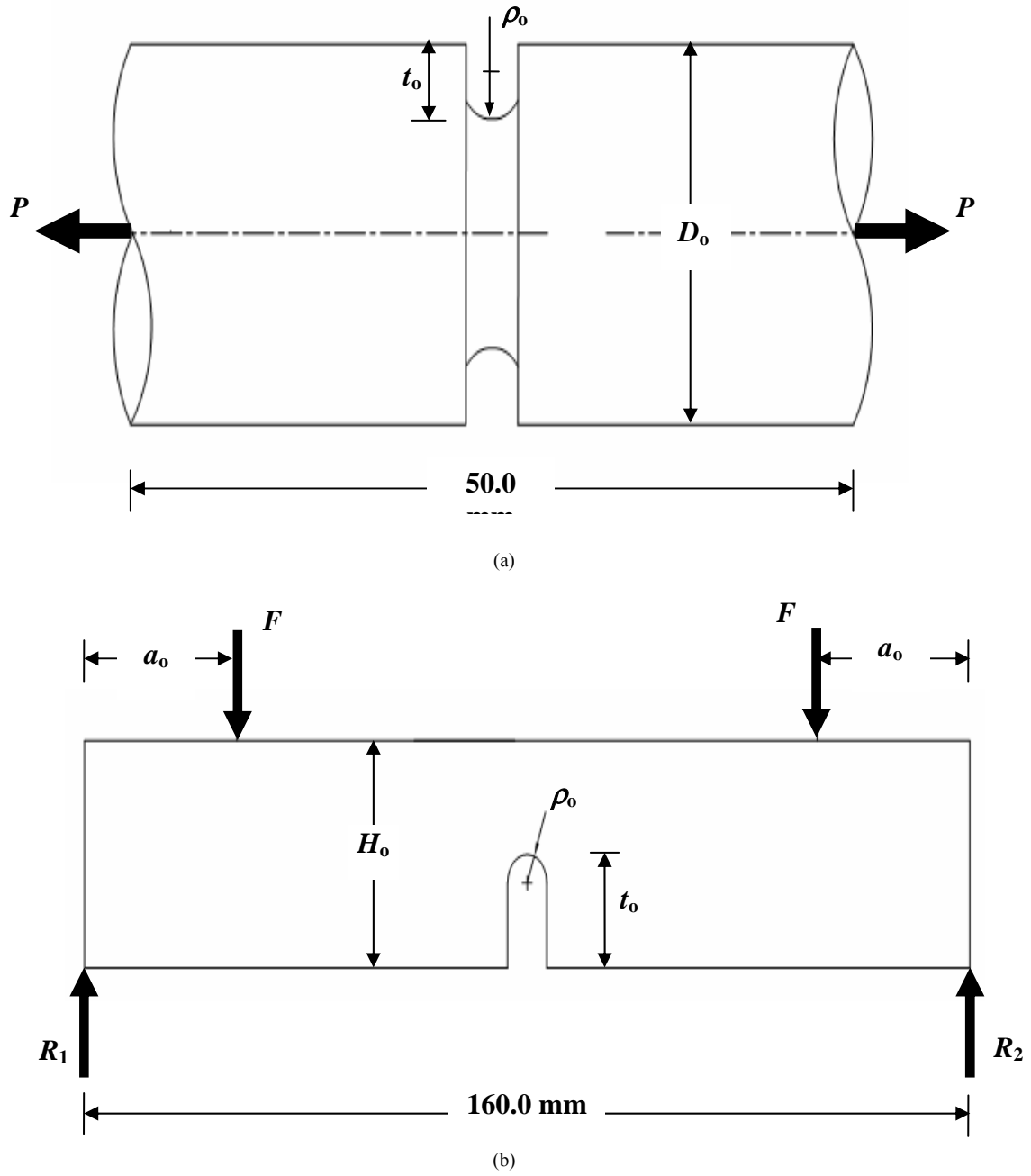


Figure 1. Geometrical properties of the employed specimens: (a) static tension; (b) pure bending.

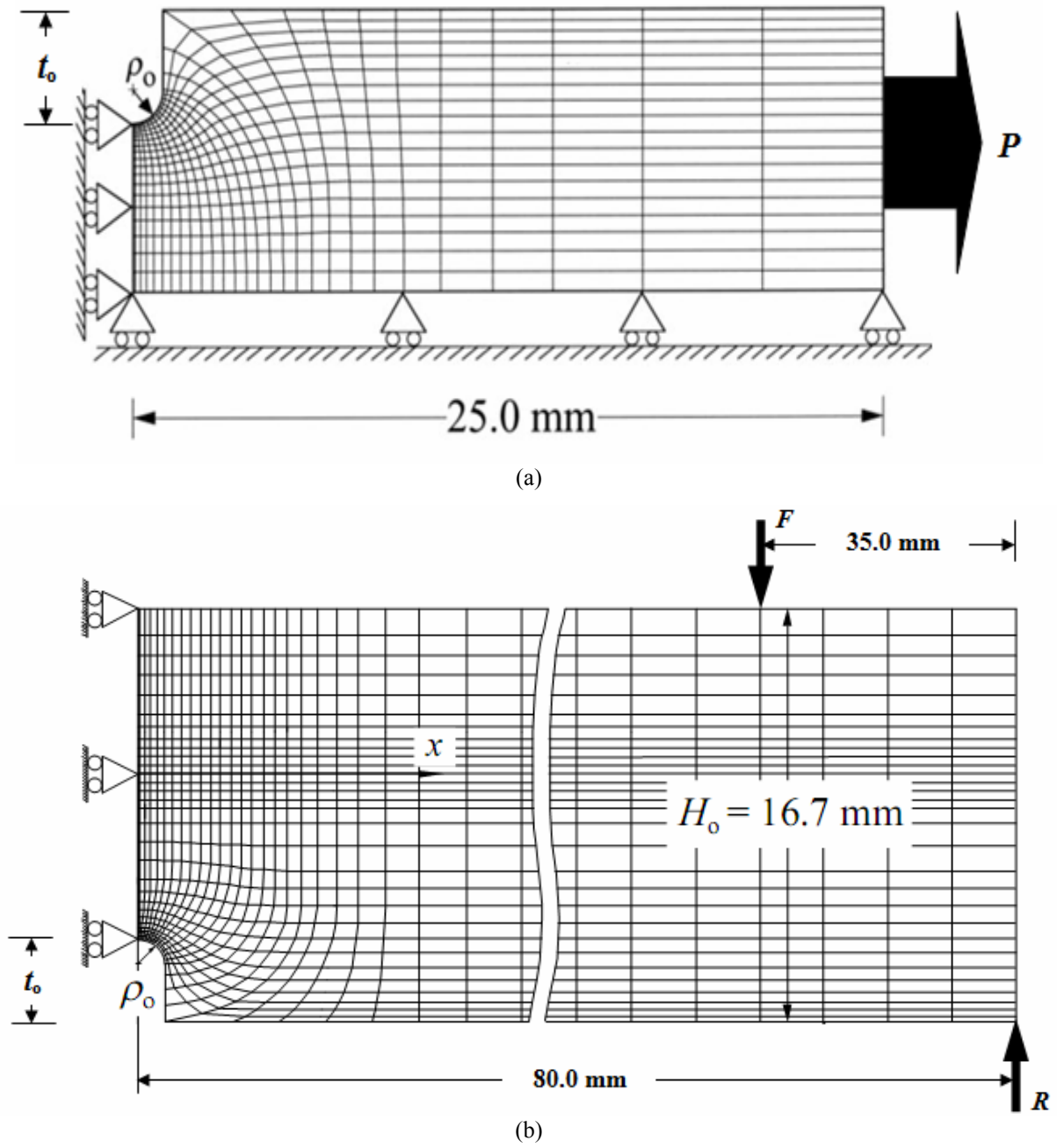


Figure 2. FEM model of the employed specimens: (a) static tension; (b) pure bending.

in the model for static tension, where as 1560 elements and 4845 nodes for pure bending. It should be noted that calculations for pure bending problem have been done under the plane strain condition [9].

4. Relation between strain concentration factor and Poisson’s ratio

4.1. Static tension

The strain concentration factor K_{ϵ}^T employed here has been recently defined under triaxial stress states (Majima, 1999; Tlilan et.al., 2005). This definition gives good consistent results with the axial strain distribution upto general yielding, while the conventional definition showed inconsistency with axial strain distribution on the net section, as it had been defined under uniaxial stress state [8]. The strain concentration factor is defined as follows:

$$K_{\epsilon}^T = \frac{(\epsilon_z)_{max}}{(\epsilon_z)_{av}} \tag{1}$$

where; $(\epsilon_z)_{max}$ is the maximum axial strain; i.e. the axial strain at the notch root. $(\epsilon_z)_{av}$ is the average or nominal axial strain on the net section. The average or nominal axial strain has been defined under triaxial stress state.

$$\begin{aligned} (\epsilon_z)_{av} &= \frac{1}{A} \int_A \epsilon_z(r) dA \\ &= \frac{1}{\pi r_n^2} \int_0^{r_n} \epsilon_z(r) 2\pi r dr \end{aligned} \tag{2}$$

In elastic deformation and using Hook’s law the axial strain is transformed to be

$$\epsilon_z = \frac{1}{E} [\sigma_z - \nu(\sigma_{\theta} + \sigma_r)] \tag{3}$$

Moreover, the axial strain at the notch root; i.e. the maximum axial strain, becomes

$$\begin{aligned} (\epsilon_z)_{max} &= \frac{1}{E} \{(\sigma_z)_{notch\ root} - \nu[(\sigma_{\theta})_{notch\ root} + (\sigma_r)_n] \\ &= \frac{1}{E} \{(\sigma_z)_{max} - \nu[(\sigma_{\theta})_{max} + (\sigma_r)_{max}] \} \end{aligned} \tag{4}$$

Substitute Eq.(3) into Eq.(2) leads to the elastic nominal or average axial strain

$$\begin{aligned} (\epsilon_z)_{av} &= \frac{1}{\pi r_n^2} \int_0^{r_n} \left[\frac{\sigma_z}{E} - \frac{\nu}{E} (\sigma_{\theta} + \sigma_r) \right] 2\pi r dr \\ &= \frac{1}{E} \left\{ (\sigma_z)_{av} - \frac{\nu}{\pi r_n^2} \int_0^{r_n} (\sigma_{\theta} + \sigma_r) 2\pi r dr \right\} \end{aligned} \tag{5}$$

Substitute Eqs. (4) and (5) into Eq.(1) gives

$$\begin{aligned} K_{\epsilon}^T &= \frac{\frac{1}{E} \{(\sigma_z)_{max} - \nu[(\sigma_{\theta})_{max} + (\sigma_r)_{max}]\}}{\frac{1}{E} \left\{ (\sigma_z)_{av} - \frac{\nu}{\pi r_n^2} \int_0^{r_n} (\sigma_{\theta} + \sigma_r) 2\pi r dr \right\}} \\ &= \frac{(\sigma_z)_{max} - \nu[(\sigma_{\theta})_{max} + (\sigma_r)_{max}]}{(\sigma_z)_{av} - \frac{\nu}{\pi r_n^2} \int_0^{r_n} (\sigma_{\theta} + \sigma_r) 2\pi r dr} \end{aligned} \tag{6}$$

It is clear from Eq.(6) that Poisson’s ratio is the only factor which affects the elastic strain concentration factor in addition to local stress values at the notch root and the stress distribution on the net section. It should be noted that the conventional strain concentration factor neglect Poisson’s ratio effect. This is due to the definition of the conventional strain concentration factor under uniaxial stress state [8].

4.2. Pure bending

For pure bending, the strain concentration factor K_{ϵ}^{PB} has been defined as the ratio of the maximum longitudinal strain at the notch root $(\epsilon_x^t)_{max}$ to the nominal longitudinal strain on the net section $(\epsilon_x)_n$ [9];

$$K_{\epsilon}^{PB} = \frac{(\epsilon_x^t)_{max}}{(\epsilon_x)_n} \tag{7}$$

This strain concentration factor has been introduced by defining the nominal longitudinal strain under triaxial state in elastic deformation as well as plastic deformation. The new nominal longitudinal strain considered the effect of transverse stress, which it was neglected in the conventional definition. The new nominal longitudinal strain is defined as [9];

$$(\epsilon_x)_n = \frac{6}{(h_t + h_c)^2} \int_{-h_c}^{h_t} \epsilon_x Y dY \tag{8}$$

Where; h_t is the current height from the neutral surface to the notch root and h_c is the current height from the neutral surface to the unnotched surface opposite to the notch root, as shown in Fig. 3. In elastic deformation; $h_t + h_c \approx h_o$, the new nominal longitudinal strain is

$$(\epsilon_x)_n = \frac{6}{E h_o^2} \int_{-h_c}^{h_t} [\sigma_x - \nu(\sigma_y + \sigma_z)] Y dY \tag{9}$$

Under plane strain condition and using Hooke's law; $(\sigma_z)_{nr} = \nu[(\sigma_x)_{nr} + (\sigma_y)_{nr}]$, the new nominal longitudinal strain can be rewritten as

$$\begin{aligned} (\varepsilon_x)_n &= \frac{6}{E h_o^2} \left[(1-\nu^2) \int_{-h_c}^{h_t} \sigma_x Y dY - \nu(1+\nu) \int_{-h_c}^{h_t} \sigma_y Y dY \right] \\ &= \frac{6}{E h_o^2} \left[(1-\nu^2)M - \nu(1+\nu) \int_{-h_c}^{h_t} \sigma_y Y dY \right] \end{aligned} \quad (10)$$

Moreover, the maximum longitudinal strain can be written as

$$(\varepsilon_x^t)_{max} = \frac{1}{E} \left\{ (\sigma_x^t)_{nr} - \nu[(\sigma_y)_{nr} + (\sigma_z)_{nr}] \right\} \quad (11)$$

which transformed to following form under plane strain condition

$$\begin{aligned} (\varepsilon_x^t)_{max} &= \frac{1}{E} \left\{ (\sigma_x^t)_{nr} - \nu[(\sigma_y)_{nr} + \nu(\sigma_x)_{nr} + \nu(\sigma_y^t)_{nr}] \right\} \\ &= \frac{1}{E} \left[(1-\nu^2)(\sigma_x^t)_{nr} - (\nu+\nu^2)(\sigma_y)_{nr} \right] \end{aligned} \quad (12)$$

However, at the notch root the transverse stress is equal to zero; i.e. $(\sigma_y)_{nr} = 0.0$ (Tilhan et al., 2006), therefore

$$(\varepsilon_x^t)_{max} = \frac{(1-\nu^2)}{E} (\sigma_x^t)_{nr} = \frac{(1-\nu^2)}{E} (\sigma_x^t)_{max} \quad (13)$$

Substitution of Eq.(10) and Eq.(13) into Eq. (7) leads to

$$\begin{aligned} K_\varepsilon^{PB} &= \frac{\frac{(1-\nu^2)}{E} (\sigma_x^t)_{max}}{\frac{6}{E h_o^2} \left[(1-\nu^2)M - \nu(1+\nu) \int_{-h_c}^{h_t} \sigma_y Y dY \right]} \\ &= \frac{(1-\nu^2)h_o^2 (\sigma_x^t)_{max}}{6 \left[(1-\nu^2)M - (\nu+\nu^2) \int_{-h_c}^{h_t} \sigma_y Y dY \right]} \end{aligned} \quad (14)$$

Rearranging the previous equation gives the elastic strain concentration factor for pure bending

$$K_\varepsilon^{PB} = \frac{h_o^2 (\sigma_x^t)_{max}}{6M - \frac{6(\nu+\nu^2)}{(1-\nu^2)} \int_{-h_c}^{h_t} \sigma_y Y dY} \quad (15)$$

It has shown that

$$\int_{-h_c}^{h_t} \sigma_y Y dY \neq 0.0$$

This indicates that Eq. (15) clearly showed the effect of Poisson's ratio on the elastic strain concentration factor. This effect can not be shown by the conventional definition, which is essentially attributed to the definition

of the strain concentration factor under uniaxial stress state (Tilhan et al., 2006).

5. Results and discussion

5.1. Static tension

The effect of varying Poisson's ratio on the elastic K_ε^T for the employed notched bars is shown in Figs. 4, respectively. In each of these figures, the elastic K_ε^T are presented for nine different values of Poisson's ratio, i.e. $\nu = 0.05, 0.1, 0.15, 0.20, 0.25, 0.30, 0.35, 0.40$ and 0.45 . The variations of K_ε^T with the ratio of notch depth to gross diameter (t_o/D_o) are shown in Fig. 4. It is shown that the variation of the strain concentration factor depends on Poisson's ratio for all notched bars employed. This is prominent in the range $0.20 < t_o/D_o \leq 0.80$, as shown in Fig. 4. Actually, the elastic K_ε^T increases with increasing Poisson's ratio for notches with $0.20 < t_o/D_o \leq 0.80$ and the intermediate notch depth has the maximum elastic K_ε^T for all Poisson's ratio values and notch radii employed.

In the former set of figures, Poisson's ratio influences the elastic K_ε^T curve only on its magnitude. As a result, the variation in the elastic K_ε^T with Poisson's ratio is not clear, especially for deep and shallow notches. In order to clarify the effect of the Poisson's ratio, the elastic K_ε^T is plotted in figures 5 - 15 as a function of Poisson's ratio ν for each of the notch depths and radii values used in the investigation. For the same notch depth, there appears to be a trend towards increasing K_ε^T with an increase in ν or $0.20 < t_o/D_o \leq 0.80$. Further, the trend appears to be greater for the all notch depths at $\rho = 0.5$ mm than for those at $\rho = 1.0$ mm. However, the elastic K_ε^T becomes nearly constant or slightly decreases with increasing ν for the shallow notches ($0.05 < t_o/D_o \leq 0.15$).

Generally, it is believed that if notch depth is constant the effect of Poisson's ratio is not very large. In the above mentioned results, it is found that for deep and intermediate notch depths under tension the effect of Poisson's ratio can not be negligible. However, for shallow notches under tension, the effect of ν is not very large. Therefore, the effect of a negative Poisson's ratio can effectively enhance the deformation capability in the deformation of materials, which is vital to the fracture mechanics of a lot of machine elements, especially when it contains irregularities.

In the finite element results mentioned above and by curve fitting; a convenient 7th order polynomial formula can be proposed. As a results, Tables 1 and 2 give the polynomials that are obtained for elastic K_ε^T as a function of ν .

5.2. Pure bending

The elastic strain concentration factor under bending (K_ε^{PB}) variations with notch depth (t_o/H_o) for different Poisson's ratios are shown in Fig. 16. It is obvious that the general trend of the variation of K_ε^{PB} with t_o/H_o is independent of Poisson's ratio. Actually, the elastic K_ε^{PB} increases with increasing t_o/H_o and reaches maximum value at $t_o/H_o = 0.2$ for Poisson's ratio of 0.45. On the other hand, the maximum elastic K_ε^{PB} occurs at $t_o/H_o = 0.25$ for Poisson's ratio values less than 0.45. The Poisson's ratio effect is prominent in the range where 0.05

$< t_o / H_o \leq 0.5$. This means that the elastic K_e^{PB} is nearly independent of Poisson's ratio for deep notches, i.e. $t_o / H_o > 0.5$. The smaller the notch radius is, the larger the effect of Poisson's ratio on strain concentration factor is.

Figures 17 - 26 show the relationship between the elastic K_e^{PB} and Poisson's ratio (ν). As it can be seen, figures 17 - 26 show the dependence of the elastic K_e^{PB} on Poisson's ratio values. For notches with $0.2 < t_o / H_o \leq 0.8$, the elastic K_e^{PB} gradually increases with increasing ν and reaches maximum values at $\nu \approx 0.3$. After that, the elastic K_e^{PB} shows a slight decrease with increasing ν . On the other hand, the elastic K_e^{PB} increases with increase in ν for the shallow notches, i.e. $t_o / H_o = 0.05, 0.1, \text{ and } 0.15$. This trend is independent of notch radius. However, for the same notch depth and Poisson's ratio, as it can be seen in figures 17 - 26; the elastic K_e^{PB} increases with decreasing notch radius.

Tables 3 and 4 gives an empirical expression for the elastic K_e^{PB} as a function of ν , which is obtained by fitting the FEM results for all notch depths and radii employed. Therefore, the empirical expression can be used conveniently in elastic K_e^{PB} prediction of single edged U-notched bars with various notch geometries and different valued of ν .

6. Conclusions

By using three-dimensional FEM analysis, the effect of Poisson's ratio on the elastic strain concentration factor, defined under triaxial stress state, of a notched bars for different specimen sizes and different loading types have been evaluated. Taking the advantage of a recent formulation of the strain concentration factor under triaxial stress state, which is suitable for expressing the actual strain and stress distributions in the vicinity of notches in machine elements. On the other hand, the conventional strain concentration factor has been defined under uniaxial stress state, which neglects or can not predict the actual effect of the Poisson's ratio on the strain concentration. The shown results in this work lead to the conclusion that Poisson's ratio has a significant effect on the elastic strain concentration factor for the geometries and, treated loading types. According to the present study the following conclusions are drawn:

1. It is established in this work that for axially loaded members and for the selected geometry treated, the values of the elastic strain concentration factor appreciably increases with increasing Poisson's ratio for notches with $0.20 < t_o / D_o \leq 0.80$. However, the elastic strain concentration factor is nearly constant or slightly decreasing with the increase in the Poisson's ratio for shallow notches, i.e. $0.05 < t_o / D_o \leq 0.15$.
2. For pure bending, the elastic strain concentration factor increases and attains a maximum value, then it decreases as the values of Poisson's ratio increase for notches with $0.2 < t_o / H_o \leq 0.8$. On the other hand, the

elastic strain concentration factor slightly increases with increasing Poisson's ratio values for $t_o / H_o = 0.05, 0.1, \text{ and } 0.15$.

3. For all loading types and notch geometries employed, the effect of Poisson's ratio on the elastic strain concentration factor is more pronounced in extremely deep and intermediate notch depths than that for shallow notches.

References

- [1] M.M. Leven, M.M. Frocht, "Stress-concentration factors for single notch in flat bar in pure and central bending". J. Appl. Mechanics, Vol. 74, 560-56; 1952.
- [2] H. Neuber, "Theory of stress concentration factor for shear-strained prismatical bodies with arbitrary nonlinear stress-strain law". J. Appl. Mechanics, Vol. 28, 544-550; 1961.
- [3] W.D. Pilkey, Peterson's Stress Concentration Factors. Wiley, New York; 1997.
- [4] K. Nishida, Stress Concentration (in Japanese). Morikita Shuppan, Tokyo; 1974.
- [5] A. Kato, "Design equation for stress concentration factors of notched strips and grooved shafts". J. strain analysis, Vol 26, 21-28; 1991.
- [6] N.-A. Noda, M. Sera, Y. Takase, "Stress concentration factors for round and flat test specimens with notches". Int. J. Fatigue, Vol. 17, No. 3, 163-178; 1995,
- [7] T. Majima, "Strain-concentration factor of circumferentially notched cylindrical bars under static tension". J. Strain Analysis, Vol. 34, No. 5, 347-360; 1999.
- [8] H.M. Tlilan, S. Yousuke, T. Majima, "Effect of notch depth on strain-concentration factor of notched cylindrical bars under static tension". European Journal of Mechanics A / Solids, Vol. 24, No. 3, 406-416; 2005.
- [9] H.M. Tlilan, N. Sakai, T. Majima, "Effect of notch depth on strain-concentration factor of rectangular bars with a single-edge notch under pure bending". Int. J. Solids and Structures, Vol. 43, 459-474; 2006.
- [10] H.M. Tlilan, A.S. Al-Shyyab, A.M. Jawarneh, A.K. Ababneh, "strain-concentration factor of circumferentially v-notched cylindrical bars under static tension". Journal of Mechanics, Vol. 24, No. 4, 419-428; 2008.
- [11] W.D. Pilkey, Formulas for stress, strain, and structural matrices. 2nd ed., John Wiley & Sons, New York; 2005.
- [12] H. Neuber, Theory of notch stresses: principles for exact calculation of strength with reference to structural form and material. 2nd ed., Springer Verlag, Berlin; 1958.
- [13] J. Dundurs, "Dependence of stress on Poisson's ratio in plane elasticity". Int J Solids Struct. Vol. 3, 1013-1021; 1967.
- [14] R.J. Grant, M. Lorenzo, J. Smart, "The effect of Poisson's ratio on stress concentrations". J Strain Anal Engng., Vol. 42, 95-104; 2007.
- [15] Y. Zheng, "Stress and strain concentration factors for tension bars of circular cross-section with semicircular groove". Engineering Fracture Mechanics., Vol. 76, 1683-1690; 2009.

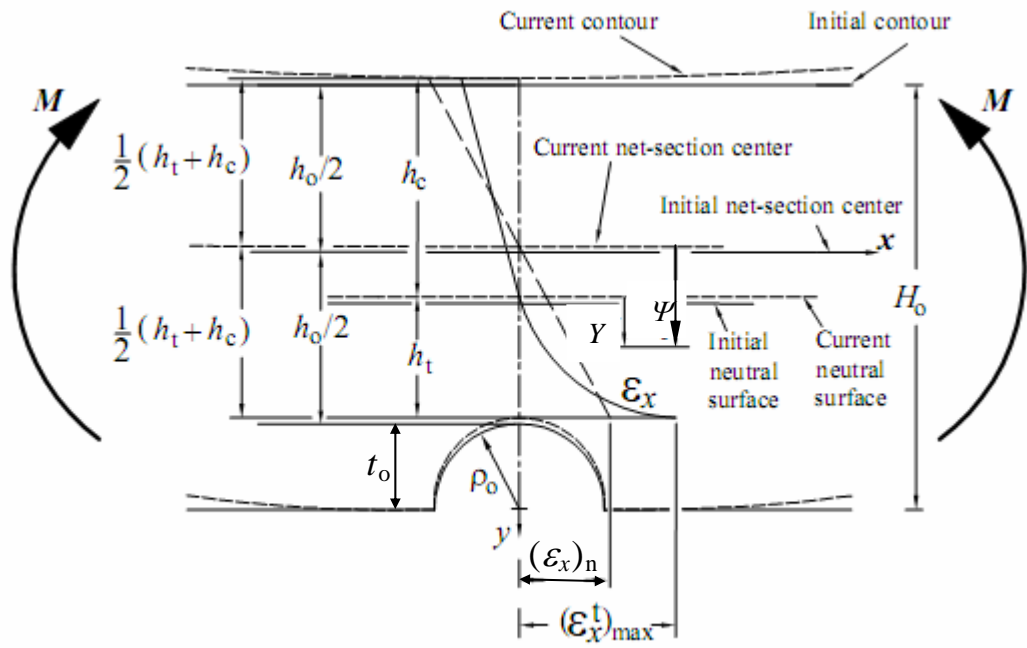
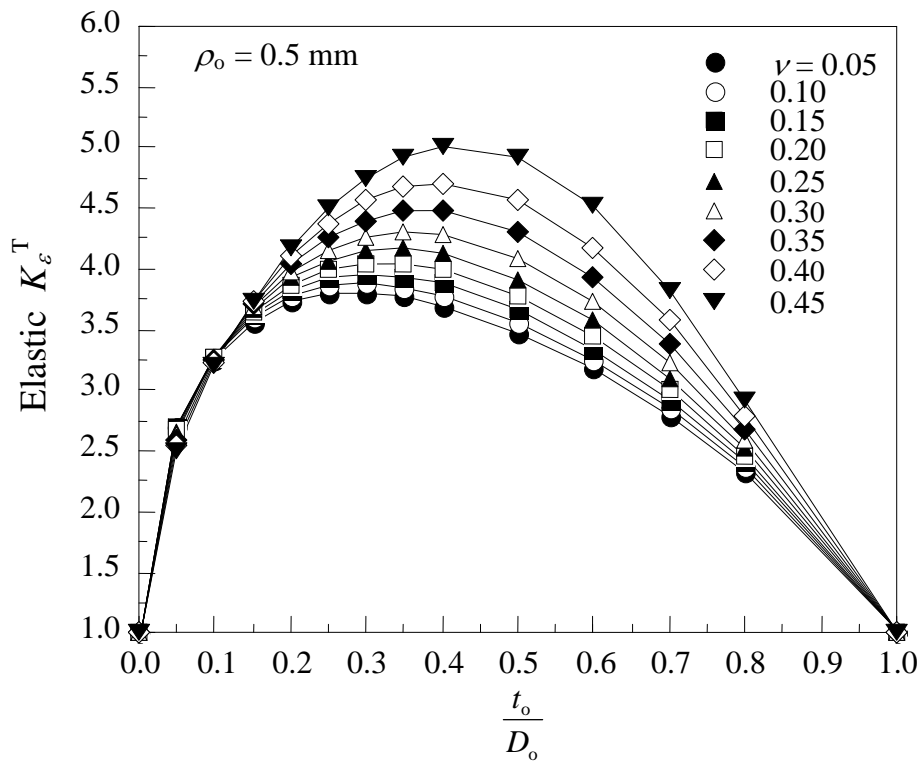
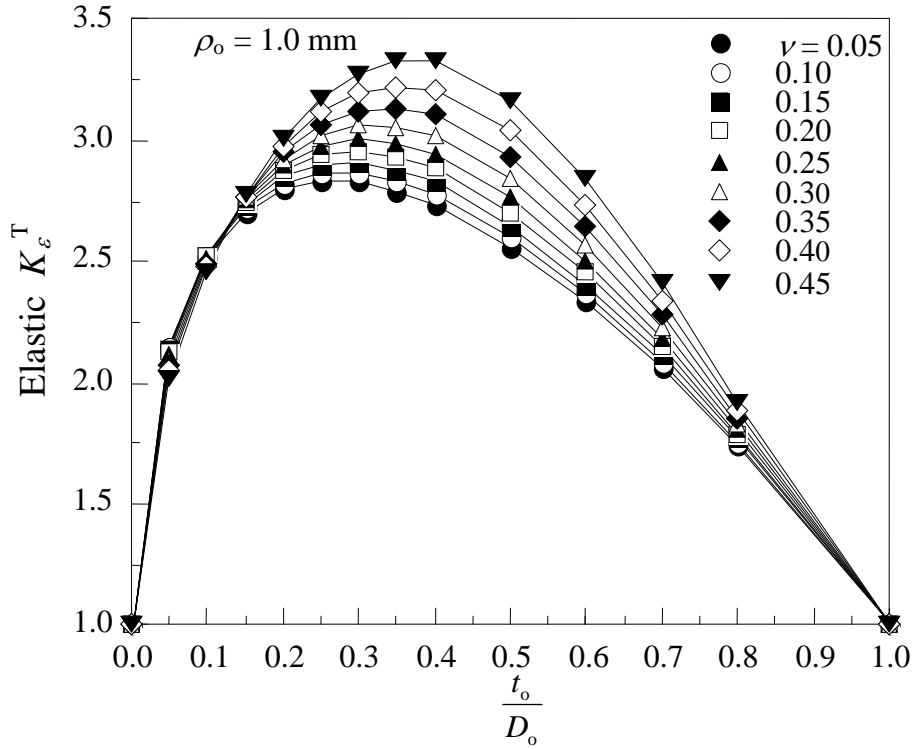


Figure 3. Initial and current contours for pure bending.



(a)



(b)

Figure 4. Effect of Poisson's ratio on the variation of elastic K_ϵ^T with notch depth: (a) $\rho_o = 0.5 \text{ mm}$; (b) $\rho_o = 1.0 \text{ mm}$.

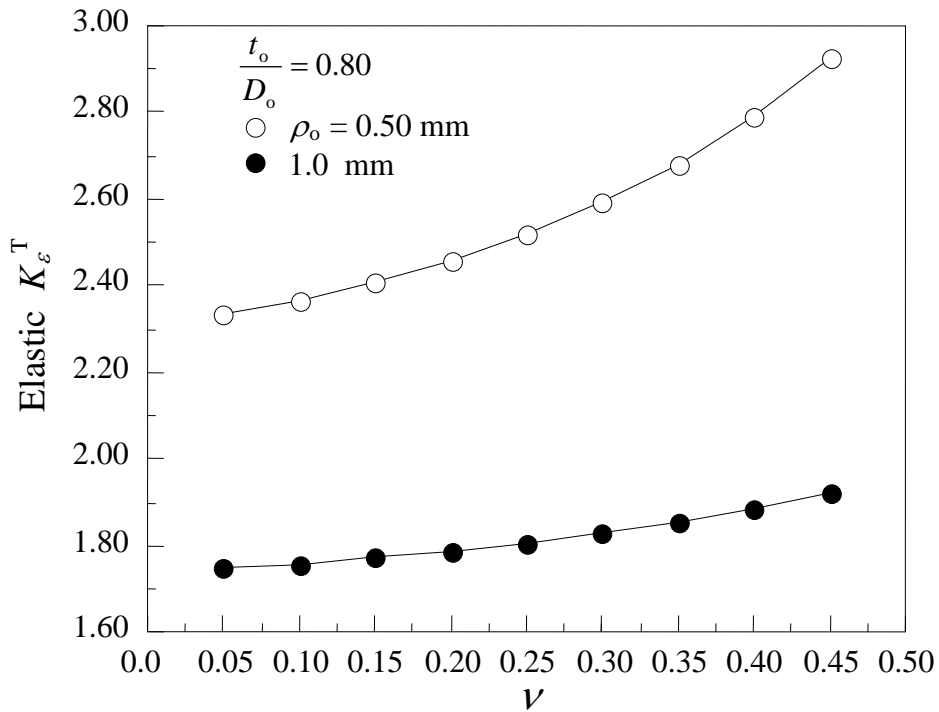


Figure 5. Variation of the elastic K_ϵ^T with Poisson's ratio for $t_o/D_o = 0.80$

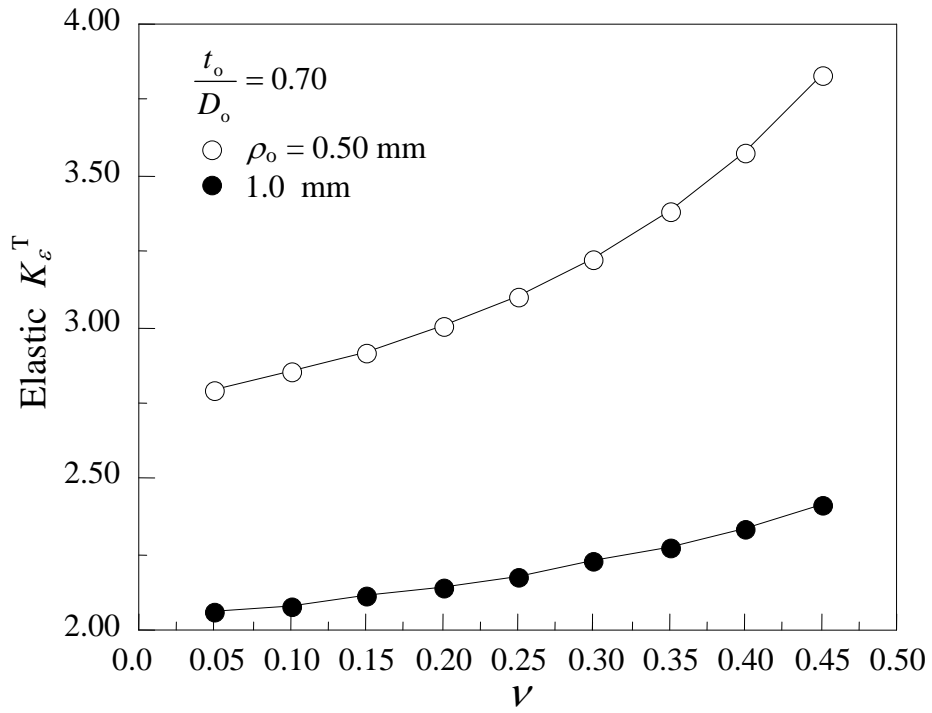


Figure 6. Variation of the elastic K_e^T with Poisson's ratio for $t_o/D_o = 0.70$

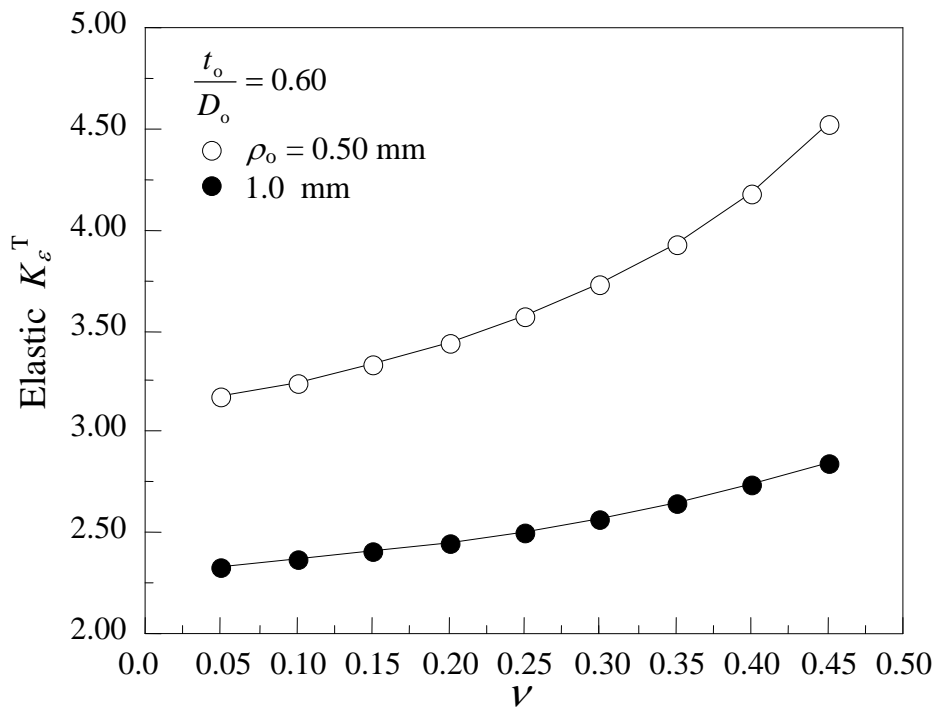


Figure 7. Variation of the elastic K_e^T with Poisson's ratio for $t_o/D_o = 0.60$

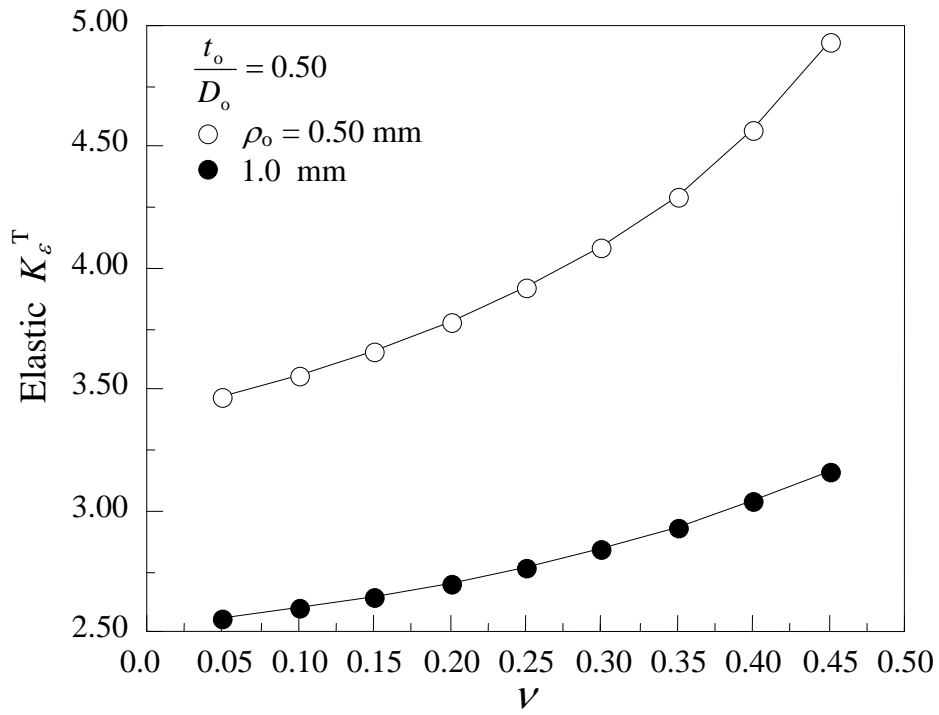


Figure 8. Variation of the elastic K_ϵ^T with Poisson's ratio for $t_o/D_o = 0.50$

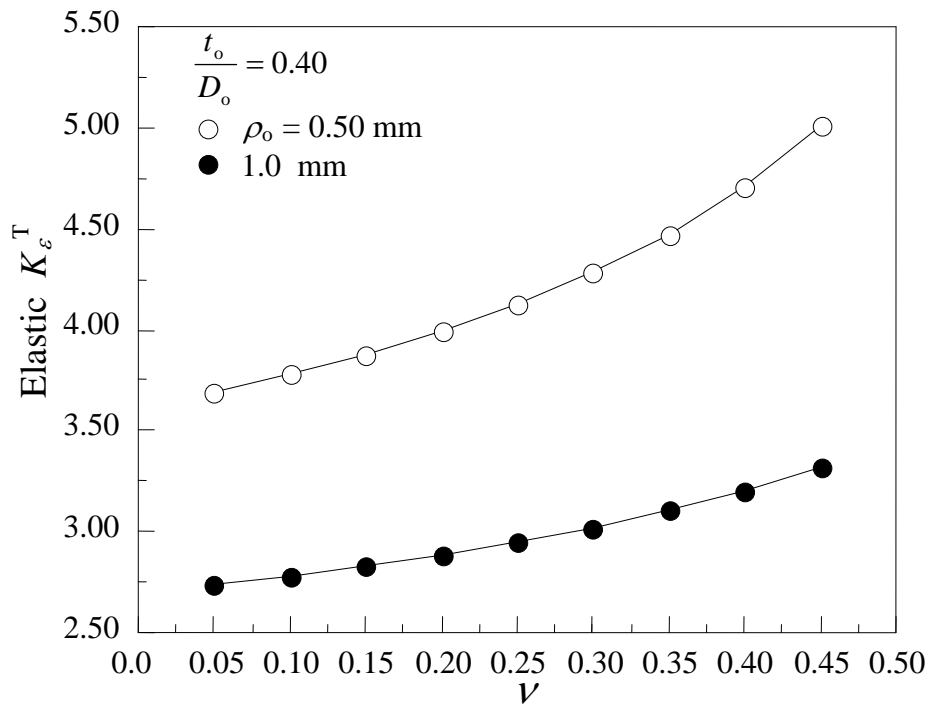


Figure 9. Variation of the elastic K_ϵ^T with Poisson's ratio for $t_o/D_o = 0.40$

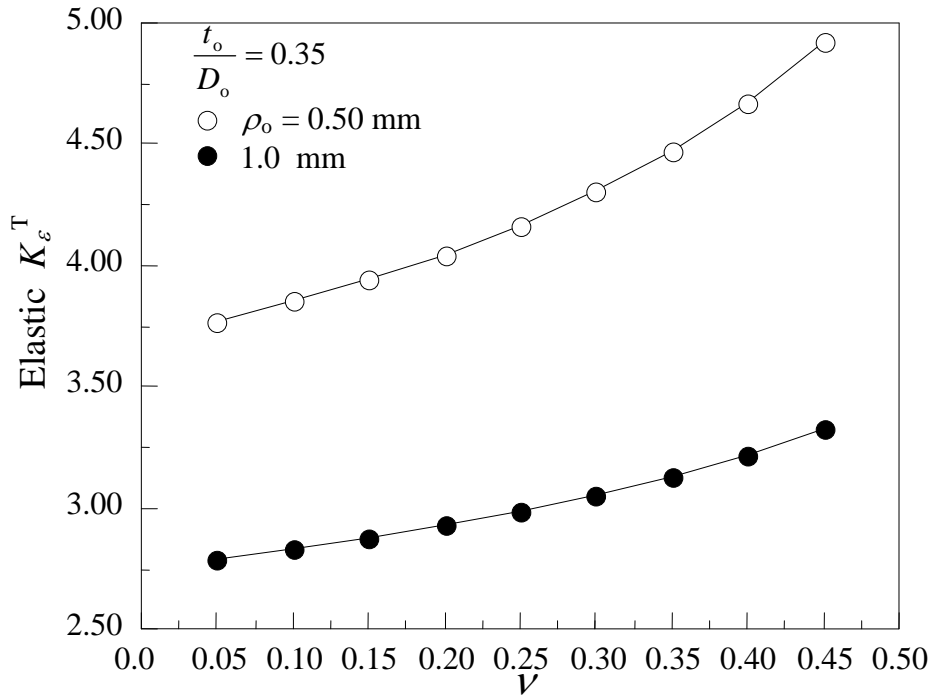


Figure 10. Variation of the elastic K_ϵ^T with Poisson's ratio for $t_o/D_o = 0.35$

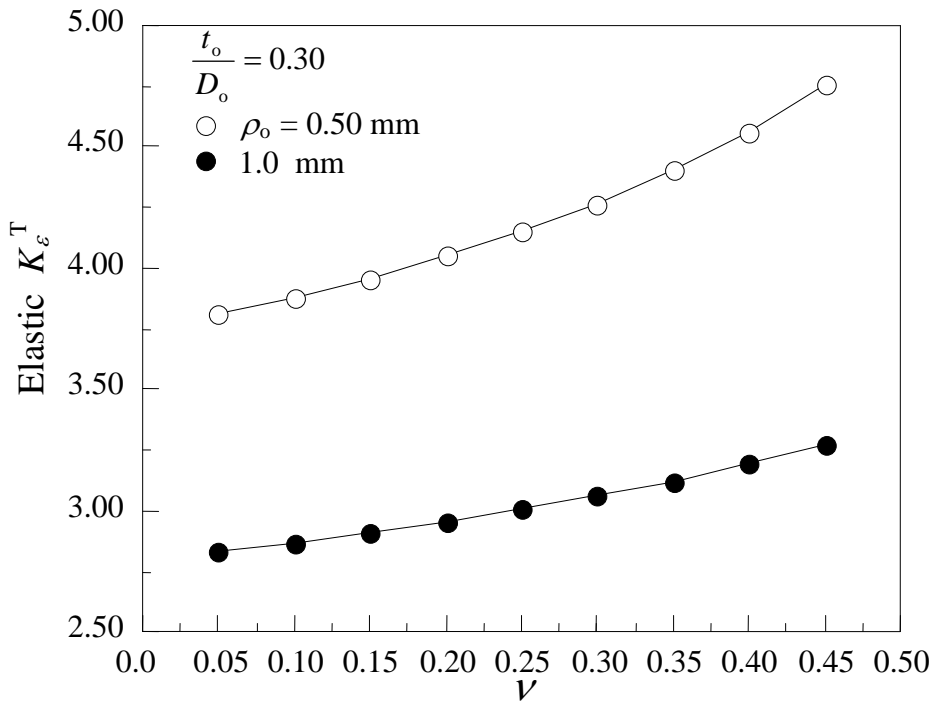


Figure 11. Variation of the elastic K_ϵ^T with Poisson's ratio for $t_o/D_o = 0.30$

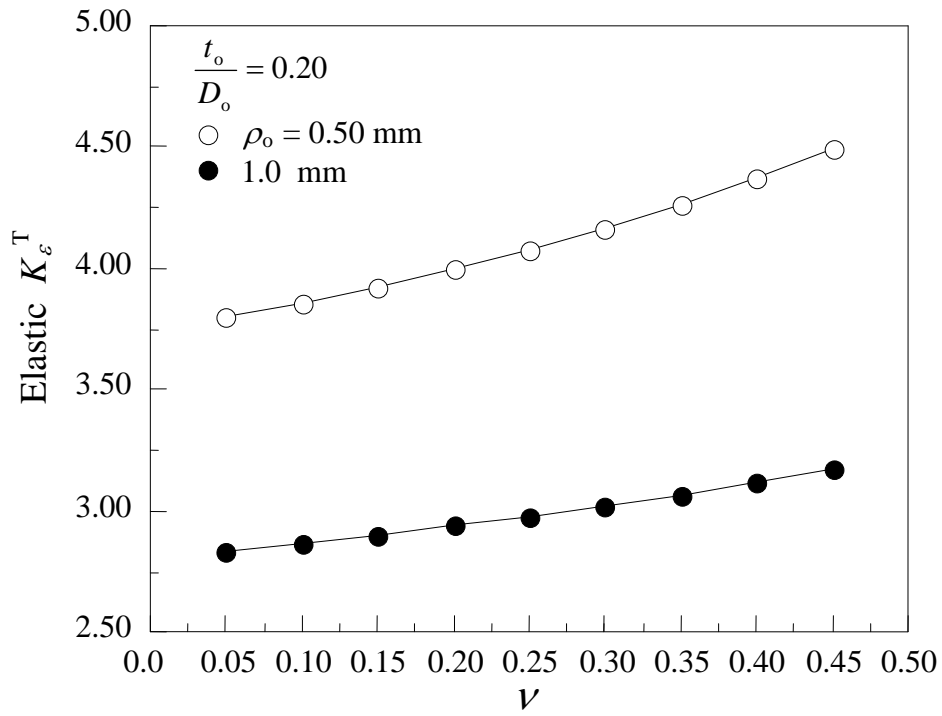


Figure 12. Variation of the elastic K_ϵ^T with Poisson's ratio for $t_o/D_o = 0.20$

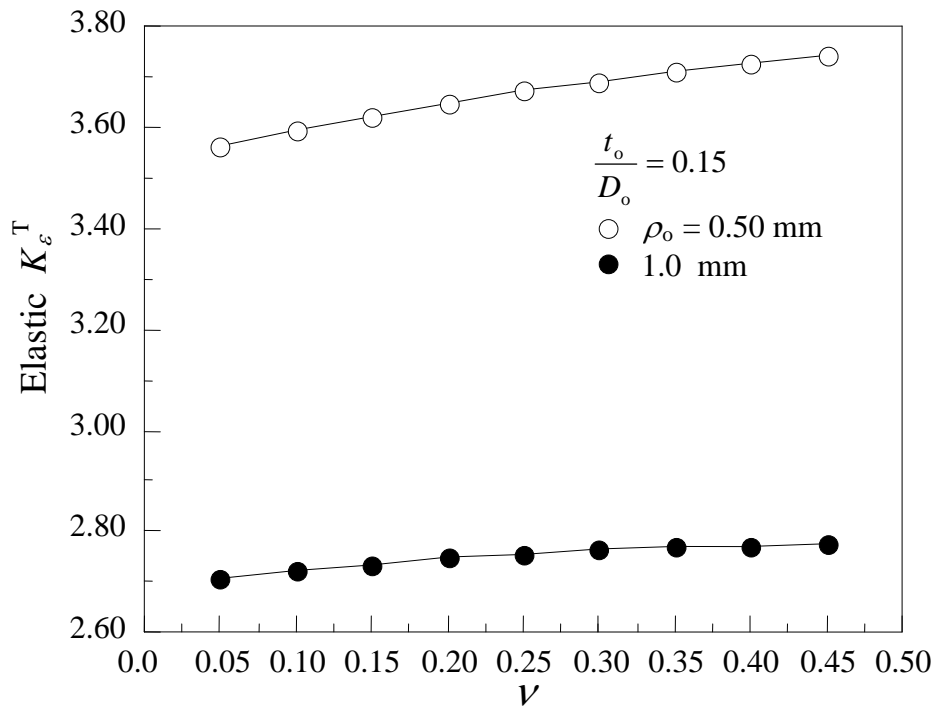


Figure 13. Variation of the elastic K_ϵ^T with Poisson's ratio for $t_o/D_o = 0.15$

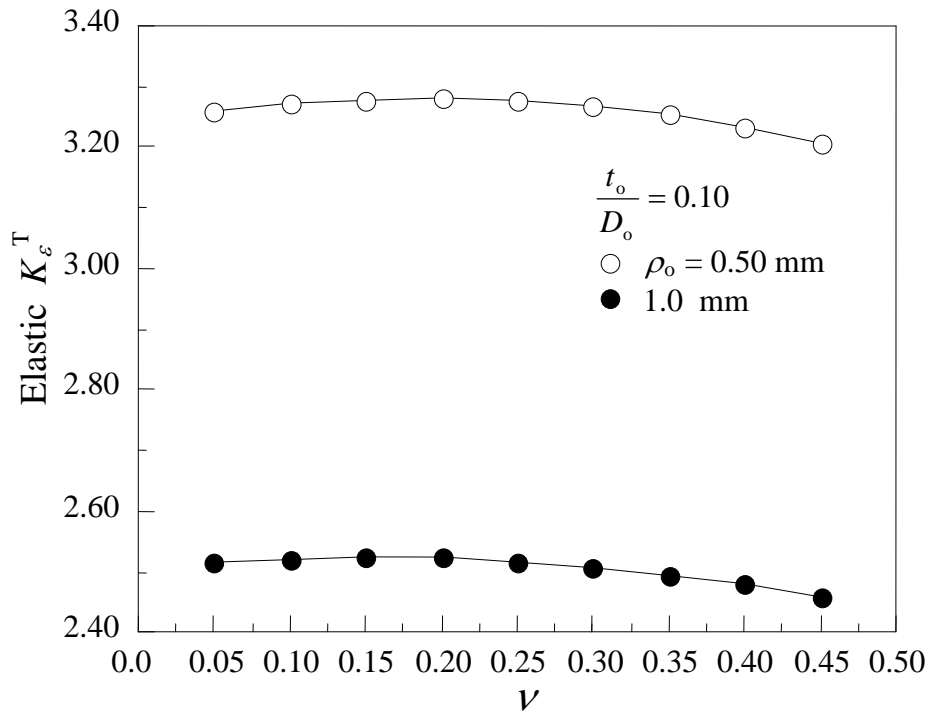


Figure 14. Variation of the elastic K_ϵ^T with Poisson's ratio for $t_o/D_o = 0.10$

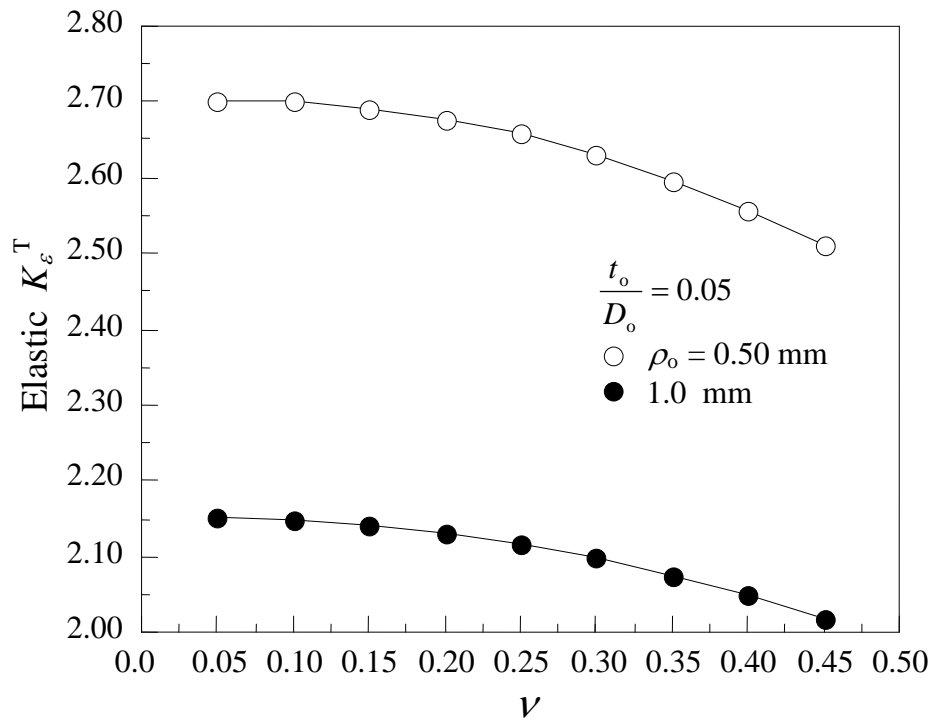
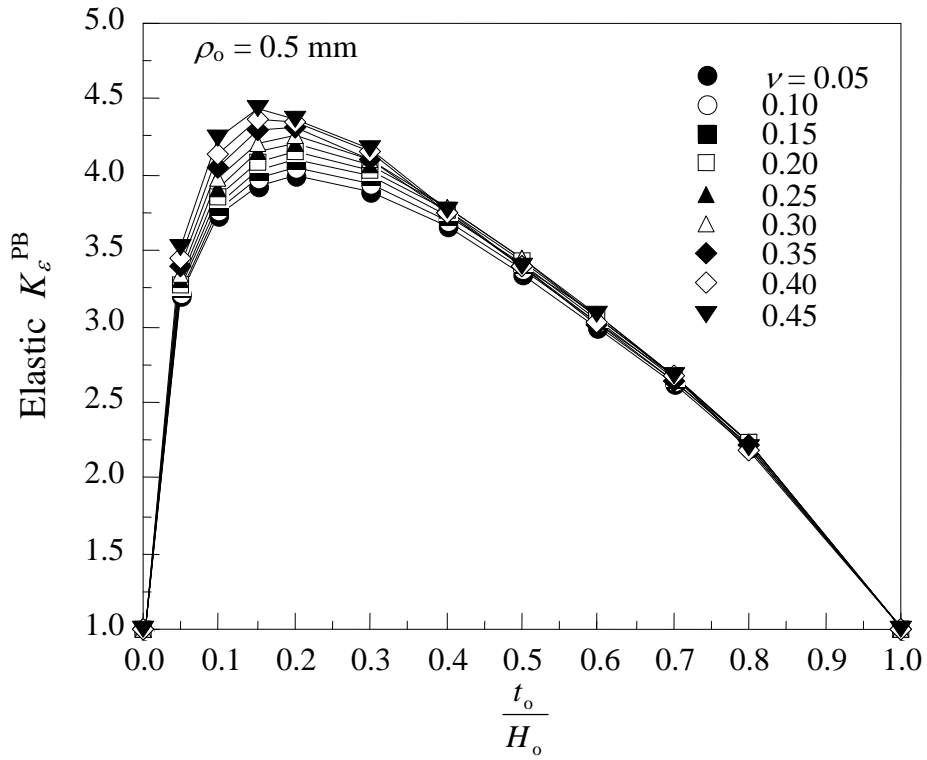
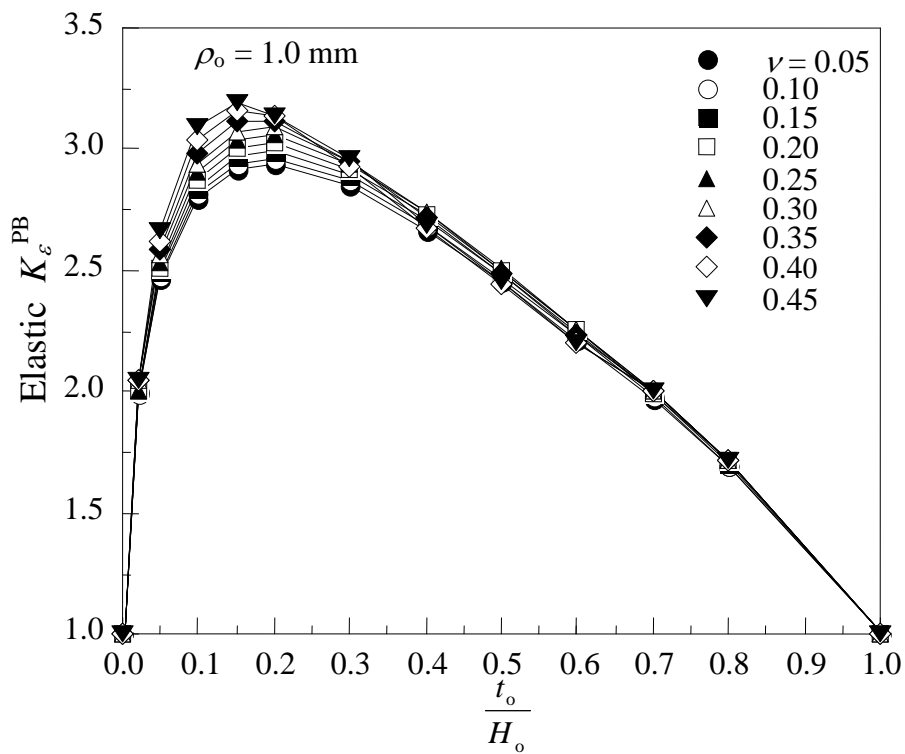


Figure 15. Variation of the elastic K_ϵ^T with Poisson's ratio for $t_o/D_o = 0.05$



(a)



(b)

Figure 16. Effect of Poisson's ratio on the variation of elastic K_ϵ^{PB} with notch depth: (a) $\rho_o = 0.5 \text{ mm}$; (b) $\rho_o = 1.0 \text{ mm}$.

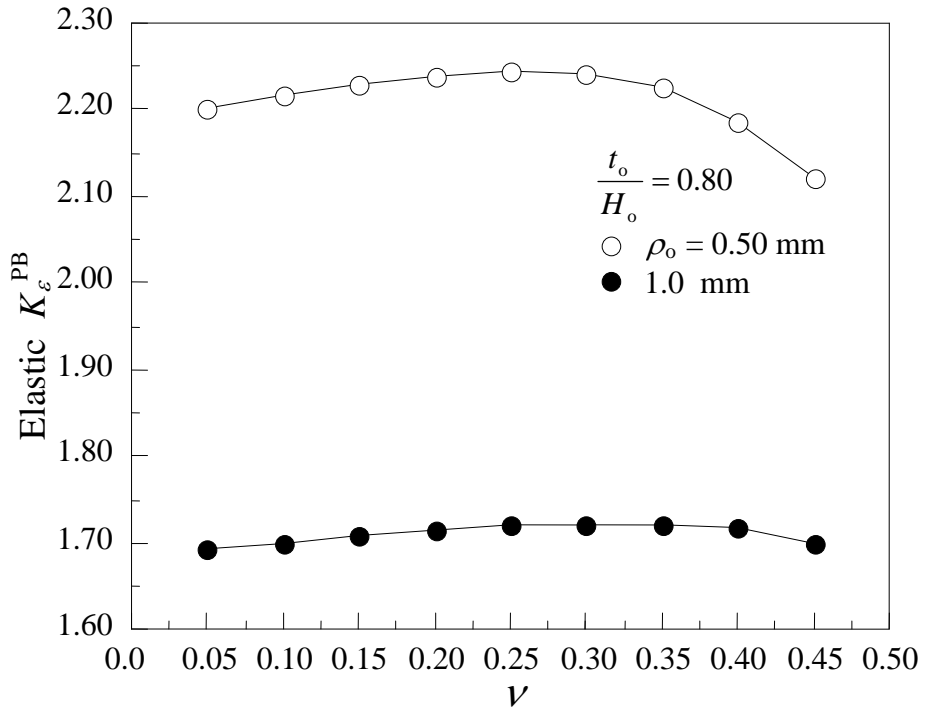


Figure 17. Variation of the elastic K_ϵ^{PB} with Poisson's ratio for $t_o/H_o = 0.80$

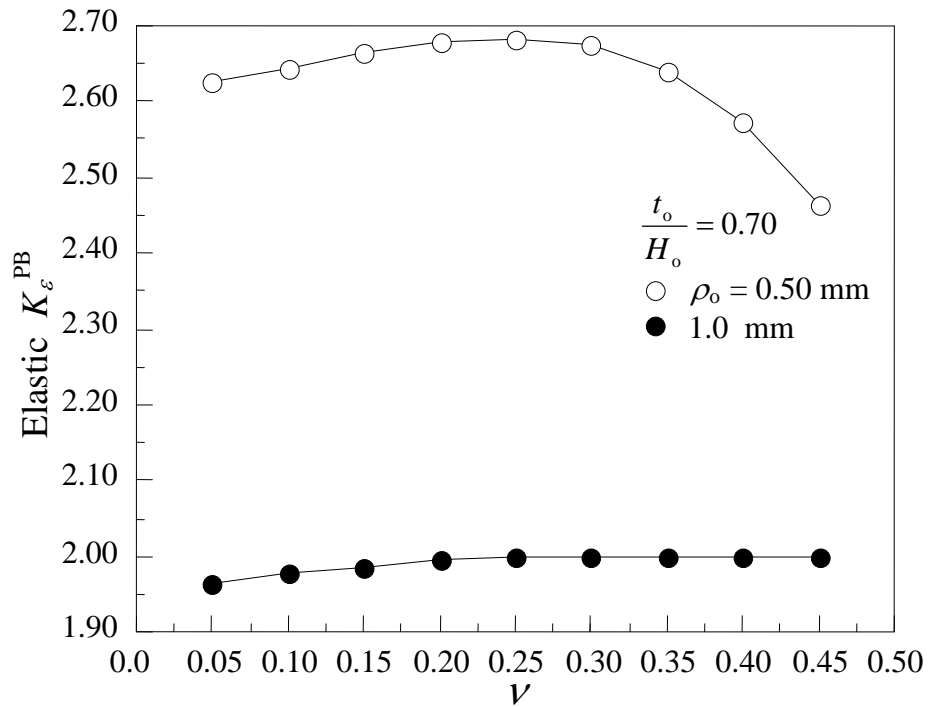


Figure 18. Variation of the elastic K_ϵ^{PB} with Poisson's ratio for $t_o/H_o = 0.70$

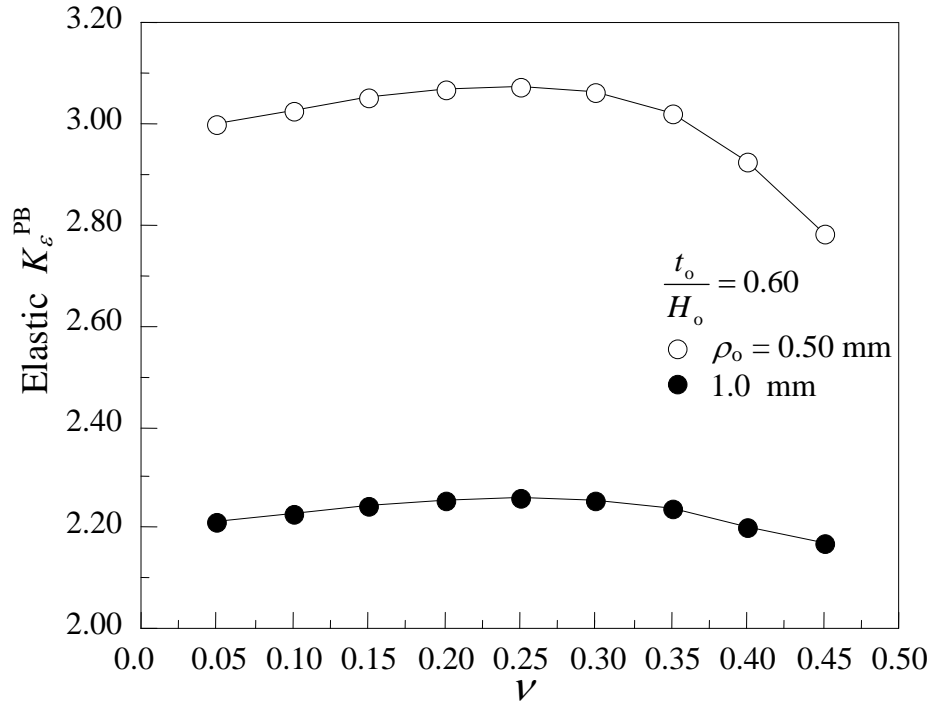


Figure 19. Variation of the elastic K_ϵ^{PB} with Poisson's ratio for $t_o/H_o = 0.60$

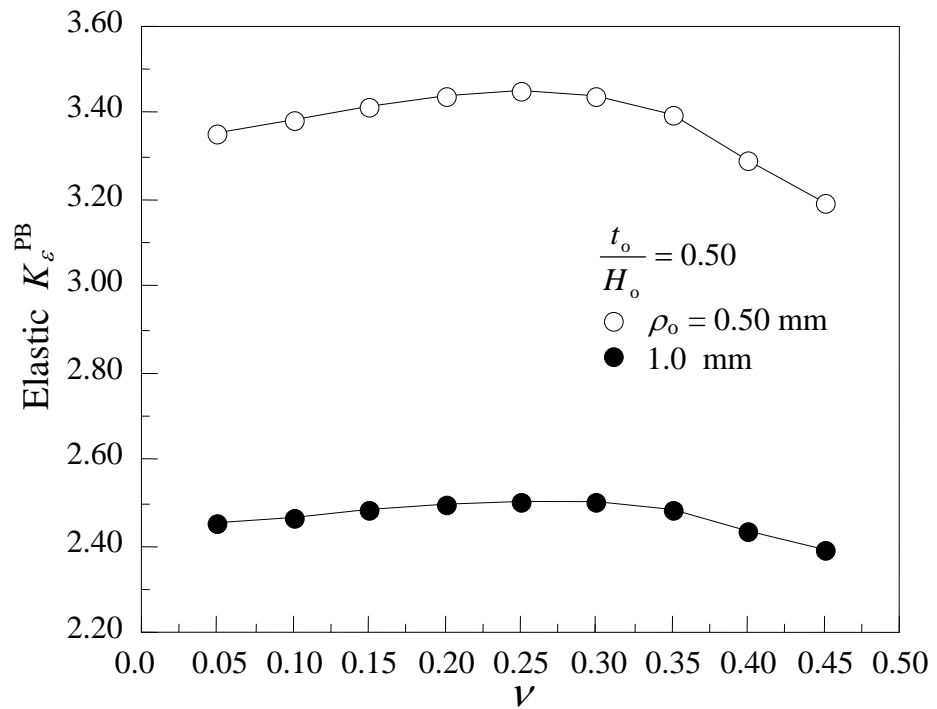


Figure 20. Variation of the elastic K_ϵ^{PB} with Poisson's ratio for $t_o/H_o = 0.50$

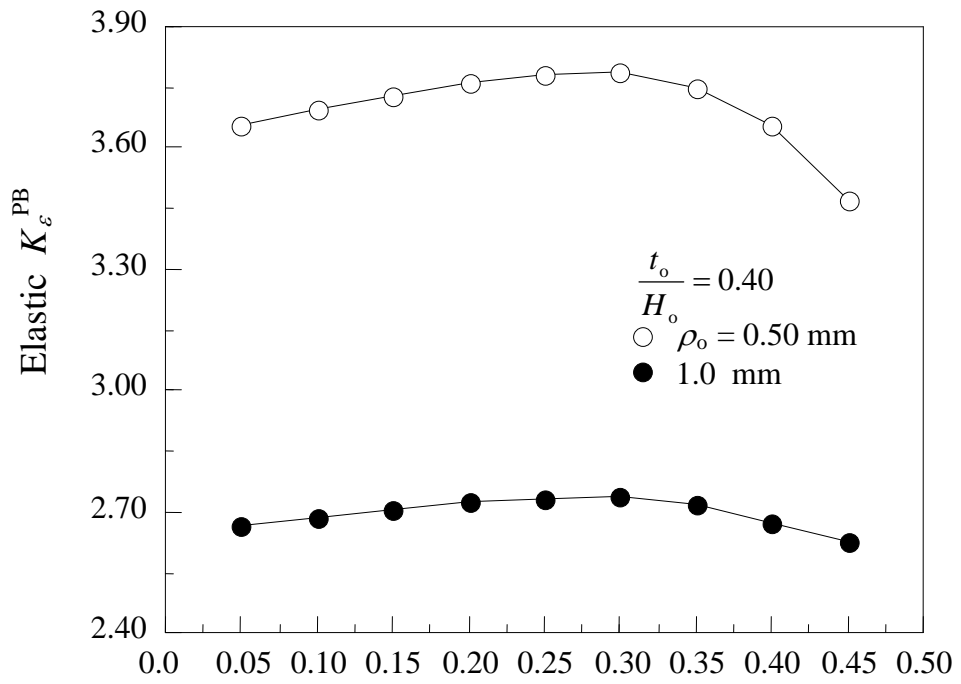


Figure 21. Variation of the elastic K_ϵ^{PB} with Poisson's ratio for $t_o/H_o = 0.40$

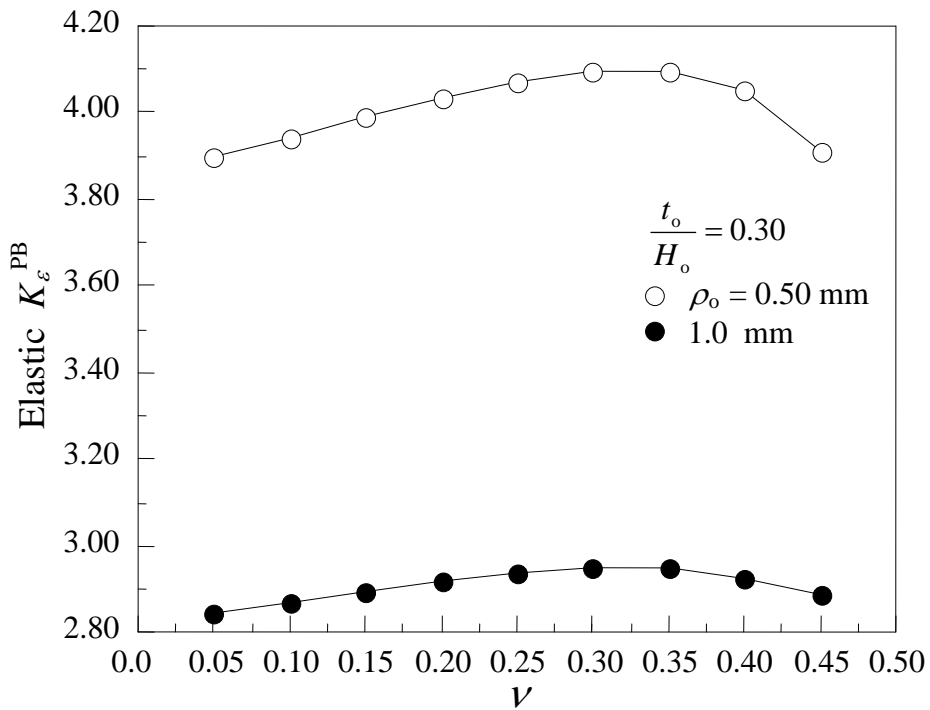


Figure 22. Variation of the elastic K_ϵ^{PB} with Poisson's ratio for $t_o/H_o = 0.30$

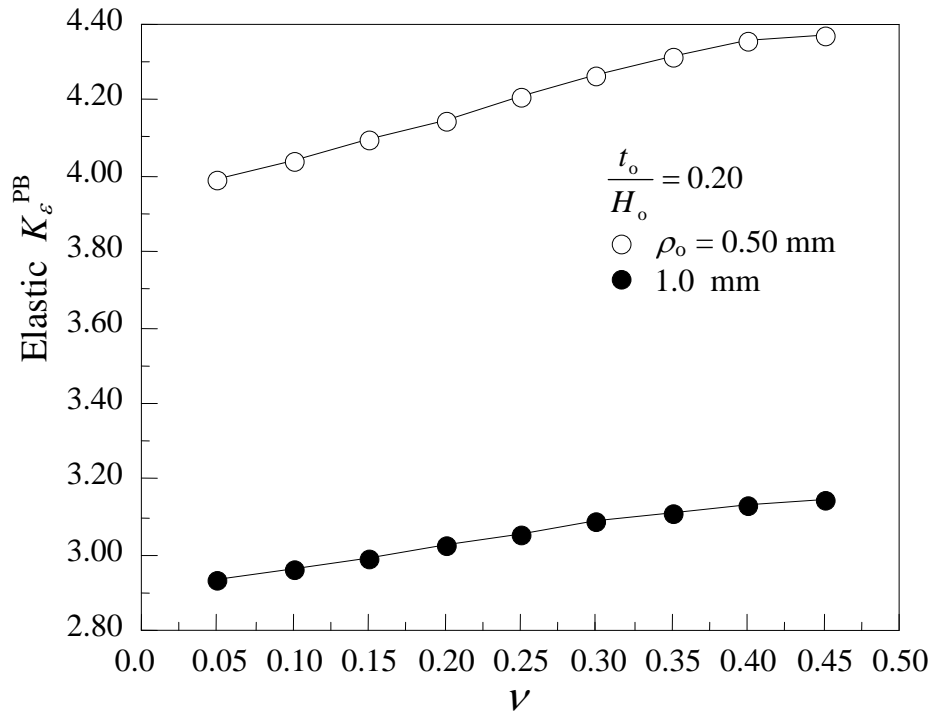


Figure 23. Variation of the elastic K_ϵ^{PB} with Poisson's ratio for $t_o/H_o = 0.20$

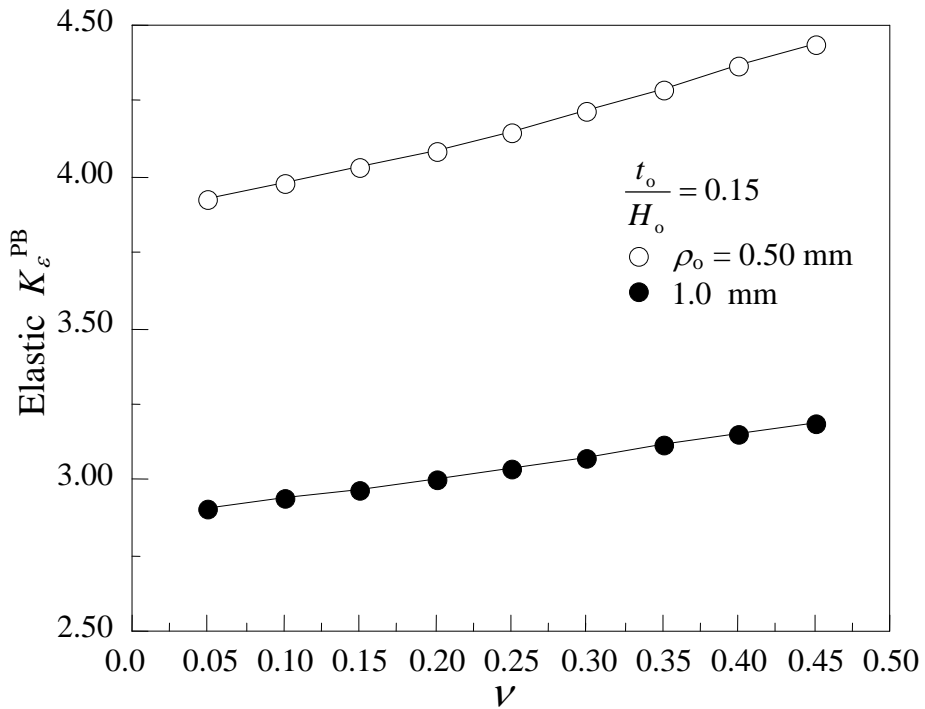


Figure 24. Variation of the elastic K_ϵ^{PB} with Poisson's ratio for $t_o/H_o = 0.15$

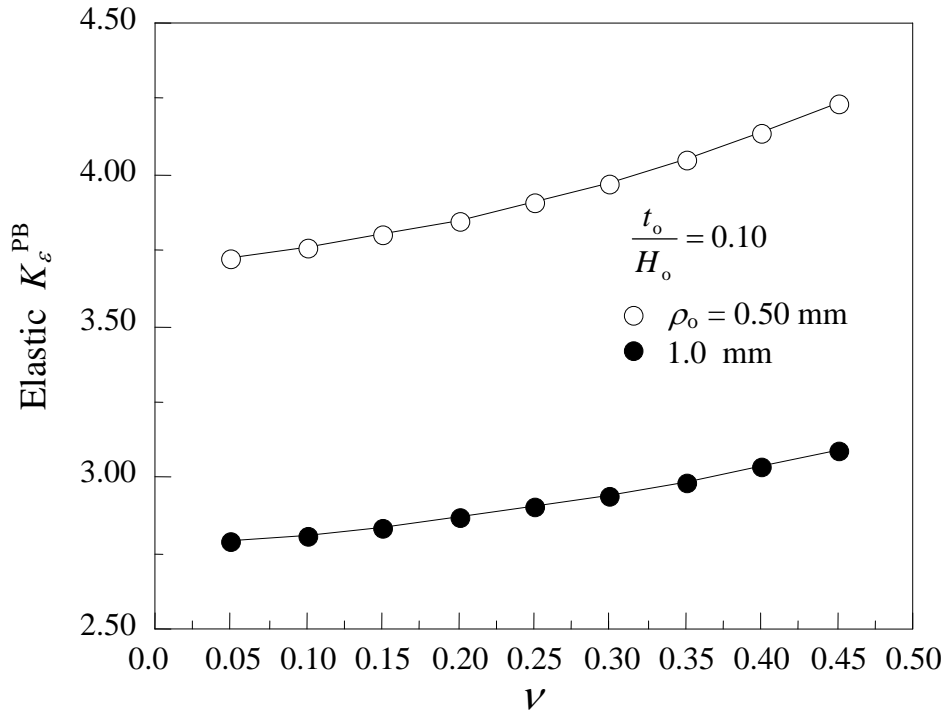


Figure 25. Variation of the elastic K_ϵ^{PB} with Poisson's ratio for $t_o/H_o = 0.10$

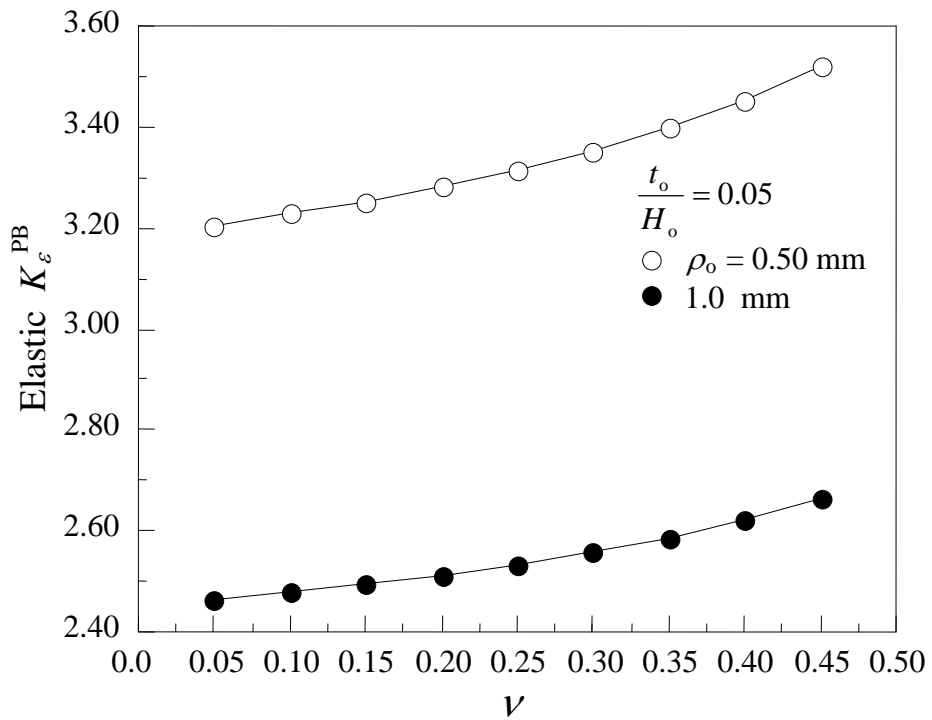


Figure 26. Variation of the elastic K_ϵ^{PB} with Poisson's ratio for $t_o/H_o = 0.05$

Table. 1. Polynomials resulting from curve fitting of the FEM results for static tension and $\rho_o = 0.50$ mm.

ρ_o [mm]	$\frac{t}{D_o}$	Equation $K_{\epsilon}^T =$
0.5	0.80	$2.303 + 0.6345 v - 1.3899 v^2 + 23.665 v^3 - 112.36 v^4 + 313.87 v^5 - 445.97 v^6 + 262.77 v^7$
	0.70	$2.748 + 0.8641 v + 1.8724 v^2 - 3.3241 v^3 + 34.302 v^4 - 90.88 v^5 + 128.69 v^6 - 48.797 v^7$
	0.60	$3.104 + 1.4191 v - 2.8240 v^2 + 44.743 v^3 - 211.89 v^4 + 620.81 v^5 - 933.28 v^6 + 603.86 v^7$
	0.50	$3.423 + 0.3905 v + 19.302 v^2 - 154.04 v^3 + 769.7 v^4 - 2072.1 v^5 + 2914.4 v^6 - 1624.4 v^7$
	0.40	$3.6097 + 1.9307 - 6.55 v^2 + 66.642 v^3 - 284.26 v^4 + 731.44 v^5 - 989.55 v^6 + 578.6 v^7$
	0.35	$3.691 + 1.6355 v - 1.7983 v^2 + 16.036 v^3 - 4.5603 v^4 - 137.21 v^5 + 398.06 v^6 - 317.54 v^7$
	0.30	$3.7024 + 3.0558 v - 30.422 v^2 + 278.71 v^3 - 1347 v^4 + 3668.7 v^5 - 5228.2 v^6 + 3047.8 v^7$
	0.25	$3.7438 + 0.8118 v + 5.8816 v^2 - 40.749 v^3 + 171.74 v^4 - 376.77 v^5 + 419.36 v^6 - 177.33 v^7$
	0.20	$3.6419 + 2.6529 v - 29.416 v^2 + 254.7 v^3 - 1209.5 v^4 + 3208.3 v^5 - 4435.3 v^6 + 2489.1 v^7$
	0.15	$3.4967 + 2.2620 v - 29.017 v^2 + 260.07 v^3 - 1301.7 v^4 + 3613.5 v^5 - 5207.3 v^6 + 3034.8 v^7$
	0.10	$3.2372 + 0.54204 v - 3.1029 v^2 + 14.464 v^3 - 49.615 v^4 + 81.029 v^5 - 51.119 v^6 - 0.25339 v^7$
	0.05	$2.7229 - 1.0816 v + 21.316 v^2 - 204.2 v^3 + 1003.4 v^4 - 2721.2 v^5 + 3823.2 v^6 - 2171.1 v^7$

Table. 2. Polynomials resulting from curve fitting of the FEM results for static tension and $\rho_o = 1.0$ mm.

ρ_o [mm]	$\frac{t}{D_o}$	Equation $K_{\epsilon}^T =$
1.0	0.80	$1.7299 + 0.5262 v - 6.0369 v^2 + 56.693 v^3 - 270.79 v^4 + 720.92 v^5 - 996.78 v^6 + 558.75 v^7$
	0.70	$2.0536 - 0.07801 v + 8.2204 v^2 - 67.199 v^3 + 332.99 v^4 - 906.09 v^5 + 1285.1 v^6 - 736.37 v^7$
	0.60	$2.297 + 0.9437 v - 6.3703 v^2 + 63.84 v^3 - 302.85 v^4 + 815.4 v^5 - 1137.6 v^6 + 647.35 v^7$
	0.50	$2.5261 + 0.5391 v + 3.5491 v^2 - 24.407 v^3 + 129.51 v^4 - 355.82 v^5 + 511.71 v^6 - 291.72 v^7$
	0.40	$2.693 + 0.9186 - 2.7365 v^2 + 35.881 v^3 - 190.41 v^4 + 573.43 v^5 - 880.16 v^6 + 546.3 v^7$
	0.35	$2.7456 + 1.1085 v - 5.6574 v^2 + 54.463 v^3 - 256.11 v^4 + 687.43 v^5 - 958.65 v^6 + 546.11 v^7$
	0.30	$2.7823 + 1.2218 v - 8.5147 v^2 + 77.625 v^3 - 368.41 v^4 + 987.75 v^5 - 1381 v^6 + 787.45 v^7$
	0.25	$2.8002 + 0.8636 v - 4.2863 v^2 + 42.374 v^3 - 216.92 v^4 + 617.76 v^5 - 904.29 v^6 + 533.34 v^7$
	0.20	$2.7716 + 0.78912 v - 5.6636 v^2 + 56.043 v^3 - 303.32 v^4 + 895.46 v^5 - 1349.2 v^6 + 812.61 v^7$
	0.15	$2.7086 - 0.54376 v + 15.579 v^2 - 139.54 v^3 + 669.2 v^4 - 1787.8 v^5 + 2491 v^6 - 1409.5 v^7$
	0.10	$2.4925 + 0.8908 v - 12.387 v^2 + 101.27 v^3 - 481.51 v^4 + 1272.6 v^5 - 1751.9 v^6 + 978.04 v^7$
	0.05	$2.1503 + 0.04384 v + 0.04198 v^2 - 11.006 v^3 + 67.815 v^4 - 213.1 v^5 + 331.52 v^6 - 202.98 v^7$

Table. 3. Polynomials resulting from curve fitting of the FEM results for pure bending and $\rho_o = 0.50$ mm.

ρ_o [mm]	$\frac{t}{H_o}$	Equation $K_{\epsilon}^{PB} =$
0.50	0.80	$2.1808 + 0.4731 v - 1.8732 v^2 + 8.3286 v^3 - 19.422 v^4 + 7.7943 v^5$
	0.70	$2.6043 + 0.4111 v + 0.0289 v^2 + 0.6716 v^3 - 8.4578 v^4 - 2.4607 v^5$
	0.60	$2.9585 + 0.9721 v - 4.8842 v^2 + 24.898 v^3 - 63.281 v^4 + 37.948 v^5$
	0.50	$3.2607 + 2.8499 v - 27.2900 v^2 + 149.6 v^3 - 374.15 v^4 + 318.87 v^5$
	0.40	$3.6145 + 0.7144v + 1.3666 v^2 - 9.5365 v^3 + 27.3440 v^4 - 54.0540 v^5$
	0.30	$3.8622 + 0.5233 v + 5.0319 v^2 - 28.972 v^3 + 80.831 v^4 - 101.85 v^5$
	0.20	$3.9553 + 0.5841 v + 4.3638 v^2 - 21.644 v^3 + 60.393 v^4 - 67.795 v^5$
	0.15	$3.8936 + 0.6563 v + 2.4926 v^2 - 9.0856 v^3 + 25.745 v^4 - 26.355 v^5$
	0.10	$3.6834 + 0.7970 v - 0.8083 v^2 + 7.2817 v^3 - 12.244 v^4 + 10.568 v^5$
	0.05	$3.1814 + 0.4898 v - 0.81951 v^2 + 6.4609 v^3 - 13.182 v^4 + 12.716 v^5$

Table. 4. Polynomials resulting from curve fitting of the FEM results for pure bending and $\rho_o = 1.0$ mm.

ρ_o [mm]	$\frac{t}{H_o}$	Equation $K_{\epsilon}^{PB} =$
1.0	0.80	$1.6891 + 0.01956 v + 1.3972 v^2 - 5.1014 v^3 + 4.0376 v^4 + 2.0317 v^5$
	0.70	$1.959 + 0.02872 v + 2.6651 v^2 - 14.388 v^3 + 28.245 v^4 - 19.385 v^5$
	0.60	$2.1794 + 1.0717 v - 9.7991 v^2 + 53.782 v^3 - 135.78 v^4 + 117.03 v^5$
	0.50	$2.4096 + 1.2559 v - 11.104 v^2 + 60.313 v^3 - 150.83 v^4 + 127.49 v^5$
	0.40	$2.6157 + 1.4347 v - 12.545 v^2 + 68.542 v^3 - 170.4 v^4 + 143.49 v^5$
	0.30	$2.8007 + 1.2122 v - 8.8776 v^2 + 48.666 v^3 - 118.13 v^4 + 94.871 v^5$
	0.20	$2.9063 + 0.6369 v - 1.2349 v^2 + 8.0993 v^3 - 16.997 v^4 + 8.4134 v^5$
	0.15	$2.8872 + 0.4217 v + 1.1411 v^2 - 3.9217 v^3 + 11.871 v^4 - 13.335 v^5$
	0.10	$2.7687 + 0.4255 v + 0.1914 v^2 + 1.4082 v^3 - 1.7842 v^4 + 2.0502 v^5$
	0.05	$2.4510 + 0.2542 v + 0.17601 v^2 + 0.8397 v^3 - 1.5334 v^4 + 2.6662 v^5$

Revision of the Recent Heterogeneous Solid Object Modeling Techniques

Wisam Abu Jadayil

Department of Industrial Engineering,

The Hashemite University,

Zarqa, Jordan 13135

Abstract

This paper discusses the most recent and common technologies for modeling heterogeneous objects composed of more than one material type. Researchers have found the great need for heterogeneous modeling of objects in order to get the required properties of the object material. Eight technologies for modeling heterogeneous objects have been explained and discussed in this review paper. The advantages and disadvantages of each method have been introduced. Two applications of heterogeneous objects were introduced, the heterogeneous turbine blades and the heterogeneous flywheel. Comparison of the most common methods of rapid prototyping has been made in the review.

It has been found that all present heterogeneous modeling technologies have many limitations. So, there it is required to develop an effective heterogeneous modeling technology that takes into consideration both the design geometry and the material composition simultaneously. Using wavelets in the mathematical representation of heterogeneous objects might greatly help in finding that perfect technology.

© 2010 Jordan Journal of Mechanical and Industrial Engineering. All rights reserved

Keywords: : Heterogeneous modeling, Wavelets, Rapid Prototyping, Composite material.

1. Introduction

The modeling and representation of heterogeneous object is an important research area that extensively published nowadays. Recently, several rapid prototyping technologies are at a point where building heterogeneous objects became more realizable. Thus, methodologies to design the 3D object computer model for free fabrication should be developed [1].

Recently, scientists and engineers have studied the manufacturing of heterogeneous objects, mainly in the form of composites. This is because of the many advantages and good properties of heterogeneous products over the homogeneous object product in many applications. But there should be a control for the heterogeneity in order to achieve the desired functionalities [1].

The recent development of heterogeneous object modeling offers new potentials of many applications. That is in heterogeneous object multiple materials are synthesized with certain proportions to provide better properties than that obtained from using any of these materials alone.

In many applications, the product object should have certain properties to be able to resolve its function, like heat resistance and anti-oxidation properties on high temperature side, mechanical toughness and strength on the low temperature side, and the effective thermal stress relaxation throughout the material. Such properties cannot be obtained by using single material or homogeneous

object, so the trend to heterogeneous object modeling is clearly noticed in the recent research [2].

On the other hand, there should be an effective design method, and effective rapid prototyping technology that allows the designer to take into consideration both the design geometry and the material composition simultaneously. In the heterogeneous object design, the properties of that object can be adjusted by controlling the material composition, microstructure and the geometry of the object. So, in order to obtain a heterogeneous object model for analysis and fabrication, an effective design method is needed.

Until recently, prototypes had to be built by model manufacturer from 2D engineering drawings. Of course this has many disadvantages, like time-consuming, high costs and the less precision in identical products. But nowadays, using CAM/CAD technologies made prototypes are rapidly produced from 3D computer model [3]. This describes how much it is important to improve these technologies.

The term for describing a process of producing accurate parts directly from CAD models in few hours, with little need for human intervention, is Rapid prototyping (RP) [3].

From the advantages of the advance of the rapid prototyping (RP), or solid free form fabrication (SSF) is that it eliminates the high cost of tooling and design changes or material substitution. This is by allowing rapid fabrication of form and fit models without the need for tooling or extensive machining. Through service bureaus, RP has become increasingly available to small businesses.

An approach for direct fabrication of components that can be used for a wide range of engineering materials is the computer-aided manufacturing [4].

The main advantage of the RP is the ability to quickly translate the computer aided design (CAD) databases into solid facsimiles of concept designs to help with production development.

Building shapes using selective material-additive processes has a far-reaching advantage; the creation of heterogeneous structure composed of multi material regions with prefabricated devices embedded into the structure. Fabrication of heterogeneous structure is so important that it enables the realization of new and complex designs. The layered manufacturing (LM) processes consist of two-step methodology. The first step is to decompose the 3D CAD model of the object into cross-sectional layers, and the second step is to use material additive processes to physically build up these layers and form the object (CAM) [5].

There are many different technologies of object modeling and rapid prototyping. Each of them has its advantages over the other technologies and has its limitations, which makes the door still opened for more research in this field.

This paper is mainly talking about the main technologies developed for object modeling. The characteristics and limitations of those technologies are described in section 2. Section 3 contains two examples of the applications of two recent technologies. And since the object modeling is the first step of object manufacturing, this paper is talking briefly, in section 4, about the rapid prototyping technologies the second and final step in the manufacturing of an object. Section 5 describes the advantages and limitations of the modeling and RP technologies, the discussion of these advantages and limitations and the need for new technology and future directions of research is in section 6. Finally, the conclusion is stated in section 7.

2. Computer Aided Design Models for Heterogeneous Objects

The following research topics clarify the development stages that the computer Aided Design models for heterogeneous objects have passed through:

2.1 Boundary Representation of Polyhedral Heterogeneous Solids

A paper of Feito and Torres in 1997 [6] presents a formal model for the boundary representation (B-Rep) of polyhedral heterogeneous solids based on a theoretical model of graphic objects. The theoretical model is the graphic object algebra, with which they managed solid modeling by enumeration, sweeping and CSG.

A formal mapping was established between the graphic objects and solid models for heterogeneous objects, which was represented by CSG and B-rep. They described the heterogeneous general polyhedron, manifold and non-manifold, with and without holes, using the algebra. Regularized operations in the algebra are the generalization of Boolean regularized operations in solid

modeling. Feito and Torres had utilized from studying of these operations to propose a B-rep method for managing graphic objects described by their boundaries. The main advantage of this is that it facilitates an abstract uniform treatment of the most important solid modeling methods.

This paper had presented a formulation of solid modeling based on the concept of graphic algebra. Feito and Torres had defined regularized operations and they proved which properties give the algebra of graphic objects a structure of vector space and Boolean algebra. This helped them so much to obtain a simple implementation. In this paper, the existence of simple objects as a generator system had been proved, which allowed them to obtain any polyhedral object starting from surplices [6].

This method presented in this paper is limited to polyhedral heterogeneous solids, which means it cannot be generalized for all heterogeneous object modeling.

2.2 Integrating the Material Information Along with the Geometry Topology in the Solid Model

Kumar and Dutta (1997) proposed a new approach for modeling and representation of heterogeneous objects. In this paper they presented an approach to model and represent heterogeneous objects by integrating the material information along with the geometry topology in the solid model. They defined new modeling operations for creating and manipulating heterogeneous models and to complement traditional modeling operations. More over, they addressed the issue of computer representation of these new models [7].

By modeling and representing heterogeneous objects, they referred to the creation of a CAD model, which contains full information about the geometry, topology and material. Which means this paper had taken into consideration both the geometry and material information?

The word 'geometry' had been used to refer to both the geometry and the topology of the object. But in this paper Kumar and Dutta focused on modeling heterogeneous objects by including the variation in composition along with the geometry in the solid model. Modeling and representing the microstructure of the heterogeneous objects is a complicated problem and is beyond the scope of this paper.

This paper produces two-step process for generating the solid model. Firstly, a valid mathematical model has to be created which precisely and fully describes the shape of the object. Then, the generated mathematical model has to be stored in the computer unambiguously with minimal loss of information.

In this paper, they developed a new modeling system for heterogeneous objects. A new mathematical model for heterogeneous objects was proposed, and a computer representation for the proposed model was developed.

Kumar and Dutta had used r-sets as the basis for representing the geometry of the heterogeneous objects, and found that \mathbf{R}^n endowed with a vector space structure, is a suitable mathematical space for defining the material composition, with each dimension representing one particular primary material. The appropriate mathematical space to model heterogeneous objects is the product space $\mathbf{T} = \mathbf{E}^3 * \mathbf{R}^n$. Specifically, the material points are restricted to lie in a subset of \mathbf{R}^n called the material space \mathbf{V} . The r_m -

object is defined as the mathematical model for representing heterogeneous objects and is termed the heterogeneous solid model. The geometry of the object is captured by r -sets and the material variation is specified in each r -set by material functions.

In the application mentioned in this paper, the heterogeneous objects have material variation in only one direction, which is across the thickness or the interface region, and the commonly used distribution (or function) for these objects, is the power law.

It can be clearly seen in this work that new model (r_m - object) for representing heterogeneous objects was proposed. But the r_m -set is not general enough to model heterogeneous objects, and hence, a heterogeneous solid model, termed as r_m -object, was defined as a set of r_m -sets $\{(P_i, B_i)\}$ which are geometrically interior disjoint and are minimal. The r_m -sets capture different regions of the objects whose material can be discrete (constant) or varying continuously.

This work came at a time when all current solid modeling techniques model physical objects by representing their geometry and topology. These methods are inadequate to handle heterogeneous objects because they do not explicitly represent the object interior. On the other hand, to include material information of an object this paper proposed solid modeling schemes for heterogeneous objects by expanding beyond geometry/topology representation (based on r -sets).

Kumar and Dutta had presented another paper in 1997 in which they proposed a solid modeling scheme for materially graded objects by extending beyond geometry and topology representation based on the r -sets, to material variation in the object. The computer representation of this model was built on the existing B-Rep scheme, which made it easy to be adapted in the solid modeling systems.

Kumar and Dutta had a third paper in 1997 that has an approach to modeling multi-material objects. In this paper new mathematical model is proposed which extends the theory of r -sets and regularized Booleans to include the material information besides the topology and the geometry. This enables the r -set classes to model objects made of a finite number of materials. To facilitate the creation and the manipulations of such models, the material based Boolean operations were defined.

It can be clearly seen that the r_m -classes and the material based Boolean operations encompasses the earlier theory of the r -sets and regularized boolean proposed in the previous papers. The main advantages of this modeling scheme are that it can be built on top of existing solid modelers.

2.3 Multi-Volume CAD Modeling for Heterogeneous Object Design and Fabrication

This is a paper for SUN Wei (2000), in which the multi-volume CAD modeling system is presented based on non-manifold topological elements. Material identifications are defined as design attributes introduced along with geometric and topological information at the design stage. According to the associated material identifications in the developed multi-volume modeling system for heterogeneous object extended Euler operation and

reasoning Boolean operations for merging and extraction are executed.

Wei see that most conventional feature-based design methods are only applicable to model homogeneous structure because the features are defined and interpreted by assuming the description of the workplace as a pre-defined fabrication processing. Further more, techniques used in most rapid prototyping systems are based on the concept of material addition. The database in STL file converted from solid CAD model only contains geometric information. Therefore, feature-based design modeling is not suitable for heterogeneous structure fabrication. And so, research on multi-material and multi-attribute CAD modeling has become a recent focus.

This paper presents the salient features of the multi-volume CAD modeling useful to construct heterogeneous design objects in non-manifold geometric space. The material information is defined as design attributes and introduced along with geometric and topological information at the design stage. Extended Euler operations are used with reasoning Boolean merging and extraction operation to manipulate the design information.

So, future work should focus on developing this approach to include the formation and construction of a hierarchical structure to link feature-based design with non-manifold geometric modeling. Application of the model to solid free-form fabrication and developing advanced control algorithm tailored for the heterogeneous-material modeling information will also need to be pursued.

2.4 Modeling and Designing Functionally Graded Material Components for Fabrication with Local Composition Control

This is a paper for Jackson et. al. (1999), it presents an approach to modeling a part's geometry, topology, and composition. Their approach is based on subdividing the solid model into sub-regions, such that each region has its associated analytic composition blending functions. The blending functions had been used to define the composition throughout the model as mixtures of the primary materials available to the Solid Free Form (SFF) machine.

This paper sees that systems used for 3D object representation are based on one of the three different classes of solid modeling methods: Decomposition Models; Constructive Solid Geometry (CSG); or Boundary Representation (B-rep). Each has its merits, but their current implementations in the CAD/CAM industry do not easily permit manufacturing parts with Local Composition Control (LCC).

In fabrication with LCC not only the data structure representing all of the relevant information for its fabrication must be established, but also solid modeling method must go one step further and represent smoothly varying compositions. To be able to do this, an FGM solid modeling method must decompose the interior of the object into simpler sub-regions, each of which references information about the composition variation over its domain. This goal had been accomplished by using FGM solid modeling method based on a representation known as the cell-tuple data structure, which had been developed in a prototype form.

In traditional cell-tuple structure, a model M is decomposed into a set of cells C with each cell c_k representing a topological feature in the model, such as a vertex, edge, face or region. To represent an FGM model within the cell-tuple structure, composition information as well as geometric information is associated with each cell. In this paper approach, they had simplified the problem by beginning with models subdivided into tetrahedral meshes, permitting the use of standard meshing algorithms to convert traditional solid models to their cell-tuple representation. However, Jackson *et. al.* see that their method of subdividing the models is not the optimum, and methods for efficiently subdivide models into optimal sub-regions remains an open issue.

This paper opens the door for future work in many possible directions in the area of FGM modeling. These include implementing a larger library of cells, proposing new design and visualization methods, and establishing efficient and logical methods for subdividing traditional B-rep models into sub-regions of graded composition.

2.5 A Computational Approach to Multi-Material Solid Free Form Design Using Simulated Annealing

A computational model using the space-filling technique was developed by Khandelwal and Kesavadas to arrive an optimum way of designing such prototypes. Simulated Annealing was successfully implemented for this problem, which has ill-behaved objective function and non-convex design space characteristics. Although the computational methodology for building such multi-material SFF parts has been demonstrated successfully in this paper, but the hardware implementation requires more research.

2.6 Multiple Material Objects: from CAD Representation to Data Format for Rapid Prototyping

The information about the materials of the objects that the CAD system is used for the design work cannot be included in the contemporary CAD systems. That the production engineer usually supplies this information at the computer aided manufacturing stage. But this arrangement is inadequate in the rapid prototyping techniques even it allows multiple material objects to be produced.

So, Chiu and Tan (2000) in this paper came to propose a scheme for representing multiple material objects in the CAD system. That is multiple material objects could be fabricated in RP machine by building the material tree of the object in the CAD system's data structure, then the information is extracted from material tree, and a modified version of the STL file format is outputting to the RP machines.

Kumar and Dutta (1998) had introduced an approach for modeling multiple material objects. Their approach incorporates the representing of the material information into the representing of the geometry and topology of the object. The object is decomposed into multiple cells such that, each cell containing one type of material.

On the other hand, Chiu and Tan (2000) had proposed an alternative representation scheme for manipulating multiple material objects. They used material tree structure to represent multiple material objects, and so there is no need to subdivide into multiple cells for storing material

information, but the material information can be obtained directly from the material tree of the material boundary surfaces together with the topological and the geometrical information.

The modified STL file is a tree structure. By grouping the facets belonging to the same material boundary together, an integer representing the material index of that material boundary is assigned to the group of the facets. The arrangement of the groups of facets in the file is according to the material tree of the object. The number of the facets contained in the modified STL is sharply increased comparing to that of the original file, because as the material boundary surfaces are added into the geometrical model, more facets are formed.

2.7 'Source-Based' Heterogeneous Solid Modeling

The 'source-based' modeling scheme for heterogeneous objects had been presented and the concept of 'grading source' is proposed in the paper of Siu and Tan (2002).

In the 'source-based' modeling scheme, the object is acting as a container that is used to keep the material composition information. The content of this container is affected only by the 'water-tap', which is termed as the grading source. Which means that the geometry of the object itself is not affected by modeling of the material grading? Hence, the modifications of the material grading such as shifting, deletion and re-assignment can be done without the rearrangement of the object geometry.

The field of grading is formed when a grading source is assigned to a reference and the Euclidean space E^3 is fully occupied by the grading source. Material grading occurs in the intersection between the object and the grading sources, and according to the material distribution function $f(d)$ three grading regions and new defining operators can be defined.

Siu and Tan (2002) believed that based on their modeling scheme; there should be a development of more complicated systems for modeling operations between the containers (heterogeneous objects). To give a larger modeling flexibility to the system, they should take into considerations a larger variety of 'grading sources' and the compromised solutions between the different grading sources after Boolean operations on the containers. Further more, a modified sliced format which supports material distribution function needs to be addressed thoroughly.

Siu and Tan came back again in 2002 to present new paper discussing the scheme for modeling the material grading and structures of heterogeneous objects. In this work they focused on discussing an enhanced heterogeneous solid modeling scheme that has the capability to incorporate structure information such as the dimensions and orientation of fiber reinforcements within the heterogeneous object. On fabrication, a contour subdivision algorithm is used to discretize the material variation in each slice of the heterogeneous object.

In Siu and Tan (2002) second paper, a modeling scheme for heterogeneous objects with structure variation in the dimensions and orientation had been described, but in this study, only 1D orientation variation had been considered.

2.8 Physics-Based Design of Heterogeneous Objects

Qian and Dutta (2003) had presented a new approach for the design of the heterogeneous objects. The modeling in this approach is physics based. By specifying the material variation constrains the designer can guide the design process in this method. Only few parameters has to be used by the designer, which have the physical meaning, to make control for material composition. The material property variation is directly conceivable to the designer during the control process.

3. Applications of the Computer Aided Design Models for Heterogeneous Objects

The following are two examples to show some of the applications of the heterogeneous objects modeling:

3.1 Design of Heterogeneous Turbine Blade

The first example had been presented by Qian and Dutta (2003). This paper presents a new approach for turbine blade design, which ties B-spline representation of a turbine blade to a physics (diffusion) process.

The mathematical formulation of the approach includes three steps: using B-spline to represent the turbine blade, using diffusion equation to generate material composition variation, using finite element method to solve the constrained diffusion equation. The implementation and example presented to validate the effectiveness of this approach for heterogeneous turbine blade design.

3.2 Heterogeneous Flywheel Modeling and Optimization

This is a paper for Huang and Fadel in 2000. They demonstrate how to apply Kumar and Dutta's modeling techniques to two different kinds of flywheels, the first one consisting of finite number of distinct materials and the other consisting of two or more primary materials with continuous volume fraction variation (gradient materials). They also developed the corresponding cell-based and basis-function-based multi-objective optimization methods. These multi-objective optimization methods can be extended to the multi-objective optimization design of other heterogeneous objects.

In the conclusion of this paper, they found that Dutta's modeling methods could be applied successfully in heterogeneous flywheel modeling.

The modeling of the flywheel had been based of the following modeling techniques proposed by Kumar and Dutta; modeling of heterogeneous objects consisting of a finite number of distinct uniform materials (HD), and modeling of heterogeneous objects consisting of two or more primary materials with continuous material variation (HC).

Dutta's modeling methods had been applied successfully in heterogeneous flywheel modeling applications. Compared with cell-based approach, the basis-function based approach gives more smooth material and stress variations and saves computational time. However the cell-

based model is more suitable for rapid prototyping fabrication than the basis-function-based model if two discrete materials are used.

4. Rapid Prototyping Techniques

4.1 Direct Photo Shaping Solid Free Form Fabrication

Ventura et. al. had presented a new multiplayer solid freeform fabrication process, 'Direct Photo Shaping' (DPS). In this technique, the visible digital light projection is used as a mask-less tool to build images on photo-curable ceramic dispersions (ceramic powders in photo-polymerizable liquid monomers) by flood exposure.

Direct photo shaping is a multiplayer fabrication process developed by SRI International. This process is based on layer-by-layer photo-curing of polymerizable compositions curable by visible light.

Ventura et. al. had proposed many advantages for DPS, from these advantages:

- Since each layer is shaped by flood exposure, we will get fast build up time, and so we can cure the entire profile at once.
- Minimum number of steps that is no post-processing after the fabrication of each layer is needed.
- Low cost.
- High resolution.

4.2 Solid Free Form Fabrication by Selective Area Laser Decomposition

This is a paper developed by Jakubenas et. al. in 1998. It talks about the Selective Area Laser Decomposition (SALD) as a gas phase solid free form fabrication approach to the shaping of materials without part specific tooling. SALD uses a laser beam to create a localized heated zone on a substrate-surrounded by a reactant gas.

As indicated in this paper, SALD using multiple gas precursors presents the potential for controlling both composition and microstructure in a defined shape for a wide range of materials. However, the work presented by Jakubenas et. al. does not exhaust the potential of SALD for multiple materials deposition. So, there still are many important issues to be examined to emphasize additional capabilities of the process.

4.3 Adaptive Slicing of Heterogeneous Solid Models for Layered Manufacturing

Kumar et. al. (1999) focuses on the adaptive slicing of heterogeneous objects for fabrication using LM. It is assumed that an appropriate build direction (set to be z-direction) has been chosen.

The aim of the adaptive slicing is two folds, the Dimensional Control and the Positional Control. Dimensional control achieves user specified quality in the least build time. The user specifies the surface quality as the maximum allowably cusp height for the LM model. By using one of the following strategies the positional control ensures the validity of the LM model with respect to the nominal shape. The first strategy is the 'excess deposition', in which the LM model completely encloses the nominal solid model (i.e., cusps lie outside requiring the excess

material to be removed). In the Alternative strategy 'deficient decomposition', the LM lies completely within the nominal solid model (i.e., cusps lie inside requiring a filler material).

In this paper, they had described a procedure for adaptive slicing of heterogeneous models to achieve dimensional and positional control of the LM part. The dimensional control was achieved by taking into considerations both the geometry and the material information. The geometry means the curvature of the user specified surfaces along the build direction, whereas the material information means the material variation along the build direction.

Kumar et. al. see that layer generation for a heterogeneous object is a complicated problem and there are several choices exist which are dedicated by the positional control parameters. They had discussed the appropriate strategies for these choices in their paper, and presented an algorithm that summarizes the procedure.

In this paper, Kumar et. al. did not consider the material resolution and the material variation for generating the tool-paths. A generic procedure for tool path generation for heterogeneous layers must consider both the material resolution and the geometry resolution of the process.

4.4 A Computational Approach to Multi-Material Solid Free Form Fabrication Using Simulated Annealing

This paper is by Khandelwal and Kesavadas, it a novel concept for rapidly building SFF parts by inserting prefabricated inserts into the fabricated part. To determine an ideal placement of inserts/cores in the CAD model of the part being prototyped, an algorithm was developed using the heuristic optimization technique called Simulated Annealing.

This approach has many advantages, that it will allow designers to build multi-material prototypes using Rapid Prototyping (RP) technique. More over, by using cheaper pre-fabricates instead of costly photopolymers, the production cost of the SFFs can be reduced, and it will result in reduction in the build up time, and so efficient machine utilization.

Although the name Rapid Prototyping suggests that the process is fast, the fact is that it is still a very slow and inefficient process, as the authors say. RP is an adaptive technique where layer upon layer is built progressively until the entire part is completed. Build-up time is often not a function of the geometric complexity of the part, but that of the volume and height of the part.

The second limitation of the RP technique is that only a limited choice of materials is available. Most of the RP techniques use photosensitive polymer resins.

4.5 Solid Free Form Fabrication Using Stereolithography

Perhaps the most popular among currently available RP technologies is stereolithography. The basis of the stereolithography is the formation of polymer from a photosensitive monomer resin when it is subjected to ultraviolet light.

The purpose of the paper presented by Lange and Bhavnani (1994) is to present information on how the SSF

using stereolithography process can help reduce cost and cycle time for cast metal parts.

To fabricate a part the stereolithography process uses a layer-by-layer solidification of the resin. The cure depth depends on three factors, the laser power, beam diameter and the type of the resin used.

4.6 A Comparison of Rapid Prototyping Technologies

Pham and Gault had presented in 1998 a comprehensive comparison between the rapid prototyping technologies known up to that day. Their paper included comments on the strengths and weaknesses of these technologies.

Pham and Gault (1998) had divided the RP technologies into two main categories, that involves the addition of the material and those involves the removal of the material. Kruth (1991) had divided the material accretion technologies according to the state of the prototype material before part information. Pham and Gault to include new technologies had adapted Kruth's classification. In this classification, the material addition can be divided into three main categories, according to the state of the prototype material before part information, liquid, discrete particles and solid sheets. The liquid may be solidification of a liquid polymer, solidification of an electro-set fluid (ES) or solidification of molten material. The solidification of a liquid polymer may be point by point (SL, LTP, and BIS), layer-by-layer (SGC) or holographic surface (HIS). On the other hand, the solidification of molten material can be point by point (BPM, FDM, 3DW), or layer by layer (SDM).

When the state of material is discrete particles, it can be treated by one of two methods, fusing of particles by laser (SLS, GPD), or joining of particles with a binder (3DP, SF, TSF). And finally when the state of material is solid sheets it can be treated by bounding of sheets with adhesive (LOM), or bounding of sheets with light (SFP).

Pham and Gault (1998) had summarized the main features of the different RP systems in two tables, one for commercial technologies and the other for the technologies still being researched. They found that the most accurate is the dual-jet BPM1 machine, but the maximum part size is small. The cheapest systems are the LOM3 machine and the entry-level DM system. However, LOM3 system has a drawback that parts produced are 'tacky' and so need manual assemblage. Also the low-cost DM machine has disadvantages, that its work envelope is small and it cannot manufacture shapes as complex as those created using the material accretion technologies.

Moreover, Pham and Gault (1998) had presented a figure as a quick guide for selecting RP processes. The selection is based on many factors, the end use of the part, the part size, the accessibility of the features, whether the part is hollow or not, the accuracy of the part and its strength.

5. Selection of the CAD Modeling and the RP Technologies

Table 1 shows the main advantages and limitations of the most recent CAD modeling techniques, whereas Table 2 shows most recent RP technologies, that Pham and Gault

(1998) had compared the RP technologies up to 1998, and summarized their detailed results in tables [3].

Table 1. Comparison of the advantages and the limitations of the most recent CAD modeling technologies

<u>CAD Modeling Technique</u>	<u>Advantages</u>	<u>Limitations</u>
Boundary representation of Polyhedral Heterogeneous Solids	facilitates an abstract uniform treatment of the most important solid modeling methods	limited to polyhedral heterogeneous solids, which means it cannot be generalized for all heterogeneous object modeling
Integrating the Material Information Along with the Geometry Topology in the Solid Model	Had taken into account both the geometry and the material information	-Excludes the modeling and the representation of the microstructure -material variation in only one direction
Multi-Volume CAD Modeling for Heterogeneous Object Design and Fabrication	-multi-volume CAD modeling system is presented based on non-manifold topological elements -material information is introduced along with the geometric and topological information	-Does not include the formation and construction of a hierarchical structure -Application of the model to solid free-form fabrication and developing advanced control algorithm is needed.
Modeling and Designing Functionally graded material Components for Fabrication with Local Composition Control	presents an approach to modeling a part's geometry, topology, and composition	Method of subdividing the models is not the optimum
A Computational Approach to Multi-Material Solid Free Form Design Using Simulated Annealing	-allow designers to build multi-material prototypes -reduction of the production cost -reduction of the build up time -efficient machine utilization	-No hardware Implementation -build up time is a function of the volume and height of the part.
Multiple Material Objects: from CAD Representation to Data Format for Rapid Prototyping	-Representing multiple material objects in the CAD system -The material information can be obtained directly from the material tree	The number of the facets contained in the modified STL is sharply increased
'Source-Based' Heterogeneous Solid Modeling	-Keep the material composition information -modification of the material grading can be done without the rearrangement of the object geometry	Only 1D orientation variation had been considered.
Physics-Based Design of Heterogeneous Turbine Blade	Only few parameters has to be used, which have the physical meaning	Need to be applicable for other applications

Table 2. Comparison of the advantages and the limitations of the most recent RP technologies

<u>RP Technology</u>	<u>Advantages</u>	<u>Limitations</u>
Direct Photo Shaping Solid Free Form Fabrication	<ul style="list-style-type: none"> -Since each layer is shaped by flood exposure, we will get fast build up time, and so we can cure the entire profile at once. -Minimum number of steps that is no post-processing after the fabrication of each layer is needed. -Low cost. -High resolution. 	This process is based on layer-by-layer photo-curing of polymerizable compositions curable by visible light
SFF Fabrication by Selective Area Laser Decomposition	Controlling both composition and microstructure in a defined shape for a wide range of materials	Does not exhaust the potential of SALD for multiple material decomposition
Adaptive Slicing of Heterogeneous Solid Models for Layered Manufacturing	Both the geometry and the material information were taken into consideration	Did not consider the material resolution and the material variation for generating the tool-paths
A Computational Approach to Multi-Material Solid Free Form Fabrication Using Simulated Annealing	<ul style="list-style-type: none"> -allow designers to build multi-material prototypes -reduction of the production cost -reduction of the build up time -efficient machine utilization 	<ul style="list-style-type: none"> -No hardware Implementation -build up time is a function of the volume and height of the part.
Solid Free Form Fabrication Using Stereolithography	Reduction in the cost and the cycle time for cast metal parts	Layer-by-layer fabrication, and the cure depth depends on three factors, the laser power, beam diameter and the type of the resin used

6. Discussion

Table 1 summarizes the main advantages and limitations of the most recent CAD technologies. Of the technologies listed, it can be clearly seen that the computational approach to multi-material solid free form design using simulated annealing has more advantages than the other technologies, but it has more limitations too. Each technology has one advantage or more, and at least one limitation.

The most recent techniques are the 'source-based' heterogeneous solid modeling and the physics-based design of heterogeneous turbine blade, although both of them have new advantages over the previous techniques, but still have some limitations, in the 'source-based' heterogeneous solid modeling only 1D orientation variation had been considered, and this is a special case. The physics-based design had been applied only in the modeling of heterogeneous turbine blade, but it should be

applicable for any application, not only for specific designs.

From this table we can see that until now there is no perfect technique that has all the advantages and no limitations, which make more research, is needed.

On the other hand, Table 2 summarizes the main advantages and limitations of the most recent RP technologies. By looking at this table and tables in reference [3], we can see that also among the recent and the previous RP technologies there is no perfect technology. In spite of this, the direct photo shaping solid free form fabrication and solid free form fabrication using Stereolithography seem to be the most popular RP technologies, because of their many advantages and less limitations.

As can be clearly seen in Table 1, no perfect CAD modeling technology is produced until now. So, more

research is still needed in this field. The perfect technology should include all or most of the listed advantages and no or very little limitations.

The advantages and limitations of a modeling method make it suitable for certain applications and unsuitable for the others. And so, the nature of the engineering application itself determines which CAD model to be used. For example, to design the heterogeneous turbine blade, Qian and Dutta (2001) physics-based approach is so efficient in the design of the heterogeneous turbine blade, but may be this approach is not applicable for other objects of non-physical function. On the other hand, other good modeling approaches may not be applicable for the heterogeneous turbine blade. Or the boundary representation, the turbine blade is not polyhedral. Integrating the material information along with the geometry topology in the solid model approach works only when the material variation is only in one direction, but in the turbine blade, the material variation may be in more than one direction. For the same reason, the 'source-based' heterogeneous solid modeling cannot be applicable for the design of the heterogeneous turbine blade.

Another example is the heterogeneous flywheel modeling; here Kumar and Dutta's modeling techniques were applied successfully, but other modeling techniques may not be applied here. The physics of the flywheel is different from the physics of the turbine blade, so to apply Qian and Dutta (2001) physics-based approach, more research is needed and new problem should be solved. The computational approach to multi-material solid free form design using simulated annealing is insufficient to be applied for the flywheel that the build up time is a function of the volume and the height of the part, and since the flywheel has large volume, the build up time will be long. So, the nature of the engineering application determines the chosen modeling method, but can we have new modeling technology that is efficiently applicable for all engineering applications, this future research should look for.

The main properties that the new technology should include are to include the material information besides the geometry, representing multiple material objects in the CAD system, reduction in the build-up time and production cost, to be efficient and applied easily, consider 2D and 3D orientation variation and to take into considerations the micro-structure. So, future work should look for a new CAD modeling technology that satisfy all or most of these characteristics.

On the other hand, although solid free form fabrication using stereolithography is a popular technique, research is still needed to get new and improved RP technology that avoids the main limitations of the present technologies.

7. Conclusion

Modeling and representation of heterogeneous objects is an important research area, and since building the heterogeneous objects became more realizable using rapid prototyping technologies, then methodologies to design the 3D object computer model for free fabrication should be developed. Although many modeling approaches and

many prototyping technologies have been developed, an effective design method and effective rapid prototyping technology that take into consideration both the design geometry and the material composition simultaneously is still needed.

Future work should be directed towards new modeling approaches of the heterogeneous objects that avoid the limitations of the preset technologies and to have some new properties that make them convenient for all applications, like to be as simply applied as required by the application, and to be applicable for all engineering modeling applications. A good suggestion in that direction is to start using the wavelets in the mathematical representation of heterogeneous objects. Research should be forwarded to this direction in order to find the perfect heterogeneous object technology.

8. References

- [1] T. R. Jackson, H. Liu, N. M. Partikalakis, E. M. Sachs, M. J. Cima, "Modeling and designing functionally graded material components for fabrication with local composition control". *Material and Design*, Vol. 20, 1999, 63-75.
- [2] K. J. Jakubenas, J. M. Sanchez, H. L. Marcus, "Multiple material solid free-form fabrication by selective area laser deposition". *Materials and Design*, Vol. 19, No. 1-2, 1998, 11-18.
- [3] D. T. Pham, R. S. Gault, "A comparison of rapid prototyping technologies". *International Journal of Machine Tools and Manufacture*, Vol. 38, No. 10-11, 1998, 1257-1287.
- [4] A. E. Lange, M. Bhavnani, "Solid free form fabrication using stereolithography". *SAMPE Journal*, Vol. 30, No. 5, 1994, 46-49.
- [5] V. Kumar, P. Kulkarni, D. Dutta, "Adaptive slicing of heterogeneous solid models for layered manufacturing". *Journal of Materials Processing and Manufacturing Science*, Vol. 7, No. 3, 1999, 294-312.
- [6] F. R. Feito, J. C. Torres, "Inclusion test for general polyhedra". *Computers and Graphics*, Vol. 21, No. 1, 1997, 23-30.
- [7] V. Kumar, D. Dutta, D., "An Approach to Modeling Multi-Material Objects". *Symposium on Solid Modeling and Applications*, 1997, 336-345.
- [8] V. Kumar, D. Dutta, "Solid model creation for materially graded objects," Published in *Proceedings of Solid Freeform Fabrication Symposium*, Austin.
- [9] Kumar, V. and Dutta, D., 1997, "An approach to modeling multi-material objects". 4th *Symposium on solid modeling and application*, August 1997, 336-345.
- [10] S. Sun Wei, "Multi-volume CAD modeling for heterogeneous object design and fabrication".

- Journal of Computer Science and Technology, Vol. 15, No. 1, 2000, 27-36.
- [11] D. Khandelwal, D. T. Kesavadas, "Computational approach to multi-material solid freeform fabrication using simulated annealing". Journal of Material Processing and Manufacturing Science, Vol. 7, No. 4, 1999, 405-415.
- [12] W. K. Chiu, S. T. Tan, "Multiple material objects: From CAD representation to data format for rapid prototyping". Computer-aided design, Vol. 32, No. 12, 2000, 707-717.
- [13] V. Kumar, D. Dutta, "An approach to modeling heterogeneous objects". ASME Journal of Mechanical Design, Vol. 120, No. 4, 1998, 659-667.
- [14] Y. K. Siu, S. T. Tan, "Source-based heterogeneous solid modeling". Computer-aided design, Vol. 34, No. 1, 2002, 41-55.
- [15] Y. K. Siu, S. T. Tan, "Modeling the material grading and structures of heterogeneous objects for layered manufacturing". Computer-aided design, Vol. 34, No. 10, 2002, 705-716.
- [16] X. Qian, D. Dutta, D., "Physics-based modeling for heterogeneous objects". Journal of Mechanical Design, Vol. 125, No. 3, 2003, 416-428.
- [17] X. Qian, D. Dutta, "Design of heterogeneous turbine blade". Computer Aided Design, Vol. 35, No. 3, 2003, 319-329.
- [18] J. Huang, G. Fadel, "Heterogeneous flywheel modeling and optimization". Journal of Materials and Design, Vol. 21, No. 2, 2000. 111-125.
- [19] S. Ventura, S. Narang, D. Twait, F. Lange, P. Khandelwal, E. Cohen, "Solid freeform fabrication and design". Ceramic Engineering and Science Proceedings, Vol. 21, No. 4, 2000, 111-119.
- [20] D. Khandelwal, T. Kesavadas, "A computational approach to multi-material solid free form fabrication using simulated annealing". ASME DETC Conference, Baltimore, MD, September 2000.
- [21] Kruth, "Material in-process manufacturing by rapid prototyping techniques". CIRP Annals - Manufacturing Technology, Vol. 40, No. 2, 1991, 603-614.

Hot Water Management of DHW Storage Tank: Supply Features

N. Beithou^{a,*}, M. Abu Hilal^b

^a Department of Mechanical and Industrial Engineering, Applied Science University, Amman, Jordan.

^b Department of Mechanical Engineering, An-Najah National University, Nablus, Palestine

Abstract

The current study is directed to analyze the mixing nature of cold and hot water inside storage tank, and the corresponding effects on the total usable and delivered energy to consumers. The analyses are done for two different supply features bottom and side supply of cold water. An experimental rig consisting of hot water reservoir, cold water reservoir, water pump, flow meter, hot water storage tank (HWST), and a PC with Lab-View data acquisition system, was constructed to collect the necessary data for analyses. Four different flow rates ranging from 1.9 to 10 L/min have been taken under consideration. The results were in a good agreement with the published expectations. As it is well known, low flow rates save more energy in both bottom and side cold water supply (CWS). The comparison between the two supply features showed that the side CWS has higher amount of usable hot water than the bottom CWS at the same flow rate. Side CWS also minimizes the turbulent mixing within the HWST which by its turn supply higher energy for consumers. The bottom supply feature which is easier for assembly, has a bad effect on the total usable hot water and the total amount of energy delivered to the customers. A special mechanism to distribute the water as a uniform layer from the bottom of the tank is currently under investigations.

© 2010 Jordan Journal of Mechanical and Industrial Engineering. All rights reserved

Keywords: Water Management, Hot Water, Cold Water, Mixing Process, Storage Tanks, Usable Energy, Energy Losses..

1. Introduction

World these days is suffering from the shortage in water and energy. Hot water is a precious commodity in most homes and businesses. Companies working with the manufacturing of HWSTs are working a lot to minimize losses of energy in their designs. Many HWST features are available in markets, which may look the same in shape but differ significantly in their heat transfer and flow patterns.

Many Researches have been performed to save energy by insulation, which reduces the heat losses from the HWST and the accompanied piping system [5, 10, and 11]. Special heat exchangers were proposed by Industrial Technology to recover the energy wasted during usage. Approximately 80% to 90% of all hot water energy flows down the drain, carrying with it up to 955 kilowatt-hours (kWh) of energy [8]. In an attempt to reduce the wasted energy, Barta [5] investigated mathematically the optimal insulation thickness. To reduce the heat losses from the plumbing attachments, Jing Song et al. [11] investigated the effects of plumbing attachments on heat losses from solar domestic hot water storage tanks. In purpose to verify the estimated energy savings for hot water systems, J. Wiehagen and J.L. Sikora [4] have studied the performance comparison of residential hot water systems,

in their study a laboratory test experiment was conducted to measure the energy performance of two different types of water heaters; electric storage tank and demand (tankless) heaters for different plumbing distribution systems. Results of simulation showed an increase in overall system efficiency for the demand water heater with a parallel piping distribution system over the storage tank water heater with copper piping.

These studies have been dealing with heat losses reduction, heat recovery from wasted hot water, for maximizing the hot water usage. None of the available published researches investigated what happens inside the storage tank.

As creating new resources of water and clean energy is a hard task, efforts are directed toward conservation and managing the available resources. Actually conservation of resources can be defined as more efficient or effective use of resources [3]. The efficient or effective use of resources requires spreading wide educational programs through people of how to use effectively the available resources. It is extremely important to investigate and analyze what happens while energy and water are consumed, how and why these resources are wasted.

This study is a part of a project aimed to investigate how to use effectively the available hot water resources. The project investigates deeply the hot water temperature variations within the HWST, for different supply features of the HWST.

* Corresponding author. nabil@asu.edu.jo

2. Experimental Test Apparatus

To analyze and investigate the nature of hot water temperature changes within the HWST, data on the variation of the hot water temperature should be collected under the different variable conditions; to achieve these data an experimental rig has been constructed (Figure 1). This experimental rig consist of Hot water reservoir: even though the water in the storage tank is usually heated by

solar energy or electrical energy, heating the water by solar or electrical energy needs time, to eliminate the time required to heat the water a hot water reservoir has been used. It supplies the storage tank by constant temperature hot water about 62 °C immediately when required.

•Cold water reservoir: supplies the hot water storage tank by cold water when required; it also gives the opportunity to control the CWS temperature.

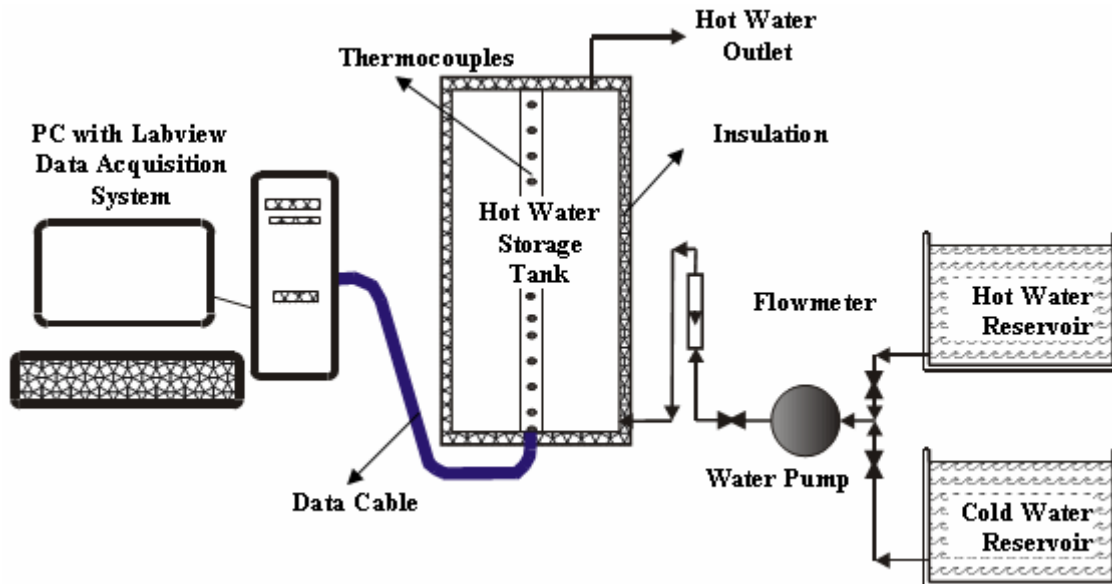


Figure 1. Schematic Diagram for the Experimental Rig

- Water pump: in order to achieve the required flow rate a water pump is used to pump hot or cold water into the storage tank, it gives the head required to overcome the losses within the piping system.
- Flow meter: Used to measure the cold water flow rate entering the hot water storage tank.
- Hot water storage tank: where hot water and cold water are mixed at the specified conditions, it is a cylindrical tank, contains a set of thermocouples to measure the temperature change within the storage tank (see table 1).

Table 1. Dimensions of the Hot Water Storage Tank.

Hot Water Storage Tank	
Height	78 cm
Internal diameter	42 cm
Number of thermocouples	15
Distance between thermocouples	5 cm
Insulation thickness	4 cm
Tank total capacity	0.108 m ³

- Data Acquisition System: (Lab-View software) consist of data cable, data acquisition card, and personal computer, it is used to collect automatically the

temperatures from the storage tank at different times and store it in a separate excel file.

In the experiments done hot water is filled into the HWST from the hot water reservoir, circulated until having a uniform temperature of 62 °C inside the tank, then the cold water from the cold water reservoir is pumped at a specific flow rate into the HWST from a side or bottom opening, the cold water is allowed to be mixed with the hot water, the temperature changes as a result of the mixing process is recorded for analyses purposes.

3. Analyses

Many hot water storage tanks are available in the markets, each has different feature as shown in figure2, some have side cold water supply others have bottom cold water supply. Manufacturers spend a lot of money to insulate the hot water tanks to minimize the heat losses, which is of a great importance in energy conservation. Nevertheless they give less attention to what happen inside the hot water storage tank during usage. The mixing nature and heat transfer mechanism associated with the different used flow rates affects the available amount of hot water to a large extend. In this work attention had been given to understand the variation of temperature for bottom and side flow CWS within the HWST, four different continuous flow rates were used from 1.9 to 10 L/min.

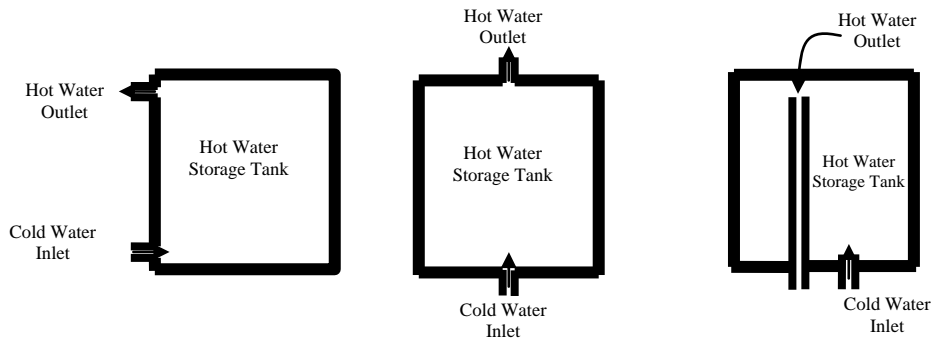


Figure 2. Features of Hot Water Storage Tanks in Markets.

For side supply of cold water, four different flow rates were used 1.9, 3.5, 5.4, and 10 L/min. Figure 3. shows the side supply cooling curves for 15 thermocouples located vertically inside the HWST (see figure1), for cold water flow rate of 1.9 L/min, the total time consumed to fill the tank with its 108 liters was 3410 sec, to cool down all thermocouples to the cold water inlet temperature it took

about 5200 sec due to heat transfer between the cold water and hot water in their mixing process. A non-uniform behavior is observed in the temperature of thermocouples 1 and 2 as a result of the turbulent mixing at the relative levels, this turbulent mixing dominates the mixing heat transfer at this region. Almost all of the other thermocouples are cooled in a uniform way, as the convection heat transfer dominates in the relative region.

Cooling Curves for Cold Water Flow Rate 1.9 L/min

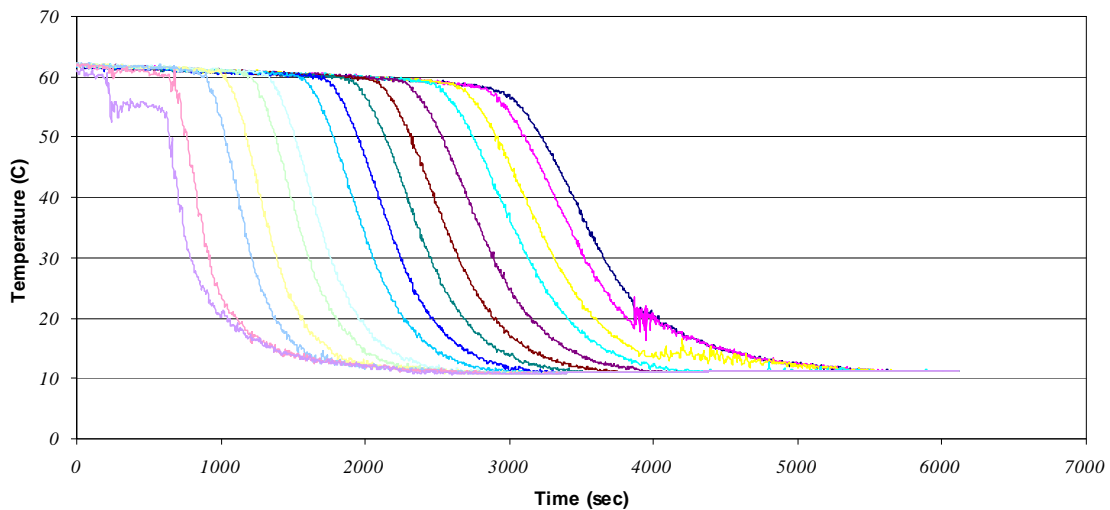


Figure 3 Cooling Curves For Cold Water Flow Rate of 1.9 L/min (side supply).

Figure 4 shows the side supply cooling curves for a cold water flow rate of 10 L/min. It is clear that a large turbulent region and non-uniform cooling curves are existed as a result of the high flow rate entering the HWST. As observed almost all of the cooling curves include a notable oscillation in temperature, this indicates the higher motion of the cold water inside the tank through the mixing process. Also it indicates that at higher flow rates a non-uniform temperature may be obtained from the HWST.

For bottom supply of cold water, again four different flow rates were taken; these are 3, 6, 8, and 9 L/min. Figure 5 shows the cooling curves within the HWST for cold water flow rate of 3 L/min, as it can be observed from figure 5 the first three thermocouples were cooled together, which means that the corresponding flow rate 3 L/min had made a turbulent flow within the first 15 cm of

the HWST. The rest of the thermocouples were cooled in a uniform way. Small oscillations were observed in the temperature at the different levels within the tank, this shows that there is a simple turbulence in the flow within the tank. Figure 6 show the cooling curves within the HWST for cold water flow rate of 9 L/min. It is clear that turbulent mixing is dominant, and almost all the tank gets to have the same low temperature after a short period of time. This means that a short amount of hot water can be used in such a case and the rest of the hot water comes to be with a low temperature which can not be used as hot water.

In general, the heat transfer mechanisms within the entire tank can be divided into two parts, one of which depends on the direct contact between the hot and cold water, and heat then is transferred as a result of convection, the other is resulted from the high flow rate in

Cooling Curves For Cold Water Flow Rate Of 10 L/min

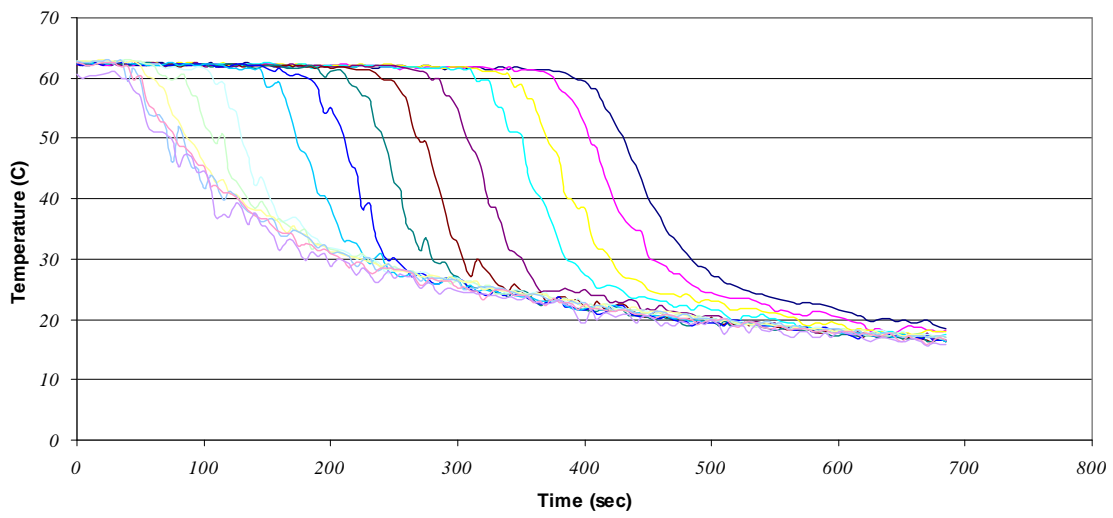


Figure 4 Cooling Curves For Cold Water Flow Rate of 10 L/min (side supply).

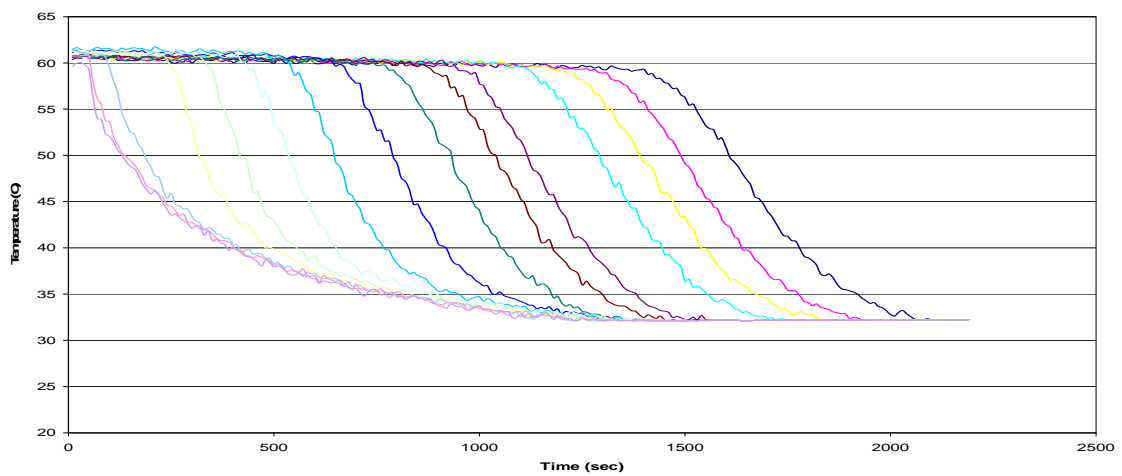


Figure 5 Cooling Curves For Cold Water Flow Rate of 3 L/min (bottom supply).

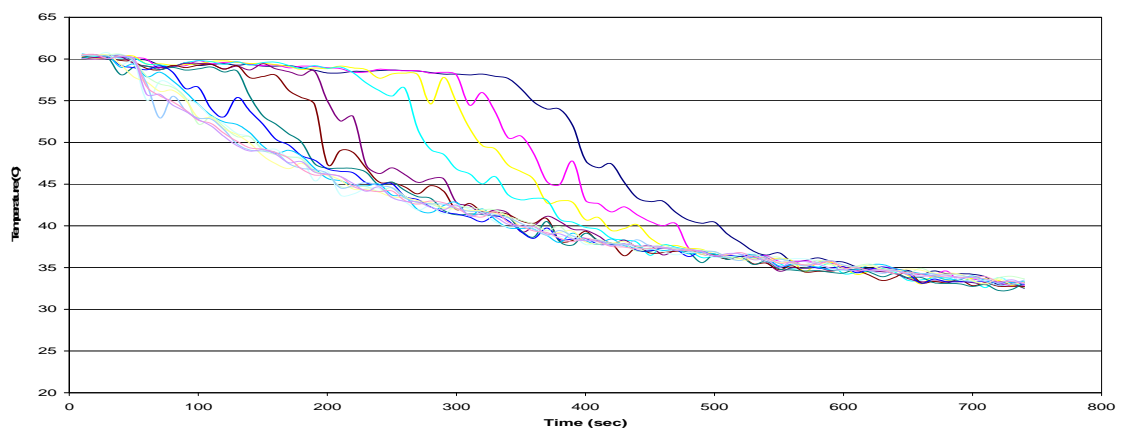


Figure 6 Cooling Curves For Cold Water Flow Rate of 9 L/min (bottom supply).

the relative levels within the tank, this create turbulent mixing of the cold and hot water inside the tank which by its turn accelerates the heat transfer between the cold and hot water layers, and drop significantly the temperature of the hot water that is supplied to consumers.

The total usable hot water available versus the cold water flow rate was drawn for both cases of bottom and side CWS features as indicated by figure 7. It has been observed that in the side CWS and for the flow rates between 1.9 to 10 L/min, a range between 110 to 75 L/min were achieved, where as for the bottom CWS feature and for a cold water flow rates between 3 to 9 L/min, a range between 90 to 55 L/min were achieved. The large drop in the amount of usable hot water is related to the high

turbulent mixing in the case of bottom CWS. Thus the use of bottom CWS in the HWST waste a large amount of the usable hot water as a result of turbulent mixing.

In figure 8, the total delivered energy to the customer was analyzed for both features. It has been found that the energy supplied to the customers ranges from 27000kJ to 19000 kJ, in the side CWS. Whereas, total delivered energy ranges from 21000 kJ to 15000 kJ in the bottom CWS. This result indicates that bottom supply of cold water does not only reduce the amount of the usable hot water, but also reduces the total energy supplied to the consumers, keeping most of the collected energy within the HWST unsuitable for use.

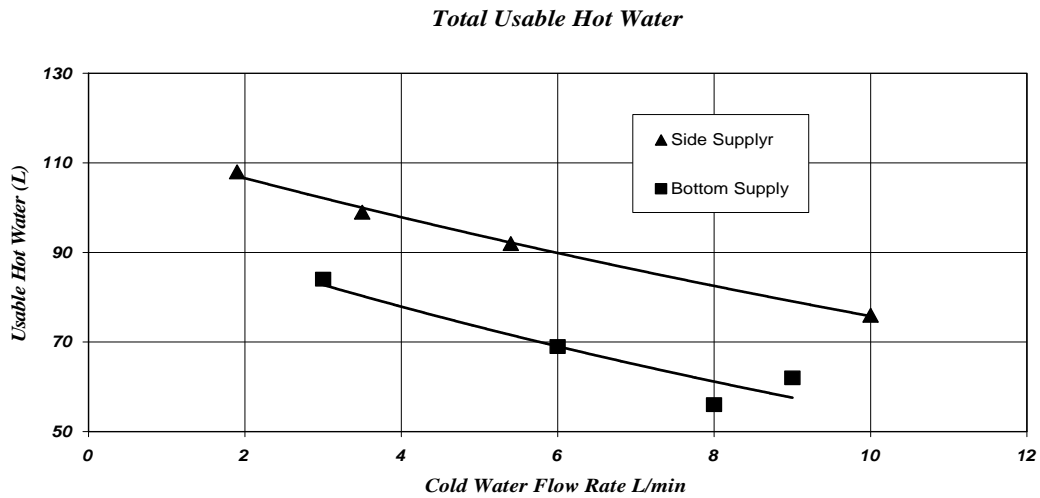


Figure 7 Total Usable Hot Water versus Cold Water Flow Rate for Bottom and Side Supply of Cold Water.

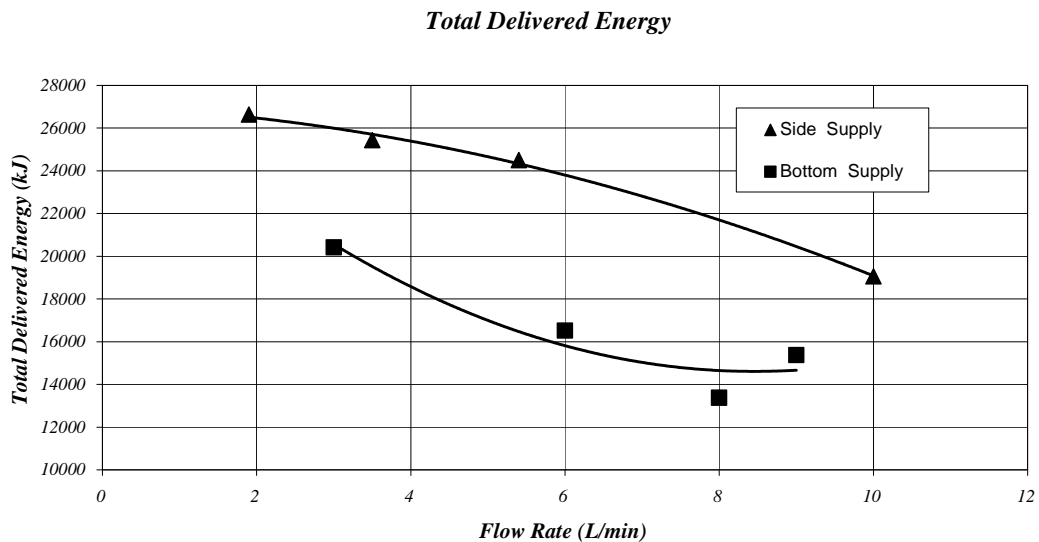


Figure 8 Total Delivered Energy For Bottom and Side Cold Water Supply.

Furthermore, the time required to cool each thermocouple (node as shown in Figure 1) in the HWST was drawn in figure 9. It has been found that for small flow rates the time needed to cool the nodes increases by going from bottom to top of the HWST, whereas, for high flow rates less time was required (as expected [14]).

Figure 9, indicates that for low flow rates the

convection heat transfer is dominant and thus more time will be required to cool the higher levels as the temperature of the higher nodes gets closer to each other thus minimizes the heat transfer rate. At the higher flow rates turbulent mixing heat transfer will dominate which by its turn will reduce the time required to cool the different thermocouple within the HWST.

Time Required to Cool Nodes From 57 C to 42 C

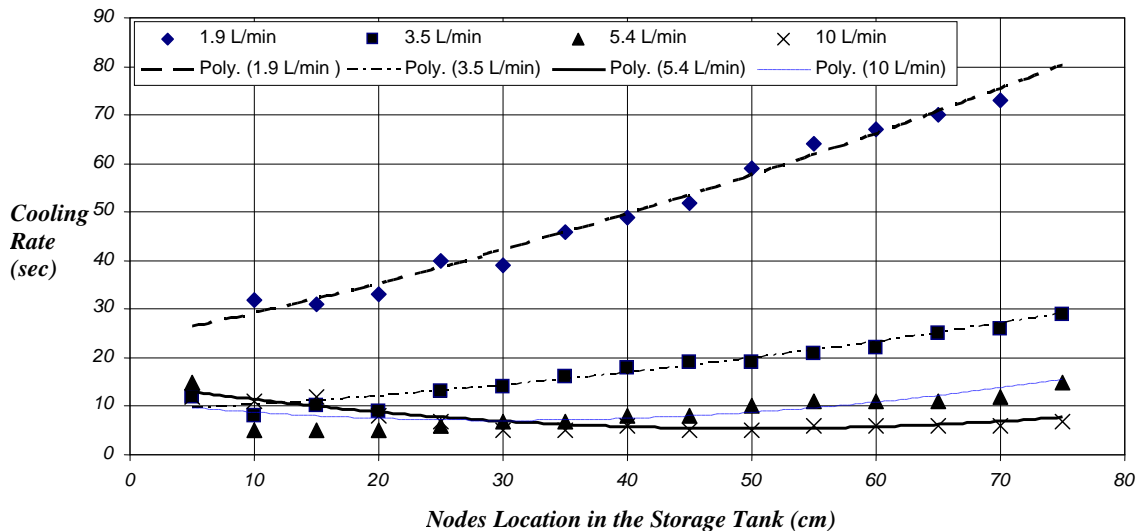


Figure 9 Time Required for Cooling Nodes From 57 °C to 42 °C.

4. Conclusion

Energy conservation is defined as more efficient or effective use of energy. As fossil fuel costs rise and environmental concerns grow, more efficient energy conservation and utilization technologies become cost effective. However, technologies alone can not produce sufficient results without continuing management efforts. This study is directed toward analyzing the heat transfer between the cold and hot water inside the storage tank for both bottom and side CWS features. Experiments Results show that low flow rates save more energy for consumption in both cases. The comparison between the two supply features suggests the use of side CWS which gives higher amount of usable hot water than bottom CWS at the same flow rates. Side CWS also minimize the turbulent mixing within the HWST which by its turn supply higher energy for consumers. For small flow rates convection heat transfer is the dominant mechanism where the turbulent mixing heat transfer dominates at high flow rates. It is clear that the bottom supply feature has a bad effect on the total usable hot water, and there is a need to stop the turbulent mixing in the HWST. A special mechanism to distribute the water as a horizontal uniform layer from the bottom of the tank is currently under investigations.

References

- [1] N. Beithou, "Heat Transfer Aspects in Bottom Flow Mixing of Cold Water and Hot Water in Domestic Hot Water Storage Tank", Accepted for publication Journal of Mechanical Engineering, 2006.
- [2] Sezai, L. B. Y. Aldabbagh, U. Atikol, H. Hacisevki "Performance Improvement by using Dual Heaters in a Storage-type Domestic Electrical Water-Heater", Applied Energy, Vol. 81, pp. 291-305, 2005.
- [3] N. Beithou, "Proposed Water Management and Control Device for Water Losses Problem in Jordan" Accepted for publication, JEES, 2005.
- [4] Wiehagen J., Sikora J.L., "Performance Comparison of Residential Hot Water Systems" NAHB Research Center, Upper Marlboro, Maryland, NREL/2003.
- [5] Barta L., "Energy Conservation of Domestic Hot Water Distribution Systems", 27th International Symposium CIB W62 Water Supply and Drainage for Buildings, September 17-20, 2001, Portoroz, Slovenia.
- [6] Takata H., Murakawa S., Nishina D., and Koshikawa Y., "An Analysis on the Load of Hot Water Consumption in the Apartment Houses", 27th International Symposium CIB W62 Water Supply and Drainage for Buildings, September 17-20, 2001, Portoroz, Slovenia.
- [7] Merrigan, T., "Residential Conservation Demonstration Program: Domestic Hot Water", Florida Solar Energy Center, Cape Canaveral (USA), Technical Report, 2001 May 13.
- [8] Industrial Technologies, "Waste Fluid Energy Recovery System Recycles Waste Energy and Cuts Utility Bills",

- Office of Industrial Technologies, Energy Efficiency and Renewable Energy, US Department of Energy, June 2000.
- [9] Calmeyer JE., Delpont GJ., " Hot water Load Control Within Communal Living Environments Such as Residences and Hostels", Domestic Use of Electrical Energy Conference, Cape Peninsula University of Technology, Cape Town South Africa, 1999.
- [10] Forlee C., " A flexible Hot Water Load Control System", Domestic Use of Electrical Energy Conference, Cape Peninsula University of Technology, Cape Town South Africa, 1999.
- [11] Jing Song, Liang-Jun Ji, Byard D. Wood," Effects of Plumbing Attachments on Heat Losses from Solar Domestic Hot Water Storage Tanks" NREL, March 1998.
- [12] Burch J., Xie Y., Murley C. S.," Field Monitoring of Solar Domestic Hot Water Systems Based on Simple Tank Temperature Measurement" , NREL, May 1995.
- [13] Papakostas, K.T. ; Papageorgiou, N.E. ; Sotiropoulos, B.A," Residential Hot Water Use Patterns in Greece", Solar Energy ; VOL. 54 ; ISSUE: 6 ; PBD: Jun 1995, pp. 369-374 ; PL
- [14] ASHRAE Handbook," Heating Ventilation and Air Conditioning Applications", ASHRAE, Inc., 1995.



الجامعة الهاشمية



المملكة الأردنية الهاشمية

المجلة الأردنية
للمهندسة الميكانيكية والصناعية

JJMIE

مجلة علمية عالمية محكمة

<http://jjmie.hu.edu.jo/>

ISSN 1995-6665

المجلة الأردنية للهندسة الميكانيكية والصناعية

مجلة علمية عالمية محكمة

المجلة الأردنية للهندسة الميكانيكية والصناعية: مجلة علمية عالمية محكمة تصدر عن عمادة البحث العلمي والدراسات العليا في الجامعة الهاشمية بالتعاون مع صندوق دعم البحث العلمي في الأردن.

هيئة التحرير

رئيس التحرير:

الأستاذ الدكتور موسى محسن
قسم الهندسة الميكانيكية، الجامعة الهاشمية، الزرقاء، الأردن .

الأعضاء:

الأستاذ الدكتور عدنان الكيلاني الجامعة الأردنية	الأستاذ الدكتور بلال العكش الجامعة الهاشمية
الأستاذ الدكتور أيمن المعاينة جامعة مؤتة	الأستاذ الدكتور علي بدران الجامعة الأردنية
الأستاذ الدكتور محمد النمر جامعة العلوم والتكنولوجيا الأردنية	الأستاذ الدكتور نسيم سواقد جامعة مؤتة

مساعد رئيس هيئة التحرير:

الدكتور أحمد الغندور
الجامعة الهاشمية

فريق الدعم:

تنفيذ وإخراج
م. أسامة الشريط

المحرر اللغوي
الدكتور عبدالله جرادات

ترسل البحوث إلى العنوان التالي :

ترسل البحوث إلى العنوان التالي:

رئيس تحرير المجلة الأردنية للهندسة الميكانيكية والصناعية
عمادة البحث العلمي والدراسات العليا
الجامعة الهاشمية
الزرقاء - الأردن

هاتف : 00962 5 3903333 فرعي 4147

Email: jjmie@hu.edu.jo

Website: www.jjmie.hu.edu.jo